Dissertation
submitted to the
Combined Faculty of Natural Sciences and Mathematics
of the Ruperto Carola University Heidelberg, Germany
for the degree of
Doctor of Natural Sciences

presented by

M.Sc. Philipp Höß
born in Lindenberg im Allgäu
Oral examination: March 10th, 2021

Towards a dynamic reconstruction of the endocytic machinery by dual-color localization microscopy

Referees: Dr. Alba Diz-Muñoz
Prof. Dr. Michael Knop

„Es geht nicht darum, woher jemand kommt, es geht darum, wie jemand ist."

Christian Streich

Parts of the work described in this thesis have been published

Mund, M., J. A. van der Beek, J. Deschamps, S. Dmitrieff, **P. Hoess**, J. L. Monster, A. Picco, F. Nédélec, M. Kaksonen, J. Ries. 2018. Systematic Nanoscale Analysis of Endocytosis Links Efficient Vesicle Formation to Patterned Actin Nucleation. *Cell* **174(4)**: 884-896.e17.

Thevathasan, J. V.*, M. Kahnwald*, K. Cieśliński, **P. Hoess**, S. K. Peneti, M. Reitberger, D. Heid, K. C. Kasuba, S. J. Hoerner, Y. Li, Y. Wu, M. Mund, U. Matti, P. M. Pereira, R. Henriques, B. Nijmeijer, M. Kueblbeck, V. J. Sabinina, J. Ellenberg, J. Ries. 2019. Nuclear Pores as Versatile Reference Standards for Quantitative Superresolution Microscopy. *Nature Methods* **16(10)**: 1045–1053.

This work was carried out at the European Molecular Biology Laboratory in Heidelberg from October 2016 to December 2020 under the supervision of Dr. Jonas Ries.

Abstract

During the process of clathrin-mediated endocytosis (CME), an invagination of the plasma membrane is formed which finally gets pinched off to form an intracellular vesicle. CME is essential for cellular function as it is important for the uptake of nutrients, regulation of signaling, and membrane homeostasis. The machinery mediating CME consists of more than 50 different proteins which are conserved from yeast to mammals. Dynamic high-resolution studies of CME remain challenging due to the small scale ($\approx 250\,\mathrm{nm}$) and the fast sequence ($\approx 20\,\mathrm{s}$) of the process. This leaves the underlying mechanisms by which spatial rearrangements of endocytic components drive membrane invagination poorly understood.

In this work, we established a new approach to dynamically reconstruct the mobile phase of CME in the budding yeast *Saccharomyces cerevisiae* at the nanoscale from static super-resolution snapshots. The approach is based on dual-color single-molecule localization microscopy (SMLM) of hundreds of endocytic sites that have been fixed at random points along the regular timeline of endocytosis. We introduced a reference structure composed of two endocytic proteins to sort the sites temporally and align them spatially by fitting a geometric model. Imaging of this reference structure in the first channel alongside an endocytic (query) protein in the second channel allowed us to reconstruct the temporal rearrangements of the query protein.

To obtain large datasets with high quality, we increased the throughput of dual-color SMLM by testing different imaging buffers. Sealing of the sample holder turned out to be crucial to maintain good imaging conditions. Furthermore, we developed a computational pipeline to automatically segment and coarsely align endocytic sites from high-throughput datasets. The segmented sites were then fitted with a geometric model based on previous knowledge from super-resolution and electron microscopy studies. This fitting process helped us to retrieve parameters from the SMLM data which were used for spatial and temporal alignment. Importantly, the fitting is only performed on the reference channel, imposing no structural assumptions on the query protein.

We first validated that the reference structure can be used to temporally sort endocytic sites and then successfully demonstrated that our approach can faithfully recover the structural rearrangements of four proteins exemplary for different endocytic modules. Future progress will enable us to integrate multiple datasets into a single dynamic reconstruction of yeast CME with multiple query proteins.

Zusammenfassung

Während Clathrin-vermittelter Endozytose (engl. *clathrin-mediated endocytosis*, CME) wird die Plasmamembran eingestülpt und letztendlich abgeschnürt, was zur Bildung eines intrazellulären Vesikels führt. CME ist essentiell für die Funktion von Zellen, da sie für die Aufnahme von Nährstoffen, die Regulation der Signalübertragung und die Membranhomöostase wichtig ist. Die Maschinerie, die die CME vermittelt, besteht aus über 50 Proteinen, die von Hefe bis zu Säugetieren konserviert sind. Dynamische hochauflösende Studien von CME sind auf Grund der geringen Größe ($\approx 250\,\mathrm{nm}$) und des schnellen Ablaufs ($\approx 20\,\mathrm{s}$) des Prozesses eine Herausforderung. Deshalb sind die Mechanismen, wie strukturelle Veränderungen der Maschinerie die Einstülpung der Plasmamembran antreiben, nur unzureichend verstanden.

In dieser Arbeit haben wir eine neue Methode entwickelt, mit der wir die Dynamik der mobilen Phase von CME in der Bäckerhefe *Saccharomyces cerevisiae* aus statischen hochaufgelösten Einzelaufnahmen rekonstruieren können. Die Methode beruht auf Einzelmolekül-Lokalisationsmikroskopie (engl. *single-molecule localization microscopy*, SMLM) in zwei Farben von hunderten endozytotischen Strukturen, die zu zufälligen Zeitpunkten während des gleichmäßigen Ablaufs der Endozytose fixiert wurden. Die endozytotischen Strukturen beinhalten eine von uns eingeführte Referenzstruktur, die aus zwei markierten Proteinen besteht und uns dabei hilft, die Einzelaufnahmen durch Fitten eines geometrischen Modells zeitlich zu sortieren und räumlich auszurichten. Wenn wir SMLM-Daten von dieser Referenzstruktur zusammen mit einem weiteren endozytotischen Protein im zweiten Kanal aufnehmen, können wir die strukturellen Veränderungen dieses zusätzlichen Proteins rekonstruieren.

Um große Datensätze mit hoher Qualität aufzunehmen, haben wir den Durchsatz der Zweifarben-SMLM gesteigert, indem wir verschiedene Probenpuffer getestet haben. Dabei hat sich die Versiegelung des Probenhalters als entscheidend erwiesen, um gute Bedingungen für die Mikroskopie aufrechtzuerhalten. Außerdem haben wir einen computergestützten Algorithmus entwickelt, um die endozytotischen Strukturen aus den Hochdurchsatz-Daten automatisch zu segmentieren und grob auszurichten. Die Strukturen wurden dann mit einem geometrischen Modell gefittet, das auf Vorwissen aus SMLM- und Elektronenmikroskopie-Studien basiert. Dieser Fitting-Prozess hat uns dabei geholfen, Parameter aus den SMLM-Daten zu gewinnen, die für die zeitliche Sortierung und räumliche Ausrichtung der Strukturen verwendet wurden. Ein wichtiger Punkt dabei ist, dass nur die Referenzstruktur gefittet wird und dadurch die Struktur des Proteins im zweiten Kanal unabhängig ist.

Wir haben zunächst validiert, dass die Referenzstruktur für die zeitliche Sortierung der endozytotischen Strukturen verwendet werden kann, und dann erfolgreich demonstriert, dass unsere Methode die strukturellen Veränderungen von vier unterschiedlichen Proteinen im zweiten Kanal, die exemplarisch für verschiedene endozytotische Module stehen, zuverlässig rekonstruieren kann. Künftige Fortschritte werden es uns ermöglichen, Datensätze mit verschiedenen endozytotischen Proteinen im zweiten Kanal zu einer dynamischen Rekonstruktion der CME in Hefe zu kombinieren.

Acknowledgments

A lot of people have contributed to making the last four years a great experience both in and outside of the lab.

I want to begin by thanking you, Jonas, for hiring me to be part of your group and giving me the opportunity to work on this exciting project. I started with basically no experience in imaging, but you had trust in me to tackle it. Thank you for giving me independence and providing motivation and guidance when things did not work out smoothly. And thank you for involving me in projects additional to my PhD project that allowed me to experience many facets of super-resolution microscopy.

I would like to thank my TAC members Dr. Alba Diz-Muñoz, Prof. Dr. Michael Knop, and Prof. Dr. Carsten Sachse for the advice and discussions during our meetings. Thank you Alba & Michael Knop for reviewing my thesis and thank you Prof. Dr. Andres Jäschke for being part of my defense committee.

Thank you Marko for discussions about the biological side of the project and invitations to Geneva.

Thanks a lot, Markus, for trusting me to continue and extend what you started as your PhD project, for being always available for very valuable scientific input, for introducing me to the (initially) mysteries of super-resolution microscopy, for sharing a room and letting me tag along at the ASCB meetings, and for involving me in the revisions of your PhD paper.

Thank you Yu-Le for tackling the challenges of this project together with me! When I started, it was not entirely clear how we would proceed once I managed to generate large amounts of data. But then one day during the PhD interviews, Jonas told me to talk to you because you would be the perfect fit for the computational side of the project. It turned out that he was right and I'm happy that we convinced you to join the project. I always enjoyed learning about the data analysis from you and discussing how we can improve experimentally and on the analysis side. Apart from that, I always appreciated talking to you about our different cultures and making recommendations for your travels all over Germany.

Merci beaucoup Joran, for the invaluable microscope support over the years, implementing most of my wishes in the microscope control (I'm still waiting for the phone notification when an acquisition is done!), and integrating the magenta LUT in SMAP.

Thank you Ulf for keeping the lab running smoothly and finding creative solutions for every problem.

Thanks to all present and past members of the Ries group that made our lab a pleasure to work in. Thank you Jonas, Markus, Joran, Ulf, Yu-Le, Kostek, Aline, Jervis,

Robin, Yiming, Takahiro, Sheng, Angie, Maurice, Anindita, Sarah, Johanna, Lucas, Andreas, Li-Ling, Eric, Leo, Tomas, Lisa, Jan, Jooske, Vincent, Sudheer, Krishna, Daniel, Alejandro, Amir, Julia, Elena, and Daniel. Together we spent awesome retreats with adrenaline rushes and late night dancing. Special thanks go to the GeoGuessr crew for exploring the world together in an always harmonic atmosphere.

I would like to thank Michael Knop & Matthias Meurer for suggesting and explaining the SGA strategy and providing the relevant strains.

Thank you Marko for the help with the microscopes in the ALMF, especially when I urgently needed to image my strains after the first lockdown, and for giving me the opportunity to broaden my knowledge as trainer in the super-resolution microscopy course.

Thanks to Ulrike & David for sharing your experience and equipment for the testing of primed conversion.

I would like to thank Eric for testing the peptide tags and Nikolay for purifying the SpyCatcher protein.

A big thank you to the people at EMBL that make our lives so much easier: thank you to the media kitchen, the mechanical and electronic workshops and our CBB secretaries Adele & Marjolein.

Thank you Joran & Markus for our FIFA nights and sharing my passion for live sports with trips to Mannheim and Cologne to watch handball & ice hockey and discussing anything sports related from the Tour de France to football clubs owing their existence to energy drinks.

I would like to thank Aline for company and conversation on countless bike tours, especially during the lockdowns.

Thanks to the predoc batch of 2016 for our great symposium, parties and outstation visits. A special thank goes to four of them who became good friends during the last four years: Ana, thank you for sharing your culinary enthusiasm with us, for inviting us to a memorable trip to Belgrade, and for all the *Barbie girl* voice messages. Thank you Esther for organizing our batch's parties, for your entertaining giggles, and for spoiling us with your baking skills. Thank you Fabian (with Corinna & Kjell) for introducing us to the secrets of Cointreau, for infecting me with the Spikeball virus, and for the most memorable wedding. Last but not least, ευχαριστω Dimitris for being an amazing flatmate during the last two years, for joining for some crazy football trips, for always accepting my FIFA challenges, for inviting us to Greece multiple times to experience the Greek way of life during our holidays, and for critically reading this thesis.

Danke an Alex & Lukas für unsere harmonische WG in den ersten zwei Jahren hier in Heidelberg und dass ich euch den Unterschied zwischen Bakterien und Hefe erklären durfte.

Vielen Dank an die Heidelberger Lokalgrupe des CdE für (Wein-)Wanderungen, ESC-Abende, Skifreizeiten und die Reisegruppe Marienkäfer zur PfingstAka.

Danke an das Pub Quiz Team *Pitcher perfect* und das Team von Roundnet Heidelberg für den wichtigen Ausgleich zum Laboralltag.

Merci an die Red Foxes United und ganz besonders Bernd für zahlreiche Auswärtsfahrten mit dem SC!

Danke an meine Freunde aus Freiburger Zeiten die ich während Reisen nach London, Cambridge, San Francisco, Wien und Genf wieder getroffen habe oder die mich in Heidelberg besucht haben.

Zu guter letzt vielen Dank an meine Familie, die mich während meines Weges immer unterstützt hat. Danke Mama, danke Papa und danke Kathrin für alles!

Table of Contents

List of Figures

List of Tables

List of Abbreviations

17×L	17× Linker
2-ME	2-Mercaptoethanol
3D	Three-Dimensional
AF488	Alexa Fluor™ 488
AF647	Alexa Fluor™ 647
ANTH	Ap180 N-Terminal Homology
AOTF	Acousto-Optic Tunable Filter
Arp2/3	Actin related protein 2/3
BAR	Bin, Amphiphysin, and Rvs
BFP	Back Focal Plane
bg	Background
bp	Base pair
BSA	Bovine Serum Albumin
CH	Calponin Homology
CME	Clathrin-Mediated Endocytosis
ConA	Concanavalin A
COT	1,3,5,7-Cyclooctatetraene
cryo-EM	Cryogenic Electron Microscopy
DMSO	Dimethyl Sulfoxide
dNTP	Deoxynucleoside Triphosphate
DTT	Dithiothreitol
EH	Eps15 Homology
ELE	Effective Labeling Efficiency
EM	Electron Microscopy
EMCCD	Electron-Multiplying Charge-Coupled Device
ER	Endoplasmic Reticulum
f.c.	Final concentration
FA	Formaldehyde
FISH	Fluorescence *In Situ* Hybridization
FOV	Field Of View
FPALM	Fluorescence Photoactivation Localization Microscopy
GFP	Green Fluorescent Protein

GLOX	Glucose Oxidase
HEPES	4-(2-hydroxyethyl)-1-piperazineethanesulfonic acid
LatA	Latrunculin A
LED	Light-Emitting Diode
LUT	Lookup Table
MINFLUX	Minimal emission Fluxes
MLE	Maximum Likelihood Estimation
mM	mMaple
mM3	mMaple3
NA	Numerical Aperture
Nb	Nanobody
NPC	Nuclear Pore Complex
NPF	Nucleation Promoting Factor
ns	Not significant
OD_{600}	Optical Density at 600 nm
paFP	Photoactivatable Fluorescent Protein
PAINT	Point Accumulation for Imaging in Nanoscale Topography
PALM	Photoactivated Localization microscopy
PBS	Phosphate-Buffered Saline
PC	Primed Conversion
PCA	Protocatechuic Acid (= 3,4-Dihydroxybenzoic acid)
PCD	Protocatechuate 3,4-Dioxygenase
pcFP	Photoconvertible Fluorescent Protein
PDF	Probability Density Function
PEG	Polythylene Glycol
P_i	inorganic Phosphate
PI(4,5)P_2	Phosphatidylinositol 4,5-bisphosphate
POX	Pyranose Oxidase
PR	Proline-Rich
PSF	Point Spread Function
RESOLFT	Reversible Saturable Optical Fluorescence Transitions
RFP	Red Fluorescent Protein
ROI	Region Of Interest
rsFP	Reversibly photoswitchable Fluorescent Protein
RT	Room Temperature
SC	Synthetic Complete
scRNA-seq	Single-cell RNA sequencing
SDS	Sodium Dodecyl Sulfate
SEM	Standard Error of the Mean
SGA	Synthetic Genetic Arraying
SH3	SRC Homology 3
SIM	Structured Illumination Microscopy

SMAP	Super-resolution Microscopy Analysis Platform
SMLM	Single-Molecule Localization Microscopy
STED	Stimulated Emission Depletion
STORM	Stochastic Optical Reconstruction Microscopy
TH	Tail Homology
TIFF	Tagged Image File Format
TIRF	Total Internal Reflection Fluorescence
Tris	Tris(hydroxymethyl)aminomethane
UV	Ultraviolet
vs.	Versus
w/o	Without
WCA	WH2, Connecting, Acidic
WH	WASP Homology
YPAD	Yeast extract Peptone Adenine Dextrose

1 Introduction

1.1 Super-resolution microscopy

Most of the current biological and medical research would be unimaginable without imaging tools. These tools include, among many others, X-rays for structure determination, medical ultrasound imaging, magnetic resonance imaging in clinic and structural biology, electron microscopy (EM) for ultrastructural analysis of biological specimens, and light microscopy as a versatile tool in cell and tissue biology. Important landmarks in the history of microscopy in biology were the invention of fluorescence microscopy (Heimstädt, 1911) and the progress in the staining of relevant structures, for example, by fluorescently labeled antibodies (Coons *et al.*, 1942).

Over the decades, advances in fluorescence microscopy like confocal detection, TIRF (Total internal reflection fluorescence) illumination, and multiphoton excitation tremendously improved the contrast and application range, but ultimately the resolution was limited by diffraction (Abbe, 1873). This limit, named after Abbe, states that two points in a sample can only be resolved if they have a minimum distance d (Fig. 1.1):

$$d = \frac{\lambda}{2n \sin\theta} = \frac{\lambda}{2\mathrm{NA}}$$

In this equation, λ is the wavelength of the detected light, n is the refractive index of the immersion medium, and θ is the half opening angle of the microscope's objective. The expression $2n \sin\theta$ gets summarized as the numerical aperture (NA), a key characteristic of microscope objectives.

In the last two decades, several techniques have been invented to overcome Abbe's diffraction limit in fluorescence microscopy. In the following sections, I will summarize their principles, applications, advantages, and disadvantages.

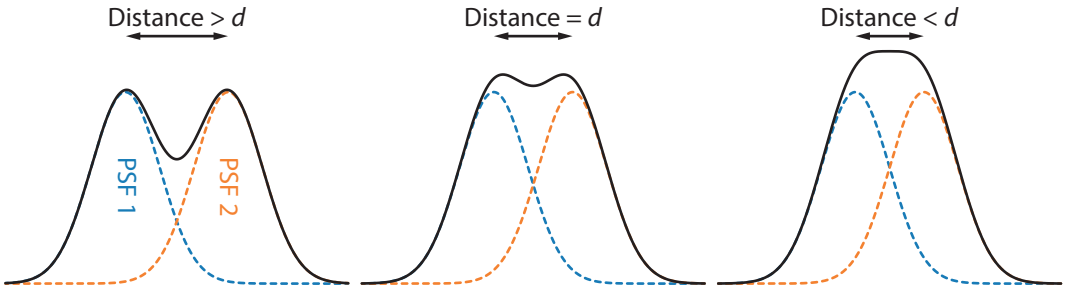

Figure 1.1 | The Abbe diffraction limit. The point spread functions (PSF) of two molecules can be distinguished if they are further apart (left) than the Abbe limit d or just at this distance (middle). If they are closer, they cannot be discriminated if they are imaged simultaneously (right).

1.1.1 Fluorescence

Fluorescence is the phenomenon when an excited molecule returns to a state of lower energy while emitting a photon. In fluorescence microscopy, a fluorophore gets excited from its ground state to a vibrational state of the first excited state when it absorbs a photon that carries the energy that matches the energy difference between these two states (Fig. 1.2A). After non-radiative relaxation from the vibrational state to the first excited state, the fluorophore returns spontaneously to a vibrational state above the ground state while emitting a photon. The return from the vibrational state to the ground state happens again non-radiatively. Because energy is dissipated as heat in these non-radiative decays, the emitted photon has less energy than the one initially absorbed and consequently the wavelength of the emitted photon is red shifted compared to the excitation wavelength. This shift between the absorption and emission wavelength is known as the Stokes shift and exploited in fluorescence microscopy to separate excitation and emission photons (Fig. 1.2B; Lichtman and Conchello, 2005). Some of the super-resolution techniques exploit additional states and transitions by optical or chemical interventions, which will be described in the following sections.

1.1.2 Structured illumination microscopy (SIM)

As the name suggests, in structured illumination microscopy the fluorophores are excited with structured light whose pattern is known. This type of illumination allows the encoding of structural information in the image that has higher spatial resolution than the diffraction limit (Gustafsson, 2000). The superposition of the structure of the sample and the structure of the illumination leads to the occurrence of moiré fringes. These fringes are detected and as the illumination structure is known, it is possible to calculate back the imaged structure in the Fourier space. Repeating this procedure with illumination patterns with different phases allows the retrieval of structural information that brings the resolution down to half the diffraction limit. To achieve the best resolution, the same region of interest has to be imaged with at least six different spatial patterns. Although this requirement makes

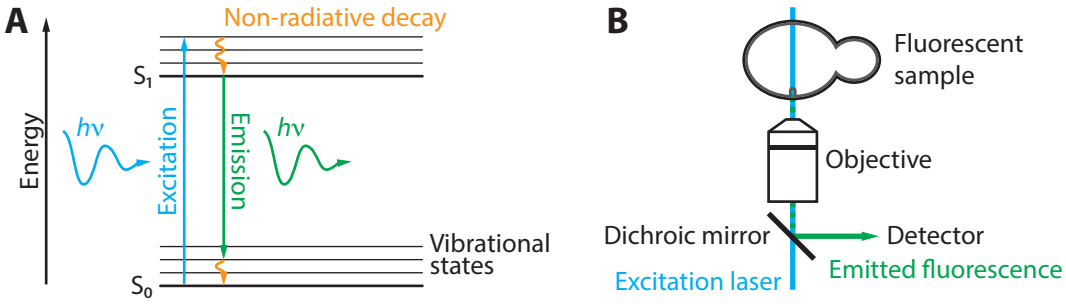

Figure 1.2 | Fluorescence microscopy. (**A**) Jablonski diagram for fluorescence. When a fluorescent molecule absorbs a photon ($h\nu$) with a wavelength that matches its energy levels (blue), it transitions to a vibrational state of its first excited state (S_1). After energy dissipation by non-radiative decay (orange arrow), the molecule transitions to a vibrational state of the ground state (S_0) while emitting a photon (green). Since energy was dissipated during the non-radiative decays, the emitted photon is red-shifted in comparison to the absorbed photon. (**B**) Principle of fluorescence microscopy. A fluorescently labeled sample is excited by a laser, the emitted fluorescence is separated and directed to the detector by a dichroic mirror.

SIM slower than normal wide-field microscopy and increases the light dose, it is the super-resolution technique that is most compatible with living cells (Wu and Shroff, 2018). Additionally, there is no specific requirement for the fluorophores used. However, it is beneficial to choose bright and bleaching resistant fluorophores as these improve the signal-to-noise ratio and imaging duration. The extension of the principle behind SIM to the third dimension results in resolution doubling also in the axial direction (Gustafsson *et al.*, 2008). Further improvements increased the accessibility of thicker samples by simple modifications to a conventional wide-field setup (York *et al.*, 2012) and a new post-processing algorithm with higher sensitivity allowed a lower excitation intensity and therefore decreased phototoxicity and longer imaging time (Huang *et al.*, 2018). Since the post-processing required in SIM makes the method susceptible to artifacts (Schaefer *et al.*, 2004), it is necessary to check for potential artifacts and avoid them (Ball *et al.*, 2015; Förster *et al.*, 2016). SIM has been successfully applied for the visualization of individual nuclear pore complexes (NPC) and localization of NPC components in multi-color three-dimensional (3D) SIM in fixed cells (Schermelleh *et al.*, 2008) and the visualization of mitochondrial cristae in living cells in 3D (Shao *et al.*, 2011).

1.1.3 Stimulated emission depletion (STED)

The method of stimulated emission depletion microscopy can achieve even higher resolutions than SIM. In contrast to the wide-field technique SIM, STED is based on confocal laser scanning, which means that the fluorophores are excited by a laser that is scanned over the sample and the fluorescence is detected pixel-wise by a point detector. Out-of-focus signal is discarded by a pinhole that is installed in front of the point detector. In 1994, it was proposed that transitions of a fluorophore between different states can help to break the diffraction limit by minimizing the effective size

of the point spread function (PSF; Hell and Wichmann, 1994). When illuminated with light of a certain wavelength (red-shifted compared to the excitation and normal emission maxima), a fluorophore in the first excited state can undergo stimulated emission (Fig. 1.3A). During this process, the molecule returns to a vibrational state of the ground state that is higher than the one after spontaneous emission while emitting a photon of the same wavelength that stimulated the emission. Since the spontaneous and stimulated emission result in different energy states of the fluorophore, the emitted light has different wavelengths and can be filtered based on that. In STED microscopy, a diffraction-limited spot gets excited upon illumination with the scanned laser beam. In parallel, a second laser beam with a donut-shaped profile is scanned, meaning it has a radial intensity distribution that is minimal in the center, ideally zero. This beam, which is also called STED beam, quenches all excited fluorophores by stimulated emission except for the ones in the intensity minimum, thereby decreasing the area of the spot that still contains fluorophores in the excited state to a subdiffractive size (Fig. 1.3B). By scanning the two beams over the desired area of the sample, a super-resolved image is generated. In 1999, this concept was successfully exploited to image and separate adjacent nanocrystals (Klar and Hell, 1999). One year later, the first biological specimen, the vacuolar membrane in yeast cells, was visualized (Klar *et al.*, 2000). In theory, the resolution could reach the dimension of detecting a single molecule by decreasing the central zero intensity to an arbitrarily small size. However, the already high intensity of the STED laser would need to be increased even further to achieve this. Since this high energy introduced into the sample is not compatible with biological samples, there is a trade-off between resolution and sample integrity.

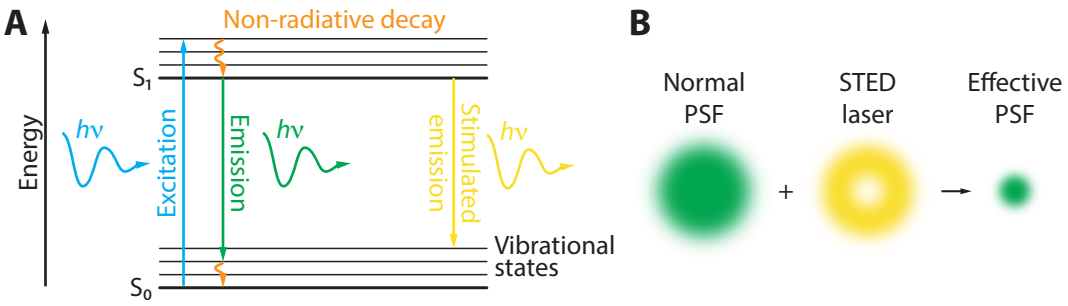

Figure 1.3 | STED microscopy. (**A**) Jablonski diagram illustrating the concept of stimulated emission. An excited fluorophore can be stimulated to return to its ground state by illumination with a laser that is red-shifted compared to the spontaneous emission. During stimulated emission, a photon is emitted that has the same wavelength as the STED (stimulated emission depletion) illumination and therefore can be distinguished from spontaneously emitted photons. (**B**) Illustration of the STED concept. The size of the normal point spread function (PSF) gets effectively reduced by stimulating the emission of fluorophores using a donut-shaped laser (yellow).

The concept of STED is generalized in RESOLFT (Reversible Saturable Optical Fluorescence Transitions). This concept states that the respective fluorescent molecules have at least two distinguishable states and that they can reversibly switch between them, with at least one of these transitions being optically inducible (Hofmann *et al.*,

2005). An example of this concept is the use of reversibly photoswitchable fluorescent proteins (rsFP). These proteins can be switched between a state that is dark (i.e., non-fluorescent) and one that is bright (i.e., fluorescent) in the channel imaged. The switching is induced by illumination with light of a different wavelength than the one used for excitation. The RESOLFT concept with the rsFP asFP595 was first shown in 2005 (Hofmann *et al.*, 2005). This rsFP is excited with yellow light and can be turned off by blue light. Thus, by using a confocal spot of yellow light to excite the fluorescent proteins and a blue donut-shaped laser to switch off all but the ones in the central minimum, the resolution of the resulting image can be substantially increased. One advantage of using rsFPs in RESOLFT instead of organic dyes in STED is that the energy of the depletion laser can be several orders of magnitude lower. Although the transitions are slower and therefore acquisition times are longer, imaging can be sped up by parallelization (Chmyrov *et al.*, 2013). Key parameters of rsFPs that determine their performance in RESOLFT are brightness, switching speed, residual fluorescence in the off-state, and the number of switching cycles they can go through (Jensen *et al.*, 2020).

Both STED and RESOLFT with rsFPs have been extended to 3D by shaping the STED laser in a way that it has a central minimum in three dimensions (Harke *et al.*, 2008; Schmidt *et al.*, 2008; Testa *et al.*, 2012). In recent years, the photodamage of STED (Kilian *et al.*, 2018) has been reduced to allow live cell imaging of intracellular structures that are prone to laser-induced stress, e.g., the endoplasmic reticulum (Schroeder *et al.*, 2018) and mitochondria (Stephan *et al.*, 2019).

1.1.4 MINFLUX

MINFLUX (Minimal emission fluxes) is the newest addition to the group of super-resolution methods. The name is based on the fact that this technique can establish "the coordinates of a molecule with minimal emission fluxes" (Balzarotti *et al.*, 2017). The basis for this method is that at a given time only a single molecule is analyzed. For excitation of the molecule, a donut shaped beam like in STED microscopy but with several orders of magnitude less energy is moved to the initially determined position of the molecule and three more positions around that, equally spaced on a circle with the diameter L. The real position of the molecule is then calculated from the measured intensities at these four positions. For imaging of a fluorescent sample, individual fluorophores are stochastically activated from a dark to a bright state (see section 1.1.6 about localization microscopy for more details). Then, the coordinates of the molecule are determined, the molecule is brought to a dark state, and the next one can be activated and localized. For the tracking of fluorescent molecules on the nanometer scale, the four positions over which the laser beam is scanned are static and the changes in the measured emission are used to calculate back the trajectory of the molecule. Using this configuration, rapid one-dimensional movements of a fluorophore were tracked with a temporal resolution of 400 µs and

a spatial resolution of 2 nm (Eilers *et al.*, 2018). Tracking on the micrometer scale is possible by adaptively updating the scan positions depending on the live calculated trajectory. MINFLUX has the strength of being remarkably fast in localizing a single molecule while using only very low illumination intensities and therefore low numbers of emitted photons. In the ideal case, the position of a molecule can be determined with the highest precision when it is exactly at the center of the donut-shaped beam and does not emit any photons.

The MINFLUX concept was further improved with a larger field of view (FOV) by automatic tiling and an increased resolution by iteratively decreasing the diameter L of the donut beam (Gwosch *et al.*, 2020). Moreover, MINFLUX was extended to simultaneous dual-color detection in three dimensions and applied to imaging of the NPC in living cells (Gwosch *et al.*, 2020). Visualization of the mitochondrial protein complex MICOS using MINFLUX showed indications of a ring-like arrangement at the mitochondrial cristae junctions (Pape *et al.*, 2020). MINFLUX could be further improved by increasing the imaging speed, e.g., by parallelization of many scanned donut-shaped beams. Equally important are considerations on the sample preparation side as with reaching almost molecular resolution, the size of the the label and its distance from the visualized structure become relevant (Gwosch *et al.*, 2020). Recently, a concept similar to MINFLUX, termed MINSTED, has been preprinted that can localize fluorophores that are individually uncaged with a precision of 1 to 3 nm by exploiting the stimulated emission of the target fluorophores (Weber *et al.*, 2020).

1.1.5 Expansion microscopy

Expansion microscopy is a super-resolution method that does not increase the optical resolution, but expands the sample physically to spread out the labeled structures in space. This is achieved by embedding the fixed sample in a polymer network based on acrylamide, which is subsequently swelled by incubation in water (Chen *et al.*, 2015a). Importantly, the biomolecules (protein/RNA/DNA) or labels of interest need to be covalently attached to the polymer to maintain their relative spatial positions in the expanded sample. In the first description of the method, the sample was labeled with dye-coupled antibodies before the expansion and the dyes were covalently linked to the hydrogel (Chen *et al.*, 2015a). Furthermore, for unhindered expansion, the sample needs to be homogenized by unspecific protein digestion, typically this is achieved by proteinase K treatment. Using this protocol on hippocampal tissue, an expansion factor of $\approx 4.5\times$ could be achieved, what resulted in a resolution of 70 nm using a confocal microscope (Chen *et al.*, 2015a).

Avoiding interprotein cross-links allowed to expand the hydrogel without protease treatment, enabling the use of fluorescent proteins and post-expansion antibody staining (Tillberg *et al.*, 2016; Ku *et al.*, 2016). Furthermore, expansion microscopy was applied to multiplexed imaging of RNA by fluorescence *in situ* hybridization

(FISH; Chen *et al.*, 2016; Wang *et al.*, 2018). Incorporation of clickable labels in the structures of interest enabled the visualization of lipids, glycans, RNA, and other biomolecules (Sun *et al.*, 2020).

The expansion could be further increased by iterative expansion microscopy, where in the first expansion step a cleavable cross-linker is used which gets hydrolyzed before the expansion of a second gel. This procedure resulted in an expansion of $4.5\times 4.5 \approx 20\times$ and a resolution of 20 nm (Chang *et al.*, 2017). A similar iterative approach allowed global protein labeling with contrast similar to heavy metal staining in EM (M'Saad and Bewersdorf, 2020). By using a different hydrogel chemistry, a $10\times$ expansion and 25 nm resolution could be achieved in a single step (Truckenbrodt *et al.*, 2018).

One advantage of expansion microscopy is its accessibility as it is inexpensive, does not require advanced knowledge about optics and microscopes, and multi-color imaging is comparably easy to achieve (Tillberg and Chen, 2019). Furthermore, the cleared and expanded sample is transparent and has an isotropic refractive index. This feature makes it ideal for tissue imaging as demonstrated in the initial publication on the hippocampus (Chen *et al.*, 2015a) and many following publications that imaged, amongst others, human tissue samples (Zhao *et al.*, 2017a), neuron circuits in the fruit fly (Guo *et al.*, 2018a), and neuronal proteins in the whole mouse cortex and the whole *Drosophila* brain using expansion microscopy in combination with lattice light sheet microscopy (Gao *et al.*, 2019).

It is important to check that the sample expansion is isotropic to ensure that the structural analysis is not biased by systematic errors. This is possible by imaging the sample before and after expansion, where an error of 1 to 5 % of the measurement length was found down to a scale of 50 nm (Chen *et al.*, 2015a). However, this approach cannot detect errors on smaller scales. To overcome this limit, a structure is necessary whose dimensions are well established by other methods. The NPC is a protein complex with a diameter of ≈ 100 nm and structural features at the sub-50 nm scale which were determined by EM (von Appen *et al.*, 2015). Therefore, it is ideally suited to investigate errors in expansion microscopy at the nanoscale (Pesce *et al.*, 2019; Thevathasan *et al.*, 2019). The results of these studies showed that the global expansion factor is larger than the expansion factor at the scale of the NPC, suggesting further method development is required to achieve uniform expansion.

1.1.6 Single-molecule localization microscopy (SMLM)

1.1.6.1 Principle of localization microscopy

In standard microscopy, all fluorophores in the excited volume fluoresce at the same time, therefore the individual molecules cannot be distinguished (Fig. 1.4A). In single-molecule localization microscopy (SMLM), the emission of individual

fluorophores is separated in time by actively switching them between a dark and a bright state (often referred to as *blinking* of the fluorophores). Imaging data are recorded as movies of thousands of frames, where in each frame only a subset of fluorophores is in the bright state (Fig. 1.4B). These individual fluorophores are further apart from each other than the diffraction limit and therefore their coordinates can be determined with high precision. The coordinates can be calculated by fitting a two-dimensional Gaussian function to each of the blinks (Thompson *et al.*, 2002). By performing this procedure on the whole recorded blinking movie, a large table with parameters like coordinates, the number of photons and background photons, and many more is generated (Fig. 1.4C). From this table, a super-resolved image can be reconstructed whose resolution is improved by about an order of magnitude compared to diffraction-limited microscopy (Fig. 1.4D). There were three initial implementations of this approach: Photoactivated localization microscopy (PALM; Betzig *et al.*, 2006), fluorescence photoactivation localization microscopy (FPALM; Hess *et al.*, 2006), and stochastic optical reconstruction microscopy (STORM; Rust *et al.*, 2006). Compared to the other optical super-resolution microscopy techniques, SMLM has the lowest hardware requirements. It is typically performed on a stable wide-field setup, special components are powerful lasers and a sensitive camera.

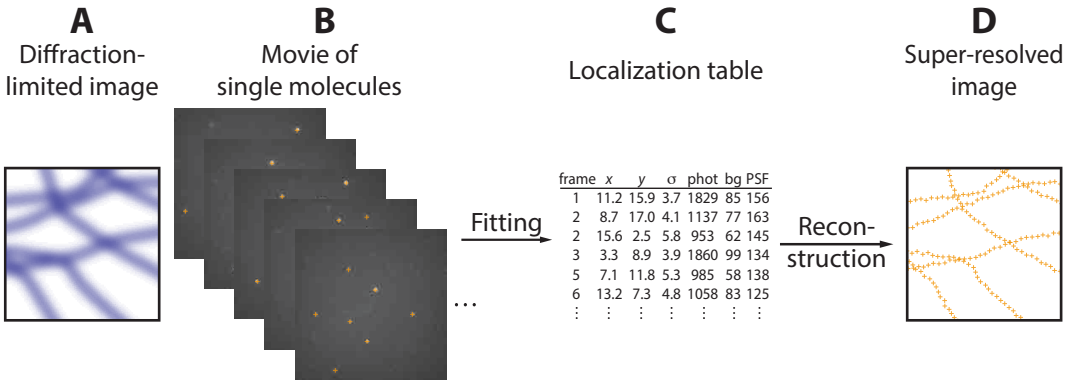

Figure 1.4 | Principle of localization microscopy. (**A**) Diffraction-limited image of cellular structures. (**B**) The blinking of single molecules is recorded over time and their positions are fitted. (**C**) The fitting process results in a table with the coordinates and other parameters of every registered molecule. (**D**) From this table, a super-resolved image can be reconstructed. σ, localization precision; phot, photons; bg, background; PSF, point spread function.

1.1.6.2 Implementations of localization microscopy

The concept of localization microscopy is based on fluorophores that transition between a dark and a bright state. In most implementations, the dark to bright transition is optically inducible. The PALM implementation (Betzig *et al.*, 2006) uses green-to-red photoconvertible fluorescent proteins (pcFPs) whose conversion is induced by a ultraviolet (UV) laser. The UV intensity is kept at a level where only a tiny fraction of the fluorophores are converted to the red channel where they are immediately excited and bleached by a high intensity red laser. In FPALM, the concept is very similar: A photoactivatable fluorescent protein (paFP) is used which

can undergo a dark to bright transition upon UV illumination (Hess *et al.*, 2006). The same type of a UV-induced transition can also be used with photoactivatable organic dyes (see section 1.1.6.6). In STORM (Rust *et al.*, 2006), a dye pair of an activator and a reporter fluorophore is used. When illuminated, the activator is able to induce switching of the reporter fluorophore between a dark and a bright state that can be excited with a laser of a different wavelength (Bates *et al.*, 2005). The concept for these three types of localization microscopy is the same and the distinction by different acronyms was not intended by the authors. In retrospect, the acronyms were assigned to the fluorophores used: (F)PALM for fluorescent proteins and STORM for synthetic dyes. Throughout this work, I will refer to the concept as SMLM or localization microscopy.

The concept of PAINT (Point Accumulation for Imaging in Nanoscale Topography; Sharonov and Hochstrasser, 2006) makes use of fluorogenic molecules. These are molecules that are in the dark state when in solution but turn bright upon binding to the target structure. This approach was generalized in DNA-PAINT (Jungmann *et al.*, 2010): Here, the structure of interest is labeled with identical single DNA strands and the imaging buffer contains the complementary DNA strands attached to a fluorescent dye. Upon binding, the fluorophore gets immobilized and can be recorded as a bright event compared to the dimmer background of the other freely diffusing molecules.

1.1.6.3 Resolution in localization microscopy

The resolution in SMLM depends on two factors: the precision with which the single fluorophores can be localized and the label density (Legant *et al.*, 2016). Under the idealized conditions of no background and small camera pixels, the position of a fluorophore in x and y can be determined with a localization precision $\sigma_{x,y}$ according to the following equation:

$$\sigma_{x,y} = \frac{\sigma_{\mathrm{PSF}}}{\sqrt{N}}$$

where σ_{PSF} is the standard deviation of the fitted Gaussian function, and N is the number of collected photons (Thompson *et al.*, 2002). Besides this resolution on the level of localizing single molecules, the resolution of the final reconstructed image depends on the density of labels on the structures of interest. According to the Nyquist–Shannon sampling theorem (Nyquist, 1928; Shannon, 1949), for a desired resolution, it is necessary to observe a signal at a spatial frequency that is double the resolution. For example, for a resolution of 10 nm in one dimension, the structure of interest needs to be labeled with a spacing of 5 nm. Generalization for multi-dimensional localization microscopy (Shroff *et al.*, 2008) resulted in the following equation to calculate the Nyquist resolution R_{Nyquist}:

$$R_{\mathrm{Nyquist}} = \frac{2}{\sqrt[d]{\rho}}$$

Here, ρ is the localization density in d dimensions. If $R_{\mathrm{Nyquist}} \gg \sigma_{x,y}$, this equation is sufficient to describe the resolution (Legant *et al.*, 2016). However, if both the localization precision and the Nyquist resolution are on similar length scales, the overall resolution R_{overall} can be approximated by the following equation (Legant *et al.*, 2016):

$$R_{\mathrm{overall}} = \sqrt{\sigma_{x,y}^2 + R_{\mathrm{Nyquist}}^2}$$

These equations are based on the Nyquist–Shannon sampling theorem, but there is an important difference between the signal considered in the theorem and the signal in a SMLM experiment. In the theorem, the signal is acquired at regular intervals, whereas the signal in localization microscopy is stochastic (Legant *et al.*, 2016). Therefore, at least fivefold oversampling is necessary to reconstruct images of the structures of interest in high resolution for localization microscopy performed by DNA-PAINT, one of the localization microscopy modalities with the highest resolution (Legant *et al.*, 2016). When directly visualizing single proteins by fusion of self-labeling enzyme tags or fluorescent proteins, not the labeling density but the labeling efficiency is important (Thevathasan *et al.*, 2019).

1.1.6.4 Analysis of high density SMLM data

As described above, localization microscopy relies on single fluorophores that can be clearly distinguished to fit their coordinates. However, with densely labeled samples or if fast imaging is required, e.g., in living specimens, this prerequisite might not be met. For these cases, high-density fitting algorithms have been developed. Multi-emitter fitters can fit overlapping PSFs either by using an approach originally intended for the analysis of crowded stellar fields in astronomy (Holden *et al.*, 2011) or by maximum likelihood estimation (Huang *et al.*, 2011). Other approaches use Bayesian analysis of raw high-density blinking data (Cox *et al.*, 2012) or split the overlapping signals using a temporal component of their blinking behavior (Marsh *et al.*, 2018). Recently, the problem of multi-emitter fitting was also successfully tackled by deep learning (Speiser *et al.*, 2020). For data with very high density, the analysis of intensity fluctuations in the fluorescence signal can be exploited to reconstruct a super-resolved image (Dertinger *et al.*, 2009; Gustafsson *et al.*, 2016).

1.1.6.5 Three-dimensional localization microscopy

The localization of a single bright fluorophore can also be extended to the third dimension by encoding the z-coordinate in the shape of the PSF. In the ideal case, the PSF of a microscope is mirror symmetric with respect to the focal plane, therefore molecules with the same offset above and below the focus cannot be distinguished. This symmetry can be broken by including an element in the detection path of the microscope that itself is asymmetric. For example, this can be done by an astigmatic lens that renders the PSF elliptical in perpendicular directions above and below the focus (Huang *et al.*, 2008). Alternatively, the PSF is turned into a double helix

by introducing a phase mask (Pavani *et al.*, 2009) or the z coordinate is encoded in a self-bending PSF with dual-channel detection (Jia *et al.*, 2014). These methods have been improved by using an experimentally determined PSF compared to using features of the theoretically calculated PSF (Li *et al.*, 2018).

There are also approaches that do not rely on shaping of the PSF. One of them uses the supercritical angle fluorescence, which depends on the z-position of the fluorophore, to retrieve the axial position of the fluorophores (Deschamps *et al.*, 2014; Bourg *et al.*, 2015). This method can also be combined with an astigmatic lens to extend the range in z (Cabriel *et al.*, 2019). Another option splits the signal into two equal parts, but one of them is imaged slightly out of focus on the camera (Juette *et al.*, 2008). The difference in focal planes can then be used to determine the axial position of the detected signal. In interferometric detection, often also referred to as 4Pi configuration, the sample is imaged with two opposing objectives, one above and one below the sample plane (Hell and Stelzer, 1992). The single-molecule signal from both arms is brought to interference, split, and detected on four different detectors (Shtengel *et al.*, 2009; Aquino *et al.*, 2011). Since the signal travels different paths through the two arms of the microscope (one arm for each objective), the interference depends on the length of the traveled path and therefore the axial position of the emitting molecule. Hence, the pattern on the camera can be used to determine the axial position of the fluorophore.

All presented methods to determine the axial position of fluorophores differ in the precision to do so, the precision with which the fluorophore can be localized in x and y after modification of the PSF or splitting of the signal, and the axial range. Due to its ease of implementation and a comparably high resolution in z, astigmatic detection is the standard choice for 3D SMLM.

1.1.6.6 Fluorophores in localization microscopy

The fluorophores used in SMLM are either fluorescent proteins or organic dyes. Fluorescent proteins used in localization microscopy can be subdivided in three classes: photoactivatable fluorescent proteins (paFPs) can undergo a transition from a dark to a bright state, photoconvertible fluorescent proteins (pcFPs) can be switched from one fluorescence wavelength to another (typically green to red), and reversibly photoswitchable fluorescent proteins (rsFPs) can be switched between different emission states multiple times (Bourgeois *et al.*, 2012).

Photoactivatable fluorescent proteins One of the initial implementations of SMLM, FPALM (Hess *et al.*, 2006), used a photoactivatable version of GFP (green fluorescent protein; Patterson and Lippincott-Schwartz, 2002), a paFP that is in the dark state but can be activated to a bright green state by illumination with 405 nm laser light. The mechanism involves the UV-induced decarboxylation of a conserved glutamate in the environment of the chromophore, which leads to an equilibrium

shift towards the fluorescent form of the chromophore (Fig. 1.5A; Patterson and Lippincott-Schwartz, 2002). Later on, also photoactivatable versions of fluorescent proteins in the red spectrum were described, whose activation also involves the decarboxylation of a conserved glutamate residue: PAmCherry (Subach *et al.*, 2009) and PAmKate (Gunewardene *et al.*, 2011).

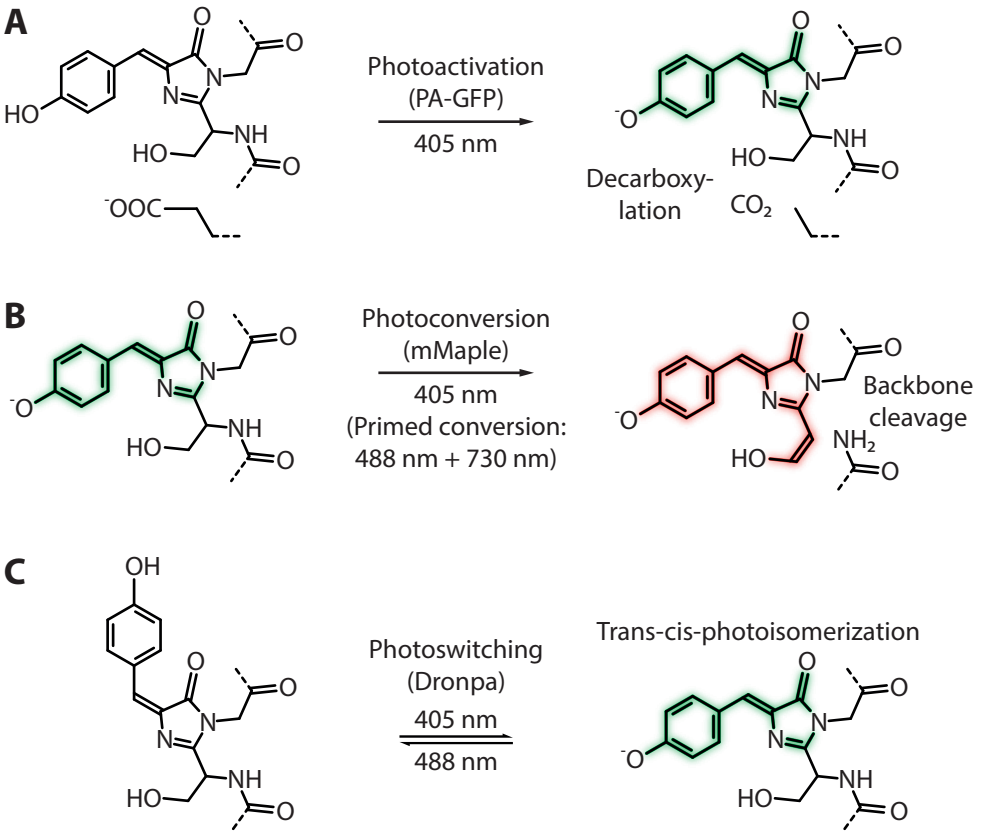

Figure 1.5 | Overview of fluorescent protein transformations used in localization microscopy. (**A**) Photoactivatable fluorescent proteins like PA-GFP undergo a decarboxylation which is induced by a 405 nm laser. The decarboxylation results in an equilibrium shift towards the fluorescent form of the chromophore. (**B**) In photoconvertible fluorescent proteins like mMaple, 405 nm light induces a backbone cleavage that leads to an extension of the conjugated system and therefore a red-shift of the absorption and emission spectra. (**C**) For photoswitchable fluorescent proteins like Dronpa, the mechanism is based on a reversible trans-cis-photoisomerization that is coupled to equilibrium shifts between the fluorescent and non-fluorescent form of the chromophore. The structures were adapted from Shaner *et al.* (2007) and Bourgeois *et al.* (2012).

Photoconvertible fluorescent proteins By contrast, PALM (Betzig *et al.*, 2006) used green-to-red pcFPs to achieve single-molecule blinking. These fluorescent proteins are in a green state and UV illumination causes the cleavage of a peptide bond in the protein's backbone close to the chromophore (Fig. 1.5B). The cleavage leads to the formation of an additional double bond and therefore an extension of the conjugated system, shifting the absorption and emission to higher wavelengths (Bourgeois *et al.*, 2012). The pcFPs initially used for PALM were EosFP (Nienhaus *et al.*, 2005), Kaede, and KikGR (Tsutsui *et al.*, 2005). Over the years, the palette of green-to-red pcFPs was extended by pcFPs that can also be switched by blue light

(Dendra2; Gurskaya *et al.*, 2006), that have higher photostability (mMaple; McEvoy *et al.*, 2012), and that are more monomeric (mMaple3; Wang *et al.*, 2014a). These pcFPs and many more also differ in their expression, maturation, and photophysical properties in different model organisms and at different temperatures, and in their compatibility with different sample preparation and imaging protocols. Therefore, it is important to screen different pcFPs when establishing SMLM in a new organism (Mund *et al.*, 2014). To combine localization and electron microscopy, variants have been developed that retain their photophysical properties also in heavy metal treated EM samples in hydrophilic (mEos4b; Paez-Segala *et al.*, 2015) or hydrophobic resin (mEosEM; Fu *et al.*, 2019).

Primed conversion of pcFPs Some green-to-red pcFPs have an alternative conversion pathway, which is called primed conversion (PC). Instead of conversion by 405 nm light, the fluorophore is first excited in its green form by 488 nm light to a *primed* state which can undergo conversion upon illumination with far-red (730 nm) light (Fig. 1.5B; Dempsey *et al.*, 2015). Therefore, PC has the advantage of not illuminating with a 405 nm laser, a wavelength that is known to induce photodamage in living cells (Wäldchen *et al.*, 2015). If a green-to-red pcFP can also be converted by PC essentially depends on certain amino acids in the environment of the fluorophore, mutation of these enables pcFPs to undergo PC that could otherwise not (Turkowyd *et al.*, 2017). An example for this is mEos3.2, which can undergo PC when alanine at position 69 is replaced by threonine (Turkowyd *et al.*, 2017).

Reversibly photoswitchable fluorescent proteins Dronpa, a member of the third group that can be reversibly switched between a dark and a green state based on a cis-trans-photoisomerization (Fig. 1.5C; Ando *et al.*, 2004), was also successfully used for SMLM (Shroff *et al.*, 2007).

Localization microscopy with mCherry A mechanism that renders the fluorescent protein mCherry photoactivatable was described recently (Cloin *et al.*, 2017). Inclusion of 2-mercaptoethanol (2-ME) in the imaging buffer results in the covalent addition of 2-ME to the chromophore of mCherry leading to a break of the conjugated system and therefore quenching of fluorescence. UV-illumination can break this bond recovering mCherry in its fluorescent state, allowing super-resolution microscopy of target proteins already tagged with mCherry without the need to generate a new construct with a SMLM-compatible fluorescent protein.

The other large group of fluorophores used in SMLM are organic molecules. In contrast to fluorescent proteins, they mainly undergo dark to bright transitions.

Photoactivation of organic fluorophores One way of using fluorescent dyes in localization microscopy is to make existing ones with desirable photophysical properties photoactivatable. This has been successfully achieved for the Janelia Farm

fluorophore series that is based on rhodamines (Grimm *et al.*, 2015). Addition of a small caging group allowed to render two dyes from the red and far-red spectra photoactivatable (Grimm *et al.*, 2016). Another example is a photoactivatable silicon rhodamine that can be activated to the fluorescent state by UV-induced protonation (Frei *et al.*, 2019).

Reaction of organic fluorophores with a thiols The initial description of STORM (Rust *et al.*, 2006) used a pair of cyanine dyes, Cy3 and Cy5, that act as activator and reporter, respectively. Illumination with red laser light (633 nm) generates Cy5 fluorescence but also transfers the fluorophore into a dark state from which it can be recovered when Cy3 is excited by a green laser (532 nm; Bates *et al.*, 2005). Low doses of green light can therefore induce blinking of Cy5 allowing super-resolving the labeled structures. This concept was simplified to a concept named *direct* STORM (*d*STORM) that only uses a single fluorophore instead of the activator reporter pair (Heilemann *et al.*, 2008). The mechanism behind this phenomenon is the reaction of excited Cy5 with thiols to form a thiol-cyanine adduct, most likely the thiol gets added to the polymethine bridge (Fig. 1.6; Dempsey *et al.*, 2009). The adduct represents a long-lived dark state, UV illumination releases the thiol from the adduct, recovering the fluorescence of Cy5. 2-ME or cysteamine are routinely used as thiols, but also the reducing agent TCEP can induce blinking (Vaughan *et al.*, 2013). The reaction scheme is depicted in figure 1.6. Similar mechanisms allow the use of other organic dyes, for example, Alexa Fluor™ 647 (AF647; Dempsey *et al.*, 2009), CF660C, and CF680 (Zhang *et al.*, 2015), for localization microscopy.

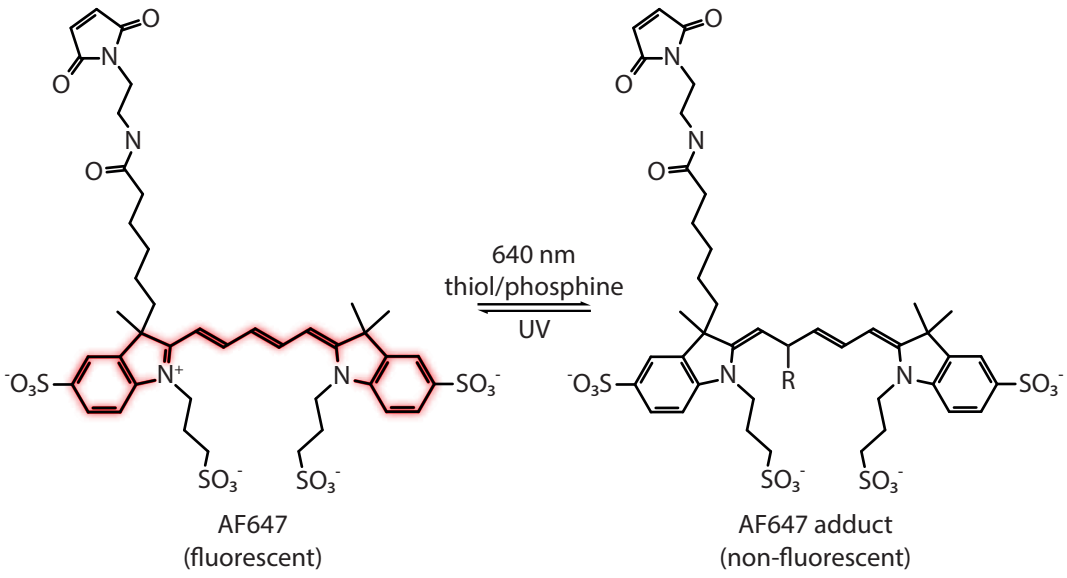

Figure 1.6 | Mechanism of AF647 blinking. Alexa Fluor™ 647 (AF647) in its excited state can react with reducing agents like thiols and phosphines to form a non-fluorescent adduct. The reverse reaction is facilitated by UV illumination. The structure of AF647 was taken from Gebhardt *et al.* (2020) and the reactions with thiols and phosphines were published in Dempsey *et al.* (2009) and Vaughan *et al.* (2013)

Photophysical parameters of organic fluorophores There are several key parameters that have to be taken into account to evaluate the performance of dyes in SMLM. Since the localization precision scales with the inverse square root of the number of photons, the brightness of the fluorophore is an important characteristic. Synthetic dyes outperform fluorescent proteins, as they emit more photons per localization. Furthermore, the on-off duty cycle, or the amount of time that a fluorescent dye is in its on-state (Dempsey *et al.*, 2011), decides on the density of emitting molecules in each acquired frame and therefore the imaging speed. The on-off duty cycle can be modulated by the thiol concentration in the imaging buffer (Dempsey *et al.*, 2011). Photostability of fluorophores and the number of switching cycles they can go through before irreversible photobleaching determine the contrast and completeness of the target structure. However, the number of cycles is typically stochastically distributed, what complicates quantitative analysis (Thevathasan *et al.*, 2019). Finally, the membrane permeability of organic dyes is an important parameter to consider while choosing the labeling strategy (see section 1.1.6.7).

Fluorophores in DNA-PAINT In DNA-PAINT, the blinking mechanism is not based on the fluorophore but on DNA double strand formation, therefore any fluorescent dye can be used. Hence, organic dyes are chosen that are very photostable and bright, e.g., dyes from the ATTO series (Jungmann *et al.*, 2010). Furthermore, the blinking kinetics (on- and off-times) can be modulated by modifying the DNA concentration, the DNA sequence, and the imaging buffer used (Schueder *et al.*, 2019; Strauss and Jungmann, 2020).

1.1.6.7 Labeling strategies for localization microscopy

After introducing the variety of fluorophores used in SMLM, I will present different approaches to label the structures of interest.

Fluorescent proteins The sequences encoding different paFPs and psFPs can be fused to the gene of interest, resulting in the production of a fusion protein (Fig. 1.7A). The easiest way of doing this is by encoding the fusion gene on a plasmid that is transfected into the model system of choice. The gene is then overexpressed additionally to the endogenous copy of the gene of interest, resulting in two major problems: Firstly, unlabeled endogenously expressed genes lead to a decrease in the labeling density of the structure of interest, thereby also decreasing the Nyquist and overall resolution (see section 1.1.6.3). Secondly, overexpression of the gene of interest can lead to aggregation of the translated fusion protein or incorrect subcellular localization (Rizzo *et al.*, 2009). The first problem can be solved by knocking down the endogenous protein using small interfering RNA (Szymborska *et al.*, 2013). Overexpression can be circumvented by using a weaker or the endogenous promoter and introducing the expression construct into the genome, e.g., by use of a lentiviral vector (Tandon *et al.*, 2018). In recent years, tagging of the endogenous

gene has become the gold standard of super-resolution microscopy (Ratz *et al.*, 2015). The advent of genome editing, first by zinc finger nucleases (Urnov *et al.*, 2010) and TALENs (Miller *et al.*, 2011) and then by CRISPR/Cas9 (Jinek *et al.*, 2013), facilitated endogenous tagging and in the meantime it has become a routine task in cell biology (Mali *et al.*, 2013). Importantly, endogenous labeling overcomes both overexpression and signal dilution by endogenous proteins at the same time. However, comprehensive controls are necessary to ensure that protein function is preserved (Koch *et al.*, 2018).

Antibody labeling Antibody labeling is the standard for fluorescence microscopy (Coons *et al.*, 1942) and can also be used for super-resolution microscopy (Rust *et al.*, 2006). The standard procedure involves a primary antibody which detects the structure of interest and a fluorophore-labeled secondary antibody binding to the constant region of the primary antibody (Fig. 1.7B). This system has three main advantages:

- The signal gets amplified because more than one secondary antibody binds to a primary antibody.
- It is modular in the sense that the same secondary antibody can be used to detect different primary antibodies, as long as they have been raised in the same species.
- Using orthogonal primary/secondary pairs from different species allows multiplexing.

However, with the high resolution and detection of single molecules, there are several parameters of antibody labeling that have to be considered. Most importantly, primary and secondary antibodies create a *linkage error* of $> 10\,\text{nm}$ (Fig. 1.7B; Mund *et al.*, 2014), meaning the detected fluorophore is shifted away from the structure of interest. The linkage error can be decreased to $\approx 10\,\text{nm}$ by direct labeling of primary antibodies (Fig. 1.7B; Ries *et al.*, 2012). It can be further reduced by using a directly labeled antigen-binding fragment (Fab) of an antibody (Heilemann *et al.*, 2008). Moreover, for quantitative studies, it is important to know the number of fluorophores per antibody (Nieuwenhuizen *et al.*, 2015). To control and quantify the labeling of antibodies, site-specific protocols have been developed (Jeger *et al.*, 2010).

Nanobody labeling One labeling strategy that decreases the linkage error is the use of fluorophore-coupled nanobodies (Fig. 1.7C). Nanobodies, also called single-domain antibodies, are fragments of antibodies that only contain a variable antibody domain which is typically derived from *Camelidae* (Muyldermans, 2001). Their small size of only $\approx 3\,\text{nm}$ ($\approx 15\,\text{kDa}$) reduces the linkage error below the typically achieved localization precision (Ries *et al.*, 2012). A versatile approach for labeling are nanobodies that bind to an epitope of GFP (Rothbauer *et al.*, 2006; Ries *et al.*,

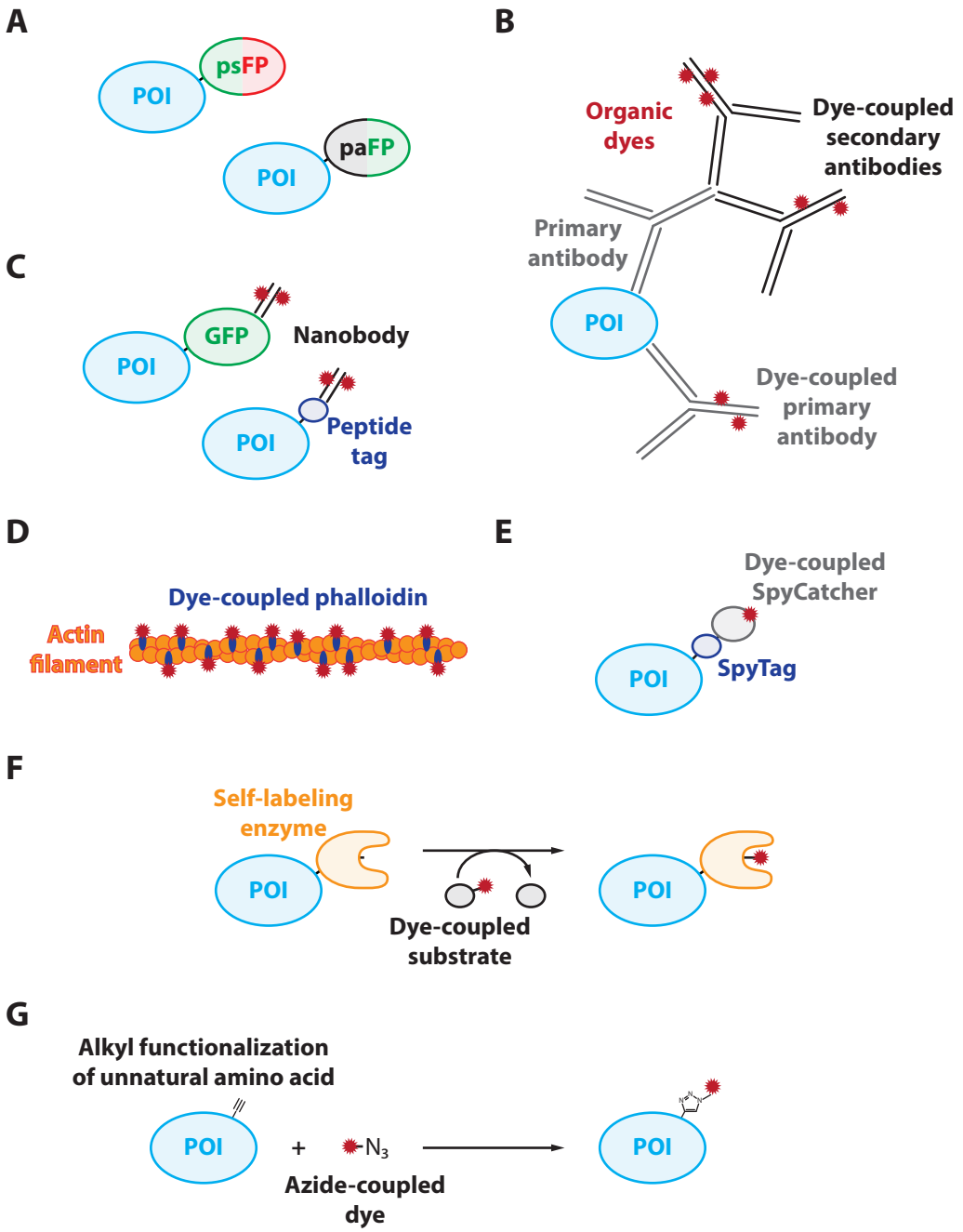

Figure 1.7 | Overview of labeling strategies for localization microscopy. (**A**) The protein of interest (POI) is fused to either a photoswitchable (psFP) or a photoactivatable fluorescent protein (paFP). (**B**) The POI is detected by a primary antibody which is visualized by a dye-coupled secondary antibody. Alternatively, the primary antibody can be directly coupled to the dye to reduce the linkage error. (**C**) GFP or peptide tags fused to the POI can be detected by the respective nanobodies. (**D**) Actin filaments can be visualized by dye-coupled phalloidin. (**E**) SpyTag fused to the POI can be detected by SpyCatcher which covalently binds to the SpyTag. (**F**) Self-labeling enzymes catalyze the covalent addition of the dye from a substrate to themselves. (**G**) An unnatural amino acid that was introduced by amber suppression can be labeled by click chemistry.

2012), since this is the most popular fluorescent protein in the life sciences and cell lines and vectors with tagged proteins are widely used. There are also nanobodies available that target endogenous proteins in wild-type cells, e.g., nanobodies binding to the cytoskeletal protein tubulin (Mikhaylova *et al.*, 2015). Furthermore, nanobodies are available that replace secondary antibodies by binding to primary antibodies from different species, achieving the same linkage error as directly labeled primary antibodies without the cumbersome coupling procedure (Pleiner *et al.*, 2018; Sograte-Idrissi *et al.*, 2020). The design and generation of new nanobodies have been facilitated by different protocols, for example, by a two-step approach exploiting known sequences of the antigen recognizing parts of antibodies (Wagner *et al.*, 2018). Another alternative are nanobodies that bind to small peptide tags that are fused to the gene of interest (Fig. 1.7C). The BC2 nanobody is derived from a nanobody developed against β-catenin (Traenkle *et al.*, 2015). The targeted epitope was identified as a peptide of 12 amino acids, which can be used for labeling of target structures by gene fusion for localization microscopy. Moreover, the labeling density was increased by making the BC2 nanobody bivalent through fusion of two BC2 nanobodies (Virant *et al.*, 2018). The ALFA-tag is a similar epitope tag with a length of 15 amino acids, which was rationally designed, forms an α-helix, and can be detected by a respective ALFA nanobody to perform super-resolution microscopy (Götzke *et al.*, 2019).

Small-molecule binders Apart from nanobodies, there are other small molecules whose specific binding to cellular structures can be exploited for localization microscopy. The fungal toxin phalloidin, which binds to actin filaments and prevents their depolymerization, can be coupled to any fluorophore (Fig. 1.7D; Wulf *et al.*, 1979) and used for SMLM (Xu *et al.*, 2012). Affimers are small proteins that can specifically bind a target with high affinity but are not antibody-based (Tiede *et al.*, 2017). An actin-affimer was shown to allow super-resolution imaging by DNA-PAINT of similar quality as with phalloidin (Schlichthaerle *et al.*, 2018). The alternative actin labeling peptide LifeAct was derived from an actin binding protein (Riedl *et al.*, 2008). Small-molecule binders are also available for other cellular structures. The lectin wheat germ agglutinin was shown to specifically bind to the NPC (Davis and Blobel, 1987) and can be used to visualize its central channel in localization microscopy (Löschberger *et al.*, 2014).

SpyTag/SpyCatcher The SpyTag/SpyCatcher system is a labeling strategy that is comparable to peptide tags detected by nanobodies. It is based on a domain of the protein FbaB from *Streptococcus pyogenes* (hence the name, *Spy*), which forms an intra-domain isopeptide bond between a lysine and an aspartate residue (Zakeri *et al.*, 2012). Isolation of this domain and splitting it into a 13 amino acid epitope tag containing the aspartate residue (SpyTag) and the rest of the domain including the lysine residue (SpyCatcher) resulted in a bipartite system which reacts to form

a covalent bond in minutes (Zakeri *et al.*, 2012). The system was used to perform localization microscopy by purifying SpyCatcher, coupling it to AF647, and using it to detect target proteins tagged with the SpyTag (Fig. 1.7E; Pessino *et al.*, 2017).

Self-labeling enzyme tags The use of self-labeling enzymes for localization microscopy is very powerful, as it combines the low linkage error of direct labeling with bright organic dyes while being genetically encodable. Self-labeling enzymes are small proteins that catalyze the covalent attachment of a specific chemical moiety to themselves (Fig. 1.7F). This enzymatic reaction is even possible after fixation and the chemical moiety can be coupled to organic fluorophores. The first example for this new generation of tags was the SNAP-tag (Keppler *et al.*, 2003). It is based on the human DNA repair protein O^6-alkylguanine-DNA alkyltransferase (hAGT) that removes the alkyl group from a modified guanine nucleotide by transferring it to itself. As its substrate specificity is comparably low, the enzyme also accepts O^6-benzylguanine (BG) instead of O^6-alkylguanine. The combination of BG with a membrane-permeable dye enabled localization microscopy in living cells (Klein *et al.*, 2011). Further developments resulted in a variant of SNAP with faster reaction kinetics, termed SNAP_f (Sun *et al.*, 2011). The HaloTag, which is based on a bacterial haloalkane dehalogenase, works analogously with chloroalkanes as the chemical moiety (Los *et al.*, 2008). A mutant of the enzyme that the SNAP-tag is based on with substrate specificity for O^2-benzylcytosine instead of BG resulted in the generation of the CLIP-tag, which is orthogonal to the SNAP-tag (Gautier *et al.*, 2008).

Unnatural amino acids Direct labeling of proteins without genetic tagging is possible by unnatural amino acids and click chemistry. In this approach, the gene of interest is altered to contain a rare codon (e.g., the amber stop codon). Additionally, a tRNA/aminoacyl-tRNA synthetase pair is introduced in the biological system of choice that is orthogonal to the endogenous pairs (Chin, 2017). The aminoacyl-tRNA synthetase loads the tRNA that recognizes the rare codon with the unnatural amino acid supplied in the medium. The unnatural amino acid carries a side chain functionalized with a small chemical group (e.g., an alkyne group), which can react with a suitable chemical group attached to the dye (e.g., azide; Fig. 1.7G; Milles *et al.*, 2012). Among many other applications, this approach has also been successfully utilized for SMLM (Vreja *et al.*, 2015).

Labeling of DNA and RNA In addition, biological molecules other than proteins can be visualized by localization microscopy. Sequence-specific labeling of nucleic acids by FISH can be combined with localization microscopy (Weiland *et al.*, 2011; Beliveau *et al.*, 2012). The bacterial nucleoid was marked by incorporation of nucleotides bearing a chemical group for click chemistry during replication. Subsequently, the DNA was labeled by addition of a SMLM-compatible dye with the

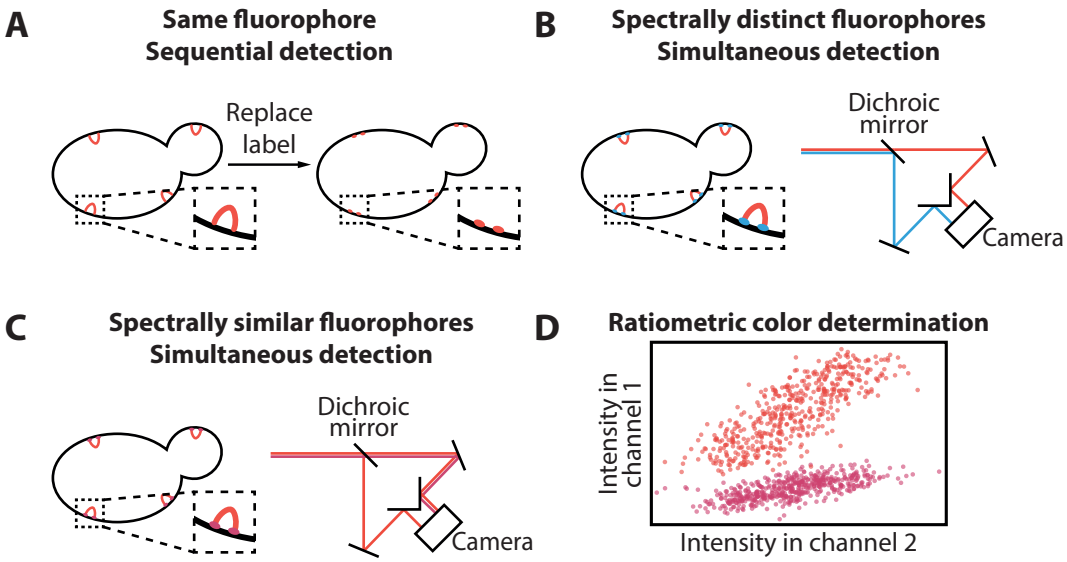

Figure 1.8 | Overview of strategies for dual-color localization microscopy. (**A**) Sequential labeling of different structures with the same fluorophore enables multi-channel super-resolution microscopy without chromatic shifts. (**B**) The signal from two fluorophores with distinct emission spectra can be separated with a dichroic mirror and imaged simultaneously on different parts of the camera. (**C**) For spectrally close fluorophores, the emitted photons can also be split and imaged on different parts of the camera. The respective localizations are detected in both channels, but they differ in their intensities. (**D**) By plotting the intensity in one channel vs. the other, the color can be assigned based on the intensity ratio.

corresponding chemical group (Spahn *et al.*, 2014). For RNA, an aptamer was developed that transiently binds a fluorogenic dye (Sunbul *et al.*, 2020). Fusion of the aptamer to the RNA of interest allows localization microscopy by PAINT.

1.1.6.8 Multi-color localization microscopy

When extending localization microscopy to multiple colors, several pitfalls have to be considered. The different fluorophores need to undergo their on-off transitions under the same conditions, possibly a compromise between the ideal conditions for both molecules has to be found. Such compromise or optical manipulation of the emitted light might result in lower localization precision compared to single-color imaging of the individual dyes. Multi-color imaging of spectrally distinct fluorophores can lead to chromatic aberrations which need to be corrected (Möckl and Moerner, 2020). Additionally, when different channels are imaged on different parts of the camera or different cameras, registration of the channels is necessary, what results in inevitable errors on the order of several nanometers. Finally, cross-talk between the channels must be considered. In the following, different approaches will be described that cope with these limitations in different ways.

Sequential acquisition of fluorophores To avoid spectral cross-talk, chromatic aberrations, and different blinking kinetics, the easiest solution is using the same fluorophore for all channels (Fig. 1.8A). The first implementation of this approach was based on STORM (Rust *et al.*, 2006). The original activator reporter pair was

extended by two more activator fluorophores that get excited with light of different wavelengths, while the reporter fluorophore was the same for all three. This setting enabled triple-color imaging of a model DNA sample and dual-color imaging of microtubules and clathrin-coated pits (Bates *et al.*, 2007). *d*STORM was expanded by performing multiple rounds of staining and imaging of the same fluorophore (Tam *et al.*, 2014; Valley *et al.*, 2015). This was achieved by preparing a single-color sample, imaging it, photobleaching and quenching all fluorophores, and relabeling the next structure before starting this cycle over again for a total of five different channels. Another option for sequential detection in the same wavelength range is the combination of primed and UV-mediated conversion of pcFPs (Virant *et al.*, 2017). Imaging of the first pcFP by PC followed by UV activation of a second pcFP, which cannot undergo PC, enables dual-color SMLM with fluorescent proteins. In DNA-PAINT, the pairing of label and dye is encoded in a DNA sequence, therefore multiplexing is easily possible by variation of the sequence (Jungmann *et al.*, 2014). After the sample has been labeled with antibodies bearing different single-stranded DNA, the structures can be super-resolved sequentially by exchanging the imaging buffer and replacing it with the next complementary DNA-PAINT imager strand, hence the name Exchange-PAINT (Jungmann *et al.*, 2014). The buffer exchange can be automated by microfluidics, e.g., by an open-source system based on LEGO® (Almada *et al.*, 2019). In an extreme case that does not involve single-molecule blinking, 100s to 1000s of RNAs were detected by automation of sequential acquisitions and post-processing with an error-robust encoding scheme (Chen *et al.*, 2015b). One drawback of sequential acquisition schemes is the lack of a structure visible throughout the acquisition that can help with drift correction. Therefore, in these approaches, fiducial markers need to be included to correct for thermal drift occuring during the experiment (Jungmann *et al.*, 2014).

Simultaneous acquisition of spectrally distinct fluorophores The emission of fluorophores that are spectrally distinct can be split by a dichroic mirror and imaged on two different parts of the camera (Fig. 1.8B). Compared to spectrally similar fluorophores, cross-talk between the two channels is less problematic. However, a transformation between the two channels has to be determined before to be able to merge them. Dual-color SMLM with spectrally distinct fluorophores was first shown combining the rsFP rsFastLime with the organic fluorophore Cy5 (Bock *et al.*, 2007) and the two pcFPs Dronpa and tdEos (Shroff *et al.*, 2007). The two organic fluorophores AF647 and AF750 were imaged together in a modified imaging buffer (Zhao *et al.*, 2015) and AF647 could be combined with the pcFP mMaple in mammalian cells (Hoess *et al.*, 2018) and yeast (Mund *et al.*, 2018). For the combination of AF647 and mMaple, one has to compromise on the thiol concentration in the imaging buffer since the presence of thiol worsens the photophysical behavior of mMaple.

Simultaneous acquisition of spectrally similar fluorophores For spectrally similar fluorophores, the emitted fluorescence is also split by a dichroic mirror and imaged separately (Fig. 1.8C). However, the dyes cannot be fully separated as their emission spectra are overlapping. Therefore, they are detected on both parts of the camera. The different dyes are distinguished by calculating the intensity ratios between the two channels (Fig. 1.8D). This way of assigning a localization to a channel is termed *ratiometric* detection. Based on this approach, SMLM with three (Bossi *et al.*, 2008) and four colors is possible (Testa *et al.*, 2010). By splitting the emitted fluorescence 50/50 and including a prism in one of the following beam paths, the spectrum of the emission of a single molecule can be split up, imaged on the camera, and the identity of the dye can be determined during post-processing, while the x and y coordinates are determined from the unmodified localization spot (Zhang *et al.*, 2015). One disadvantage common to all these approaches is splitting of the signal, which decreases the localization precision in x and y. This limitation was overcome by analyzing the fluorescence that gets reflected by the main dichroic of the microscope (Zhang *et al.*, 2020). The largest part of the fluorophore's emitted fluorescence is transmitted through the main dichroic, but a small amount is reflected and usually discarded. After filtering out the reflected excitation laser, this *salvaged fluorescence* can be imaged on a separate sensitive camera and used to assign colors to molecules imaged in the normal detection path.

1.1.6.9 High-throughput SMLM studies

Because of comparably long individual acquisitions (minutes to hours), the throughput in SMLM is rather low. However, there have been several examples that increased the throughput by automation, larger FOVs, and faster imaging (Mahecic *et al.*, 2019) that will be described in the following. Moreover, important considerations about illumination and post-processing will be introduced.

Microscope automation & homogenous illumination To be able to let the microscope run autonomously, a constant blinking density and therefore activation of the fluorophores needs to be ensured. This can be achieved by an algorithm that counts or estimates the number of fluorophores in each frame. The count is then compared to a target and the UV power is adjusted in real-time to meet the target (Kechkar *et al.*, 2013; Mund *et al.*, 2018). Based on this, multiple regions of interest (ROIs) that were pre-selected (Beghin *et al.*, 2017; Mund *et al.*, 2018; Deschamps and Ries, 2020) or defined by automated cell detection (Holden *et al.*, 2014) are imaged sequentially. In most cases, high-throughput microscopy is followed by quantitative analyses. To ensure that the SMLM data has no field-dependent bias caused by differences in illumination intensity in large FOVs, a homogenous illumination of the whole FOV is desirable. In the last years, this was achieved for multi-mode lasers by a commercial speckle reducer (Deschamps *et al.*, 2016), a new laser combiner (Zhao *et al.*, 2017b), and a vibrational mixing of the laser modes by an imbalanced

motor (Schroeder *et al.*, 2019). For single-mode lasers, homogenous illumination was accomplished by a rotating diffuser in combination with two microlens arrays (Douglass *et al.*, 2016) and a commercial beam-shaping device that allowed SMLM in TIRF configuration (Stehr *et al.*, 2019).

Increase of acquisition speed The speed of the acquisition can be increased by either a larger FOV or faster imaging. The first development that allowed larger FOVs in SMLM was the use of sCMOS (scientific Complementary Metal Oxide Semiconductor) cameras with a large chip and fast readout. Their use for single-molecule studies was enabled by algorithms that correct the pixel-dependent readout noise (Huang *et al.*, 2013). Homogenous illumination with multi-mode lasers (see previous paragraph) allowed to exploit the larger detection FOVs. Other implementations with large FOVs are based on waveguides (Diekmann *et al.*, 2017; Archetti *et al.*, 2019) and fast scanning of the laser over the FOV (Mau *et al.*, 2020). It was shown that fast switching of fluorophores using very high laser powers combined with a fast acquisition rate can decrease the imaging time of a single FOV to several seconds (Lin *et al.*, 2015). Using these acquisition parameters allowed imaging of 10 000 cells in 26 h (Barentine *et al.*, 2019). However, a very high illumination intensity reduces the number of localizations per fluorophore and the effective labeling efficiency (ELE) by increasing the rate of irreversible photobleaching (Diekmann *et al.*, 2020).

Imaging buffer for long-term SMLM Another limitation of high-throughput localization microscopy is sample durability. During the whole imaging session, the sample quality and thus also the blinking behavior of the fluorophores should stay at an optimal level. For SMLM based on fluorescent proteins, this can be achieved fairly easy as there are no special buffer requirements. When evaporation is prevented, the sample can be imaged for several days (Mund *et al.*, 2018). For organic dyes, however, the imaging buffer has to be devoid of oxygen and supplemented with a thiol to mediate blinking. The removal of oxygen is necessary to prevent reaction of the dye in its triplet state with molecular oxygen. The routinely used enzymatic system to remove oxygen from the buffer is the glucose oxidase (GLOX)/catalase system (Heilemann *et al.*, 2005). The GLOX catalyzes the reaction of molecular oxygen with glucose to hydrogen peroxide and gluconolactone which spontaneously hydrolyzes to glucuronic acid (Fig. 1.9A). The hydrogen peroxide is detoxified by catalase to water and half a mole of O_2 (Fig. 1.9B). As the accumulation of glucuronic acid leads to an acidification of the imaging buffer over time, the GLOX system is not ideal for long-term imaging. A system based on pyranose oxidase (POX) represents a good alternative because it catalyzes the oxidation of glucose to 2-keto-glucose with hydrogen peroxide as a by-product that gets degraded by catalase (Fig. 1.9C; Swoboda *et al.*, 2012). The product 2-keto-glucose is stable, hence the imaging buffer is not acidified. Another enzymatic oxygen scavenging system is based on protocatechuate 3,4-dioxygenase (PCD), which catalyzes the oxidation of 3,4-dihydroxybenzoic acid

to 3-carboxy-cis,cis-muconic acid (Fig. 1.9D; Patil and Ballou, 2000; Aitken *et al.*, 2008; Shi *et al.*, 2010). The commercially available OxyFluor™ consists of membrane fragments from *Enterococcus coli* containing enzymes that reduce the concentration of O_2 (Ho *et al.*, 2003), and this system has been successfully used for SMLM experiments (Nahidiazar *et al.*, 2016). Moreover, the addition of inorganic sulfite that reacts with molecular oxygen to sulfate (Fig. 1.9E) is compatible with SMLM and it is a good alternative in refractive index-matched index buffers containing high concentrations of glycerol (Hartwich *et al.*, 2018).

Post-processing High-throughput SMLM generates large amounts of raw data, especially when imaging is performed at high frame rates, where several 10s of TB per day can accumulate. This was dealt with by online compression of the data and distributed storage and analysis (Barentine *et al.*, 2019). In cases where the amount of data allows it, manual data management is possible. Furthermore, analysis of SMLM data was performed similar to that of high content screening (Beghin *et al.*, 2017).

1.1.6.10 Quantitative analyses of SMLM data

SMLM images and the tables of localizations with all their different parameters allow a variety of quantitative analyses (Wu *et al.*, 2020). However, in comparison to image analysis in standard microscopy techniques, the stochasticity of blinking events and background has to be taken into account. To quantify clustering, methods from spatial statistics like Ripley's K-function (Owen *et al.*, 2010) and pair-correlation analysis (Sengupta *et al.*, 2011) were exploited. Furthermore, dual-color localization microscopy was used to verify the clustering of transferrin receptors (Arnold *et al.*, 2020). Segmentation of clusters on the level of localization coordinates can, for example, be achieved by the DBSCAN algorithm (Endesfelder *et al.*, 2013) or topological analysis of the data to perform persistence-based clustering (Pike *et al.*, 2019). Colocalization of molecules can be analyzed in single- (Malkusch *et al.*, 2012) and multi-color (Rossy *et al.*, 2014) as well as using tessellation-based colocalization analysis extended to the third dimension (Levet *et al.*, 2019). Geometric analysis of the structure of interest is popular in the evaluation of SMLM data. For example, a Gaussian distribution can be fitted to a cross section of a cytoskeletal element to quantify its apparent size (Xu *et al.*, 2012). In another example, the diameter of NPCs was quantified for each individual protein complex by fitting it with a ring-shaped model (Thevathasan *et al.*, 2019).

The visualization of single molecules in localization microscopy allows their counting, especially when fluorescent proteins are used. However, undercounting due to incomplete fluorophore maturation and overcounting caused by fluorophore blinking have to be taken into account when translating localization counts to molecule

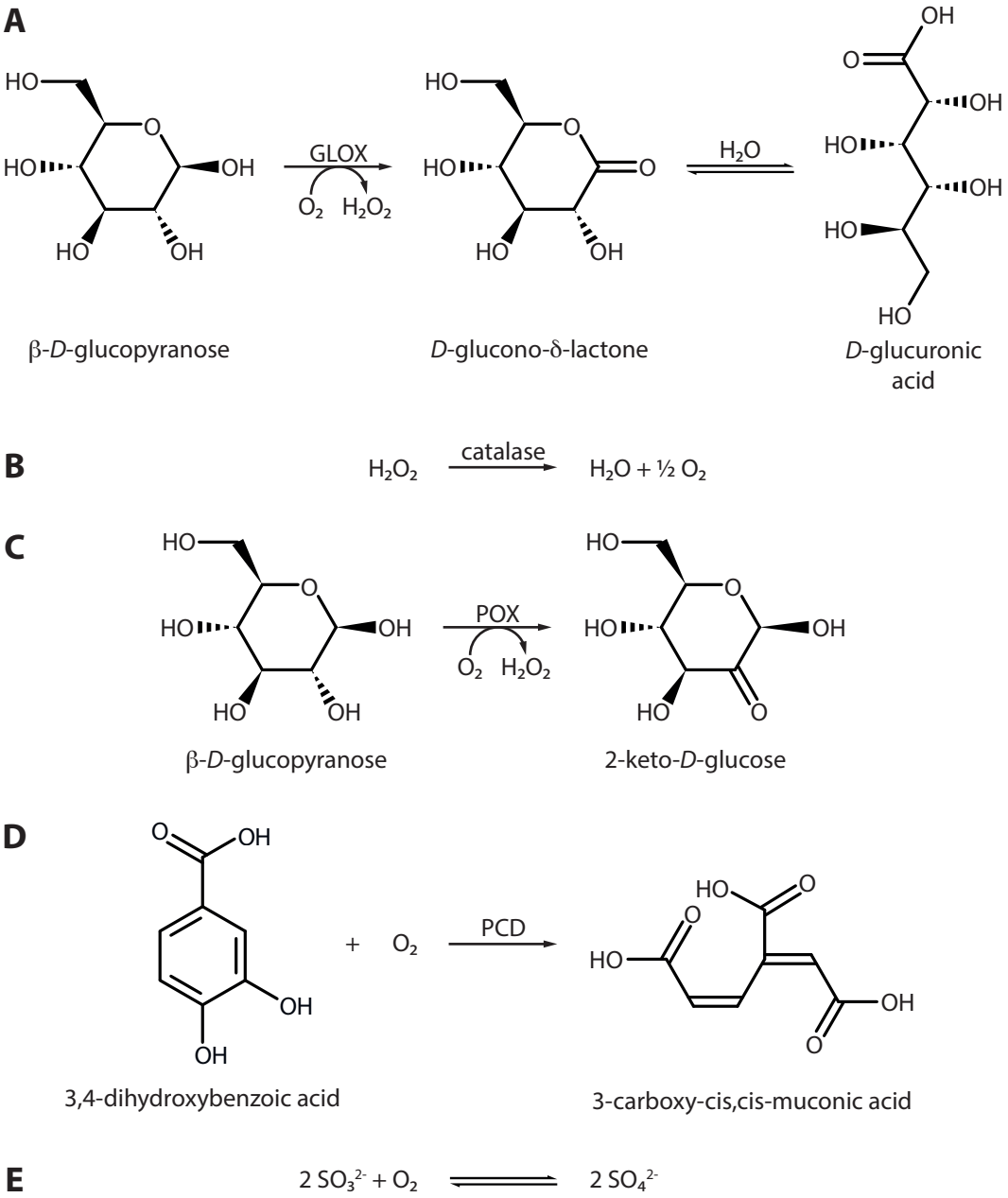

Figure 1.9 | Overview of oxygen scavenging systems. Reaction schemes of (**A**) glucose oxidase (GLOX), (**B**) catalase, (**C**) pyranose oxidase (POX), and (**D**) protocatechuate 3,4-dioxygenase (PCD). (**A**) After the oxidation of β-*D*-glucopyranose to *D*-glucono-δ-lactone, the latter gets hydrolyzed spontaneously to *D*-glucuronic acid. (**B**) Catalase detoxifies the generated hydrogen peroxide produced by GLOX or POX. (**C**) POX oxidizes β-*D*-glucopyranose to 2-keto-*D*-glucose which is stable in aqueous solution. (**D**) PCD oxidizes 3,4-dihydroxybenzoic acid to 3-carboxy-cis,cis-muconic acid. (**E**) Oxidation of sulfite to sulfate.

counts. For paFPs, this was achieved by setting up a model for the observed blinking kinetics (Lee *et al.*, 2012). Similarly, DNA-PAINT was exploited for counting of molecular numbers (Jungmann *et al.*, 2016). An alternative to photophysical models is to perform a calibration that helps to relate the counted localizations to the number of molecules. Examples for this approach are the introduction of labeled homo-oligomers of known stoichiometry (Finan *et al.*, 2015) or the use of subunits of endogenous protein complexes with known stoichiometry, like components of the NPC (Thevathasan *et al.*, 2019), to exploit their number of localizations as a reference to determine the unknown number of proteins in a target structure. Moreover, for structural analysis of protein complexes, a single particle reconstruction pipeline from EM (Sieben *et al.*, 2018) and template-free particle fusion in two and three dimensions (Heydarian *et al.*, 2018; Heydarian *et al.*, 2019) were applied to the centrosome and the NPC, respectively.

1.1.6.11 Biological applications of SMLM

Application of localization microscopy led to many new insights in the life sciences. Here, I want to highlight some selected examples where SMLM was the key to elucidate subcellular structures that were not resolvable with conventional microscopy. Kanchanawong *et al.* (2010) mapped the nanoscale organization of focal adhesions by imaging nine different proteins, for three of them both N- and C-terminus, by 4Pi-based 3D-SMLM. In addition, periodic patterns in the actin and spectrin network in axons were revealed by three-dimensional localization microscopy (Xu *et al.*, 2013). SMLM of different proteins of the same subcomplex of the NPC together with averaging of individual NPCs elucidated the orientation of this subcomplex within the NPC (Szymborska *et al.*, 2013). Bax is a key protein in the apoptotic pathway and is involved in the permeabilization of mitochondria to release cytochrome C. By using localization microscopy, it could be shown that Bax forms rings and arcs on the mitochondrial outer membrane (Salvador-Gallego *et al.*, 2016). Moreover, dual-color SMLM of the synaptonemal complex in *C. elegans*, a structure important for the homologous pairing of chromosomes in meiosis, helped with mapping different proteins of the complex to generate a 3D model (Köhler *et al.*, 2017; Hurlock *et al.*, 2020).

1.1.7 Combination of super-resolution modalities

The combination of different super-resolution techniques extends the boundaries of microscopy even more. The combination of expansion microscopy and SIM facilitated analysis of the cytoskeleton of the human pathogen *Giardia* by annotating the localization of proteins in the adhesive disk (Halpern *et al.*, 2017). Furthermore, performing SIM and STED on expanded isolated centrioles unveiled nanoscale structures that were previously only observed by EM (Gambarotto *et al.*, 2018). The use of charged hydrogels in expansion microscopy makes the method incompatible with

SMLM as the salty imaging buffer would result in shrinkage of the gel. However, embedding the expanded sample in a neutral hydrogel overcame this obstacle and allowed to combine these two super-resolution methods (Zwettler *et al.*, 2020). Combining a structured illumination pattern with the localization of single molecules to further increase the resolution has recently been named modulation enhanced localization microscopy, the fourth optical super-resolution method after SIM, STED, and SMLM (Reymond *et al.*, 2020). The concept encompasses MINFLUX (section 1.1.4), and four implementations of a SIM-like sinusoidal illumination pattern that is displaced during localization of single emitters. (Reymond *et al.*, 2019; Gu *et al.*, 2019; Cnossen *et al.*, 2019; Jouchet *et al.*, 2019).

1.2 Extraction of dynamic information from static data in biology

Many approaches used in the life sciences are only able to detect a static snapshot of a dynamic process. On the one hand, this is because high resolution techniques in microscopy are inherently slower than the studied process or because they can only be applied to static structures. On the other hand, some methods are destructive, meaning the same sample cannot be reanalyzed at a later time point. However, to obtain insights into the functions of biological processes, dynamic information like structural rearrangements or cell lineages are required. In the following, I want to highlight a few examples where dynamic information was retrieved through the analysis of static data.

Staging of limb development at the macroscale Describing the stage of embryonal development by the age of the embryo is inaccurate as the timing of conception is hard to estimate and the developmental speed of different embryos and even littermates can be quite different (Musy *et al.*, 2018). To improve accuracy, a framework was established that can reliably stage mouse embryos based on the shape of the developing hindlimb in the range of embryonic days 10 to 15. For this, several embryos were collected at 12 h intervals in this time frame, the hindlimbs' average shape was calculated, and the data was interpolated between the different time points to complete a reference map for the whole time range (Musy *et al.*, 2018). The tool is available online so any researcher can stage their microscopy image of a mouse embryo to the common reference.

Lineage tracing in single cell studies In recent years, technological advances allowed the analysis of many parameters in single cells. For example, mass cytometry can measure dozens of parameters per cell (Bendall *et al.*, 2011). Bendall *et al.* (2014) developed the algorithm *Wanderlust* that can find a trajectory in this multidimensional parameter space to retrieve the path individual cells take during B cell lymphopoiesis. Another example is single-cell RNA sequencing (scRNA-seq), where the parameter space is several orders of magnitude larger as the expression levels of thousands of genes are analyzed. To reconstruct the developmental trajectories from these data, several approaches have been developed that can infer pseudotime (Saelens *et al.*, 2019). To increase the reliability of these approaches, it is helpful to encode the cells' pedigree by molecular biological methods, e.g., by Cas9-based encoding of lineage (Chan *et al.*, 2019). In this approach, random mutations are introduced by Cas9 at a defined genomic region throughout development. Analysis of these mutations helps to reconstruct the lineage from scRNA-seq data.

Structural biology Structural biology was mainly based on crystallized proteins for decades, hence the obtained structures are static. Different intermediates of, e.g.,

an enzymatic reaction cycle, could be obtained by mutagenesis or non-processable substrate analogs, like non-hydrolyzable ATP-γ-S. For interpolation between the different intermediate states, typically morphing algorithms are employed (Weiss and Levitt, 2009). Recently, cryogenic electron microscopy (cryo-EM) revolutionized structural biology by enabling the analysis of a wider range of proteins and large protein complexes (Kühlbrandt, 2014). This method relies on particle averaging of thousands of individual particles (electron micrographs of protein complexes) in different orientations for structure determination. Also here, different states can be distinguished by multiple rounds of advanced classification algorithms and input of previous knowledge. For example, five structural states of a human transcription factor could be solved this way (Patel *et al.*, 2018). An alternative strategy to investigate different structural states is time-resolved cryo-EM (Kaledhonkar *et al.*, 2018). In this approach, two interacting proteins are mixed in a microfluidic chip and plunge frozen milliseconds after. Among other applications, the intermediates of ribosome recycling were structurally investigated using this method (Fu *et al.*, 2016). Moreover, the structures of the NPC obtained by cryo-electron tomography in yeast cells under normal and energy-depleted conditions show the complex's different states that can be transitioned by morphing (Zimmerli *et al.*, 2020).

Modeling of protein folding For processes that are too fast to be examined by time-resolved cryo-EM, like protein folding, molecular dynamics simulations are the method of choice (Klepeis *et al.*, 2009). These simulations model the movement of every single atom and are therefore very calculation-intensive. Even though machine learning (Wang *et al.*, 2020) and constraints by experimental data, e.g., the distances between residues measured by FRET (Matsunaga and Sugita, 2018), improve the simulations, the time scales that are accessible to the simulations are in the microseconds range.

1.3 Membrane trafficking in eukaryotic cells

One key difference between prokaryotic and eukaryotic cells is the higher compartmentalization in eukaryotes. Most of the compartments are membrane-bound organelles, a big part of them is summarized as the endomembrane system. The most important members of this system are the endoplasmic reticulum (ER), the Golgi apparatus, endosomes, and lysosomes. The lumen of these compartments topologically correspond to each other and the extracellular space. The endomembrane system relies on vesicular trafficking to exchange molecules between its different compartments. In general, trafficking can be subdivided into uptake and secretion. The basis for these pathways are membrane vesicles that bud off one compartment and fuse with another (Alberts *et al.*, 2008).

The pathway of a secreted protein starts at the rough ER where it is translated into the lumen of the ER. It is then trafficked to the Golgi apparatus as cargo of a vesicle which is budding off of the ER. The Golgi apparatus consists of membrane stacks, termed cisternae, whose ER-facing side is termed the *cis* face whereas the other side is called the *trans* face. Secreted proteins are entering the Golgi apparatus on the cis face, are trafficked through the cisternae while being post-translationally modified (e.g., glycosylation, sulfation, and phosphorylation), and leave the Golgi apparatus on its trans side. This pathway through the Golgi apparatus is called the anterograde pathway, which is counterbalanced by the retrograde pathway going in the opposite direction. After exiting the Golgi apparatus, secreted proteins are trafficked via secretory vesicles that fuse with the plasma membrane to release their cargo into the extracellular space, a process called exocytosis. Secretion can be subdivided in constitutive (e.g., components of the extracellular matrix; Unlu *et al.*, 2014) and regulated secretion (e.g., hormones, digestive enzymes; Park and Loh, 2008; Palade, 1975).

The pathway that takes up molecules from the extracellular space and the plasma membrane is termed the endocytic pathway. In the first step, a vesicle buds off the plasma membrane containing the internalized cargo in a process called endocytosis. Multiple endocytic vesicles fuse to form an early endosome. Early endosomes mature to late endosomes and finally fuse with a lysosome where their content is digested. During maturation, endosomes exchange vesicles, and therefore cargo, with the Golgi apparatus and the plasma membrane. The latter two pathways are important as they allow cargo to escape degradation, for example, endocytosed receptors can be recycled back to the plasma membrane (Doherty and McMahon, 2009).

1.4 Endocytosis

Endocytosis can be subdivided into different types that differ in their cargo and the mechanism of uptake. During phagocytosis, cells take up pathogens or solid particles (Fig. 1.10A). This pathway is specific to cells of the immune system and it is crucial for the clearance of pathogens and humoral immunity (Uribe-Querol and Rosales, 2020). Pinocytosis, often also referred to as cell drinking, describes the process of unspecific uptake of molecules (Fig. 1.10B). It is important for immune surveillance and clearing of extracellular fluid (Canton, 2018). The third major endocytic pathway is named after the characteristic clathrin coat that is involved in membrane shaping and encases the vesicle: Clathrin-mediated endocytosis (CME; Fig. 1.10C; McMahon and Boucrot, 2011). Other endocytic pathways depend on the integral membrane protein caveolin, which is also part of caveolae, or are independent of both clathrin and caveolin (Mayor and Pagano, 2007).

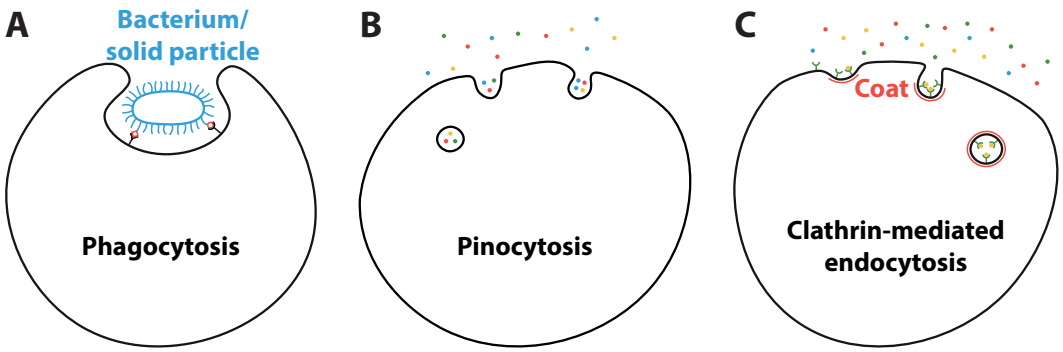

Figure 1.10 | Overview of the three main endocytic pathways. (**A**) Phagocytosis is the process when immune cells take up large particles or organisms. (**B**) Using pinocytosis ("cell drinking"), cells unspecifically take up extracellular fluid. (**C**) Integral and associated membrane proteins are taken up during clathrin-mediated endocytosis. The process is named after the clathrin coat, which covers the pinched-off vesicle.

1.4.1 Clathrin-mediated endocytosis (CME)

Apart from clathrin, more than 50 other proteins are part of the molecular machinery that carries out CME (Goode *et al.*, 2015). The process of CME begins with early proteins marking the future endocytic site. Transmembrane cargo is recognized by these early proteins and adaptor proteins, like the AP2 complex, that bind to the cargo and phosphoinositide within the membrane (Sorkin, 2004). The adaptor proteins themselves bear domains that interact with each other and recruit clathrin and other coat proteins to the endocytic site. This multitude of interactions results in clustering of coat proteins and the assembly of a clathrin coat. The building blocks of the clathrin coat are triskelia, where each of the three legs consists of a heavy and a light chain (Ungewickell and Branton, 1981). The triskelia can assemble to a flat hexagonal lattice that can be rearranged to a sphere that is surrounded with a mixture of hexagons and pentagons like the patches of a soccer ball (Fotin *et al.*, 2004). Therefore, the assembly and rearrangement of the clathrin lattice can drive

membrane bending and formation of an invagination (Hinrichsen *et al.*, 2006). Moreover, actin polymerization can contribute to extending the invagination, especially under conditions of high membrane tension (Boulant *et al.*, 2011). When the membrane invagination has reached a certain depth, proteins of the scission module bind to the neck of the invagination and mediate the separation of the vesicle from the plasma membrane (Daumke *et al.*, 2014). The most prominent member of the scission module is the GTPase dynamin, which constricts the neck in mammalian cells to pinch off the vesicle (Antonny *et al.*, 2016). After scission, the coat is disassembled and the vesicle is directed to intracellular trafficking.

The main cargoes internalized by CME are transmembrane proteins, especially transporters, proteins crucial for cell adhesion, and receptors together with their ligands. Therefore, CME plays an important role in nutrient uptake, cell motility, and regulation of signaling (Kaksonen and Roux, 2018). As the dysregulation of these pathways is key in the formation of cancer, CME can be implicated in the evasion of apoptosis, proliferation, and migration of cancer cells (Schmid, 2017). In neurobiology, CME counterbalances the exocytosis of synaptic vesicles by recycling the plasma membrane with associated proteins in the presynapse and regulates the availability of receptors in the postsynapse (Jung and Haucke, 2007). Dysfunction of CME in these processes is reported to be associated with neurodegenerative diseases, for example Alzheimer's disease (Cataldo *et al.*, 2001; Wu and Yao, 2009). Furthermore, various viruses hijack the CME machinery to enter the cell (Mercer *et al.*, 2010), for example, the influenza virus uses the CME pathway (Rust *et al.*, 2004) and also for SARS-CoV-2, the coronavirus responsible for the current pandemic, an early report described CME as an entry point into the cell (Bayati *et al.*, 2020).

1.4.2 CME in *Saccharomyces cerevisiae*

CME has been extensively studied in the budding yeast *Saccharomyces cerevisiae* (Boettner *et al.*, 2012; Goode *et al.*, 2015). This model organism offers several traits that make it a good choice for CME research:

- The powerful genetics of yeast facilitated the discovery of proteins involved in CME early on (Raths *et al.*, 1993).
- The genome of *S. cerevisiae* is easy to manipulate, hence endogenous tagging can be readily achieved (Longtine *et al.*, 1998; Janke *et al.*, 2004).
- The temporal progression of CME is fairly regular (Picco *et al.*, 2015).
- CME is the major endocytic pathway in budding yeast (Boettner *et al.*, 2012).

For similar reasons, CME research was also performed in the fission yeast *Schizosaccharomyces pombe*, providing the chance to study similarities and differences between the two organisms (Sun *et al.*, 2019).

The proteins involved in CME can be subdivided into different functional modules, according to their time of arrival throughout the process and the function they fulfill at the endocytic site (Fig. 1.11; Kaksonen *et al.*, 2005). These modules and their most important representatives will be described in the following sections.

A

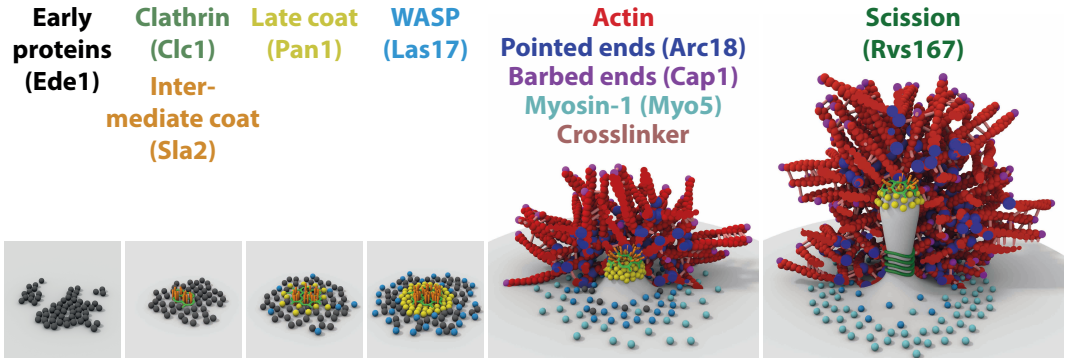

B

Early	Early coat	Intermediate coat	Late coat	WASP/Myo	Actin		Scission
Ede1	Clc1	Yap1801/2	Pan1	Las17	Arp2/3 complex		Rvs161/7
Syp1	Chc1	Sla2	End3	Myo3/5	Sac6	Crn1	
	AP-2 complex	Ent1/2	Sla1	Vrp1	Abp1	Aim7	
				Bbc1	Cap1/2	Scp1	
				Bzz1	Ldb17	Twf1	
				Lsb3	Aip1	Srv2	
					Cof1		

Figure 1.11 | Model of the endocytic process in yeast and its modular organization. (**A**) Proteins of the different functional modules arrive at the endocytic site at different time points and have a characteristic spatial arrangement. Early coat proteins can be found in the center, proteins of the late coat are distributed a bit further away from the center, and proteins of the WASP/Myo module form a ring around the coat proteins. Once the actin network is initiated, membrane invagination starts. The actin network contains Arp2/3 (Actin related protein 2/3) complexes that nucleate actin filaments, proteins that cross-link actin, and capping proteins. The actin network depicted here is taken from a simulation and half of it has been removed for clarity. *Adapted from Mund* et al. *(2018) under the CC BY 4.0 license. I am one of the authors of the original figure.* (**B**) The functional modules of yeast endocytosis and important members mentioned in the text.

1.4.2.1 The early module

In the temporally most variable early phase, transmembrane cargo proteins are recognized by short peptide motifs or ubiquitination on their cytosolic domains (Traub and Bonifacino, 2013). Hence, the endocytosis of cargo can, for example, be regulated by E3 ligases that attach ubiquitin to their substrates (Lin *et al.*, 2008). The first proteins to arrive at the future site of endocytosis are Ede1 (yeast homolog of mammalian Eps15) and Syp1 (yeast homolog of FCHO1/2). The two adaptor proteins bind to each other (Reider *et al.*, 2009) and recognize cargo. Ede1 has three N-terminal EH-domains (Eps15 homology), that can bind to peptide motifs of cargo proteins, and a C-terminal ubiquitin-binding UBA (ubiquitin-associated) domain (Gagny *et al.*, 2000). The N-terminus of Syp1 contains a membrane-binding F-BAR

(named after the proteins it is found in: Bin, Amphiphysin, and Rvs) domain and its C-terminus can recognize cargo via a μ-homology domain (homolog to a domain in the μ subunit of the adaptor complex AP2; Stimpson *et al.*, 2009). The central part of Ede1 contains a coiled-coil domain and a low complexity domain. The coiled-coil domain was reported to mediate oligomerization of Ede1 in the cytosol, which is crucial for its localization to endocytic sites (Boeke *et al.*, 2014). Recently, a preprint showed that Ede1 can phase separate. This feature depends on the two central domains and is important for the endocytic function of Ede1 (Kozak and Kaksonen, 2019). Independently, Ede1 was detected in a large screen for autophagy and it was reported that large phase-separated clusters of Ede1 are important for the clearance of unproductive endocytic sites (Wilfling *et al.*, 2020). Single deletions of both EDE1 and SYP1 have a rather mild phenotype, even in a strain where these two and five more early proteins are knocked out endocytic dynamics are relatively normal (Brach *et al.*, 2014). However, cargo recruitment to endocytic sites is defective in these mutants.

1.4.2.2 The coat module

The coat module consists of clathrin and various adaptor proteins. Two of them have been described in the previous section, the others will be described in the following three paragraphs reflecting the division into early, intermediate, and late coat according to their time of arrival at the endocytic site. Common features among most coat proteins are their interactions: They bind cargo, the membrane, and each other, giving rise to a large connected network (Skruzny *et al.*, 2020).

The early coat After the proteins of the early module, clathrin and the AP2 adaptor complex arrive at the endocytic site. In yeast, CHC1 and CLC1 code for the heavy and light chain of clathrin, respectively. Interestingly, clathrin is not essential for CME in yeast, however it plays a role in regulating scission and therefore vesicle size (Kukulski *et al.*, 2016). In contrast to mammalian cells, clathrin does not bind to the AP2 complex (Yeung *et al.*, 1999), but its light chain binds to the adaptor protein Sla2 (see next paragraph).

The intermediate coat The two paralogs Yap1801/2 (yeast homologs of mammalian Picalm) are clathrin adaptors. They contain an N-terminal ANTH (Ap180 N-terminal homology) domain that binds to PI(4,5)P_2 (phosphatidylinositol 4,5-bisphosphate) in the inner leaflet of the plasma membrane, an EH domain for interaction with cargo, and a C-terminal clathrin-binding motif (CBM; Wendland and Emr, 1998). Sla2 (yeast homolog of mammalian Hip1r) and the paralogs Ent1/2 (epsin-like proteins) are important adaptors as they link the membrane to the growing actin network (Skruzny *et al.*, 2012; see below). The coat protein Sla2 is present at endocytic sites as a homodimer and contains an N-terminal ANTH domain for membrane binding via PI(4,5)P_2, a central coiled-coil domain that interacts with

clathrin and a C-terminal THATCH (talin-HIP1/R/Sla2p actin-tethering C-terminal homology) domain that binds to actin filaments (Wesp *et al.*, 1997). The deletion of Sla2 leads to the occurrence of actin comet tails shooting into the cytosol, demonstrating that the interactions with both the membrane and the actin network are crucial for coupling of force generation by actin polymerization to pulling of the membrane (Kaksonen *et al.*, 2003). However, endocytic function is partially rescued by Ent1/2, which have a similar domain architecture. They contain an ENTH (Epsin N-terminal homology) domain at their N-terminus that also binds to PI(4,5)P_2 and a C-terminal domain that interacts with actin (Wendland *et al.*, 1999). In between these two domains, Ent1/2 have two ubiquitin-interacting motifs, a domain binding to peptide motifs in cargo, and a clathrin-binding domain. It was reported recently that after the arrival of the intermediate coat proteins, a cargo-sensitive checkpoint exists (Pedersen *et al.*, 2020). In the absence of cargo, the endocytic site is stalled until the checkpoint is satisfied. This is also in line with the observation that the phase from initiation up to the checkpoint is much more variable than the following phase (Carroll *et al.*, 2011).

The late coat The three late coat proteins Pan1, End3, and Sla1 form a complex that fulfills similar functions as the mammalian protein intersectin (Tang *et al.*, 2000). Pan1 is the only essential coat protein and it contains EH domains that interact with Ent1/2 and Yap1801/2 (Wendland *et al.*, 1996). Moreover, it can stimulate actin nucleation by the Arp2/3 (Actin related protein 2/3) complex and activate the type-I myosins Myo3/5 (see next two sections; Barker *et al.*, 2007; Duncan *et al.*, 2001). Together with End3 and cargo peptide motifs, Pan1 recruits the adaptor protein Sla1 to endocytic sites (Tang *et al.*, 2000; Tolsma *et al.*, 2020). The recruitment of Sla1 leads to a functional endocytic event in line with the checkpoint described above. Sla1 has three SH3 (SRC homology 3) domains that mediate interactions with proline-rich (PR) regions in other endocytic proteins, two Sla1 homology domains that bind to peptide motifs in cargo, a clathrin-binding motif, and its C-terminal domain bears several phosphorylation sites that are important for uncoating after vesicle scission (Warren *et al.*, 2002). Sla1 is involved in the recruitment of Las17, which is part of the actin assembly machinery (Sun *et al.*, 2015).

1.4.2.3 The WASP/Myo module

The WASP/Myo module consists of proteins that directly regulate the formation of the actin network at endocytic sites. To understand their functions, it is necessary to first introduce the architecture of the actin network and how its assembly is initiated (Goode *et al.*, 2015).

The Arp2/3-nucleated actin network Actin is a globular protein which can form a two-stranded helical filament with distinct ends: a *pointed* end where filament growth is slow and a *barbed* end which grows fast. However, monomers of actin

do not spontaneously nucleate to form an actin filament. For this reason, actin nucleators are necessary. At endocytic sites, the actin network is generated by the Arp2/3 complex which consists of seven subunits. This complex binds to an existing *mother* filament and nucleates a new *daughter* filament in a characteristic 70° angle, thereby creating a branched network (Goley and Welch, 2006). However, the nucleation activity of the Arp2/3 complex is relatively weak. In the inactive state of the Arp2/3 complex, the two subunits Arp2 and Arp3, which are structurally related to actin, are in an open conformation that cannot nucleate an actin filament. The binding to the mother filament leads to a conformational change, bringing the two subunits closer together and increasing the activity of the Arp2/3 complex slightly. Full Arp2/3 activity requires the interaction with NPFs (nucleation promoting factors) that induce further structural rearrangements that bring Arp2 and Arp3 into a conformation that mimicks the barbed end of an actin filament (Goley and Welch, 2006).

NPFs in endocytosis NPFs can be subdivided into classes I and II that differ in how strongly they activate the Arp2/3 complex (Goley and Welch, 2006). Class I NPFs have a higher activation potential and provide the first actin monomer. The ones implicated in CME are Las17 and the type-I myosins Myo3/5 (Goode *et al.*, 2015). The main NPF of CME in yeast is Las17 (yeast homolog of mammalian WASP), a protein that contains an N-terminal WH1 (WASP homology 1) domain, a PR region that mediates interactions with SH3 domains in other endocytic proteins, and a C-terminal WCA domain (Winter *et al.*, 1999). The WCA domain consists of three subdomains: the WH2 (W; WASP homology 2) domain, which is responsible for supplying an actin monomer to the Arp2/3 complex, a connecting (C) region, and an acidic (A) patch that binds to the Arp2/3 complex inducing a conformational change. Myo3 and Myo5 have an N-terminal motor domain, two tail homology (TH) domains of which one is membrane-binding and one is actin-binding, a SH3 domain, and an acidic patch at the C-terminus. Together with their interaction partner Vrp1 (verprolin), which contains two WH2 domains, the type-I myosins have all three parts of the WCA domain to activate nucleation by the Arp2/3 complex and provide an actin monomer (Sun *et al.*, 2006). The two proteins Pan1 and Abp1 (yeast homolog of mammalian HIP-55/ABP1) are class II NPFs, as they only contain an acidic patch to bind the Arp2/3 complex but lack the WH2 domain (Duncan *et al.*, 2001; Goode *et al.*, 2001).

Regulation of NPF activity Las17 arrives at the endocytic site about 20 s before actin polymerization and was shown to be constitutively active as NPF *in vitro* (Rodal *et al.*, 2003). Therefore, inhibiting mechanisms have to be in place to keep Las17 inactive until actin polymerization starts (Rodal *et al.*, 2003). Bbc1 from the WASP/Myo module, which arrives after Las17, and the early protein Syp1 were shown to inhibit Las17 activity. Furthermore, Sla1, which arrives together with

Las17, inhibits Las17 via binding of its SH3 domains to Las17's PR regions (Boettner *et al.*, 2009; Rodal *et al.*, 2003). The nanoscale distribution of Las17 at the endocytic site was reported to be a ring around the coat proteins, including Sla1 (Mund *et al.*, 2014). In the same study, Bbc1 was shown to form an even larger ring around the Las17 ring, suggesting Las17 is inhibited from the center by Sla1 and from the periphery by Bbc1, creating patterned Arp2/3 activity. Las17 gets released from its inactive state by departure of Syp1 and arrival of Bzz1 (yeast homolog of mammalian syndapin), which might compete with Sla1 for binding to the same PR regions in Las17 (Boettner *et al.*, 2009; Soulard *et al.*, 2005). Additionally, Bzz1 has a F-BAR domain that mediates membrane binding and homodimerization. Hence, it could potentially dimerize Las17, thereby increasing its NPF activity (Goode *et al.*, 2015). The protein Lsb3 is another binding partner of Las17 and has an activating effect on it whose functional basis is not very well characterized (Robertson *et al.*, 2009). The proteins of the WASP/Myo module stay at the base of the plasma membrane during actin assembly and formation of the invagination. However, it was reported that Wsp1, the fission yeast homolog of Las17, and a subset of Las17 in budding yeast move inwards with the growing tip of the invagination (Arasada and Pollard, 2011; Idrissi *et al.*, 2008; Idrissi *et al.*, 2012).

Origin of the first actin filament One important question for the start of actin nucleation by the Arp2/3 complex is: Where does the first actin filament, which serves as the mother filament for Arp2/3 activation, come from? One possibility is that a severed filament diffuses from another endocytic site close by that is already in the mobile phase (Chen and Pollard, 2013). Another option is the nucleation of a linear filament by the Arp2/3 complex. The fission yeast protein Dip1 (Ldb17 in *S. cerevisiae*) can activate the Arp2/3 complex without the need of an actin filament binding, thereby generating linear filaments (Wagner *et al.*, 2013). Dip1 activates Arp2/3 in a single-turnover fashion, ensuring that a branched network is generated (Balzer *et al.*, 2019).

1.4.2.4 The actin module

Peripheral actin patches have been identified as a characteristic structure in yeast early on. Together with actin cables and the cytokinetic ring, they constitute the main actin structures in yeast (Adams and Pringle, 1984). It took ten years until the actin patches were associated with endocytosis (Mulholland *et al.*, 1994). With the start of actin polymerization, the mobile phase of CME starts as this is when the invagination together with the bound coat proteins begins to move inside the cell. The proteins that make up the actin network are the most abundant ones at endocytic sites by copy number (Picco *et al.*, 2015). Two key players that make up the actin network have been introduced in the previous section: actin and the Arp2/3 complex. However, other actin-interacting proteins are necessary to generate a dense

and highly branched network composed of short actin filaments that grows over time and encloses the growing invagination in the shape of a hemi-ellipsoid.

Capping of actin filaments Growing actin filaments are capped quickly at their barbed end to prevent further growth and keep them relatively short at a length of $\approx 100\,\text{nm}$ (Rodal *et al.*, 2004). Capping is realized by the heterodimer Cap1/2 (Amatruda and Cooper, 1992), but also Aip1/Cof1 (Balcer *et al.*, 2003), or Abp1/Aim3 (Michelot *et al.*, 2013). Interestingly, the binding of Cap1/2 to the barbed end is weakened by PI(4,5)P_2 *in vitro*, proposing a mechanism how actin polymerization can be enhanced at the plasma membrane (Schafer *et al.*, 1996).

Nucleotide state of actin When monomeric actin gets added to the growing filament, it has a molecule of ATP bound. Upon binding, ATP gets quickly hydrolyzed to ADP and inorganic phosphate (P_i). The subsequent dissociation of the P_i is rather slow. Therefore, the monomers in filamentous actin can be in three different states that correspond to the age of this part of the filament (ATP, ADP + P_i, and ADP). Each of the states has a distinct conformation which mediates the specificity of actin-binding proteins (Dominguez and Holmes, 2011).

Turnover of the actin network The assembled branched actin network is not static but gets constantly turned over. ADP-actin, which is comparably older, gets disassembled to ensure renewal of the network. For example, Cof1 (yeast homolog of mammalian cofilin) binds to ADP-actin and induces severing by twisting of the actin filament, which gets subsequently disassembled. This severing mechanism is enhanced by Crn1 (yeast homolog of mammalian coronin) (Mikati *et al.*, 2015). Also the two actin mimicking subunits of the Arp2/3 complex bind to ATP, therefore, also their age can be recognized by other proteins (Ingerman *et al.*, 2013). The protein Aim7 (yeast homolog of mammalian GMF) mediates debranching of the network preferentially at Arp2/3 complexes that are in the ADP state and inhibits new nucleation of the bound Arp2/3 complex (Gandhi *et al.*, 2010; Boczkowska *et al.*, 2013). The debranching activity of Aim7 is antagonized by Abp1 (Guo *et al.*, 2018b). Severed and debranched actin filaments depolymerize on their own, but the proteins Twf1 (yeast homolog of mammalian twinfilin) and Srv2 (yeast homolog of mammalian CAP) increase the rate of depolymerization at both the pointed and barbed ends (Johnston *et al.*, 2015). Based on these and other mechanisms, the whole actin network was reported to turnover between 3 and 5 times during a single endocytic event (Kaksonen *et al.*, 2003; Lacy *et al.*, 2019). Apart from its NPF activity, Abp1 binds to actin filaments via its N-terminal actin depolymerization factor (ADF)/cofilin-homology domain thereby linking its numerous interaction partners to the actin network (Quintero-Monzon *et al.*, 2005).

Cross-linking of actin filaments Another important modification of the actin network achieved by actin-binding proteins is stiffening by cross-linking of actin

filaments. In endocytic patches in *S. cerevisiae*, cross-linking is mainly achieved by Sac6 (yeast homolog of mammalian fimbrin) and Scp1 (yeast homolog of mammalian calponin). Sac6 has four tandem calponin homology (CH) domains that are organized in two separate actin-binding regions (Klein *et al.*, 2004). Also Scp1 contains an N-terminal CH domain, but actin bundling is mediated by two distinct actin-binding regions in its PR motif and C-terminal calponin-like repeat (Gheorghe *et al.*, 2008).

1.4.2.5 The scission module

Scission of the invaginated membrane to produce a vesicle is mediated by the heterodimer Rvs161/167 (Friesen *et al.*, 2006). The pair of BAR domain proteins is homolog to mammalian endophilin/amphiphysin and forms a scaffold at the tubular part of the invagination (Idrissi *et al.*, 2008). The mode of action is not fully understood yet, one hypothesis is that binding to the neck limits lipid diffusion. Together with the pulling force of the actin network, this can create friction at the narrow tubular part of the invagination that leads to membrane fission (Kaksonen and Roux, 2018). The homolog of mammalian dynamin in yeast is Vps1. However, it is not necessary for scission and may have regulatory functions (Nannapaneni *et al.*, 2010).

After membrane scission, the vesicle gets quickly uncoated to allow fusion with an early endosome and recycling of the involved proteins. This process is mediated by chaperones like Ssa1 (yeast homolog of mammalian Hsc70), protein kinases like Ark1 and Prk1 (yeast homolog of mammalian AAK1) that phosphorylate coat proteins, and lipid phosphatases like Inp51/52/53 (yeast homologs of mammalian synaptojanin) that dephosphorylate PI(4,5)P_2 to PI(4)P thereby weakening interactions of coat proteins with the membrane (Goode *et al.*, 2015).

1.4.3 Force generation in CME

The largest difference between endocytosis in mammalian cells and yeast is that in yeast actin is strictly necessary for productive endocytosis (Aghamohammadzadeh and Ayscough, 2009). In fact, membrane bending in yeast only starts after actin polymerization has started (Kukulski *et al.*, 2012). The network provides the force to pull in the membrane against the intracellular turgor pressure (Fig. 1.12). This osmotically caused pressure is present in walled cells like plants and yeasts. In budding yeast, it is reported to be in the range of 0.5 to 1 MPa (Minc *et al.*, 2009; Schaber *et al.*, 2010). On the contrary, in cultured mammalian cells the membrane is mainly invaginated by the clathrin coat and curvature inducing proteins, actin aids in the final steps and is required for endocytosis under increased membrane tension (Yarar *et al.*, 2005; Boulant *et al.*, 2011). One feature of mammalian cells that complicates the analysis of actin at endocytic sites is the actin cortex, which is hard to distinguish from an actin network contributing to endocytosis. Moreover, CME

research was mainly focused on cultured cells and has only recently transitioned to investigate these questions in other systems like organoids and tissues where force requirements might differ substantially (Schöneberg *et al.*, 2018).

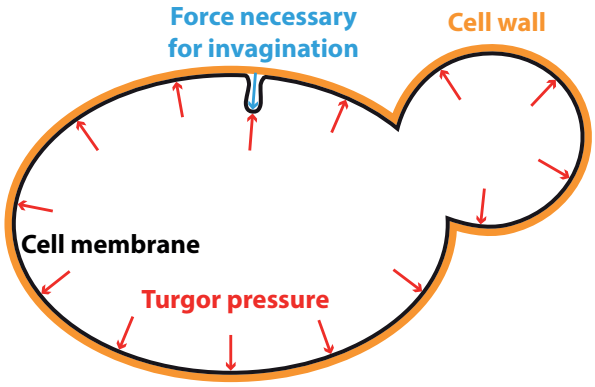

Figure 1.12 | Membrane invagination against turgor pressure. The intracellular turgor pressure pushes the cell membrane against the yeast's cell wall. Therefore, force is necessary to invaginate the membrane during an endocytic event.

Force generation by actin polymerization Modeling of yeast endocytosis showed that the forces required to overcome the turgor pressure are larger than 1000 pN per endocytic site (Dmitrieff and Nédélec, 2015; Ma and Berro, 2020). This value is in accordance to the range of 450 to 1300 pN which was measured using a FRET-based force sensor in a recent preprint (Abella *et al.*, 2020). Reconstitution of actin assembly *in vitro* by coating beads with Las17 and incubating them in cytosolic extract demonstrated that the system is able to assemble an actin network that in some cases propels the bead (Michelot *et al.*, 2010). The current model for force generation by the actin network is based on localized filament nucleation and physical attachment of the network to the endocytic coat (Kaksonen and Roux, 2018). The network is oriented in a way that the barbed ends of actin filaments are oriented towards the membrane where new monomers are added (Picco *et al.*, 2015). This network organization is similar to that in lamellipodia in mammalian cells, where a dendritic actin network generates force by polymerization at the barbed ends of actin filaments against the membrane while being disassembled on the cytoplasmic side (Pollard and Borisy, 2003). The addition of new monomers at the membrane provides force by a Brownian ratchet mechanism: The filament diffuses because of Brownian motion and if there is enough space between the membrane and the barbed end, a new monomer is added (Mogilner and Oster, 1996; Kaksonen *et al.*, 2006). As the filament was extended, it then pushes against the membrane. However, the membrane is very rigid because of the cell wall, therefore the force gets transmitted to the whole actin network which is attached to the tip of the invagination via the coat proteins Sla2 and Ent1/2 (Skruzny *et al.*, 2012). In *S. pombe*, NPFs can be found at the base and at the tip of the invagination: The fission yeast homolog of Las17, Wsp1, was reported to move in with the invagination, whereas the type-I myosin Myo1 stays at the base (Arasada and Pollard, 2011).

This arrangement gives rise to two actin networks that can push against each other (Arasada and Pollard, 2011; Arasada *et al.*, 2018). Per endocytic event, it is estimated that 150 to 200 actin filaments are present (Sirotkin *et al.*, 2010; Picco *et al.*, 2015). Assuming the maximum polymerization force measured *in vitro* of 1 pN per actin filament (Footer *et al.*, 2007), the force provided by the network is not enough to provide the 1000 pN to overcome the turgor pressure.

Role of type-I myosins Type-I myosins contain a motor domain that binds to actin, a TH1 domain that binds to lipids, and an Arp2/3 complex activating CA domain (see section 1.4.2.3). Budding yeast's type-I myosins Myo3 and Myo5 are essential for endocytosis as a strain with both genes deleted is not viable (Geli and Riezman, 1996). Furthermore, their motor domain is necessary for productive endocytosis (Sun *et al.*, 2006; Lewellyn *et al.*, 2015), but it is unclear if the force stroke of the motor domain is required. In two recent reports, hypotheses for type-I myosin function in yeast endocytosis were formulated. According to Pedersen and Drubin (2019), Myo3/5 are important to anchor NPFs at the membrane to activate the Arp2/3 close to the membrane and ensure an ordered actin network. Manenschijn *et al.* (2019) report that type-I myosins rather stimulate actin polymerization than nucleation by decreasing the load on actin filaments and thereby facilitating the addition of the next monomers at the plasma membrane.

Force generation by elastically stored energy Recently, modeling and experimental evidence suggested additional modes of force generation for CME. Modeling of actin networks with cross-linkers proposed that the chemical binding energy of actin and cross-linkers can be converted to elastic energy because of the geometric constraints given by the twist of actin filaments (Ma and Berro, 2018). This stored energy can be used later during the invagination process. It can provide more than 1000 pN of force, but the amount critically depends on the stiffness of the cross-linkers (Ma and Berro, 2019). Another modeling approach with parameters from mammalian endocytosis resulted in the observation of bent actin filaments in the simulation, whose presence was experimentally confirmed by cryo-electron tomography and is thought to store elastic energy (Akamatsu *et al.*, 2020).

Alternative mechanisms for force generation Most simulations mentioned so far assume a solid actin network without turnover. However, the actin network is thought to turn over up to five times during a single endocytic event (Lacy *et al.*, 2019). Taking the turnover into account by simulating a viscoelastic actin network increases the generated force for both budding and fission yeast to 2000 to 3000 pN, which would be enough force to overcome the turgor pressure (Nickaeen *et al.*, 2019). These results highlight the importance of network turnover for force generation. Another modeling approach, published as a preprint, reported that the force requirement for invaginating the membrane can be reduced by covering the

membrane with curvature generating proteins, e.g., BAR domain proteins (Ma and Berro, 2020). In mammalian cells, a recent preprint suggests that the clathrin lattice assembling on the plasma membrane already contains pentagons (which are typical for the spherical shape of the clathrin coat) and is only kept flat by a flattening force. Once this force is released, the coat bends spontaneously (Sochacki *et al.*, 2020).

Open questions Despite the recent progress, there are still open questions about force generation in CME. Some hypotheses generated by modeling, e.g., the storage of elastic energy in cross-linkers and the influence of membrane binding proteins, need to be substantiated experimentally. For more realistic modeling and generation of further hypotheses, it is important to get more insight into the orientation of the actin filaments. Moreover, the nanoscale organization of actin-remodeling proteins and how actin nucleation is terminated further away from the membrane are not well understood. Additionally, it is an open question which of the different models contributes how much and at which time point to invaginating the membrane.

1.4.4 Localization microscopy of CME

The machinery at endocytic sites is about 200 to 300 nm in size and therefore substructures cannot be resolved using diffraction-limited microscopy. To overcome this limitation, numerous studies used high-resolution imaging techniques like EM, SIM, STED, and SMLM to gain new insights into CME (Baranov *et al.*, 2019). One correlative study combined platinum replica EM with SMLM to localize endocytic proteins relative to the clathrin coat in mammalian cells and generate a model of their average positions (Sochacki *et al.*, 2017). Arasada *et al.* (2018) performed live localization microscopy in fission yeast using the pcFP mMaple3 with 35 nm spatial and ≈ 1 s temporal resolution. This approach allowed them to visualize the localization of the NPFs Myo1 (type-I myosin) and Wsp1 (fission yeast homolog of Las17) and the Arp2/3 complex during endocytosis corroborating the two-zone model of the actin network in fission yeast endocytosis (Arasada and Pollard, 2011). A large-scale SMLM study of CME in budding yeast showed the average radial distributions of 23 different endocytic proteins across all functional modules (Mund *et al.*, 2018; Fig. 1.13). Except for the early proteins, which form rather irregular structures, the average radial distribution of the different endocytic proteins correlated with the time of arrival at the endocytic sites, suggesting a layered structure where newly arriving proteins are localized in the periphery of the site. Furthermore, the study reported that Las17 is localized in a ring pattern around the endocytic site, giving rise to patterned actin nucleation at the plasma membrane, which was shown to be advantageous for endocytic progression by modeling. The same study also introduced the concept of using the intensity of a diffraction-limited marker protein to temporally sort endocytic snapshots which were fixed at random time points (Mund *et al.*, 2018). Dual-color SMLM of clathrin and actin in mammalian cells was used in a recently published preprint to investigate the role of actin at endocytic

sites with super-resolution microscopy (Kaplan *et al.*, 2020). The authors found that actin polymerizes at the base of the invagination close to the plasma membrane and that the size of the actin network grows larger under conditions of increased membrane tension.

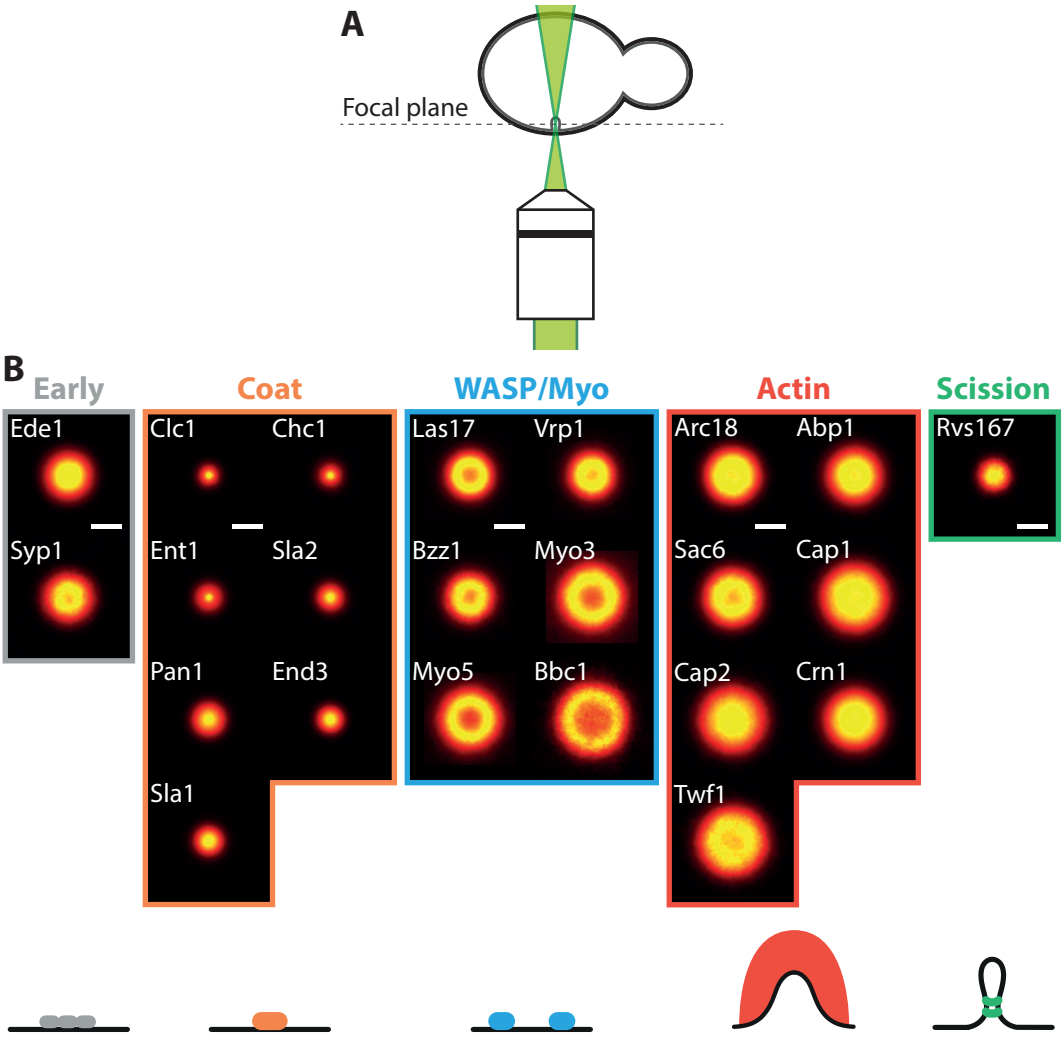

Figure 1.13 | Localization microscopy of yeast CME. (**A**) Thousands of endocytic sites at the bottom of yeast cells were imaged. (**B**) Average distributions of 23 different endocytic proteins across all functional modules. The distribution of early proteins that initiate endocytosis are rather irregular, therefore their averages are quite large. The coat proteins form smaller structures that increase in size from early (Clc1/Chc1) to late coat proteins (Pan1/End3/Sla1). Proteins of the WASP/Myo module form larger rings and proteins of the actin network form large structures that are dome-shaped for some of them (e.g., Twf1). Rvs167, as representative of the scission module, forms smaller structures as it binds to the neck of the invagination. Scale bars are 100 nm. *Adapted from Mund* et al. *(2018) under the CC BY 4.0 license.*

2 Research objectives

Clathrin-mediated endocytosis is accomplished by a dynamic protein machinery at small spatial scales. Major rearrangements take place in less than 20 s on a scale of 200 to 300 nm. Methodological advances in recent years enabled high-resolution studies by super-resolution and cryo-electron microscopy *in situ*, advancing our knowledge about the organization of the endocytic machinery at the nanoscale. However, the high resolution typically compromises on the achievable temporal resolution as samples need to be fixed.

In this work, we propose to establish a new concept to retrieve dynamic information from fixed snapshots of endocytosis obtained by localization microscopy. The concept is based on imaging of a reference structure, based on which temporal and spatial alignment are performed, and a query protein. The individual snapshots could then be sorted according to the extracted temporal information from the reference structure and averaged to reconstruct spatial rearrangements of the query protein during the progression of CME in yeast. The approach required acquisition of high quality dual-color SMLM data by high-throughput microscopy in yeast. Subsequently, due to the large amount of data, it was necessary to automate data analysis. Finally, the new concept needed to be validated.

Based on this project outline, the following research objectives will be addressed in the results chapter:

- Establishment a protocol for long-term dual-color localization microscopy in yeast (section 3.3).
- Development of a pipeline to automatically analyze high-throughput SMLM data and apply the reference structure concept (sections 3.4.1 to 3.4.3).
- Validation of the new concept for dynamic reconstruction based on a reference structure with different query proteins (section 3.4.5).

As we experienced problems with tagging of multiple endocytic proteins in the same strain, I tested different approaches to solve these problems (section 3.4.4).

3 Results

3.1 Complementary experiments for the radial analysis of endocytic structures

The results described in this section were performed or extended during the revision of Mund *et al.* (2018). In this paper, the average radial distribution of the protein machinery mediating CME in yeast was investigated. To exclude that the endocytic structures are affected by our sample preparation protocol, we performed control experiments. Furthermore, we extended the diffraction-limited timing approach to cover proteins from different functional modules. The experiments were performed by Markus Mund and me (Fig. 3.1 and Fig. 3.2B, D) and by Markus Mund and Jan van der Beek (Fig. 3.2A, C). The data analysis was performed by Markus Mund and Jonas Ries.

3.1.1 Effect of fixation on endocytic structures

The mode of fixation is crucial for any localization microscopy experiment and potential artifacts caused by the fixation agent need to be considered (Pereira *et al.*, 2019). For example, in yeast it was reported that formaldehyde fixation can have detrimental effects on actin-based structures (Vasicova *et al.*, 2016).

For these reasons, we wanted to investigate the influence of fixation on the radial organization of endocytic proteins. To be able to perform localization microscopy in living yeast cells, we arrested the endocytic process on the flat membrane just before actin polymerization begins by treating cells with the actin polymerization inhibitor Latrunculin A (LatA; Kukulski *et al.*, 2012). We either performed the drug treatment on the microscope and then imaged endocytic structures in living cells for up to 45 min after drug addition or we added LatA while the yeast cells were settled prior to fixation. We then imaged the samples manually (live) or in high-throughput (fixed) and analyzed the structures by fitting a geometric model to each individual endocytic site and subsequently calculating the average radial density of the localizations. Fig. 3.1 shows exemplary cells and endocytic sites (left and middle) and average radial densities (right) for both conditions in cells where either the early protein Ede1, the coat protein Pan1, or the actin nucleation promoting factor Las17

was imaged by localization microscopy. In all three cases, the endocytic sites are visually similar between fixed and living cells and the average radial densities agree well.

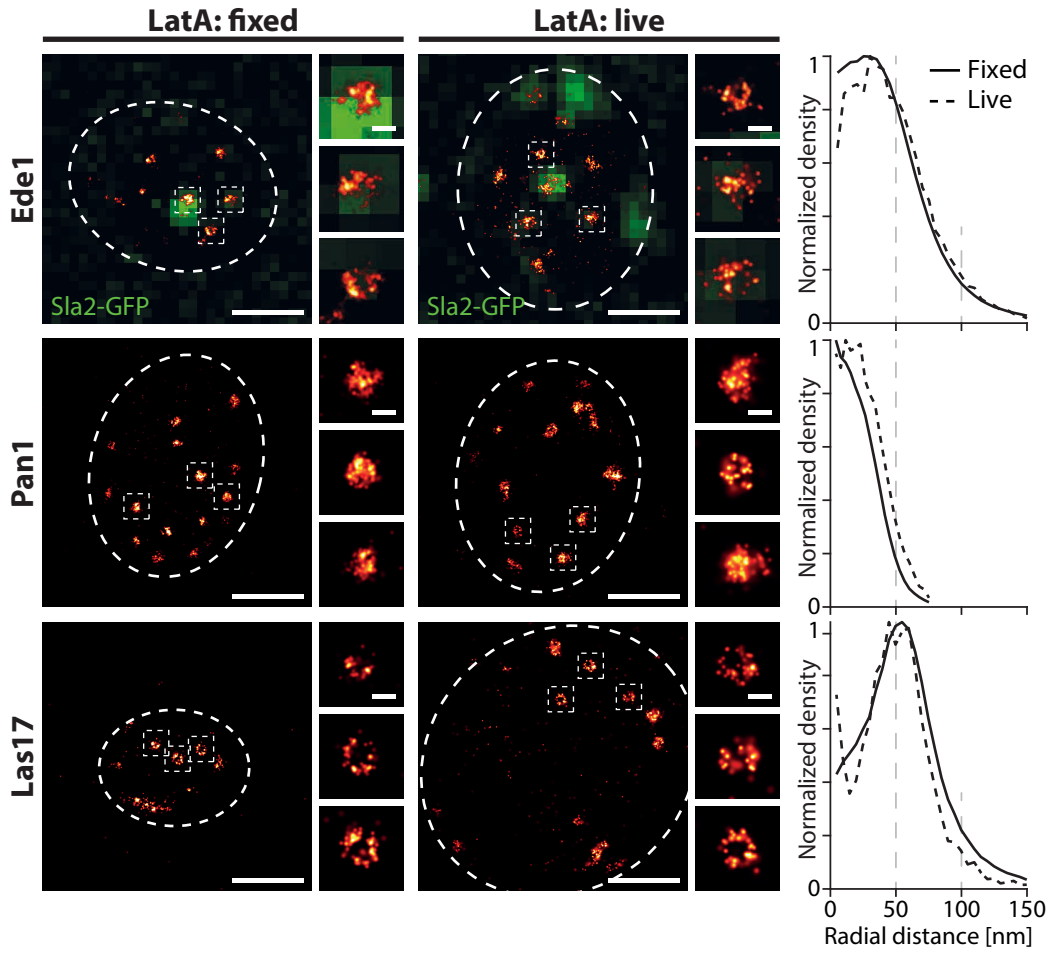

Figure 3.1 | Arrested endocytic structures imaged with and without fixation. Yeast cells in which the indicated proteins (Ede1, Pan1, and Las17) were tagged with mMaple were treated with Latrunculin A (LatA) and either imaged fixed (left) or live (middle). A radial model was fitted to the data and the average radial density was plotted for both experimental conditions (right). In the Ede1-mMaple strain, additionally Sla2 was tagged with GFP; in the Pan1-mMaple and Las17-mMaple, additionally Abp1 was tagged with GFP but the signal is left out because it was too diffuse due to the LatA treatment. Scale bars are 1 µm (images of whole cells) and 100 nm (zoom-ins of endocytic sites). The data presented in this figure were produced jointly with Markus Mund. *Adapted from Mund* et al. *(2018) under the CC BY 4.0 license. I am one of the authors of the original figure.*

3.1.2 Temporal sorting of super-resolution data by diffraction-limited intensity

In high-throughput super-resolution microscopy experiments with individually labeled endocytic proteins, it is possible to obtain datasets with thousands of endocytic sites that can then be combined to average radial distributions. However, each endocytic site was fixed at a random point along the whole endocytic timeline and in the averages these data get merged, meaning there is no temporal resolution.

To get an estimate at which relative endocytic time point an endocytic site was fixed, we imaged a second protein (timing marker) tagged with GFP diffraction-limited after the acquisition of the super-resolved data. By sorting the individual snapshots of endocytic sites by increasing GFP intensity of the timing marker, we can then retrieve temporal information from the large dataset. We divided the individual endocytic sites into four groups to quantify temporal changes: one for the sites where no GFP signal was present and the GFP positive sites were distributed equally in three bins (low, medium, and high GFP signal). For the choice of the timing marker, it is important that its presence at the endocytic site overlaps with the protein imaged in super-resolution and that its abundance changes during that time.

For the early protein Ede1 (Fig. 3.2A) the ideal timing marker is the coat protein Sla2. It arrives at the endocytic site relatively early and its molecular numbers increase monotonically during the presence of Ede1 (Picco *et al.*, 2015). In this case, the four groups of no and increasing GFP signal correspond to the sequence of rearrangements of Ede1 over time. The outer radius for Ede1 increases from 60.8 ± 0.4 nm (no GFP; mean $\pm$ SEM; n = 2514; SD = 20.9 nm) over 63.0 ± 0.4 nm (low GFP; mean $\pm$ SEM; n = 2634; SD = 19.2 nm) and 67.1 ± 0.4 nm (medium GFP; mean $\pm$ SEM; n = 2634; SD = 20.0 nm) to 69.9 ± 0.4 nm (high GFP; mean $\pm$ SEM; n = 2634; SD = 22.4 nm).

We then timed the coat protein Pan1 with the actin binding protein Abp1 (Fig. 3.2B). With this combination, it is possible to distinguish the average distribution of Pan1 before (no GFP) and after actin polymerization (low, medium, and high GFP). For Pan1 patches prior to actin polymerization, we found an average outer radius of 41.8 ± 0.9 nm (no GFP; mean $\pm$ SEM; n = 494; SD = 19.7 nm) which increases to 50.1 ± 1.6 nm (high GFP; mean $\pm$ SEM; n = 98; SD = 16.2 nm). There is no detectable change in the outer radius during the actin assembly phase since the bins with low and medium GFP intensity are not significantly different from the bin with high GFP.

Next, we wanted to investigate how the radial distribution of the actin NPF Las17 changes during membrane ingression by also timing it with Abp1-GFP. Prior to actin polymerization, Las17 already forms rings with an outer radius of 67.1 ± 0.5 nm (no GFP; mean $\pm$ SEM; n = 2550; SD = 23.2 nm) which increase to values of 69.4 ± 0.6 nm (low GFP; mean $\pm$ SEM; n = 1595; SD = 23.5 nm), 69.8 ± 0.6 nm (medium GFP; mean $\pm$ SEM; n = 1595; SD = 25.6 nm), and 70.3 ± 0.7 nm (high GFP; mean $\pm$ SEM; n = 1595; SD = 27.4 nm) while the invagination is formed.

Finally, we investigated the temporal changes of Abp1 as a representative protein of the actin network by using Rvs167-GFP as a marker for scission. Before arrival of Rvs167-GFP, Abp1 forms structures with an outer radius of 79.3 ± 0.8 nm (no GFP; mean $\pm$ SEM; n = 1044; SD = 26.8 nm). This hardly changes upon arrival of Rvs167 when the outer radius is 79.6 ± 1.0 nm (low GFP; mean $\pm$ SEM; n = 568;

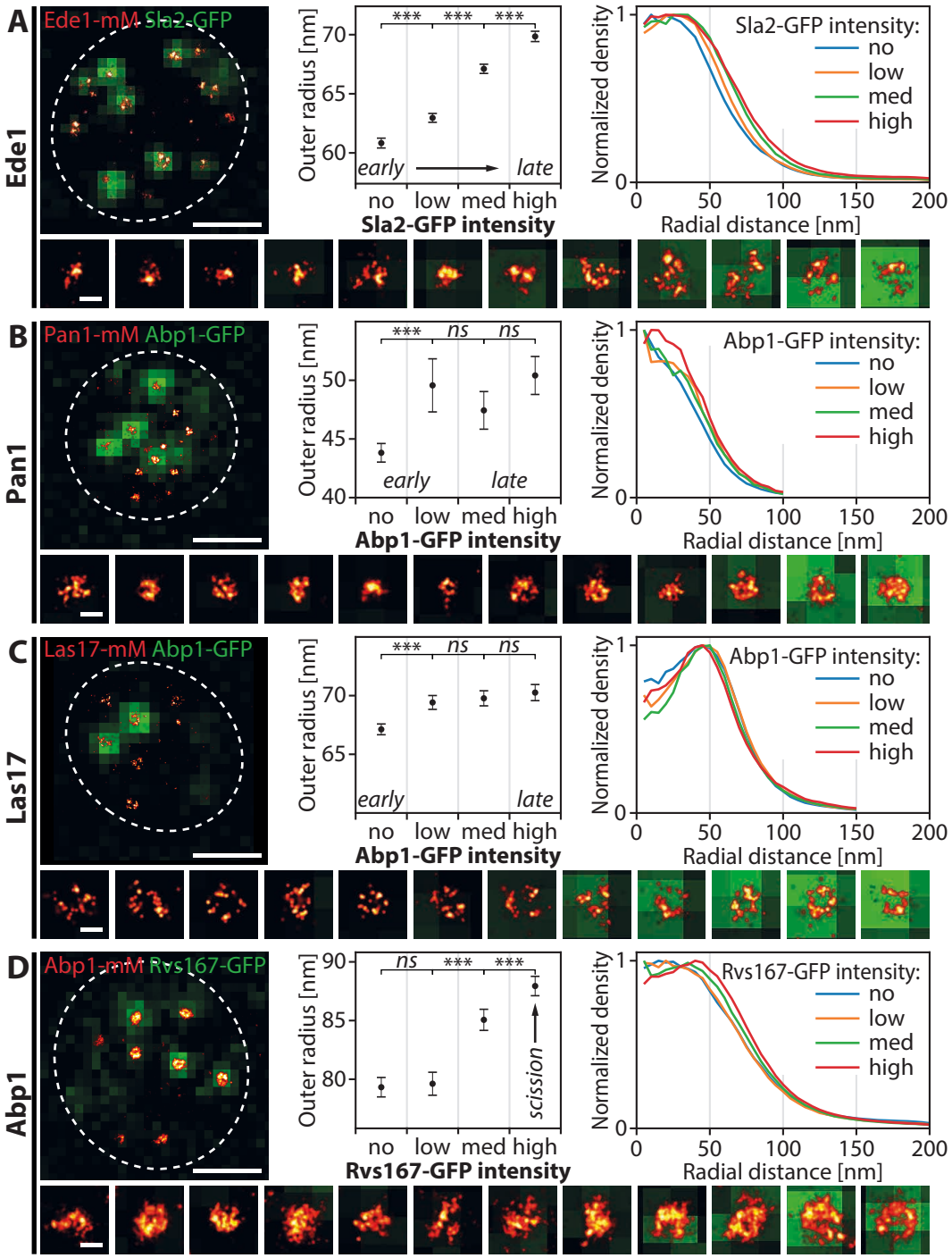

Figure 3.2 | Temporal sorting of super-resolution data by diffraction-limited GFP intensity. (**A** to **D**) The indicated endocytic proteins (red) were imaged in super-resolution alongside with a diffraction-limited timing marker tagged with GFP (green). Endocytic sites without GFP signal were assigned to the *no* GFP group whereas the rest was sorted by GFP intensity and then binned into the equally sized groups *low*, *med*ium, and *high* GFP intensity. For each group, the radial profiles (right) and outer radii (middle) were calculated. The overview images show representative cells, the individual endocytic sites below are equally spaced according to their GFP rank. Number of analyzed structures: **A**: $n_{\mathrm{no}} = 2514$; $n_{\mathrm{low}} = n_{\mathrm{med}} = n_{\mathrm{high}} = 2634$; **B**: $n_{\mathrm{no}} = 494$; $n_{\mathrm{low}} = n_{\mathrm{med}} = n_{\mathrm{high}} = 98$; **C**: $n_{\mathrm{no}} = 2550$; $n_{\mathrm{low}} = n_{\mathrm{med}} = n_{\mathrm{high}} = 1595$; **D**: $n_{\mathrm{no}} = 1044$; $n_{\mathrm{low}} = n_{\mathrm{med}} = n_{\mathrm{high}} = 568$. Scale bars are 1 µm (whole cells) and 100 nm (endocytic sites). *** $p < 0.001$ from Wilcoxon rank-sum test. Error bars represent the mean ± SEM. The data presented in this figure were produced by Markus Mund and Jan van der Beek (A, C) and jointly with Markus Mund (B, D). *Adapted from Mund* et al. *(2018) under the CC BY 4.0 license. I am one of the authors of the original figure.*

SD = 23.4 nm). The outer radius increased to 85.1 ± 0.9 nm (mean $\pm$ SEM; n = 568; SD = 21.5 nm) for medium GFP intensities and further to 87.9 ± 0.8 nm around scission (high GFP; mean $\pm$ SEM; n = 568; SD = 19.7 nm). Apart from the change in radius, the minimum in the center of the radial distribution became more apparent in the group with high GFP intensity.

3.2 Temporal sorting of endocytic snapshots in dual-color localization microscopy

Dual-color localization microscopy is another option to retrieve temporal information from individual endocytic sites that are randomly sampled along the endocytic timeline. In this approach, we imaged two endocytic proteins in different channels and used their relative geometry to sort the sites assuming regularity of the endocytic progress.

3.2.1 Concept of sorting side views of endocytic snapshots

For the different concepts we want to introduce here and in later sections, we imaged endocytic sites in the equatorial plane of yeast cells (Fig. 3.3B). The resulting images showed a projection of endocytosis in side view (Fig. 3.3A, C). From centroid tracking in living yeast cells, we know the relative movement of many endocytic proteins (Picco *et al.*, 2015) and based on this, the following approach was developed by Markus Mund in our lab (Mund, 2016; Mund *et al.*, 2018).

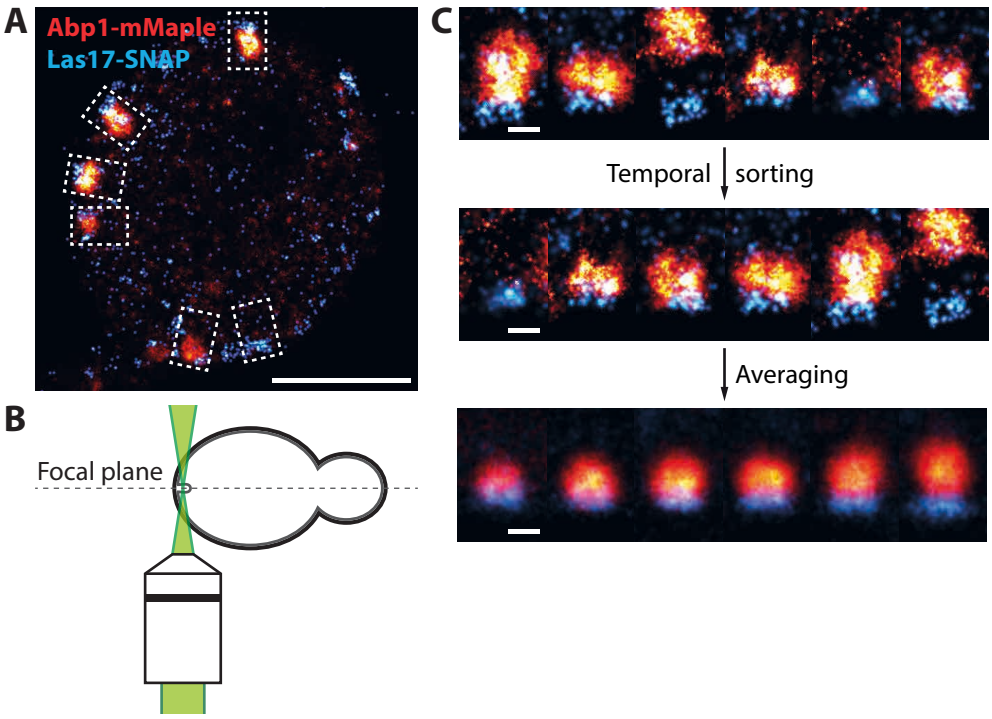

Figure 3.3 | Concept of sorting individual endocytic sites in dual-color localization microscopy. (**A**) Yeast cell imaged by dual-color localization microscopy in the equatorial plane. (**B**) Illustration for imaging of endocytic sites in the equatorial plane of yeast cells. (**C**) Individual endocytic sites (top) were sorted by increasing distance between the centroids of Las17 and Abp1 (middle) and averaged by a running window (bottom; window size: 22 sites). The depicted sites are equally spaced along the sorted sites. In total, $n = 131$ sites were analyzed. Scale bars are 1 µm (A) and 100 nm (C).

In this approach for sorting of endocytic sites based on dual-color SMLM data, we imaged the actin NPF Las17 (blue) and the actin binding protein Abp1 (red) together

(Fig. 3.3A, C). Las17 stays at the base of the plasma membrane, whereas over time the centroid of Abp1 moves inwards together with the growing invagination. For each endocytic site, we computed the distance between the centroid of the two super-resolved channels and sorted the sites increasingly by this value (Fig. 3.3C middle). We manually placed snapshots that only contained signal from the Las17 channel at the beginning of the sorted list because the protein arrives at the endocytic site before Abp1. Then, we aligned the sorted sites to the Las17 signal, averaged them by a running window (size: 22 sites), and displayed the result either as a movie or equally spaced snapshots thereof (Fig. 3.3C bottom).

3.2.2 Experimental limitations of dual-color localization microscopy and data analysis

The approach described above works well but has several limitations that we wanted to tackle. Dual-color localization microscopy was achieved by imaging the pcFP mMaple (McEvoy *et al.*, 2012) together with AF647 that was covalently linked to the SNAP-tag (Keppler *et al.*, 2003) during sample preparation. We chose this dual-color scheme with spectrally different fluorophores because the lack of post-fixation labeling schemes in yeast prevented us from using the standard ratiometric dye pair AF647/CF680 (Mund, 2016; Lehmann *et al.*, 2015). AF647 is the standard synthetic dye used in STORM, however, it requires a special buffer that contains a thiol and is devoid of oxygen. Oxygen depletion is achieved enzymatically, but this comes at the prize of acidification of the buffer over time, which is detrimental for localization microscopy. Therefore, the buffer needs to be replaced every couple of hours, which hinders high-throughput acquisition of dual-color super-resolution data. I resolved this first limitation by testing different dual-color approaches and alternative oxygen depletion systems (section 3.3).

The post-processing of the localization data is also limited in throughput. For the data presented above (Fig. 3.3A, C), each endocytic site was manually selected and rotated in a way so that the plasma membrane is at the bottom of the images of the endocytic site. This issue was solved by Yu-Le Wu, another PhD student in our lab, who developed an automated segmentation pipeline with my input (section 3.4.1).

Beyond these improvements, we came up with a new way of extracting features from individual snapshots. The analysis described above uses the centroid and can be extended to using quantiles, but it does not extract more quantitative features. By fitting a model to the data that also includes prior knowledge, we were able to represent the localization data better and extract more quantitative data (section 3.4.2).

3.3 Increasing the throughput of dual-color localization microscopy in yeast

3.3.1 Primed conversion

Our lab's standard dual-color labels for localization microscopy in yeast are mMaple and AF647. These two labels have different fluorescence emission wavelengths, therefore, their fluorescence emission spectra are recorded simultaneously by splitting the signal with a dichroic mirror. One way to extend the sample durability is to use a different dual-color strategy where imaging is performed in a long-lived buffer.

One such approach is based on the primed conversion of pcFPs, which is an illumination scheme to convert some, but not all, green to red pcFPs (see section 1.1.6.6). This allows the sequential combination of a pcFP that can undergo PC with a pcFP that can only be activated by UV activation (Turkowyd *et al.*, 2017; Virant *et al.*, 2017). In PC, the fluorophore gets excited from its green state to enter the so-called primed state and is then converted to the red state by excitation with a 730 nm laser. It is reported that the conversion from the primed to the red state can also be achieved by an excitation wavelength of 640 nm (Turkowyd *et al.*, 2017). PC-compatible pcFPs encompass mMaple, mMaple3, and mEos3.2 with the alanine to tyrosine substitution at position 69 (mEos3.2A69T) which have been tested in *Escherichia coli*, *Schizosaccharomyces pombe*, and cultured mammalian cells (Turkowyd *et al.*, 2017; Virant *et al.*, 2017).

To test whether PC also works in *Saccharomyces cerevisiae*, I endogenously tagged the NPC component Nup49 with mMaple3 and mEos3.2A69T. Then, I prepared samples and acquired super-resolution images of these strains under different conditions together with David Virant on the setup in Ulrike Endesfelder's lab in Marburg (Fig. 3.4). The positive control with UV activation showed a staining of the nuclear envelope for both pcFPs and individual nuclear pores were visible when zooming in (Fig. 3.4A, B). When imaging with primed conversion, the nuclear envelope was discernible for both mMaple3 and the mEos variant (Fig. 3.4C, D). However, the labeling with mMaple3 was more sparse and the signal-to-noise ratio was worse (Fig. 3.4C), whereas the super-resolution images for mEos3.2A69T under UV activation and primed conversion were visually comparable (Fig. 3.4D). For both pcFPs, the primed conversion was complete as UV activation after the image acquired with PC only activated very few fluorescent molecules (Fig. 3.4E, F).

As this initial test was promising, I imaged Nup188, a different component of the NPC, tagged with mMaple3 with our microscope. The image acquired with standard UV activation as a positive control showed the nuclear envelope with good contrast (Fig. 3.5A). Our setup does not offer 730 nm excitation, which is why I performed the primed conversion with the 638 nm laser (Fig. 3.5B). The nuclear envelope was

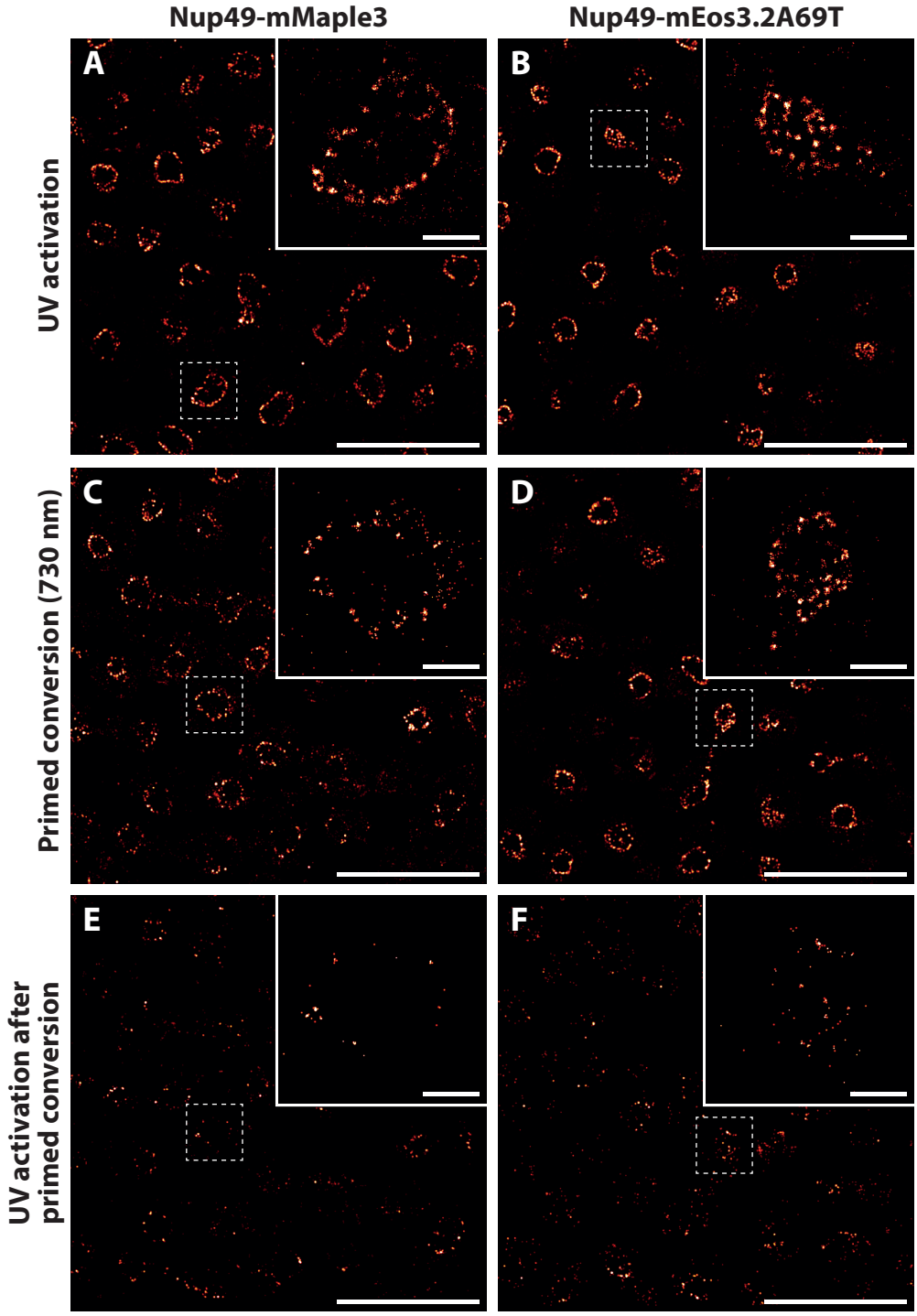

Figure 3.4 | Primed conversion with a 730 nm laser. Nup49 was endogenously tagged with either mMaple3 (A, C, E) or mEos3.2A69T (B, D, F) in yeast. The samples were either imaged using standard UV activation (A, B) or primed conversion (C, D). After primed conversion, the completeness of activation was checked by imaging with UV activation of the same field of view (E, F). The insets show detailed views of the nuclei in dashed boxes in the overview image. Scale bars are 10 µm (overview images) and 1 µm (insets of single nuclei). The data presented in this figure were produced jointly with David Virant.

apparent again, however, the localizations were quite sparse and individual nuclear pores were hardly discernible. UV activation of the same field of view revealed that the primed conversion was incomplete as many fluorescent molecules got activated and localized (Fig. 3.5C).

As other efforts were successful (section 3.3.2), I stopped to pursue this avenue of increasing the throughput of dual-color localization microscopy.

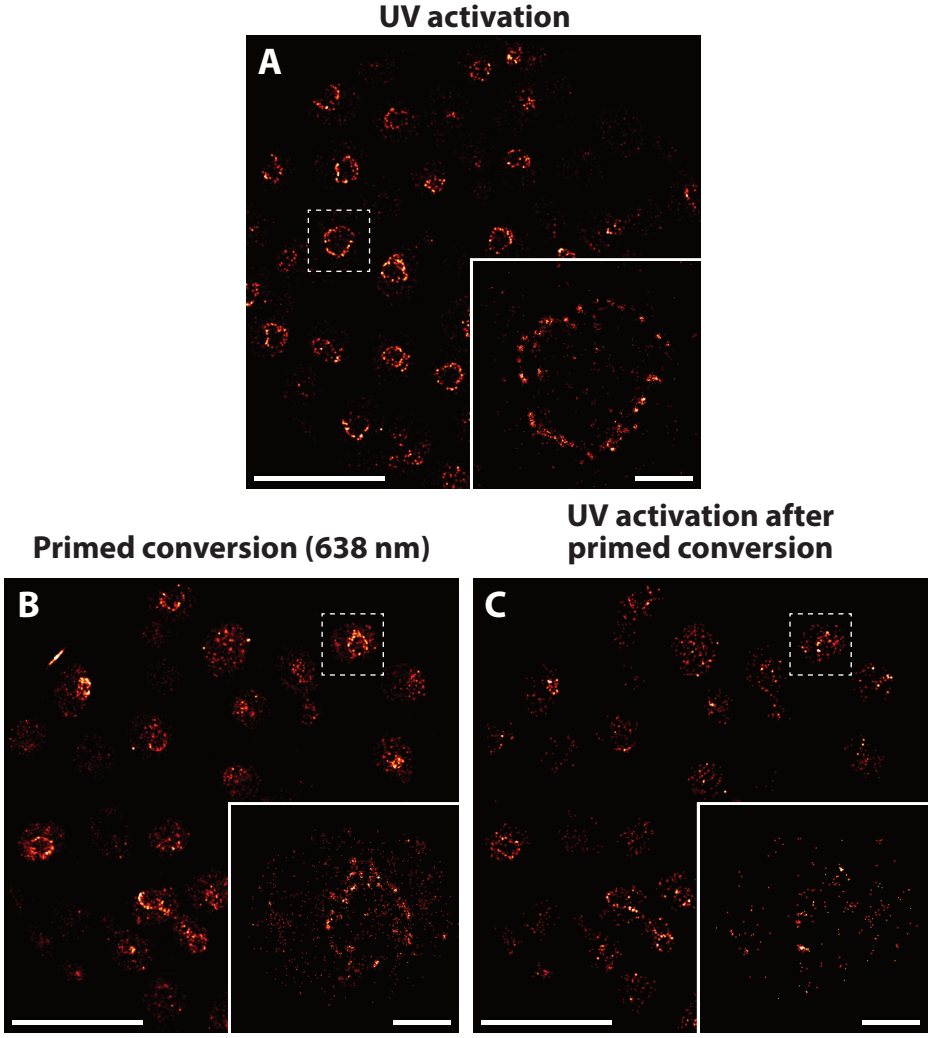

Figure 3.5 | Primed conversion with a 638 nm laser. In cells expressing NUP188 tagged with mMaple3, the nuclear pores were imaged in super-resolution using different modalities. (**A**) A first region was imaged with standard UV activation as control. (**B**) Primed conversion was performed with a 638 nm laser in a second region; (**C**) afterwards unbleached mMaple was imaged with standard UV activation in the same field of view. Scale bars are 10 µm (overview images) and 1 µm (insets of single nuclei).

3.3.2 Increasing the durability of the imaging buffer

The standard sample in our lab to test localization microscopy conditions is the NPC. We have developed mammalian cell lines where Nup017 or Nup96 was endogenously tagged with the SNAP-tag which can be labeled with benzylguanine coupled to AF647 (Li *et al.*, 2018; Thevathasan *et al.*, 2019). A NPC-SNAP-AF647

sample is ideally suited for optimizing imaging conditions because it can be prepared and stored easily and because it offers quantitative readouts by automated analysis.

At the beginning of this section, I want to illustrate why the GLOX buffer in its standard use is not suitable for long-term imaging. To induce blinking in AF647, two important criteria have to be met by the buffer: Firstly, it needs to contain a thiol that reacts with AF647 to create a long-lived non-fluorescent species (Fig. 1.6). Secondly, the buffer needs to be devoid of oxygen, which is achieved by an oxygen scavenging system. The typical GLOX/catalase system used for this purpose produces an acid. Since we typically use an open buffer system, oxygen gets introduced from the environment continuously. The constant addition of oxygen gets depleted by GLOX, but over time this leads to acidification as the buffer capacity is exceeded. An exemplary super-resolution microscopy acquisition during which the pH of the imaging buffer drops is shown in figure 3.6. Initially, normal single-molecule blinking can be observed (Fig. 3.6A, B: ii & iii) from which a high-quality image can be reconstructed (Fig. 3.6C). In this period, the automated UV activation ensures a constant value of localizations. After approximately half of this acquisition, which was several hours after preparation of the buffer, a change in the buffer occurred. This change led to an increase in detected localizations (Fig. 3.6A: v to viii) and bright background (3.6B: v to viii) and the reconstructed image showed unspecific structures (Fig. 3.6D). The unspecific localizations were also detected by the algorithm controlling the UV activation as the maximum activation was not reached and the acquisition was stopped by the maximum amount of frames. During an overnight acquisition, the pH can drop from an initial value of 8 to 2. In this state, the sample is decayed in a way that it cannot be recovered by replacing the imaging buffer with one that was freshly prepared.

3.3.2.1 Characterization of oxygen scavenging systems

In the first screen, I tested four alternative oxygen scavenging systems where the oxygen depletion is not connected with the generation of acidic compounds. Pyranose oxidase oxidizes glucose to 2-dehydro-glucose, PCD oxidizes 3,4-dihydroxybenzoate, OxyFluor™ reduces oxygen to water with a proprietary enzyme formulation supplemented with lactate and sulfite reacts with oxygen to sulfate. Before the super-resolution experiments, I measured the pH of the imaging buffers with different oxygen scavenging systems after leaving them open for 24 h and confirmed that only the GLOX system causes an acidification. I prepared Nup107-SNAP-AF647 samples and imaged them with different oxygen scavenging systems. In all of them, the nuclear membrane is clearly stained and individual nuclear pores are discernible (Fig. 3.7). However, the labeling density is already visually quite different. For GLOX and POX, the individual NPC rings appear the most complete, followed by PCD and sulfite. For OxyFluor™, the NPCs are mostly incomplete and the number of localizations is lower than for all other conditions (Fig. 3.7).

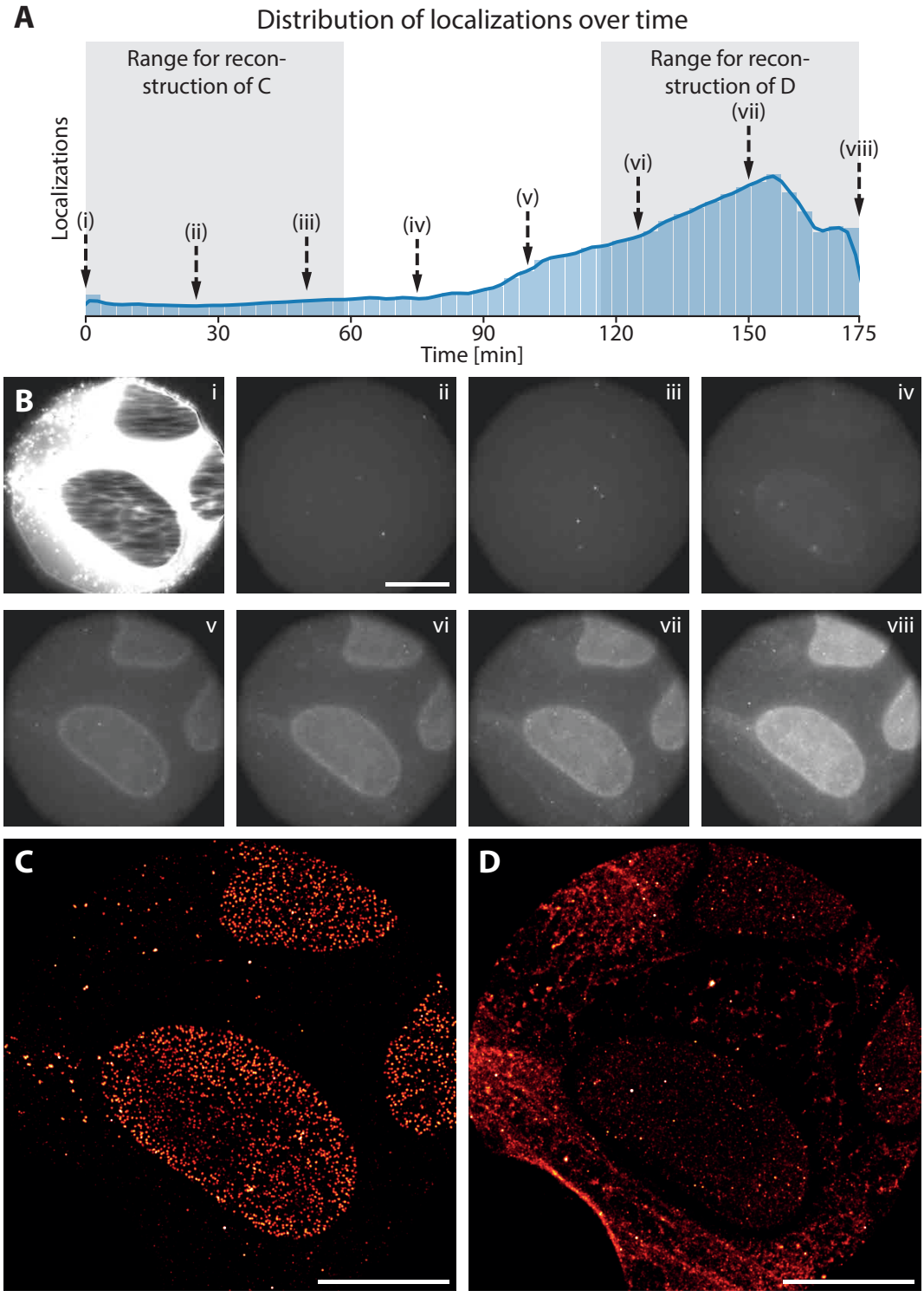

Figure 3.6 | Effect of long-term imaging in open GLOX buffer. (**A**) Histogram and fitted kernel density estimation (solid blue line) of the number of localizations over time. Approximately in the middle of the experiment, a change in the buffer led to an increase of detected localizations. The dashed arrows label the time points of the individual raw frames in B. The ranges indicated in gray are reconstructed as super-resolution images in C and D. (**B**) Exemplary raw data from the indicated frames. At the beginning of the experiment, the blinking of single molecules was as expected, whereas in the second half the blinking and bright background increased substantially, which was several hours after the buffer was originally prepared. (**C**) Reconstructed super-resolution image of the first third of the experiment. (**D**) Same as C, but for the last third. Scale bars are 10 µm.

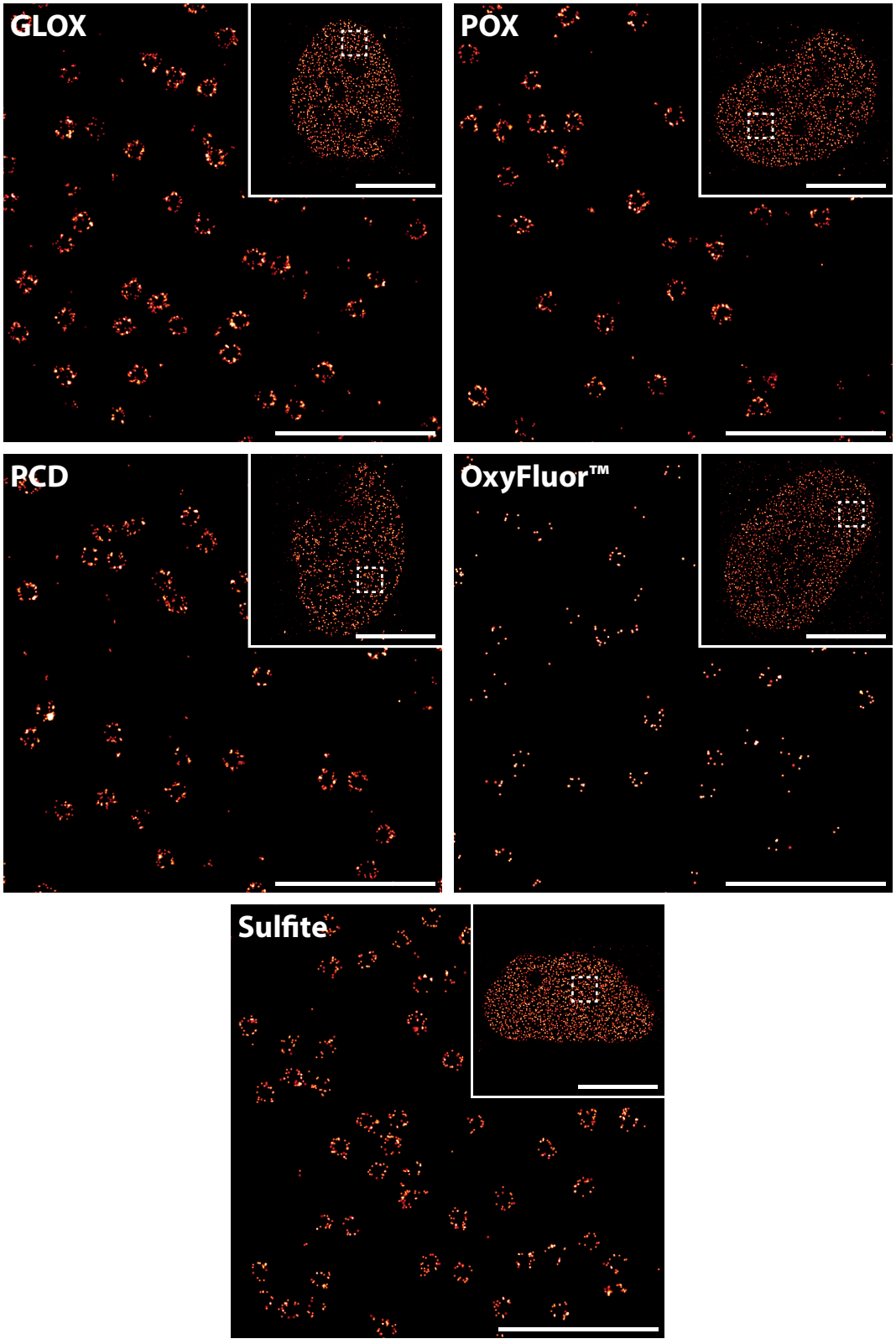

Figure 3.7 | Visual comparison of oxygen scavenging systems. U2OS Nup107-SNAP cells have been stained with BG-AF647 and imaged in buffers containing different oxygen scavenging buffers: Glucose oxidase/catalase (GLOX), pyranose oxidase/catalase (POX), protocatechuate dioxygenase (PCD), OxyFluor™, or inorganic sulfite. Shown are representative overview images (top right) and magnifications of the regions indicated by dashed boxes. See figure 3.8 for quantitative results. Scale bars are 10 µm (overview images) and 1 µm (zoom-ins).

I then analyzed the different oxygen scavenging systems quantitatively. From the whole field of view, the number of photons and background photons per grouped localization, the localization precision (rising edge of the distribution), and the on-time of fluorophores for each localization were measured and averaged. Additionally, the ELE and the mean number of localizations were calculated per NPC (Fig. 3.8). The ELE is a measure of how many target structures appear labeled, taking into account the labeling reaction but also photophysical effects during the acquisition. It was calculated based on counting the number of corners observed per NPC and a binomial model (see section 6.2.7.9). The values reported here, are averages per nucleus.

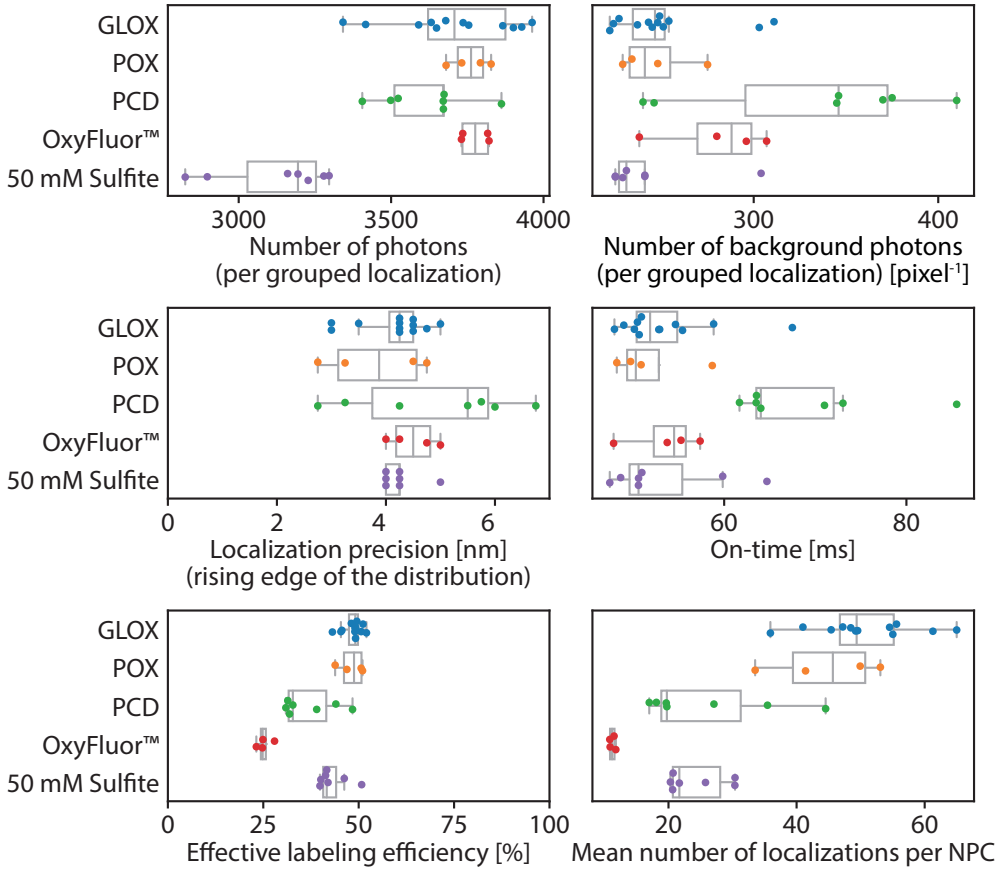

Figure 3.8 | Quantitative comparison of oxygen scavenging systems in single images. Single images of nuclei were acquired using different oxygen scavenging systems: glucose oxidase/catalase (GLOX), pyranose oxidase/catalase (POX), protocatechuate dioxygenase (PCD), OxyFluor™, and sulfite. For each image, the number of photons and background photons per grouped localization, the localization precision (rising edge of the distribution), and the average on-time per localization were determined. The nuclear pore complexes (NPC) were segmented and the effective labeling efficiency as well as the mean number of localizations per NPC were computed. The following number of nuclear pore complexes and nuclei were analyzed: 8538 NPCs in 12 nuclei (GLOX), 2609 NPCs in 4 nuclei (POX), 4020 NPCs in 7 nuclei (PCD), 270 NPCs in 4 nuclei (OxyFluor™), and 5526 NPCs in 7 nuclei (Sulfite). Boxplots show the median, quartiles, and the rest of the distribution (whiskers). Outliers (values beyond 1.5 times the interquartile range) are not included in the boxplot but are visualized in the dot plot.

The number of photons per grouped localization was in the range of 3700 to 3800 for GLOX, POX, and OxyFluor™ with PCD being slightly lower and sulfite being the lowest with around 3200 photons. In addition, the number of background photons does not show big differences between the different systems: It typically is in the range of 250 photons per pixel per grouped localization with some outliers towards 400 background photons. Consequently, the localization precision is with 4 to 5 nm very similar for all conditions. During post-processing of the raw imaging data, we can compute for how many frames each molecule was fluorescing. By multiplication with the exposure time of a single frame during the acquisition, we can determine the average on-time per molecule. This number provides information on the lifetime of the fluorescent state. It was similar with about 50 ms for all oxygen scavenging systems except for PCD, where the median on-time increased to about 65 ms. I then used the automated analysis pipeline to automatically segment individual NPCs (see section 6.2.7.7) and subsequently analyzed their ELE and the number of localizations per NPC. These values are quantitative measures of the completeness of labeling of the structures of interest. Here, bigger differences between the different oxygen scavenging systems become apparent. GLOX and POX reach the highest values for the ELE with 49 %, sulfite has a slightly decreased ELE with 42 %, and PCD and OxyFluor™ are even lower with 33 and 25 %, respectively. A similar trend can be observed for the mean number of localizations per NPC, what corroborates the observations in the respective images from above (Fig. 3.7). Because of the inferior results for OxyFluor™, I excluded it from the subsequent experiments.

3.3.2.2 Long-term testing of oxygen scavenging systems

After the initial characterization, I subjected the different oxygen scavenging systems to long-term tests. I again prepared Nup107-SNAP-AF647 samples, defined the positions of different nuclei on the microscope stage, and then imaged one position after the other with our automated localization microscope. The overnight imaging sessions lasted for 10 to 12 h and super-resolved reconstructions of the first and last acquisitions are shown in figure 3.9. As shown before (Fig. 3.6), long-term imaging was not possible with GLOX as after some time the structures of interest were not imaged faithfully as the background and the signal from other cellular structures increased (Fig. 3.9, first column). A similar effect, albeit weaker, was also observed when the buffer capacity was increased from 50 mM to 150 mM (Fig. 3.9, second column). In buffers with the other oxygen scavenging systems, the pH was stable for 24 h as determined by pH strips. Nevertheless, the specific signal got a lot weaker over time for the oxygen scavenger POX and individual NPCs were not discernible any more, but there was no unspecific signal like for GLOX (Fig. 3.9, third column). Long-term imaging with PCD resulted in apparent NPCs, but they had a visually detectable lower labeling efficiency (Fig. 3.9, fourth column). On the contrary, super-resolution images acquired with the oxygen scavenger sulfite in the buffer had the same quality at the start and end of the overnight acquisitions (Fig. 3.9, last column).

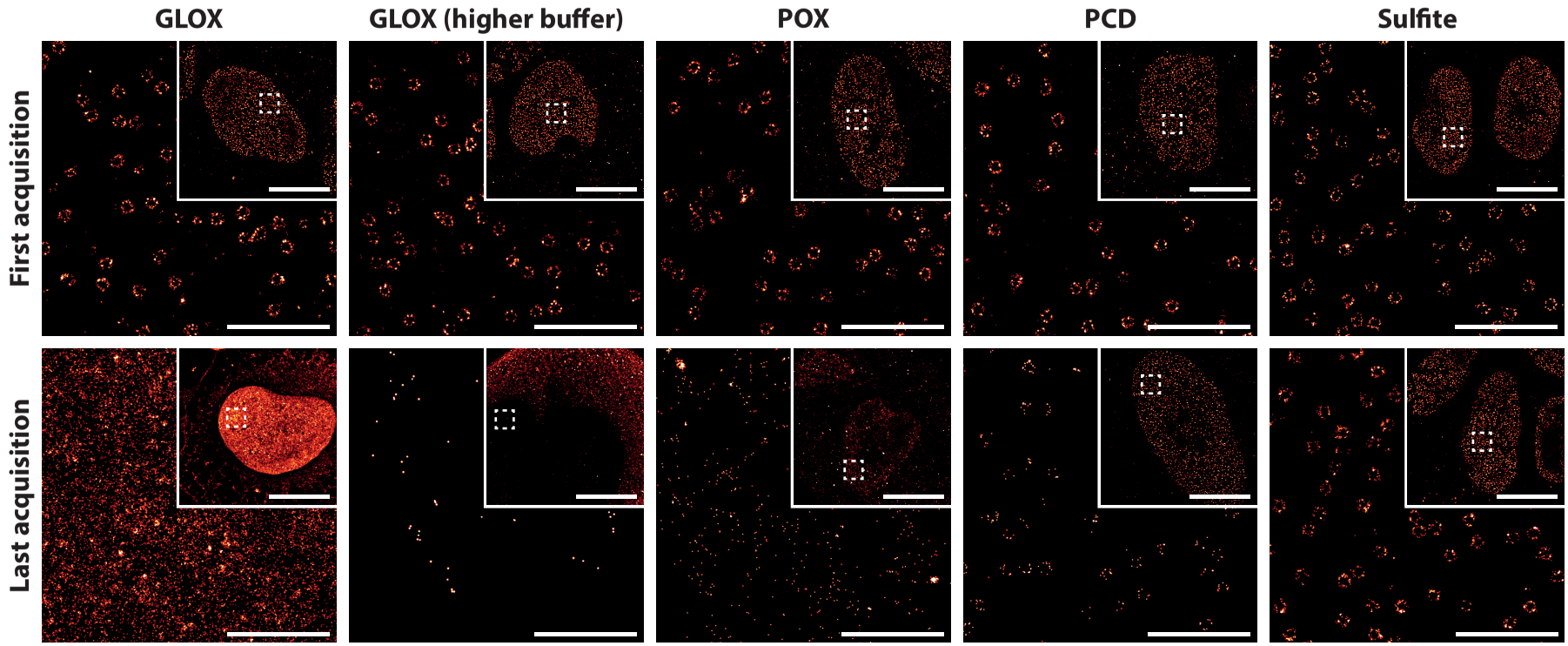

Figure 3.9 | Visual comparison of oxygen scavenging systems in long-term imaging. U2OS Nup107-SNAP-AF647 samples were subjected to overnight super-resolution microscopy with imaging buffers containing the indicated oxygen scavenging systems: glucose oxidase/catalase (GLOX), GLOX with higher buffer capacity, pyranose oxidase/catalase (POX), protocatechuate dioxygenase (PCD), and sulfite. In the top row, reconstructions of individual nuclei and zoom-ins thereof are shown at the start of the imaging session. The bottom row shows the same for the last acquisition which was acquired the next morning. See figure 3.10 for quantitative results. Dashed boxes indicate the positions of the zoom-ins. Scale bars are 10 µm (overview images) and 1 µm (zoom-ins).

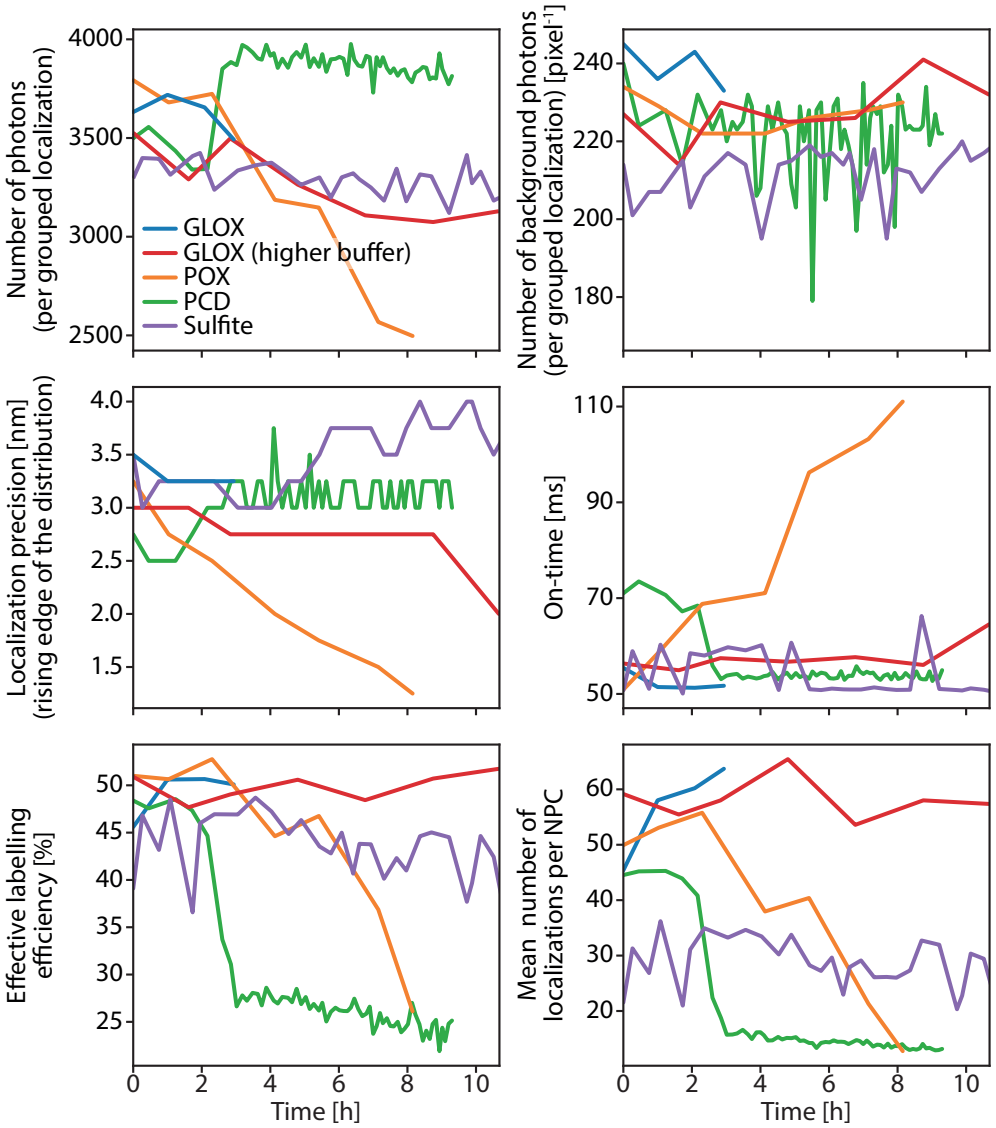

Figure 3.10 | Quantitative comparison of oxygen scavenging systems in long-term imaging. The long-term imaging sessions visualized in figure 3.9 were quantified and the respective measurements plotted over time. If a line ends before the maximum value of the x-axis, it was not possible to analyze the localization microscopy data after that time point. For each condition, one coverslip was imaged, each data point represents the quantification of a single nucleus.

The trends observed in the images can also be seen in the quantitative analysis of the long-term acquisitions (Fig. 3.10). For GLOX, only the first four images could be analyzed before the sample deteriorated. The duration until the data was not analyzable increased to a bit above 10 h for the GLOX system with increased buffer capacity (maximum of the x-axis in Fig. 3.10). During the long-term acquisition with POX as an oxygen scavenger, the on-time of the fluorophores was more than doubled before analysis was impossible. With a fall in the number of photons per grouped localization, the effective labeling efficiency as well as the mean number of localizations per NPC decreased. Unexpectedly, the localization precision also decreased over time for POX, although the number of photons decreased and the number of background photons stayed at a similar level. In the imaging buffer with PCD as an oxygen scavenger, a sudden steep decrease in the ELE and the mean number of localizations could be observed. The change also became apparent by a decrease in fluorophore on-time and the fact that the acquisition of individual nuclei got shorter as the frequency of values increased. For the buffer system supplemented with sulfite as oxygen scavenger, the different quantitative measurements stayed relatively constant over a period of 10 h and more. However, the ELE was slightly decreased and the mean number of localizations per NPC was substantially lower compared to the standard GLOX system in the beginning. With these results at hand, I decided to only pursue sulfite as replacement for the GLOX oxygen scavenging system.

3.3.2.3 Titration of the oxygen scavenger sulfite

All data presented for sulfite-based imaging buffers so far contained 50 mM of sulfite. We reasoned that decreasing the sulfite concentration could improve the relevant quantitative measures. To test this, I imaged Nup96-SNAP-AF647 samples with concentrations of 10 mM, 20 mM, and 30 mM sulfite, and with GLOX as positive control (Fig. 3.11). The sample changed from Nup107-SNAP to Nup96-SNAP because in the meantime other members of our lab had found that with Nup96 the individual corners of the eightfold symmetric NPC are better separated from each other what makes the ELE analysis more robust. The measurements showed that with lowering the sulfite concentration, the number of photons per grouped localization increased almost to the same level as with GLOX. The number of background photons was barely affected and consequently the localization precision decreased with lower sulfite concentrations. The values for the fluorescence on-time were scattering too much to make a reasoned statement. With decreasing sulfite concentration, the average ELE increased from 42 % for 10 mM sulfite over 44 % for 20 mM sulfite to 48 % ELE for 30 mM sulfite. Compared to that, in GLOX buffer, the ELE had a mean value of 55 %. Despite this increase in ELE with decreasing sulfite concentration, the mean number of localizations stayed below 50 % of the value for GLOX. As this value is one of the most important to get a good signal-to-noise ratio and a

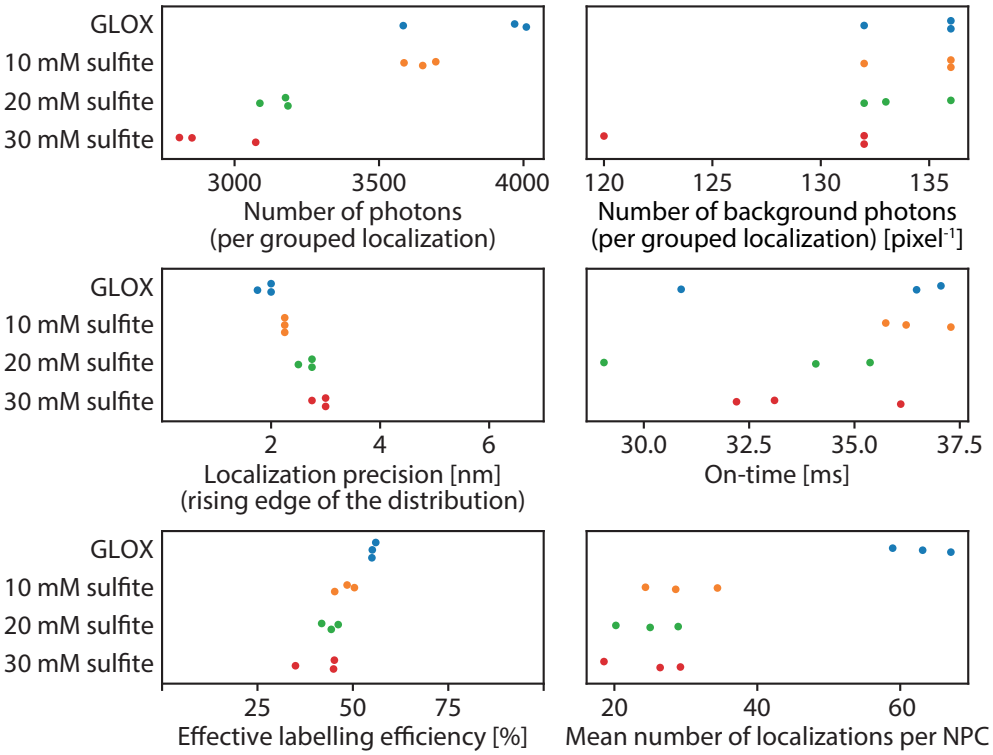

Figure 3.11 | Influence of sulfite concentration on quantitative measurements of localization microscopy. U2OS Nup96-SNAP cells were stained, super-resolution data was acquired in different imaging buffers, and the indicated parameters were determined. Different concentrations of sulfite as oxygen scavenger were tested and as positive control the buffer contained GLOX. $n = 3$ nuclei were analyzed per condition. The following number of nuclear pore complexes were analyzed in 3 nuclei each: 1797 NPCs (GLOX), 2609 NPCs (10 mM sulfite), 2170 NPCs (20 mM sulfite), and 2392 NPCs (30 mM sulfite).

higher sulfite concentration has a higher capacity to deplete oxygen, we stayed with a sulfite concentration of 50 mM for subsequent experiments.

3.3.2.4 Characterization of triplet state quenchers

Molecular oxygen can act as a triplet state quencher (Kawaoka *et al.*, 1967). Since sulfite solutions are used as zero in the calibration of oxygen sensors (Pickering, 1979), the lower number of localizations could be caused by the lack of minute amounts of oxygen in comparison to the enzymatic GLOX system. Based on this reasoning, I tested the addition of two triplet state quenchers to the imaging buffer. The polyunsaturated hydrocarbon cyclooctatetraene (COT), that acts as a triplet state quencher, was reported to stabilize AF647 (Dave *et al.*, 2009) and improve the resolution in STORM experiments (Olivier *et al.*, 2013). Additionally, the vitamin E analogue trolox was reported as a triplet state quencher (Zheng *et al.*, 2012) whose mode of action is based on a redox reaction (Cordes *et al.*, 2009).

Based on this line of reasoning, I tested the influence of the triplet state quenchers COT and trolox on the statistics of imaging Nup96-SNAP-AF647 (Fig. 3.12). When added to the GLOX buffer, COT led to a slight rise the number of photons per

grouped localization and therefore the localization precision was diminished. The on-time increased from an average of 35 ms to 42 ms. Furthermore, the ELE decreased from 59 % to 54 % and the average number of localizations dropped from 76 to 64. The addition of trolox to the GLOX buffer only led to a reduction in both the ELE and the mean number of localizations (36 % and 31 localizations per NPC). For the imaging buffer based on sulfite, the influence of COT was similar as described for GLOX: The photon count and on-time increased and the localization precision was reduced, each in a concentration-dependent manner. The addition of COT in different concentrations had no influence on the ELE and the mean number of localizations per NPC. For sulfite-based imaging buffer supplemented with trolox, the number of photons per grouped localization dropped and consequently the localization precision increased. The on-time was diminished and the ELE increased slightly (55 % compared to 49 % for pure sulfite). Moreover, the mean number of localizations rose from 26 to 39. Taken together, the addition of COT could not improve the sulfite-based imaging buffer, whereas supplementation of trolox led to a rise in the average number of localizations but at the prize of less photons and thus a worse localization precision. This is why in the following experiments with yeast I did not put any supplement to the imaging buffer based on sulfite.

3.3.2.5 Characterization of oxygen scavenging systems with yeast samples

After having characterized the sulfite-based buffer to be an adequate replacement to perform long-term localization microscopy on mammalian samples, I went on to also test it on dual-color yeast samples. In these experiments, I assessed the compatibility of sulfite with imaging in yeast and the second fluorophore mMaple. The experimental setting I chose was as follows: I took one yeast strain in which the NPC component Nic96 was tagged with the SNAP-tag and mixed the cells during sample preparation with a second strain in which the NPC component Nup188 was tagged with mMaple. I stained the SNAP-tag with BG-AF647 and imaged the two fluorophores side-by-side on the same coverslip in an overnight high-throughput experiment. Importantly, the cysteamine concentration was reduced from 35 mM to 20 mM to reduce thiol-induced flickering of mMaple. During post-processing, I semi-automatically picked 100 individual NPCs at the beginning and at the end of the experiment for both fluorophores. I then quantified the number of photons and background photons per grouped localization, the localization precision, the on-time, and the number of localizations per NPC for both fluorophores independently (Fig. 3.13). The number of photons and the localization precision are reported as median, the on-time as mean, and the number of background photons as the most frequently occurring value per NPC. Exemplary reconstructed images for promising imaging conditions are shown in figure 3.14. I tested the fluorophores under five different conditions:

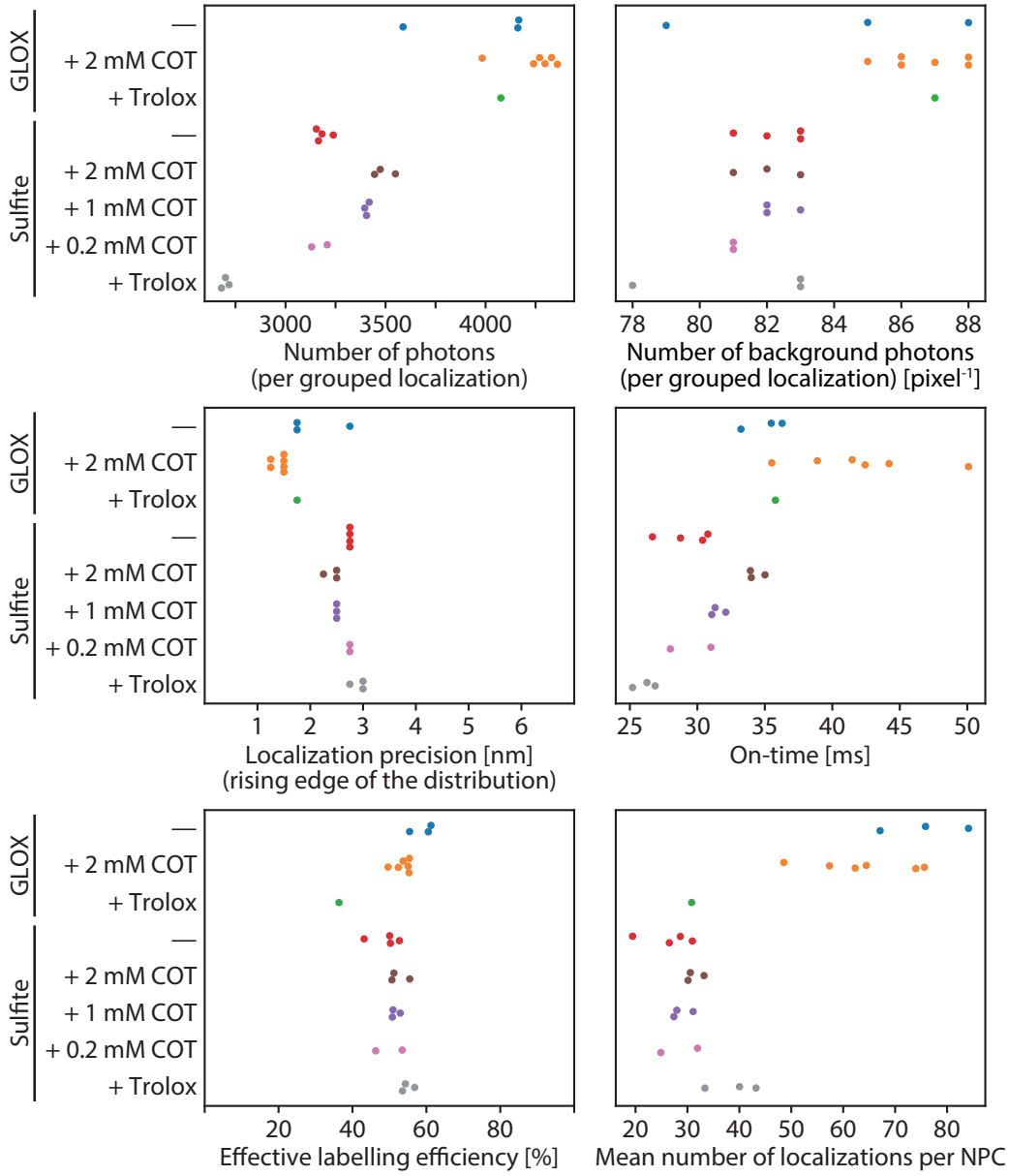

Figure 3.12 | Influence of triplet state quenchers on GLOX- and sulfite-based oxygen scavenging systems. The two triplet state quenchers cyclooctatetraene (COT) and trolox were added to the imaging buffer either based on GLOX or sulfite. Subsequently, the statistics of super-resolution acquisitions of Nup96-SNAP-AF647 were quantified. The following number of nuclear pore complexes and nuclei were analyzed: 2819 NPCs in 3 nuclei (GLOX), 4367 NPCs in 6 nuclei (GLOX + 2 mM COT), 729 NPCs in 1 nucleus (GLOX + Trolox), 3427 NPCs in 4 nuclei (Sulfite), 2393 NPCs in 3 nuclei (Sulfite + 2 mM COT), 2489 NPCs in 3 nuclei (Sulfite + 1 mM COT), 1700 NPCs in 2 nuclei (Sulfite + 0.2 mM COT), and 2458 NPCs in 3 nuclei (Sulfite + Trolox).

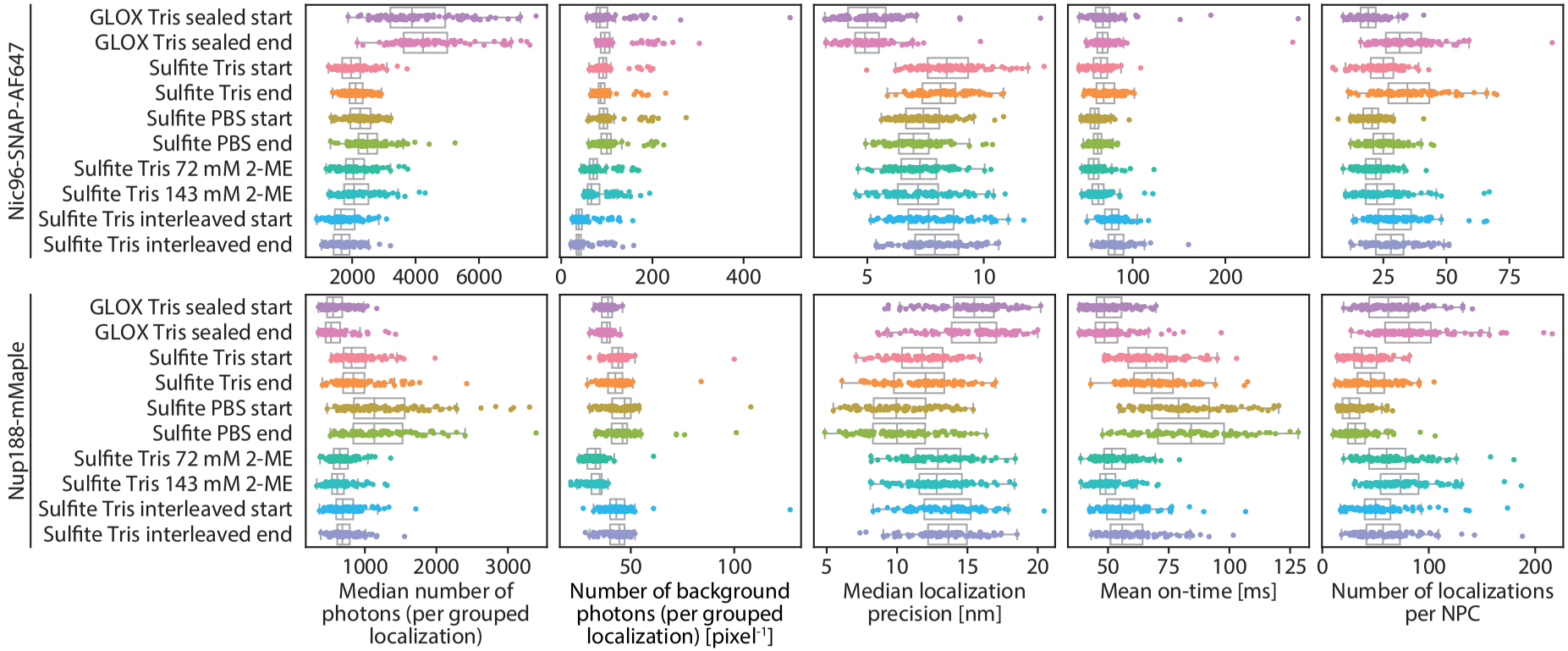

Figure 3.13 | Quantitative comparison of imaging buffers in yeast. Yeast cells with either Nic96-SNAP-AF647 or Nup188-mMaple were subjected to localization microscopy with different imaging buffers and imaging modalities. The buffers were the standard GLOX-based imaging buffer with cysteamine in a sealed sample holder, sulfite-based buffers with cysteamine that were either buffered by phosphate (phosphate-buffered saline, PBS) or Tris, and one buffer containing Tris, sulfite, and 2-mercaptoethanol (2-ME). The alternative imaging scheme was interleaved excitation where the two fluorophores were excited alternating for one frame each, contrasting with the otherwise continuous illumination. For each condition, 100 nuclear pore complexes per fluorophore were segmented and quantified. Where indicated, the quantification was performed at the start and at the end of an overnight imaging session.

- GLOX as oxygen scavenger in an imaging buffer based on Tris pH 8 in a sealed sample holder under continuous excitation.
- Sulfite as oxygen scavenger in an imaging buffer based on Tris pH 8 and cysteamine under continuous excitation.
- Sulfite as oxygen scavenger in an imaging buffer based on PBS pH 7.4 and cysteamine under continuous excitation.
- Sulfite as oxygen scavenger in an imaging buffer based on Tris pH 8 and 2-ME under continuous excitation.
- Sulfite as oxygen scavenger in an imaging buffer based on Tris pH 8 and cysteamine under interleaved excitation.

After having performed all experiments in the mammalian system, Ulf Matti in our lab had found that the pH of the standard GLOX imaging buffer stays constant when the buffer chamber is sealed by parafilm. Originally, we had not taken this solution into account because according to its datasheet, parafilm is oxygen permeable. However, the permeability seems to be low enough to not exceed the buffer capacity with the introduced oxygen over 48 to 72 h. Since the ideal pH for imaging of mMaple is around 8 (McEvoy *et al.*, 2012), I also wanted to test the sulfite-based system in a Tris buffer with this pH. Besides that, I examined if the substitution of cysteamine by 2-ME had any effect on the fluorophore statistics. Finally, I tested the influence of a different illumination scheme during imaging. Typically, we excite both fluorophores at the same time, but the laser that excites mMaple induces a high background fluorescence in the AF647 channel. Thus, I tested an illumination scheme where the fluorophores are excited interleaved, meaning the two lasers are switched on alternating for one frame each.

The sealed sample holder allowed imaging of both AF647 and mMaple in high quality for more than 12 h (Fig. 3.13 and 3.14). The key parameters of the acquisitions stayed the same, only the number of localizations per NPC increased over time in both channels. Next, I compared sulfite as an oxygen scavenger in Tris and in PBS. In PBS, the number of photons per grouped localization and therefore the localization precision was slightly better, however, the number of localizations per NPC was higher for both fluorophores in Tris buffer. The substitution of cysteamine by 2-ME in the Tris-based sulfite buffer resulted in a lower number of photons for mMaple but also a lower number of background photons for both fluorophores. For AF647, the number of localizations per NPC decreased whereas it increased for mMaple. The effect on mMaple is caused by thiol-induced flickering of the fluorophore as it is concentration dependent (72 mM vs. 143 mM). Interleaved excitation of the fluorophores had the expected effect as the the number of background photons per grouped localization in the AF647 channel decreased by more than 50 %. However, the number of photons got reduced as well by the new illumination scheme. After

these initial experiments, the electronic control system of the microscope had to be exchanged and with the new system the interleaved excitation is not possible to date.

Based on the quantitative results (Fig. 3.13), the high quality localization microscopy data (Fig. 3.14), and the unavailability of interleaved excitation, I decided to use the GLOX-based oxygen scavenging system in a sealed sample holder for all subsequent long-term experiments.

3.3.2.6 Comparison of mMaple and mMaple3 under different imaging conditions

Since the original publication of mMaple (McEvoy *et al.*, 2012), an improved version termed mMaple3 was presented (Wang *et al.*, 2014a). mMaple3 was reported to have a lower dimerization tendency than mMaple while maintaining other features that make it a good choice for pcFP-based localization microscopy. Before making the switch to the new version, I compared the photophysical properties of the two proteins in yeast under our standard single- and dual-color super-resolution microscopy conditions. For this, I generated a new strain in which the NPC component Nup188 was tagged with mMaple3. I then imaged this strain together with the Nup188-mMaple strain from the earlier described buffer tests on the same coverslip. The latter strain additionally had the endocytic protein Abp1 tagged with GFP, which allowed to distinguish the two strains during post-processing of the imaging data. There was no visual difference between mMaple and mMaple detectable (Fig. 3.15A). Moreover, the quantification of key parameters showed that the two pcFPs behaved virtually the same. When comparing the two buffers, it was apparent that with the dual-color GLOX system both mMaple versions had a higher number of localizations. This was caused by the flickering of the fluorophores induced by the thiol cysteamine. The flickering led to a smaller number of photons per grouped localization and therefore worse localization precision that we have to compromise on when performing dual-color localization microscopy. Based on these results, I decided to use mMaple3 for all newly constructed yeast strains. As the work of the following sections was partially performed before the characterization of mMaple3, some strains described there were tagged with mMaple. Which version of mMaple was used is described in the text and the respective figures.

The NPC in both mammalian and yeast cells provides a valuable reference to investigate the influence of different buffer systems on the photophysics of the respective fluorophores. Here, we exploited the NPC system to establish imaging conditions to perform dual-color localization microscopy in yeast for long time periods, allowing us to perform high-throughput studies.

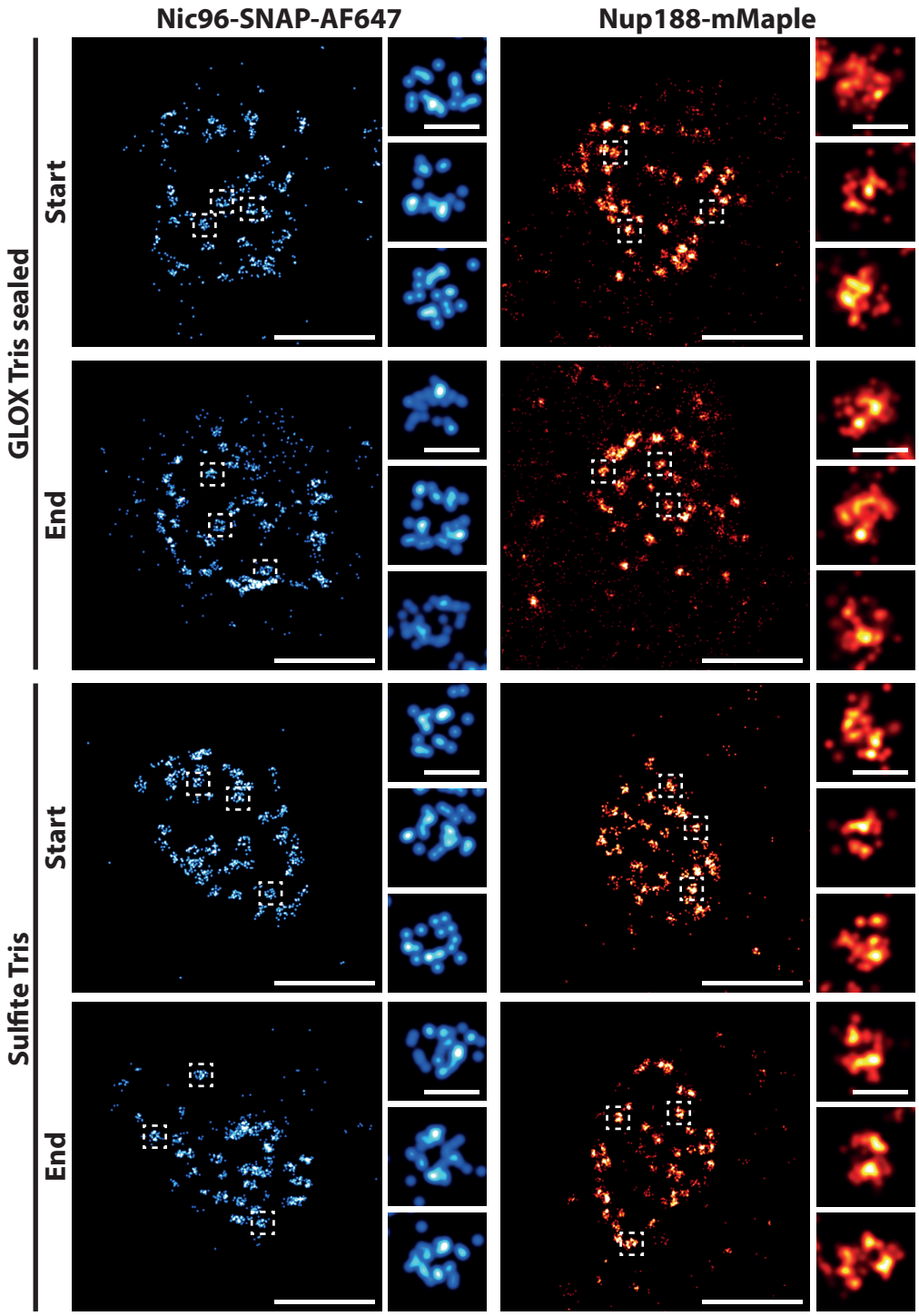

Figure 3.14 | Visual comparison of GLOX and sulfite-based imaging buffers in yeast. Localization microscopy was performed on yeast samples where either of the nuclear pore complex components Nic96-SNAP-AF647 (left, blue) or Nup188-mMaple (right, red) was imaged in a dual-color setting. The imaging was performed in GLOX buffer in a sealed sample holder (top) or in the sulfite-based buffer (bottom). Representative images of nuclei and individual nuclear pores are shown at the start and end of a long-term imaging experiment. Scale bars are 1 µm (overview images) and 1 µm (individual NPCs).

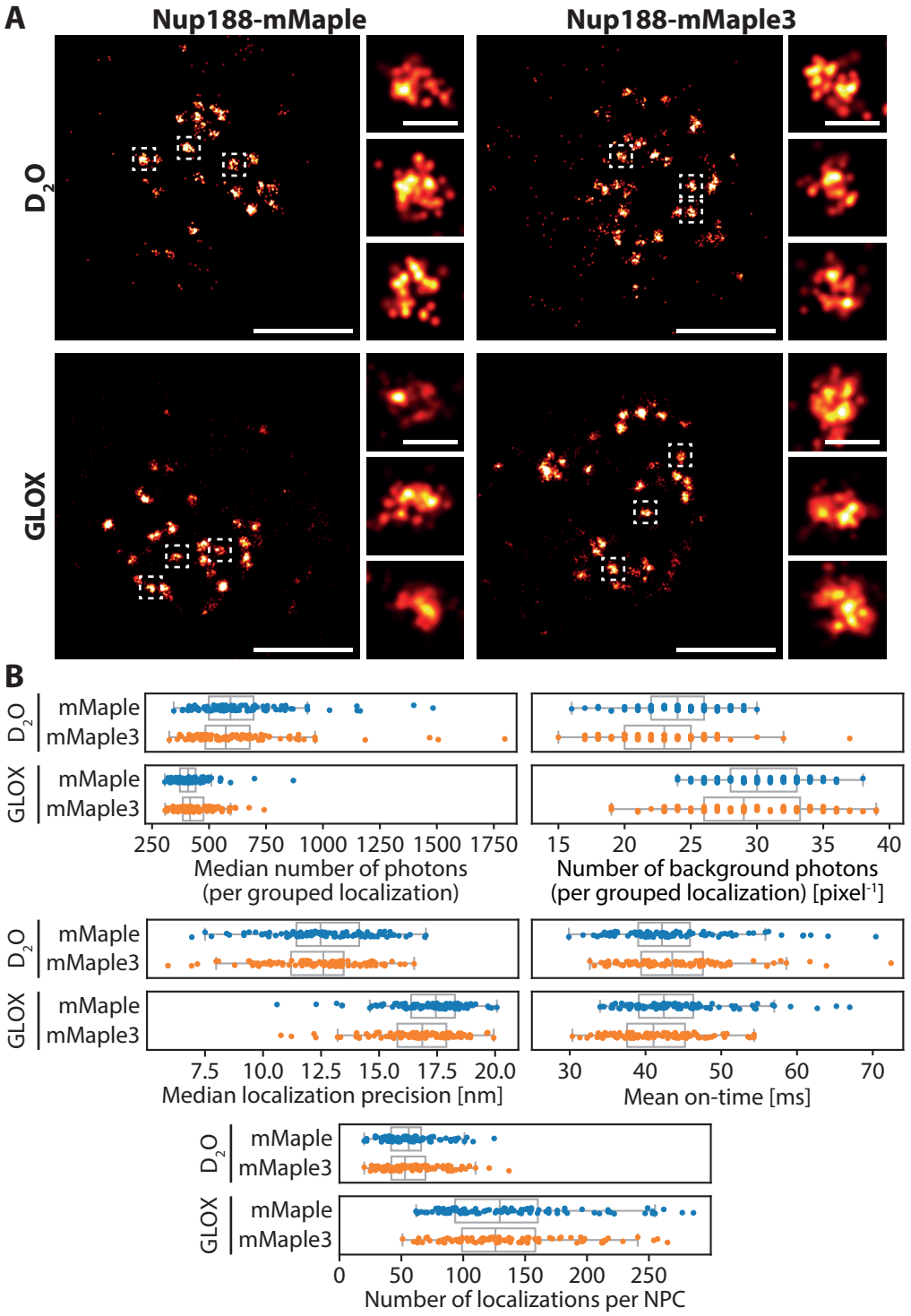

Figure 3.15 | Visual and quantitative comparison of mMaple and mMaple3 The nuclear pore complex (NPC) component Nup188 was tagged with mMaple or mMaple3 in different strains. The strains were imaged side by side under identical conditions and analyzed quantitatively. (**A**) Exemplary images of nuclei and NPCs for the indicated mMaple variant under standard single- (D_2O) or dual-color (GLOX) conditions. (**B**) Per condition, 100 NPCs were segmented and quantitatively analyzed. Scale bars are 1 µm (overview images) and 100 nm (individual NPCs).

3.4 Temporal sorting of dual-color endocytic snapshots by model fitting

Having established a protocol for high-throughput imaging, we continued with automating the post-processing and improving the temporal sorting of super-resolution snapshots.

The data presented in the first three parts of this section were acquired by me and Yu-Le Wu, the concept was developed by Yu-Le Wu and me with input from Jonas Ries and Markus Mund and it was computationally implemented by Yu-Le Wu.

3.4.1 Segmentation pipeline and model fitting

During an automated overnight imaging session, we acquire blinking movies of dozens of ROIs that are automatically fitted to get super-resolved images. The first improvement in the post-processing of the super-resolution data was the automation of segmentation. Initially, the automated pipeline segmented all cells and discarded those that were at the rim of the field of view (red dashed boxes) and those cells where the SNAP-tag had not been stained (blue dashed box) due to the absence of cell permeabilization (Fig. 3.16A, left). Then, the endocytic sites were picked and rotated so that the direction of membrane invagination was pointing upwards (Fig. 3.16A, middle & right). Endocytic sites that were too close to each other were discarded (Fig. 3.16A, middle, red dashed boxes) because the neighboring signal might have interfered with subsequent analysis. The rotation was obtained by fitting the outline of the cell and then calculating the normal to it at the position of the endocytic site.

To retrieve quantitative information from each individual endocytic site, we fitted it with a model that is based on previous knowledge. Previous super-resolution studies reported that Las17 forms a ring at the base of the plasma membrane (Mund *et al.*, 2018). In the same study and in another one using correlative light-electron microscopy (Kukulski *et al.*, 2012) it was shown that the actin network is distributed hemi-elliptic around the growing invagination (Fig. 3.16B). Hence, our model consisted of a ring at the bottom representing Las17 and a hemi-ellipsoid representing Abp1 (Fig. 3.16C). As the data were two-dimensional, the model was projected into two dimensions resulting in a density function. During the fitting process, the position of the ring, the axial length of the hemi-ellipsoid, the rotational angle of the model, and the relative intensity of the two parts were free parameters (blue text in Fig. 3.16C). Figure 3.16D shows examples of the fitting process. The model (bottom row) was fitted to the localization data of endocytic sites (top row). The dataset used is the same as in figure 3.3. Here, the data were not sorted by the centroid distance between the Las17 and the Abp1 signal, but by the axial length of the hemi-ellipsoid.

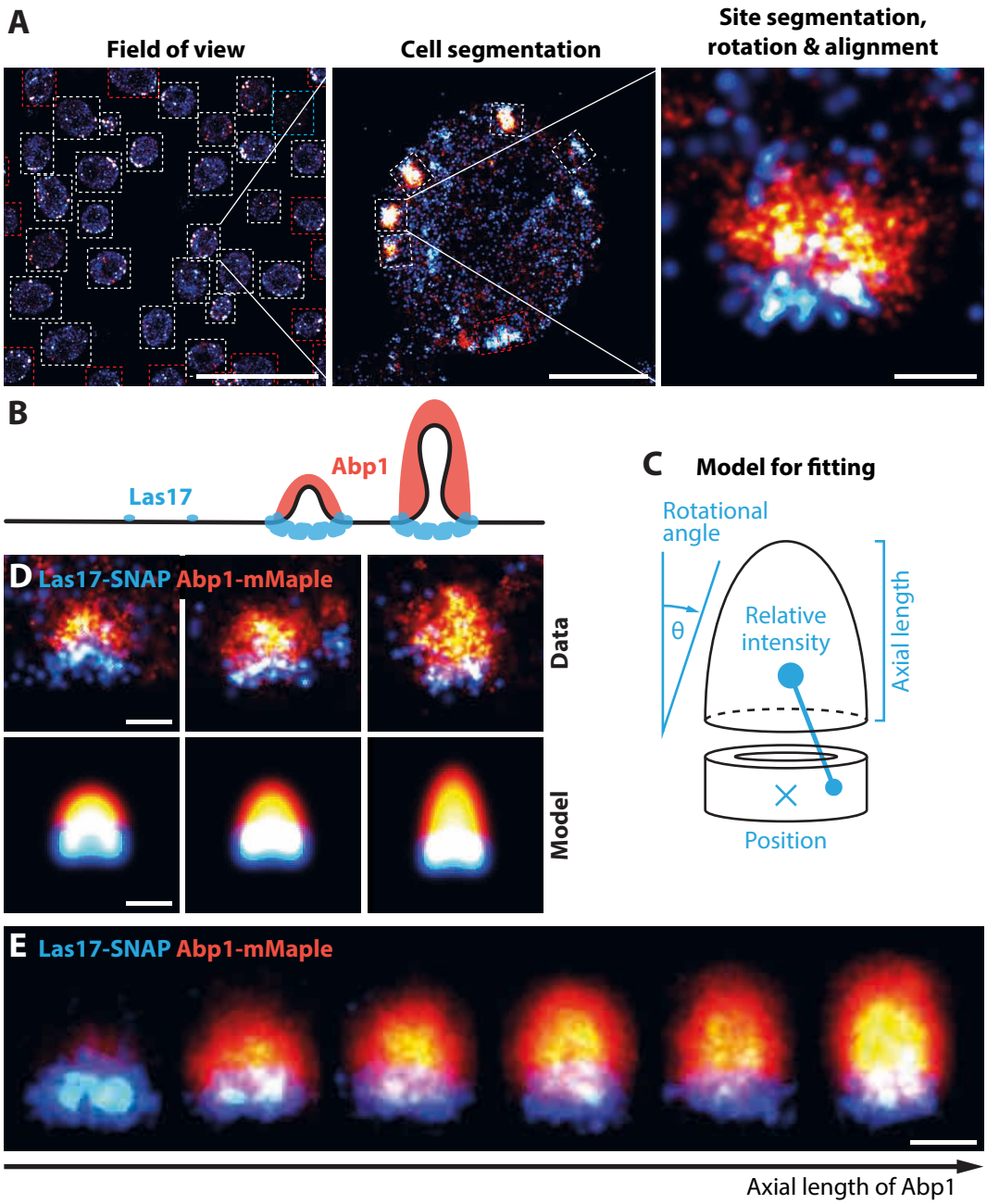

Figure 3.16 | Pipeline for automatic segmentation and model fitting of endocytic sites. (**A**) In the segmentation pipeline cells and endocytic sites were segmented (white dashed boxes). Cells that are at the rim of the field of view (left, red dashed boxes) or that have not been stained by BG-AF647 (left, blue dashed box) and sites that are too close together (middle, red dashed boxes) were excluded from further analysis. The endocytic sites were rotated so that the direction of invagination is pointing upwards. (**B**) Illustration of Las17 and Abp1 structures along the endocytic timeline. (**C**) Depiction of the model used for fitting. Blue parameters are free parameters during the fitting process. (**D**) Exemplary endocytic sites (top) and the respective result of the fitted model (bottom). (**E**) Reconstruction of the same dataset as in figure 3.3 but this time using the model fitting concept instead of a centroid-based approach. The sites were fitted with the model from C, sorted by increasing axial length of the part of the model representing Abp1, and averaged with a running window (bin width: 24 sites; $n = 131$ sites in total). Scale bars are 10 µm (A, left), 1 µm (A, middle), and 100 nm (A, right, D, and E). The data presented in this figure were produced jointly with Yu-Le Wu.

The sorted data were again averaged by a running window (bin width: 24 sites; $n = 131$ sites in total) and equally spaced averages are shown in figure 3.16E.

3.4.2 Concept of a reference structure for temporal sorting

After having established the model fitting as a method to extract quantitative geometric features, we wanted to develop a more general approach that we can use to generate a temporal reconstruction of more than two proteins. For this, we chose to use a combination of proteins where one stays at the base of the plasma membrane during the course of endocytosis, whereas the second one is a coat protein that moves inwards with the growing invagination (Fig. 3.17A). With this combination, we can time individual sites in the late stages of endocytosis once membrane invagination has begun. Ideally, we would then like to image a third protein whose structural rearrangements can be visualized over time. However, triple-color localization microscopy has not been achieved in budding yeast to the best of our knowledge, mainly because of the lack of compatible labeling strategies and fluorophores. Therefore, we decided to image the two proteins in the same color (Fig. 3.17B) and the *query protein* in the second color (Fig. 3.17C to E). From here on, I will refer to the combination of the base and the coat protein in one color as the *reference structure*. The reference structure is used to align the individual endocytic sites spatially and temporally, whereas the query protein is treated totally independent of this. From the combination of several dual-color datasets of the reference structure with different query proteins in the second color (Fig. 3.17C to E), a final reconstruction of the structural rearrangements can be computed (Fig. 3.17F).

3.4.3 Establishing a reference structure in single-color

As a first proof of concept, we wanted to show that the model fitting actually works on single-color data. To do so, we imaged a yeast strain with Las17-mMaple (base protein) and Sla2-SNAP (coat protein) in dual-color. We then used the localization data as input for the model fitting, but we merged the two colors to a single channel (Fig. 3.18A). The model we fitted consisted of a ring representing Las17 and a hemisphere representing the coat protein Sla2 (Fig. 3.18B). The bottom position, the distance and relative intensity between the two parts of the model, and the rotational angle of the whole model were free parameters during the fit. Figure 3.18C shows the model that was fitted to two exemplary endocytic sites. For better comparison with the fitted model, the site is shown in two different lookup tables (red hot and green). We then sorted the endocytic sites by increasing distance between the two parts of the model and generated the reconstruction of the late phase of endocytosis by applying a moving average (Fig. 3.18D; only the part depicting the mobile phase of endocytosis is depicted). The reconstruction showed that using the model fitting and subsequent sorting, we can recapitulate the inward movement of the coat protein Sla2. This became even more apparent when reintroducing the two colors (Fig. 3.18E).

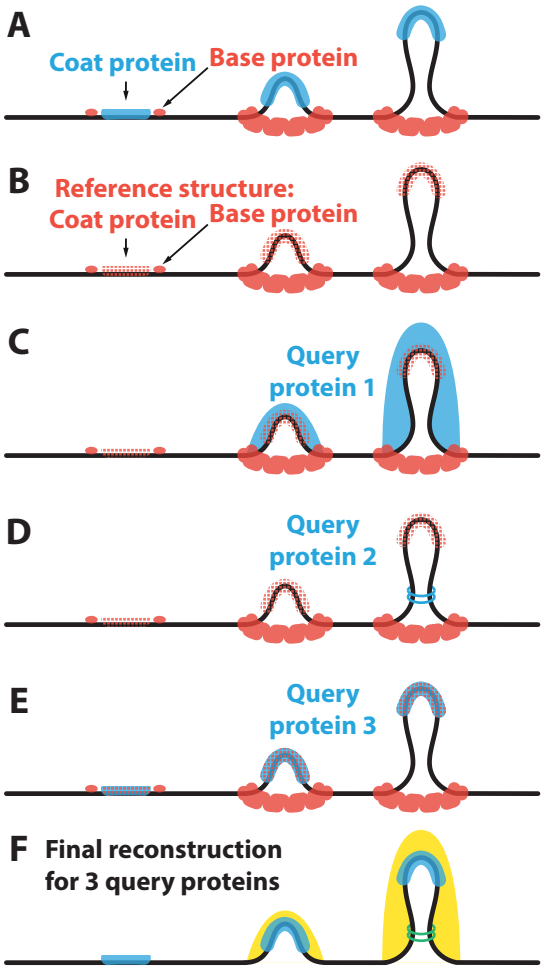

Figure 3.17 | Concept for a single-color reference structure to reconstruct the positioning of different endocytic proteins. (**A**) Imaging of a protein that stays at the base of the plasma membrane during the course of invagination (*base protein*, red) in combination with a *coat protein* (blue) that moves inwards with the growing invagination allows temporal sorting of individual endocytic sites arrested at random time points. (**B**) As triple-color localization microscopy was not possible, the *reference structure* consisting of the base and the coat protein was imaged in one color. (**C** to **E**) Imaging the reference structure used for temporal and spatial alignment in a single color allows imaging of different query proteins independently in the second channel. (**F**) Since the different query proteins are mapped to the same reference structure, they can be merged into one reconstruction that shows their temporal rearrangements over time.

The two colors are clearly separated into two distinct structures with very little cross-talk. Based on this positive evaluation, we continued by generating different strains with the reference structure in single-color and several query proteins in the second color.

3.4.4 Tagging artifacts in yeast strains with multiple tags

The yeast strains we generated had Las17 and Sla2 tagged with mMaple and different query proteins tagged with SNAP. The strains were additionally expressing ABP1 tagged with GFP as a diffraction limited marker from which we could potentially extract additional temporal information. Thus, in total, four different proteins of the endocytic machinery were tagged. When subjecting these strains to super-resolution microscopy, we observed a relatively high fraction of yeast cells with an unusual cell shape. An example for the query protein Sla1 (late coat) is shown in figure 3.19A. Additionally, some endocytic sites in this strain showed an unexpected distribution of the query protein (Fig. 3.19B) as the coat protein Sla1 was colocalizing with both the base and the coat part of the reference structure.

As we reasoned these observations might be caused by tagging four different endocytic proteins, we generated the same strain with only the two proteins of the reference structure and the query protein tagged, leaving out the diffraction limited marker. However, we still detected similar trends as before (Fig. 3.19C, D). We then also tried replacing the base protein Las17 by Myo5 to generate a different reference structure but again experienced aberrant cell shapes, and the endocytic sites showed occasionally unexpected structures (Fig. 3.19E, F). We observed similar trends for Sac6 as the query protein (Fig. 3.19G, H), but also for Las17 and End3 (data not shown).

We decided to try three different approaches to overcome these problems:

- Using smaller peptide tags.
- Combinatorially testing different base and coat proteins for the reference structure.
- Increasing the linker length between the target protein and the respective tag.

3.4.4.1 Peptide tags to overcome tagging artifacts

The experimental part of this section was performed by Eric Maurer, an intern in our lab, who I supervised.

Including the linker, the SNAP-tag, mMaple/mMaple3 and GFP have sizes of 20.8 kDa, 28.6 kDa, and 28.2 kDa, respectively. Calculating the minimum radius of the tags as a perfect sphere (Erickson, 2009), the values are in the range of $R_{min} = 1.8$ to 2 nm. Adding a tag of this size to four of the 50 to 60 proteins of the dense network

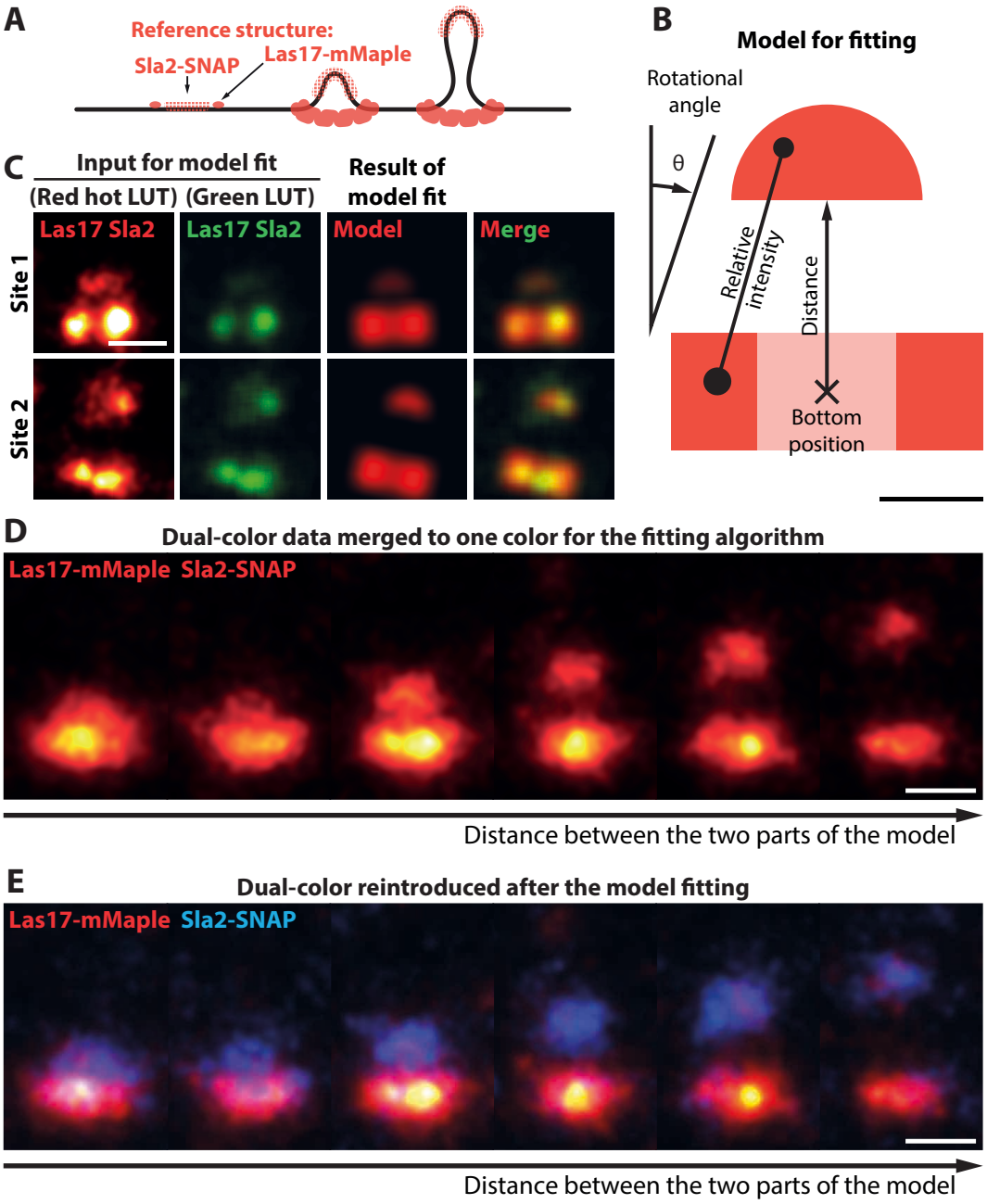

Figure 3.18 | Establishing and evaluating a reference structure in single-color. (**A**) Illustration of the reference structure with Las17 as base protein and Sla2 as coat protein. (**B**) Schematic representation of the model that is fitted to the data. The bottom position, distance between the two parts of the model, and their relative intensity as well as the rotational angle of the whole model are parameters of the fit. (**C**) Two exemplary sites and the results of the model fit are shown. The sites are visualized in the red hot (first column) and green (second column) lookup tables. The result of the model fit is visualized in red and merged with the input data for comparison. (**D**) Endocytic sites imaged in dual-color were treated as single-color data by the algorithm and fitted with the model as in B. The sites were sorted by increasing distance between the two parts of the model and a moving average was applied (bin width: 10 sites, $n \approx 1000$ in total); only the part depicting the mobile phase of endocytosis is displayed here. (**E**) Same data as in D, but with the original colors reintroduced. Scale bars are 100 nm (C, D, and E) and 20 nm (B). The data presented in this figure were produced jointly with Yu-Le Wu.

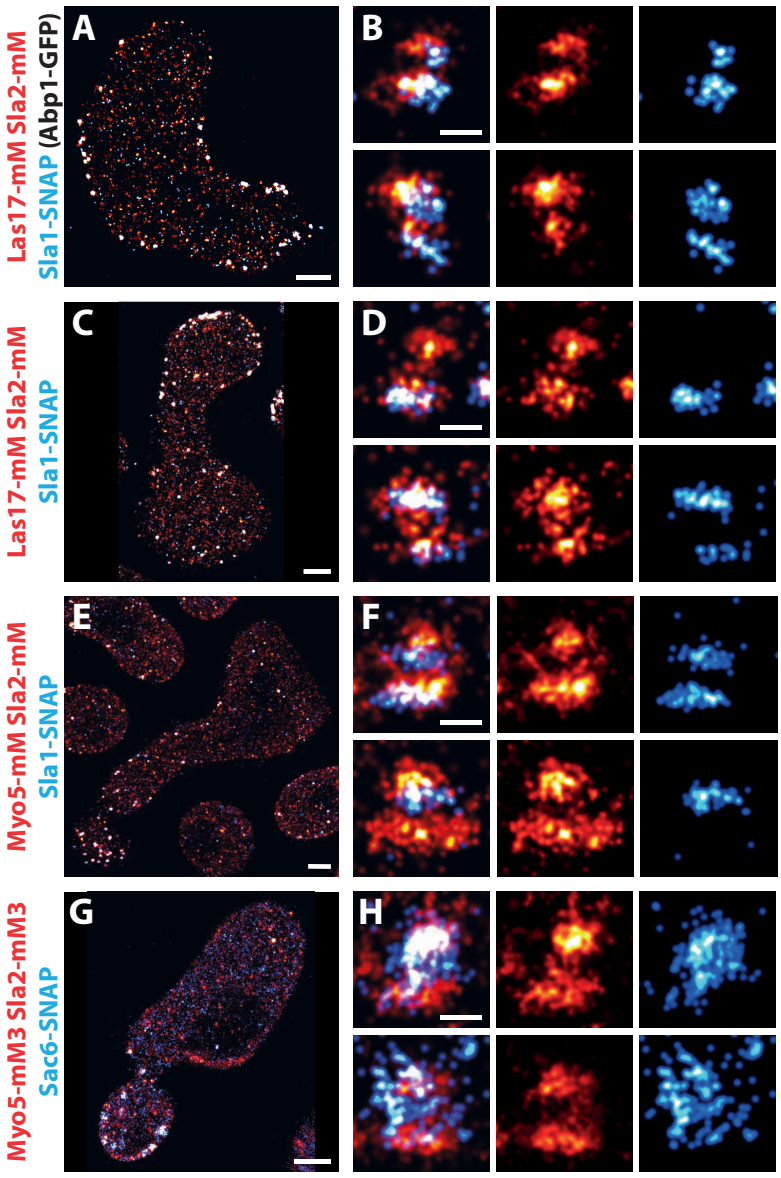

Figure 3.19 | Aberrant cell shapes in yeast strains with multiple tags. (**A**) Exemplary cell with aberrant shape for the strain Las17-mMaple Sla2-mMaple Sla1-SNAP Abp1-GFP and (**B**) endocytic sites from the same strain. (**C**), (**D**) Same as in A and B but for the strain Las17-mMaple Sla2-mMaple Sla1-SNAP. (**E**), (**F**) Same as in A and B but for the strain Myo5-mMaple Sla2-mMaple Sla1-SNAP. (**G**), (**H**) Same as in A and B but for the strain Myo5-mMaple Sla2-mMaple Sac6-SNAP. Scale bars are 1 µm (A, C, and E) and 100 nm (B, D, and F). mM, mMaple; mM3, mMaple3. The data presented in this figure were produced jointly with Yu-Le Wu.

of protein-protein interactions at the endocytic site could lead to disruptions and mechanistic alterations causing the appearance of the observed phenotype. Therefore, we decided to try out various smaller tags that are compatible with localization microscopy. In recent years, three different approaches have been published that are based on peptide tags in the size range of 12 to 15 amino acids (Pessino *et al.*, 2017; Virant *et al.*, 2018; Götzke *et al.*, 2019).

For the SpyTag/SpyCatcher system (Pessino *et al.*, 2017), I cloned a plasmid for the expression of SpyCatcher in *E. coli*. The protein was then produced and purified by Nikolay Dobrev from EMBL's Protein Expression and Purification Core Facility and we subsequently labeled it with AF647. The bivalent nanobody to stain the BC2-tag was kindly provided by Ulrich Rothbauer (Virant *et al.*, 2018) and the anti-ALFA nanobody coupled to AF647 was purchased from NanoTag (Götzke *et al.*, 2019).

After initial unsuccessful experiments in yeast, we decided to systematically test the three peptide tags on NPCs in mammalian cells. We took a plasmid in which the NPC component Nup107 was tagged N-terminally with GFP (Szymborska *et al.*, 2013) and additionally introduced the ALFA-tag, the BC2-tag, or the SpyTag at the N-terminus. Then, we transfected the plasmids into wild-type U2OS cells, stained the samples with the respective nanobody or SpyCatcher, and performed localization microscopy (Fig. 3.20). Additionally, we included a positive control where we stained GFP with an anti-GFP nanobody (Fig. 3.20A to C). In the positive control, the super-resolution staining matched the GFP expression and in the zoom-in individual NPCs were clearly discernible. The GFP staining of the nuclear envelope in the samples with the different peptide tags was comparable to the GFP-only control (3.20A, D, G, J). However, both for the SpyTag/SpyCatcher system (3.20E, F) and the ALFA-tag (3.20K, L) no specific staining was detectable. For the bivalent BC2-nanobody, a very weak nuclear staining was observed, but it was too sparse to visualize individual nuclear pores (3.20H, I). Based on these results, we did not pursue this avenue any further.

3.4.4.2 Different sets of proteins for the reference structure by synthetic genetic arraying

We reasoned that by chance we had chosen two pairs of proteins for the reference structure (Las17/Sla2 and Myo5/Sla2) whose C-termini provide crucial interactions for functional endocytosis that we have disturbed by tagging. Based on this argument, we decided to try a combinatorial approach where we generated reference structures from different base and coat proteins. In a second step, we could then characterize the cell shapes to determine a suitable reference structure. Based on previous super-resolution data from our lab and literature research, I decided on seven base proteins (Las17, Bbc1, Myo5, Vrp1, Lsb3, Bzz1, and Myo3) and six coat proteins (Sla1, Sla2, End3, Pan1, Ent1, and Yap1801).

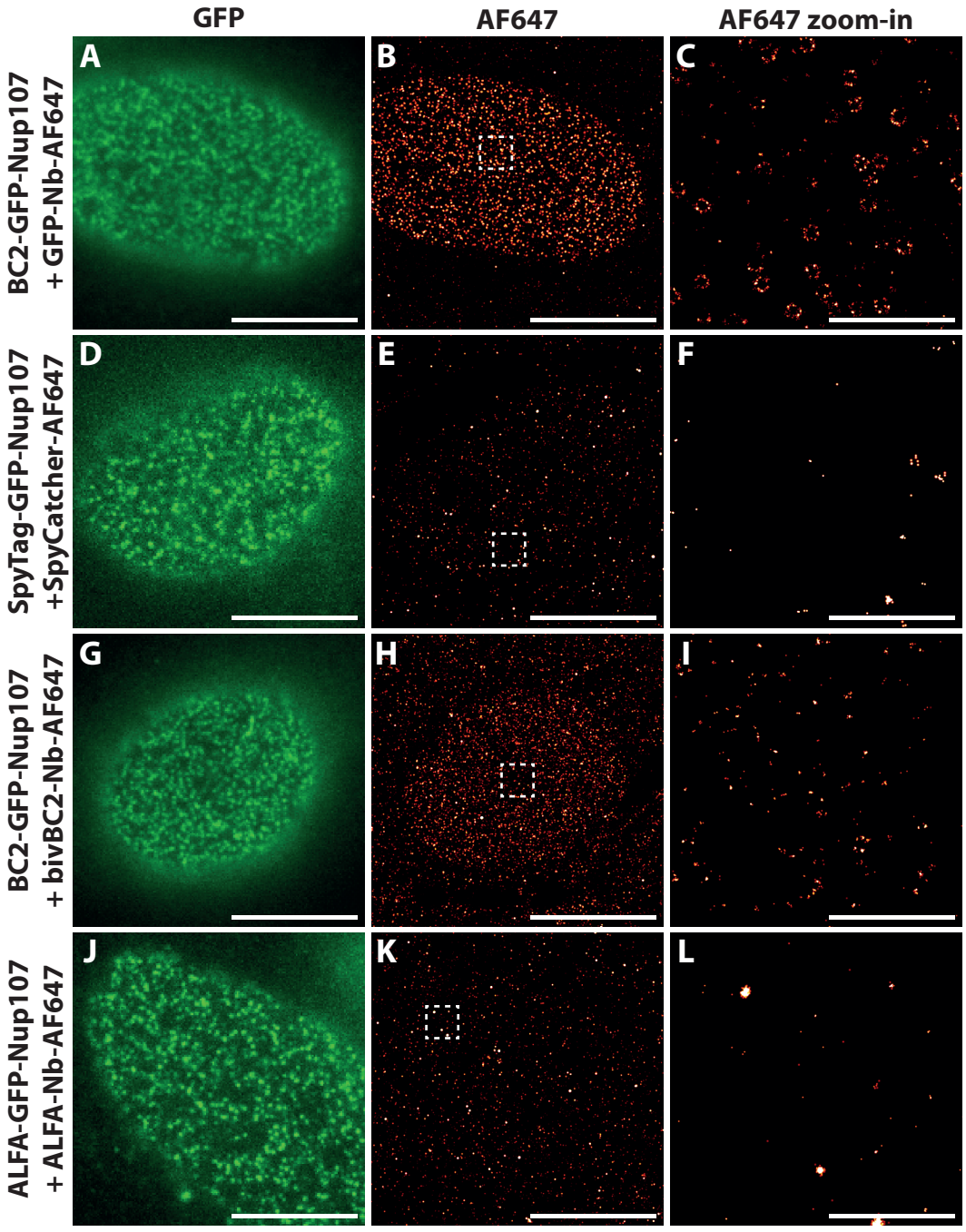

Figure 3.20 | Testing different peptide tags for localization microscopy. U2OS cells were transfected with plasmids encoding the nuclear pore complex (NPC) Nup107 tagged with GFP and three different peptide tags on its N-terminus. (**A**) Cells with BC2-GFP-Nup107 were imaged in the GFP channel, (**B**) the NPCs were stained by a nanobody against GFP, and imaged using localization microscopy. (**C**) Zoom-in of B showing individual NPCs. (**D** to **F**) As A to C but for the SpyTag/SpyCatcher system. (**G** to **I**) As A to C but for the BC2-tag stained with the biv-BC2 nanobody. (**J** to **L**) As A to C but for the ALFA-tag stained with the anti-ALFA nanobody. Scale bars are 10 µm (A, B, D, E, G, H, J, K) and 1 µm (C, F, I, L). Nb, nanobody; biv, bivalent. The experiments presented in this figure were performed by Eric Maurer under my supervision.

Manual SGA For the generation of yeast strains with these combinatorial reference structures, I consulted Michael Knop and Matthias Meurer from Heidelberg University and they suggested the following concept that I then put into practice.

The concept is based on a synthetic genetic array (SGA; Tong *et al.*, 2001) to systematically generate all $7 \times 6 = 42$ strains. In this approach, yeast strains are mated and their genetic background allows subsequent selection of the desired haploid strains without the necessity to manually pick and separate tetrads. Usually, SGA is performed on large yeast libraries composed of 1000s of strains with the help of a robot. As the number of strains in my case was more manageable, we decided to perform the SGA creation manually on large agar plates (Fig. 3.21). First, I generated yeast strains with each of the coat proteins tagged with mMaple3, respectively, in the BY4741 wild-type background. Similarly, the base proteins were tagged with mMaple3 in the query strain background Y8205. Additionally, I generated the strains with tagged coat proteins in the background of the query proteins Las17-SNAP, Sac6-SNAP, and End3-SNAP, respectively. I chose these proteins as their tagging along with the reference structure had caused aberrant cell shapes previously, similar to Sla1. After confirming all strains by colony PCR and imaging, I streaked them in stripes on large agar plates (Fig. 3.21A). Next, I replicated the base and coat strains on the same plate with 90° rotation for mating (Fig. 3.21B). I selected successfully mated diploid yeast cells in two consecutive steps with two (or three in the case of the SNAP-tagged strains) antibiotics present (Fig. 3.21C) and subsequently replicated them on sporulation plates (Fig. 3.21D). Finally, I selected haploid cells with both mating types, isolated single colonies, tested a small subset of them by PCR for correct tags and mating type, and stored all strains as glycerol stocks. In total, I generated 310 strains:

$$(n_{\text{base}} \times n_{\text{coat}} \times n_{\text{backgrounds}} - n_{\text{End3}} - n_{\text{Las17}}) \times n_{\text{mating types}} = (7 \times 6 \times 4 - 7 - 6) \times 2 = 310$$

In this equation, n_{base} is the number of base strains, n_{coat} the number of coat strains, and $n_{\text{backgrounds}}$ the number of backgrounds (BY4741, Las17-SNAP, Sac6-SNAP, and End3-SNAP). From the combination of these strains, the strains where End3-SNAP and End3-mMaple would be tagged in the same strain (n_{End3}) and the same for Las17 (n_{Las17}) have to be subtracted. $n_{\text{mating types}}$ is the number of mating types.

Increased linker length between target protein and tag Additionally to the SGA strains, I generated strains where the reference structure Myo5/Sla2 and the query proteins End3, Las17, Sac6, and Rvs167 were tagged with mMaple3 and SNAP, respectively, but with a longer linker consisting of 17 instead of 10 amino acids (Haruki *et al.*, 2008).

Confocal imaging of SGA strains The imaging of the different yeast strains was performed on a spinning-disc confocal microscope in EMBL's Advanced Light

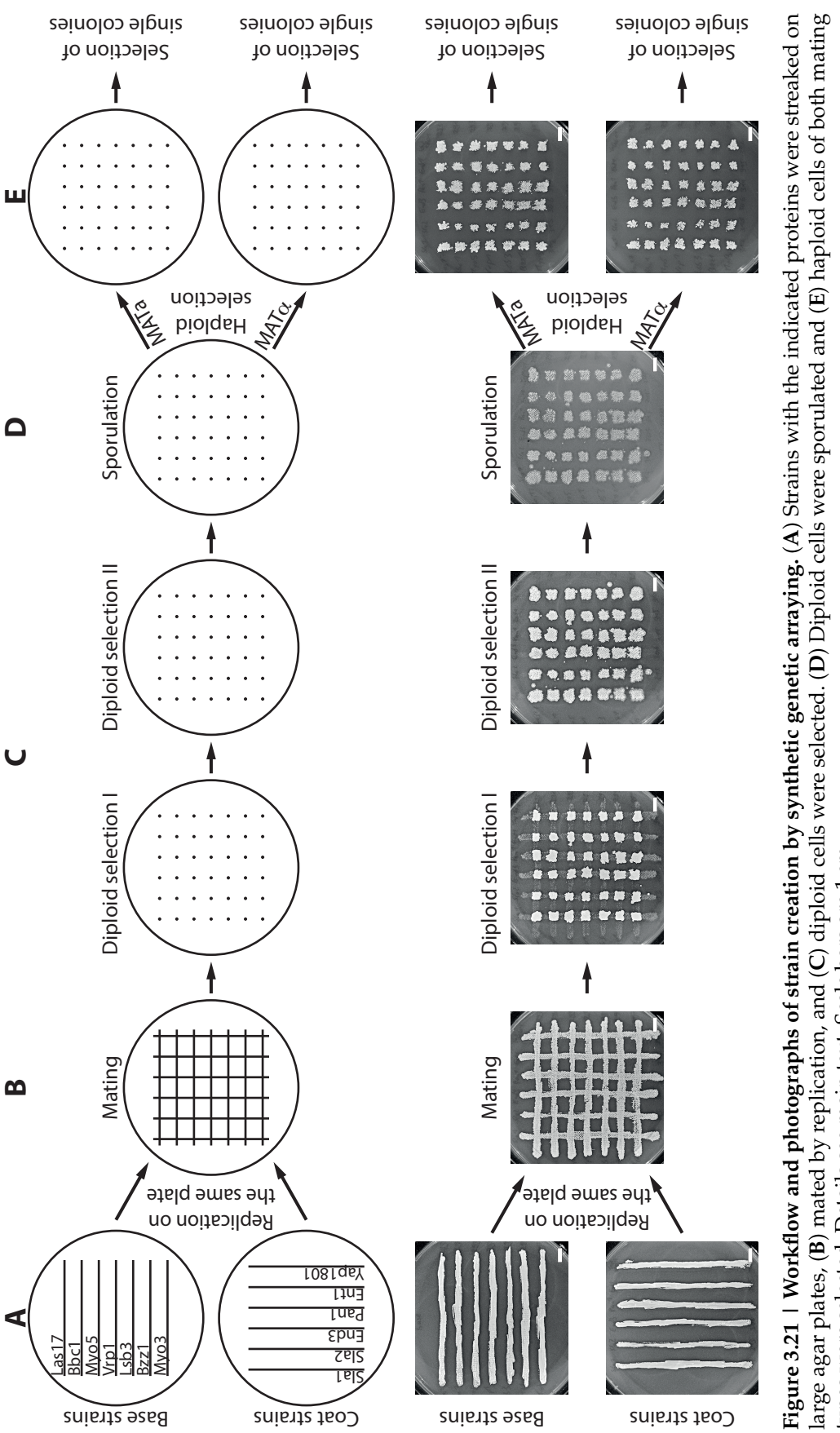

Figure 3.21 | Workflow and photographs of strain creation by synthetic genetic arraying. (**A**) Strains with the indicated proteins were streaked on large agar plates, (**B**) mated by replication, and (**C**) diploid cells were selected. (**D**) Diploid cells were sporulated and (**E**) haploid cells of both mating types were selected. Details see main text. Scale bars are 1 cm.

Microscopy Facility with help from Marko Lampe. To quantify the cell shape of many different yeast strains, we decided to stain the cell wall with concanavalin A (ConA) coupled to Alexa Flour™ (AF488; Fig. 3.22A, C) and visualize the imaging buffer around the cells with dextran coupled to AF647 (Fig. 3.22B, C). Additionally, we acquired a wide-field image of the field of view.

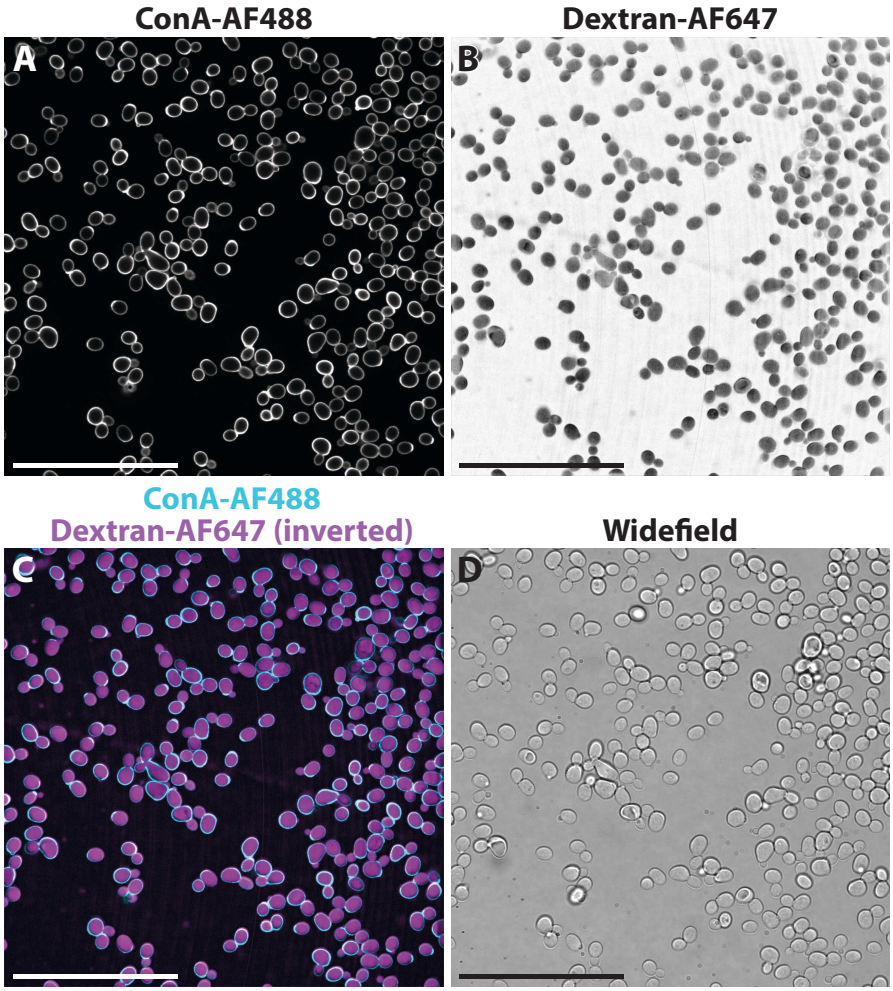

Figure 3.22 | Confocal imaging of one exemplary yeast strain. (**A**) Wild-type yeast cells stained with concanavalin A coupled to Alexa Flour™ 488 (AF488) and imaged with a confocal microscope. (**B**) Dextran-Alexa Flour™ 647 (AF647) channel of the same field of view. (**C**) Merged image of the ConA and the inverted dextran-AF647 channel. (**D**) Widefield imaging with transmitted light. Scale bars are 50 µm.

Automatic segmentation As an initial test, I imaged four wild-type controls and 14 strains with three endocytic proteins tagged in three technical replicates. The tagged strains were:

- Myo5/Sla2 as reference structure in the MK100 background with End3, Las17, Sac6, and Rvs167 as query proteins (4 strains).
- Myo5/Sla2 as reference structure with longer linkers in the BY4741 background with End3, Las17, Sac6, and Rvs167 as query proteins with longer linkers (4 strains).

- Myo5/Sla2 as reference structure with End3, Las17, and Sac6 as query proteins in both mating types from the manual SGA (6 strains).

I then developed a pipeline in Python to automatically segment the shape of individual cells and quantified their geometry starting from the raw data (Fig. 3.23). First, I applied a Gaussian blur to the inverted dextran channel to eliminate noise (Fig. 3.23A) and binarized the image by local thresholding (Fig. 3.23B). Using a distance transform and local peak finding (Fig. 3.23C), I generated seeds for a watershed-based segmentation of the ConA channel (Fig. 3.23D, E). I then compared different geometric features like area, axis lengths, and solidity of the cells but could not find a measure that distinguished the cells where we previously had seen the phenotype of aberrant cell shapes. Figure 3.23F shows an exemplary plot for the roundness of yeast cells across all 18 strains.

Manual classification As it was not possible to detect differences between the strains by automatic segmentation, I was wondering if it was possible to distinguish them by manual classification. For classification, I implemented a script that automatically loads the confocal data in the graphical user interface napari (Sofroniew *et al.*, 2020). This Python image viewer makes it easy to look at the different channels and annotate them in a way that is easily accessible for downstream processing. I loaded the datasets in a random order without me knowing which yeast strain I was looking at to annotate them as unbiased as possible. The classes I chose were: normal cells, aberrantly shaped cells, cells that were intermediate between these two classes, buds, unusually large cells, and unclassified cells that were touching the rim in any dimension. Figure 3.24A shows an example of a classified field of view. In total, more than 20 000 cells were annotated. I then plotted the distribution of cell annotations for the 18 strains (Fig. 3.24). When comparing them, it became apparent that there were barely any differences and aberrant cell shapes were detected in similar ratios for wild-type and triple-tagged strains.

Growth tests Another way to test for strain fitness is to compare their growth. For this, I performed growth tests both on solid and in liquid medium (Fig. 3.25). Serial dilution spot tests of the different strains showed differences between the wild-type backgrounds (Fig. 3.25A to D). In MK100 cells, the tagging of the reference structure Myo5/Sla2 led to smaller colony sizes at all temperatures (Fig. 3.25A, rows 1 and 2). Tagging of the query proteins End3 and Las17 had no further effect, whereas tagging of Sac6 decreased the colony size further (Fig. 3.25A, rows 3 to 5). However, in the BY4741 background, all of the double- or triple-tagged strains with a longer linker showed the same fitness as the wild-type strain (Fig. 3.25B). The same observation could be made for double- and triple-tagging with the normal linker in the SGA strains that originated from the BY4741 background (Fig. 3.25C, D).

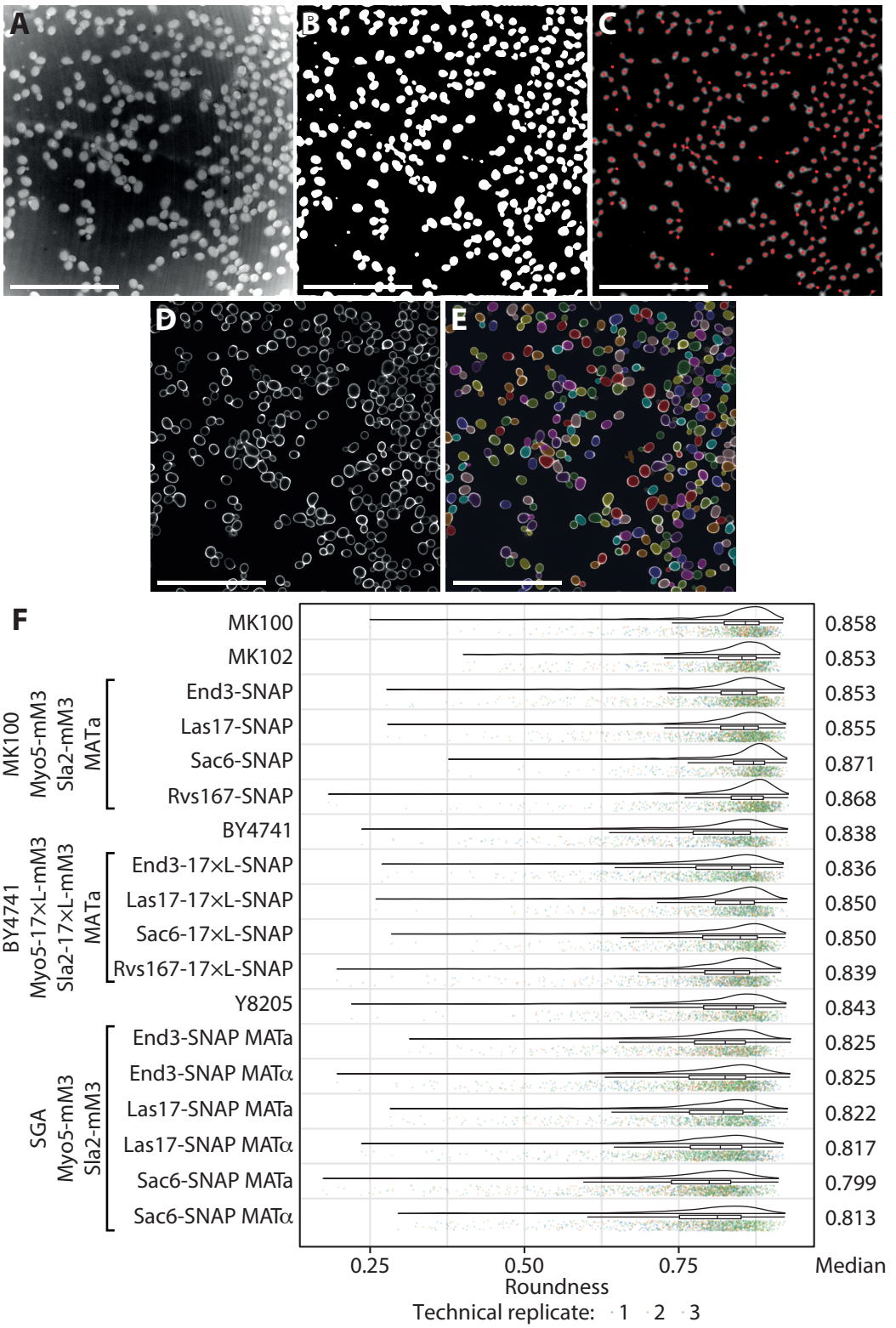

Figure 3.23 | Automatic segmentation pipeline and comparison of roundness across 18 strains. (**A**) Image of the inverted dextran channel blurred with a Gaussian kernel. (**B**) Binarized dextran channel and (**C**) distance transform with locally detected maxima (red), which were used as seeds for a watershed segmentation of the (**D**) ConA channel. (**E**) Overlay of the segmentation and the ConA channel. (**F**) Quantification of the roundness of cells across all imaged strains. Colors represent technical replicates. Scale bars are 50 µm. Number of cells analyzed can be found in appendix A. mM, mMaple; mM3, mMaple3; 17×L, 17×Linker. The values for every technical replicate can be found in appendix A.

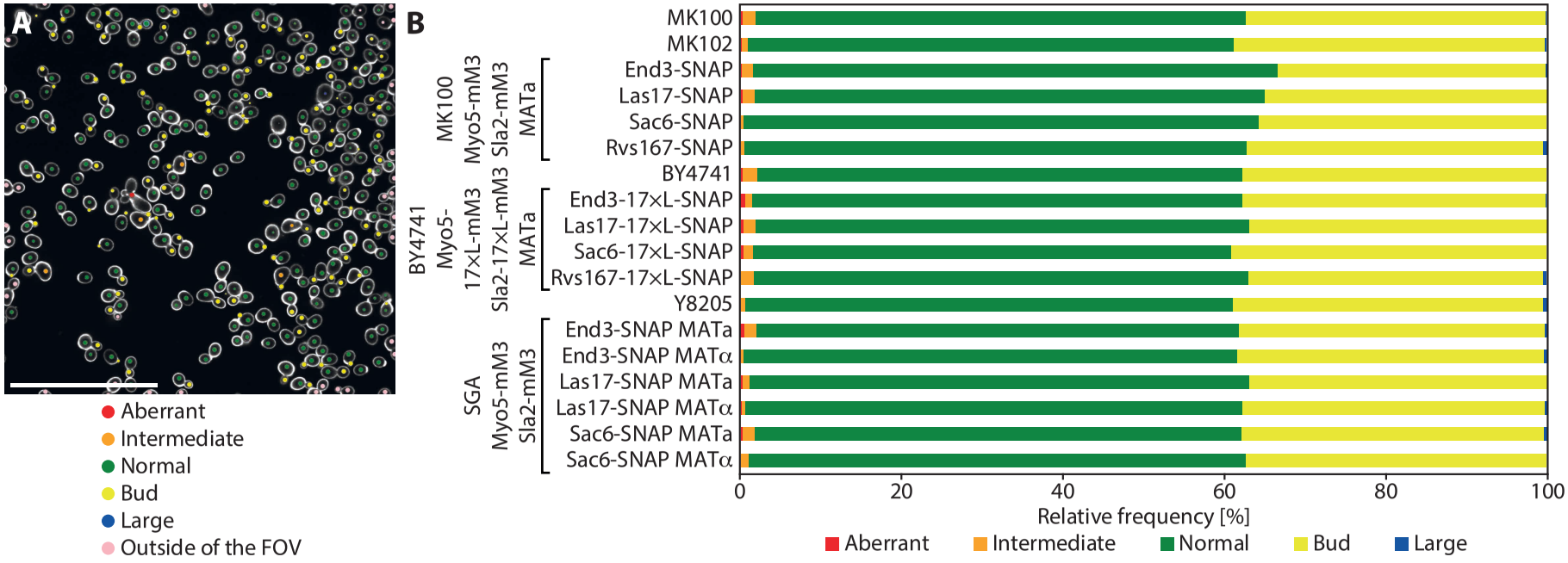

Figure 3.24 | Manual classification of the cell shapes in different yeast strains. All yeast cells have been classified according to their shape without knowing the identity of the strain. (**A**) Example field of view with classification markers. (**B**) Distribution of cell classifications for all quantified yeast strains. Scale bar is 50 µm. Number of cells for each classification can be found in appendix A. mM, mMaple; mM3, mMaple3; 17×L, 17×Linker. The absolute frequency values for every technical replicate can be found in appendix A.

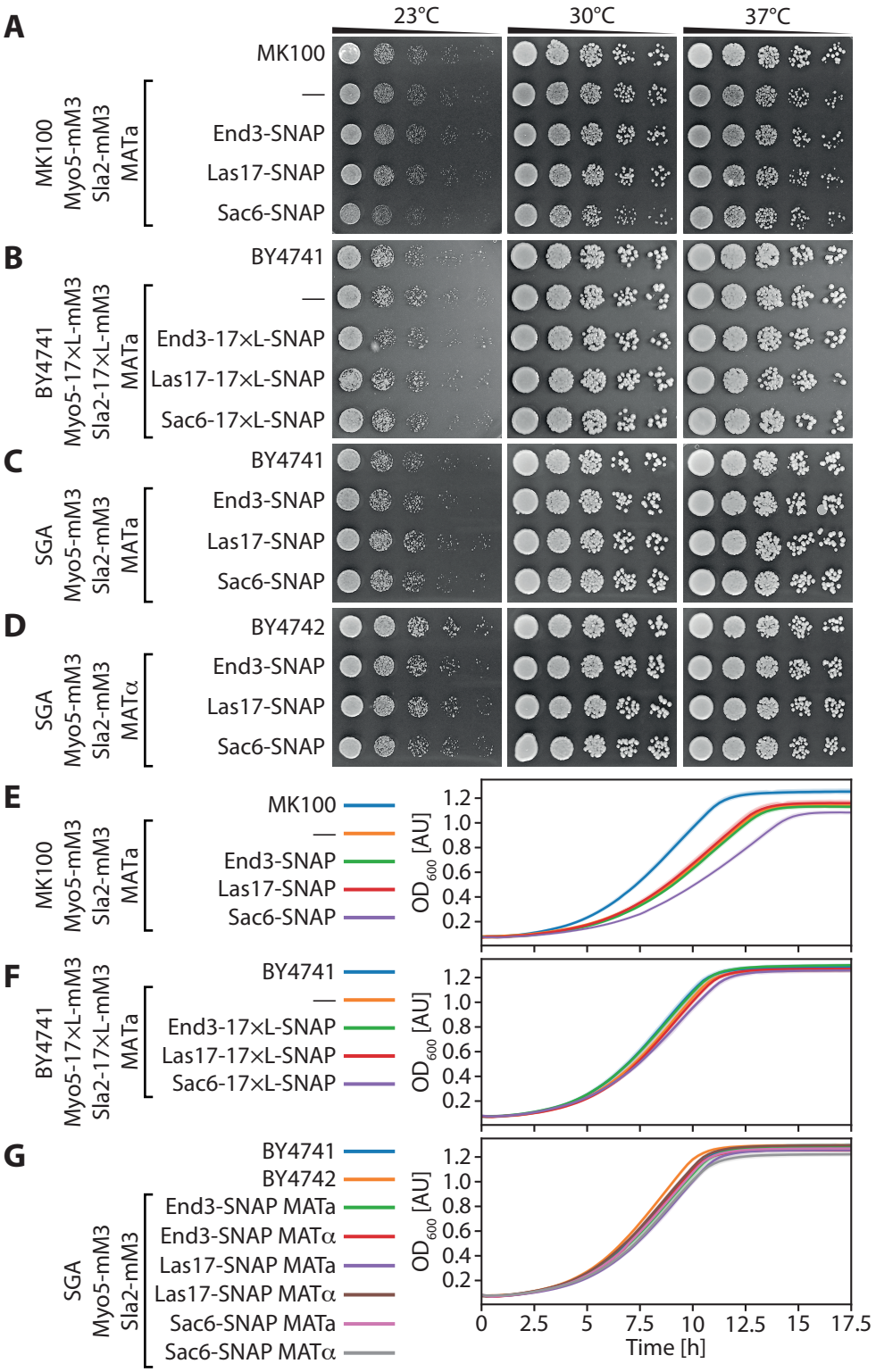

Figure 3.25 | Growth tests of selected double- and triple-tagged yeast strains. (**A** to **D**) The indicated strains were grown in rich medium, their optical density was adjusted, and serial dilutions were spotted on agar plates with rich medium. The plates were incubated at the indicated temperatures and photographed after 2 days of growth. (**E** to **G**) The indicated strains were prepared as in A, but then diluted to an OD_{600} (optical density at 600 nm) of 0.1 and incubated overnight in a microplate reader without shaking at 30 °C. The absorption was measured every 15 min until the stationary phase was reached. Measurements were performed in three technical replicates, the shaded area indicates their standard deviation. mM, mMaple; mM3, mMaple3; 17×L, 17×Linker.

The results from spot tests on solid media could be confirmed by following the growth curves of the same strains in liquid medium. Again, tagging of the reference structure in MK100 led to a delay in growth which did not get enhanced by tagging of End3 or Las17 as query proteins, while the addition of Sac6-SNAP led to even slower growth (Fig. 3.25E). These trends could not be observed in the BY4741 background with longer linkers and with the strains generated by SGA (Fig. 3.25F, G).

Taking into account the classification of cell shapes, all strains would be suitable for analysis of structural rearrangements by our dynamic reconstruction approach. The different growth phenotypes by themselves do not offer an easy decision as additional experiments are needed to investigate the observed discrepancies in more detail.

3.4.5 Dynamic reconstruction of representative proteins

To validate the dynamic reconstruction, we chose to use the original strains generated in the MK100 background. As query proteins, we selected the coat protein End3, Las17 from the WASP/Myo module, the actin cross-linker Sac6, and Rvs167, which is involved in vesicle scission. We performed high-throughput localization experiments with the corresponding four strains. During quality control, we did not observe an unusually high frequency of aberrant cell shapes. For each dataset, I picked 203 sites manually and rotated them. Subsequently, they were fitted with the model described in figure 3.18B. For these first validation experiments, we decided to segment the sites manually to be sure that the quality of the reconstruction is not influenced by the automatic segmentation. The endocytic sites were sorted by increasing distance between Myo5 and Sla2 in the model. However, sites where only one of the reference structures were fitted (model weight $< 5\,\%$), were sorted to the top of the list. The list was split into seven equally sized bins and each bin was averaged. The resulting dynamic reconstructions for the different datasets are shown in figure 3.26A to D. For End3, the signal correlated with both parts of the reference structure, especially in late time points (3.26A). The actin NPF Las17 stayed at the base of the invagination, for the last two time points the signal got more diffuse along the axis of invagination (3.26B). The size of the actin network, decorated by Sac6, increased over time and it encompassed the whole endocytic site (3.26C). Rvs167 was localized between the two parts of the reference structure and was present at the late time points, but also at the first one (3.26D). Moreover, the final time point for each reconstruction was aligned and merged into a four-channel image (Fig. 3.26E), showing the distributions of four proteins representative for the different endocytic modules.

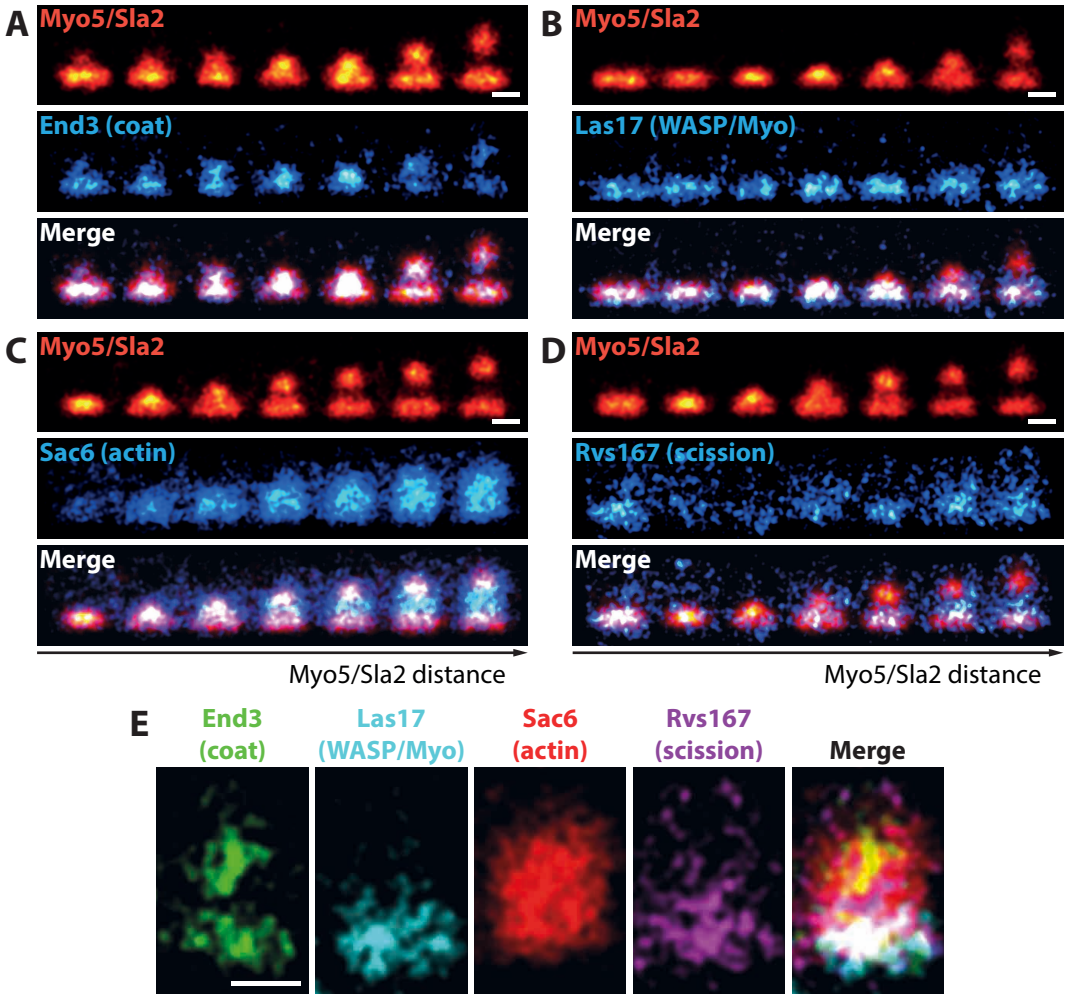

Figure 3.26 | Dynamic reconstructions of four representative proteins. (**A** to **D**) Temporal reconstructions for the proteins End3, Las17, Sac6, and Rvs167. Each of these proteins was imaged alongside the reference structure (Myo5/Sla2) on which the temporal and spatial alignment was performed. The sites were sorted by increasing distance between Myo5 and Sla2; sites where only one of the two models was fitted were sorted to the beginning of the trajectory. (**E**) Query protein distributions for the last bins from A to D in single channels and merged. For each query protein, 203 sites were analyzed; per time point 29 sites were averaged. Scale bars are 100 nm. The data presented in this figure were produced jointly with Yu-Le Wu.

4 Discussion

In this work, we characterized different oxygen scavenging systems for long-term localization microscopy and identified sealing of the sample holder as critical for the durability of the imaging buffer. High-throughput data acquisition of dual-color super-resolution data together with automated post-processing allowed us to establish a new concept to extract dynamic information from static snapshots of individual endocytic sites. Using the extracted dynamic information from the reference structure in one channel, we sorted the snapshots in time and reconstructed the temporal rearrangements of four different query proteins in the second channel (Fig. 3.26).

4.1 Increasing the throughput of dual-color SMLM

The limiting factor of long-term imaging of synthetic dyes is the buffer lifetime. Therefore, we pursued two different strategies to increase the throughput of dual-color localization microscopy:

1. Performing dual-color localization microscopy with two pcFPs that are converted using different strategies.

2. Testing different oxygen scavenging systems that have a longer lifetime.

4.1.1 Primed conversion in budding yeast

Green-to-red pcFPs are converted by UV light (405 nm), some of them can also be primed converted by illumination with green and far-red light (488 nm & 730 nm). Dual-color localization microscopy by combining UV and primed conversion had been shown in different organisms, but not in the budding yeast *S. cerevisiae* (Turkowyd *et al.*, 2017; Virant *et al.*, 2017). Using the pcFPs mMaple3 and mEos3.2A69T, we could show that PC also worked in budding yeast and resulted in high quality images with almost complete conversion (Fig. 3.4). However, these data were acquired in a different lab and in our setup we did not have a 730 nm laser available. As primed conversion was also reported to occur with lower efficiency under green and red illumination (488 nm & 640 nm; Turkowyd *et al.*, 2017), I tested PC under these illumination condition with our microscope (Fig. 3.5). mMaple3 could

be converted by primed conversion with a red laser, but less efficient and incomplete. This is in line with the 34 % reported efficiency of 640 nm PC for mMaple3 relative to 730 nm PC (Turkowyd *et al.*, 2017). Due to these unsuccessful results, I did not perform dual-color experiments involving PC. Taken together, primed conversion with far-red light is a valuable tool to perform dual-color SMLM without having to consider chromatic aberrations, but the quality of data with 640 nm PC was not suitable for our needs.

4.1.2 Testing of oxygen scavenging systems on mammalian NPC samples

The limiting factor in the imaging buffer for dual-color SMLM with mMaple and AF647 is the oxygen scavenging system. The routinely used GLOX/catalase system leads to acidification of the buffer, which is incompatible with imaging (Fig. 3.6). The acidic conditions led to a fluorescence increase in the stained structure that was masking any residual blinking (Fig. 3.6B v-viii). Therefore, no more molecules could be localized in the structure of interest. On the contrary, single molecule blinking could be observed in other cellular structures, presumably cytoskeletal elements. These single molecules could be localized during the fitting procedure resulting in these structures dominating the super-resolved image (Fig. 3.6D). In this particular example, the fluorophores staining the NPCs were most likely already bleached to a large extent when the background increased, explaining the prominence of the undesired structures. This explanation is substantiated by the observation of a bright nuclear staining at later time points (Fig. 3.7, first column).

Characterization of oxygen scavenging systems in single acquisitions I used the well-characterized mammalian NPC samples as reference standard (Li *et al.*, 2018; Thevathasan *et al.*, 2019) to test different alternative oxygen scavenging systems (Fig. 1.9 and section 1.1.6.9). The recovered NPC structures with OxyFluor™ were very sparse (Fig. 3.7) and consequently the ELE and the number of localizations per NPC were comparably low (Fig. 3.10). These observations might have been caused by a higher residual oxygen concentration in the buffer that led to an irreversible photobleaching reaction of the excited dye with oxygen (Ha and Tinnefeld, 2012). OxyFluor™ was reported in SMLM of structures with a higher labeling density, e.g., cytoskeletal elements, where the loss of individual fluorophores due to bleaching is less obvious (Nahidiazar *et al.*, 2016). The super-resolved images of the other oxygen scavenging systems were of quality comparable to GLOX (Fig. 3.9). The performance of POX was very similar to GLOX, imaging in the PCD buffer led to a lower ELE and number of localizations per NPC, and oxygen scavenging by sulfite resulted in a decrease in the number of photons and localizations per NPC (Fig. 3.10). Based on these results, GLOX and POX are the oxygen scavenging systems of choice for single SMLM acquisitions of high quality.

Long-term experiments with GLOX and POX Long-term experiments with the mammalian NPC samples showed that also tripling the buffer capacity was not enough to prevent the acidification of the GLOX buffer (Fig. 3.9, second column). The considerable difference between the two GLOX conditions at the end of a long-term experiment might be caused by a lower decrease in the pH at that time point. Using the POX-based system, the structures of interest were not visible anymore after several hours of imaging (Fig. 3.9, third column). Interestingly, the number of photons decreased while the localization precision decreased as well (Fig. 3.10). This counterintuitive observation can be explained by how the localization precision was measured. The distribution of localization precision of the individual localized molecules was fitted with a log-normal distribution and the rising edge of the distribution was reported. By manual inspection of the corresponding datasets, it became obvious that the decrease in localization precision was caused by a shift in the distribution towards higher values of the localization precision with a simultaneous increase in very well localized fluorophores. Therefore, the practice of reporting the rising edge, which is a valid procedure for normal localization data, led to quantification of these high quality localizations while obscuring the change in the distribution towards higher values. Moreover, the fluorophore on-time increased over time in imaging buffer with POX as oxygen scavenger (Fig. 3.10). The fluorophore on-time correlates inversely with the thiol concentration (Dempsey *et al.*, 2009). Therefore, the observed increase in on-time could be explained by a decrease in the effective thiol concentration, but further experiments are needed to confirm this hypothesis and determine the cause of the effective decrease of the thiol concentration.

Long-term experiments with PCD For the PCD-based system, the NPC structures were incomplete at the end of a long-term experiment (Fig. 3.9, fourth column). As a consequence, the ELE and the mean number of localizations per NPC decreased after several hours of imaging and the imaging time of individual nuclei decreased considerably (Fig. 3.10). This effect could be explained by irreversible photobleaching of a large number of fluorophores during the initial off-switching, which could be caused by insufficient oxygen depletion. Although PCD was reported to decrease the oxygen concentration to lower levels than the GLOX system (Aitken *et al.*, 2008), it would be necessary to measure the oxygen concentration in the imaging buffers to make more substantiated statements. Importantly, the observations for both the POX- and PCD-based systems were not caused by a change in the pH. Even though PCD's reaction has 3-carboxy-cis,cis-muconic acid as product (Fig. 1.9D), the system was reported to not affect the pH when incubated for several hours (Aitken *et al.*, 2008).

Long-term experiments with sulfite When using a sulfite-based imaging buffer for long-term localization microscopy, image quality and quantitative measures

were invariable over time (Fig. 3.9, fifth column, and Fig. 3.10). This behavior makes sulfite as an oxygen scavenger a good choice for long-term experiments, and for refractive index-matched buffers (Hartwich *et al.*, 2018). However, these advantages come at the price of less localizations in the same structures in comparison to the GLOX system (Fig. 3.8). The fact that the ELE is very similar indicates that the fluorophores go through fewer cycles of switching between the dark and bright state. We tried to increase this number by titrating the amount of sulfite in the buffer (Fig. 3.11) and by adding triplet state quenchers (Fig. 3.12) but both attempts did not improve the mean numbers of localizations per NPC. However, with the characteristic of decreasing the number of cycles per fluorophore, the sulfite-based buffer might be a good choice for densely labeled samples like stainings of the cytoskeleton.

Comparison of the labeling efficiency of NPCs The ELE of NPCs, where Nup96 was labeled, has been extensively analyzed under different buffer conditions (Thevathasan *et al.*, 2019). Large parts of the data in this work have been acquired with Nup107 cells, therefore only the subset that was also acquired with Nup96 cells can be compared to that study. The reported value of 58 % ELE in normal GLOX buffer is similar to the 55 % average determined here. However, the ELE in sulfite-based buffer is different: Their reported value of 40 % is lower than the 50 % measured in this work. The sample preparation and the effective concentration of cysteamine should be comparable as there is no difference in the GLOX system. Therefore, the higher ELE reported here could be explained by differences in imaging conditions, for example, laser intensities for activation and imaging, or differences in post-processing, e.g., filtering of localizations. The ELE and number of localizations per NPC can be further increased by replacing cysteamine with 2-ME or by using low laser intensities during the initial off-switching step (Thevathasan *et al.*, 2019; Diekmann *et al.*, 2020). However, the addition of 2-ME led to higher flickering of mMaple in the dual-color imaging of yeast (Fig. 3.13).

4.1.3 Labeling the NPC with peptide tags

The NPC system was also used to evaluate the performance of three different peptide tags for localization microscopy (section 3.4.4.1). The NPC component Nup107, encoded on a plasmid, was tagged on its N-terminus with GFP and different peptide tags. Labeling of the NPC by nanobodies directed against GFP resulted in high quality super-resolution images, whereas labeling of the peptide tags was not successful (Fig. 3.20). For the SpyTag/SpyCatcher system, the absence of specific labeling can be partially explained by the low degree of labeling ($\approx$ 15 %) of SpyCatcher with AF647. Some specific labeling of the nucleus could be observed for the bivalent BC2 nanobody, but the labeling efficiency was very low (Fig. 3.20H and I). When staining with the ALFA nanobody, there was no specific staining observed (Fig. 3.20K and L). For all four stainings, the GFP signal was similar, therefore staining comparable

to the GFP nanobody should be achievable. As the Nup107 construct is expressed from a plasmid in a wild-type cell line, there is also endogenous untagged Nup107 present. As a result, the expected labeling density is lower than for the endogenously tagged cell lines, but as the GFP nanobody control showed, this fact does not hamper the visualization of individual NPCs (Fig. 3.20B and C). Furthermore, the peptide tags should be at least as accessible as the epitope on GFP as they were added at the N-terminus of the fusion protein. SpyCatcher and all nanobodies used for detection are in a similar size range. For this reason, the crowdedness of the environment within the NPC should affect all of them. Further experiments are needed to troubleshoot these stainings. Testing of different nanobody batches and labeling of more abundant cellular structures, e.g., mitochondria or cytoskeleton, might help with the optimization of peptide tag labeling for localization microscopy.

4.1.4 Testing of oxygen scavenging systems on yeast samples

Performance of AF647 in imaging buffers based on GLOX or sulfite Testing of GLOX and the sulfite system on yeast dual-color samples showed that the results for AF647 from imaging of mammalian samples were transferable (Fig. 3.13, upper row). Similarly to mammalian NPCs, the number of photons for each localization of AF647 was reduced, but to an even larger extent ($\approx$ 2000 photons for sulfite compared to $\approx$ 4000 for GLOX). Consequently, the localization precision was lower for GLOX ($\approx$ 5 nm vs. $\approx$ 7.5 nm). The background in the AF647 channel was comparable for GLOX and sulfite ($\approx$ 100 photons /px), however, it was decreased to $\approx$ 80 photons /px when substituting cysteamine with 2-ME. It could be further reduced to $\approx$ 50 photons /px by exciting the two fluorophores alternatingly in sulfite-based buffer. Therefore, alternating excitation should be favored to continuous excitation, if available.

Performance of mMaple in imaging buffers based on GLOX or sulfite In the yeast samples, the different imaging buffers were also tested with the second fluorophore, mMaple (Fig. 3.13, lower row). In the sulfite-based buffer, mMaple emitted about twice as many photons per blinking event as GLOX ($\approx$ 1200 vs. $\approx$ 600). A part of this increase can be explained by the increased fluorophore on-time (70 to 80 ms for sulfite compared to 50 ms for GLOX). The substitution of cysteamine with 2-ME led to a decrease in both the number of photons per localization and the number of background photons. The reason for the lower photons per blinking event was the increased thiol-induced flickering of mMaple as manifested by the reduced fluorophore on-time and the increased number of localizations per NPC. The super-resolution data was grouped (localizations in close proximity in subsequent frames were merged as they are very likely to originate from the same molecule) to minimize the effect of flickering on this quantitative parameter, however, the off-time during the flickering might have been too long to be corrected by the grouping

algorithm. The thiol-induced flickering is detrimental for the mMaple channel in dual-color SMLM, but it is inevitable for this fluorophore combination.

A potential solution for this compromise would be the use of different photoconvertible or photoswitchable fluorescent proteins whose emission spectra differ enough to be separated in a ratiometric approach (see section 1.1.6.8). So far, ratiometric detection was not extended to fluorescent proteins as they emit less photons than synthetic dyes and splitting of the signal would further decrease the achievable localization precision. A recent approach using fluorescence salvaged from the microscope's main dichroic (Zhang *et al.*, 2020) raised hopes to also apply the approach to fluorescent proteins. As splitting of the emitted fluorescence is not necessary, the localization precision is as low as for imaging each channel in the single-color setting. Another advantage of this concept would be that fluorescent proteins do not depend on an oxygen-free imaging buffer, facilitating long-term acquisitions.

Furthermore, mMaple and its newer version mMaple3 were compared and the two pcFPs behave virtually the same in the GLOX buffer used for dual-color experiments and the Tris D_2O buffer used for single-color SMLM (Fig. 3.15).

Long-term dual-color imaging in yeast Performing long-term experiments with a GLOX-based buffer and a sealed sample holder showed that limiting the introduced oxygen was sufficient to keep the imaging quality high over several hours (Fig. 3.13 and 3.14). This observation raises the question how the other oxygen scavenging systems would perform in long-term imaging with a sealed buffer compartment. However, as the imaging buffer with GLOX and a reduced amount of cysteamine performed well in dual-color localization microscopy in yeast, we chose this condition for the high-throughput experiments. Another important conclusion from the quantification of the long-term experiments were the increase in the number of localizations per NPC for both AF647 and mMaple (Fig. 3.13, start vs. end for both GLOX Tris and sulfite Tris). This was most likely the effect of a rise in temperature as the increase occurred for both conditions and as we have seen such an increase previously for single-color long-term imaging of mMaple without an oxygen scavenging system. However, this increase has to be considered, or ideally prevented, when using the number of localizations as a parameter during post-processing to perform an unbiased analysis. Moreover, for both mMaple and AF647, the photon count was lower when excited alternatingly. The reason for this could be that the exposure and therefore also excitation time did not match the fluorophore on-time, meaning the excitation was stopped before the fluorophore emitted its whole photon budget. Optimizing the exposure time and testing of different illumination schemes (e.g., two frames in one channel, then two in the other) could help to reduce this effect.

4.2 Dynamic nanoscale characterization of the endocytic machinery

4.2.1 Influence of fixation on the nanoscale organization of the endocytic machinery

To rule out fixation-induced biases in the endocytic structures analyzed, we performed control experiments of the same structures in living and fixed cells (Fig. 3.1). We analyzed representative proteins of the early, the coat and the WASP/Myo module in endocytic sites arrested just prior to the start of actin polymerization. The average radial distributions of the three chosen proteins were similar in both live and fixed cells, suggesting that the arrested flat structures were not affected by formaldehyde fixation. The fidelity of the fixed structures during the mobile phase gets supported by the fact that the outline of the actin network in the side view in our previous work (Mund *et al.*, 2018) is in good agreement with the ribosome exclusion zones detected in high-pressure frozen EM samples (Kukulski *et al.*, 2012). Moreover, endocytic sites are in the cell's periphery, therefore, they should be fixed as one of the first structures when formaldehyde diffuses into the cell. The indications mentioned here show that the fixed structures we image are close to the structures in living cells, however, they could be biased towards certain structures when endocytic sites get preferentially fixed at certain time points leading to an overrepresentation of those states in our datasets. As far as we can tell from previous experiments, there is no bias that is very obvious. Hence, the analysis of averages across the whole endocytic timeline or in large bins should not be affected by biased fixation. The influence on the dynamic reconstruction in dual-color side views will be discussed below.

4.2.2 Temporal sorting of super-resolved endocytic sites by GFP intensity

When performing single-color SMLM experiments on fixed endocytic sites, all different stages are sampled and it is hardly possible to determine the time point of fixation. Counting the number of localizations and relating this value to the number of molecules can give some temporal information, but due to the stochastic nature of both the biological process and the blinking, it is not very accurate. Furthermore, the number of molecules increases and decreases for most proteins during an endocytic event (Picco *et al.*, 2015), making it impossible to distinguish endocytic sites that are assembling from those that are disassembling. Diffraction-limited imaging of a second endocytic protein alongside the super-resolved one expands the possibilities of retrieving dynamic information. The fluorescence intensity measured for the second protein can be used to sort the endocytic snapshots temporally. As normal fluorescence is less stochastic, one source of error is reduced. Moreover, when choosing the pair of imaged proteins strategically, assembly and disassembly can

be distinguished. For example, the coat protein Sla2 arrives after Ede1 and gets disassembled only when Ede1 has left the endocytic site. Therefore, when timing super-resolved snapshots of Ede1 with Sla2, the snapshots can be sorted into a bin with structures prior to the arrival of Sla2 (no diffraction-limited signal) and bins with increasing amounts of Sla2 (increasing diffraction-limited signal) which correspond to the temporal progression of Ede1 structures (Fig. 3.2A). In contrast, when timing Las17 structures with Abp1, the same classification does not represent the sequence of structural rearrangements at the endocytic sites (Fig. 3.2C). This is because Las17 only leaves the endocytic site slightly after Abp1's disassembly has begun (Picco *et al.*, 2015). Thus, sites slightly before and after the maximum intensity of diffraction-limited Abp1 cannot be distinguished. Similarly, Rvs167 has relatively fast assembly and disassembly kinetics peaking at scission and can therefore only faithfully mark the time point of scission with maximum intensity, but structures prior to and after the peak cannot be differenced. Another important requirement for this approach to work faithfully is that the intensity of the protein imaged diffraction-limited increases and decreases monotonically.

We used this approach to time proteins of the early, coat, WASP/Myo, and actin modules and investigated their structural rearrangement over time. The size and irregularity of the structures of the early protein Ede1 increased over time (Fig. 3.2A). These observations could be explained by the small number of proteins being present at the beginning of an endocytic site's lifetime. The lack of interaction partners could give rise to larger structures with less regularity. The structures formed by the coat protein Pan1 were slightly smaller before the start of actin assembly and did not change during the mobile phase (Fig. 3.2B). This result indicates that there are no major rearrangements of Pan1 that would impact the size of its distribution. The size of Las17 structures was slightly smaller prior to actin assembly and relatively stable during the actin phase (Fig. 3.2C). But more importantly, Las17 forms rings already before membrane invagination resulting in a nanotemplate for efficient force generation and productive endocytosis (Mund *et al.*, 2018). Analysis of the structures formed by Abp1, which decorates the whole actin network, showed that they are largest at the time point of scission (Fig. 3.2D). Furthermore, the minimum in the center of the Abp1 structure was more remarkable as the dome-shaped network grows in size. These two observations make sense as the invagination is deepest (Kukulski *et al.*, 2012) and the number of Abp1 peaks around scission (Picco *et al.*, 2015).

4.2.3 Temporal sorting of dual-color super-resolution images of endocytic sites

Diffraction-limited timing in side view The main objective of this work was to establish a timing approach for endocytic sites imaged in side view (Fig. 3.3). Retrieving temporal information in this configuration by imaging of a diffraction-limited

timing marker is hampered by potentially overlapping signals from endocytic sites above and below the site of interest. In the strategy described in the previous section, neighboring sites could be faithfully accounted for as the lateral resolution is way better than the axial resolution in a wide-field microscope. However, when performing localization microscopy, the depth of field can be reduced by discarding out-of-focus blinks that are larger, resulting in a z-slice of $\approx 600\,\mathrm{nm}$. Because of this, we decided to tackle the problem of retrieving dynamic information from single snapshots of endocytosis in side view by performing dual-color localization microscopy.

Problems caused by heterogeneous cell size Changing the focal plane from the bottom of yeast cells (Fig. 1.13A) to the equator (Fig. 3.3B) results in the following problem: As yeast cells have different sizes depending on the cell cycle and the stochasticity of size control (Di Talia *et al.*, 2007), the z coordinate of the equatorial plane varies from cell to cell. Some of the side view snapshots are therefore out of focus or slightly tilted as the membrane is not perfectly perpendicular to the focal plane. We discarded endocytic sites that were out of focus by filtering the localization table by the size determined for every localization. Furthermore, tilted structures affect the subsequent analysis only marginally since the error goes with the cosine of the tilt angle. For example, a tilt of 18° results in a 5 % error when estimating the height of the endocytic site. This error is probably smaller than the error we make due to the stochasticity of the localization data and background localizations.

Temporal sorting by centroid distance As all pcFPs that yield good SMLM results in yeast have very similar emission spectra and as AF647 is the only synthetic dye that works well on intracellular targets in yeast in SMLM (Mund, 2016), we performed dual-color imaging using mMaple(3) and AF647 (Mund *et al.*, 2018). The resulting dual-color super-resolution data together with knowledge from tracking of individual endocytic events in living cells (Picco *et al.*, 2015) allowed us to sort the individual snapshots by increasing distance of the centroids in each channel and visualize the dynamics of two proteins in the endocytic network (Fig. 3.3C). This procedure is based on the assumption that endocytosis progresses regularly. Temporal differences in the progression do not matter as long as each endocytic event goes through the same sequence of events. Therefore, even if fixation of endocytic events leads to a bias and consequently higher frequency of certain states, we can correct for that if we sample the whole timeline and align the data to the trajectory known from live cell experiments (Picco *et al.*, 2015). The resulting averaged structures (Fig. 3.3C) visualize the growth of the actin network over time with Las17 at its lower end. However, features that were visible at the single site level as, for example, the two maxima of Las17's ring at both sides of the growing invagination, got lost during averaging. This was one of the reasons why we wanted to improve the sorting and alignment procedure.

4.2.3.1 Automatic segmentation of high-throughput data

With the established high-throughput protocol at hand, we could image several hundreds of cells with thousands of endocytic sites. As manual picking and rotation of endocytic sites is cumbersome, we wanted to develop a pipeline that automatically segments endocytic sites with multiple entry points for quality control (Fig. 3.16A). After initial detection of all cells, we removed those at the edges and those not stained in the AF647 channel. Removal of incomplete cells was necessary because in subsequent steps the outline of the cell was fitted. The few cells that were not stained with the SNAP ligand, most likely due to incomplete permeabilization, were discarded as they did not contain any signal in the second channel. Fitting of the outline of the remaining cells with a spline helped with detection and preliminary rotation of endocytic sites. The following analysis of the endocytic sites could be influenced by close by signals not belonging to the structure of interest. Therefore, we discarded sites that were too close together within one cell or too close to a neighboring cell. This pipeline was successfully used to segment a dataset of ≈ 400 cells containing ≈ 1000 endocytic sites (Fig. 3.18).

4.2.3.2 Fitting of endocytic structures with a model

The new approach for the extraction of temporal information from snapshots of endocytic sites should use a model based on previous knowledge to automatically and precisely extract more quantitative information than just centroid distances. Additionally, the new approach should improve the spatial alignment of the endocytic structures. The procedure we devised used geometric models with fixed parameters that were based on previous knowledge from EM (Kukulski *et al.*, 2012) and SMLM (Mund *et al.*, 2018) and free parameters that conveyed temporal information and improved the spatial alignment. As an example, we used the same data that was already sorted by centroid distance and fitted it with a model consisting of two parts. The actin network was fitted with a hemi-ellipsoid with flexible length and the structure of Las17 was represented by a ring of defined dimensions (Fig. 3.16C). Moreover, the position of the model was a free parameter to increase the fidelity of the spatial alignment, and the rotation of the model was fitted to further improve the coarse rotational alignment obtained during segmentation. Another fitted parameter that could be used to retrieve temporal information was the relative intensity of the two models.

When comparing the results from sorting the endocytic sites by increasing centroid distance with the ones obtained from sorting by length of the actin network (Fig. 4.1), it becomes clear that the dynamic reconstruction has improved when fitting the snapshots with a model. The first reconstructed time point has less signal from the Abp1 channel and the actin network grows over time. Furthermore, it is evident that the spatial alignment of the model fit is better than the one performed manually. However, also with model fitting, the ring-like arrangement of Las17 did not become

apparent by the occurrence of two maxima. Taken together, model fitting of dual-color SMLM data improved the dynamic reconstruction, but it requires the model to be adapted to the imaged proteins, to a certain extent, it implies the model on the data, and the integration of multiple datasets is not straightforward.

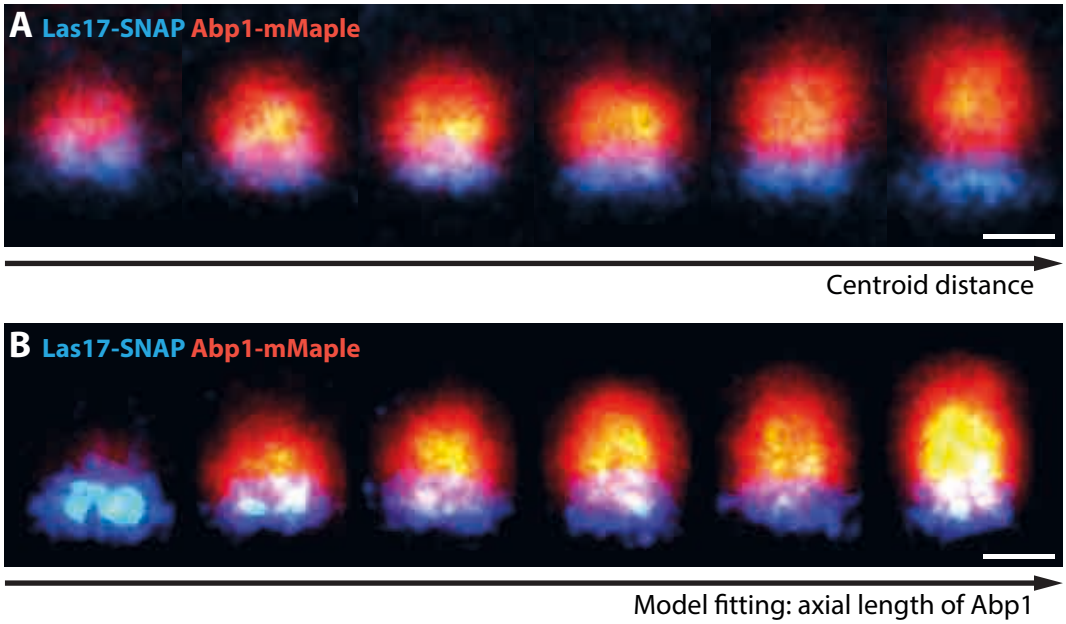

Figure 4.1 | Comparison of temporal sorting by centroid distance and model fitting. Snapshots of endocytic sites ($n = 131$) were either sorted by (**A**) centroid distance or (**B**) the axial length of the actin network obtained from model fitting. The data was reproduced from figures 3.3C and 3.16E, respectively, and was partially rearranged to facilitate comparison. The data presented in (B) was analyzed by Yu-Le Wu. Scale bars are 100 nm.

4.2.3.3 A reference structure for spatial and temporal alignment

A static reference structure These disadvantages can be overcome by using a reference structure in one channel that is used for alignment and averaging of the second channel. This strategy was recently used to map the NPC in 3D by localization microscopy (Jimenez Sabinina *et al.*, 2020). In this preprint, five different subunits of the NPC were imaged alongside one common reference subunit that allowed registration of thousands of single NPCs. Applying methods from particle averaging, which are typically used in single-particle cryo-EM, resulted in a comprehensive 3D representation of the NPC, which for the first time included the structural heterogeneity of flexible subunits. Different from this procedure, we wanted to apply the concept to a very dynamic structure and use model fitting instead of particle averaging.

A reference structure in endocytosis In our approach, the reference structure was formed by two proteins that were imaged in the same color. We used this reference structure to temporally and spatially align snapshots of endocytic sites and thereby reconstructed the dynamic rearrangement of a third independent query protein that was imaged in the second channel (Fig. 3.17). The model can be fitted

to multiple datasets with the same reference structure but different query proteins. This procedure has the advantage that the determined structural rearrangements of the query protein are independent from the reference structure and it facilitates the integration of multiple datasets.

Composition of the reference structure One important choice was which two proteins were used as the reference structure. For the structural alignment, it was important that the lower end of the endocytic site was marked faithfully. To be able to reconstruct the whole mobile phase of endocytosis, it was necessary that both proteins were present throughout and that their relative structure changes as much as possible. Based on these prerequisites, it made the most sense to image a protein of the WASP/Myo module, which stays at the plasma membrane, alongside a coat protein, which moves inwards together with the growing invagination.

Validation of the reference structure For the first validation experiment, we chose the combination of the NPF Las17 from the WASP/Myo module and the coat protein Sla2 as the proteins the reference structure was composed of (Fig. 3.18A). We imaged the two proteins in different colors without a query protein being present but merged the two channels prior to performing the model fit. We chose this setting to assess if we can retrieve temporal information from a single color reference structure by reintroducing the two colors at the end of the analysis. As figure 3.18E shows, this approach worked well as the rearrangement could be visualized with only minor amounts of cross-talk between the two structures. Assignment of absolute time to the averages at the different stages would be possible by comparing the distances to the live cell centroid tracking experiments performed by Picco *et al.* (2015).

Limitations of a dynamic reconstruction based on a reference structure As mentioned above, one assumption for the dynamic reconstruction is the regularity of the process. Even though recent reports challenge the early view that endocytic kinetics are very regular (Pedersen *et al.*, 2020; Kaksonen *et al.*, 2003), temporal differences in the progression do not affect the temporal sorting by our approach. If the structures go through the same stages on their way to form a vesicle, we randomly sample the whole process and can reconstruct it. A retracting endocytic event could influence our analysis as it most likely undergoes different structural changes than during its build-up. As we have no knowledge about the previous and subsequent trajectory of the individual endocytic sites, we cannot distinguish productive from retracting endocytic sites. However, in wild-type yeast, less than 1 % of the endocytic sites were reported to retract (Kaksonen *et al.*, 2005). Moreover, endocytic sites where only one of the two proteins is present cannot be sorted by the geometric parameters of the reference structure. Since this state exclusively occurs before the mobile phase starts, it particularly affects the very beginning of the reconstruction. At the same time, this

limitation could be overcome by using other parameters (see next paragraph) for temporal sorting of these structures.

Improvement by additional quantitative measures Additionally to the geometric features, the model fit yielded the relative intensity ratios of the two parts of the model (3.18B). On the one hand, the implementation of this intensity as a free parameter improved the quality of the fit. On the other hand, we did not exploit this parameter for the dynamic reconstruction so far. This could be especially beneficial for the early sites where only one of the two proteins is present (see previous paragraph). Counting the number of localizations within each part of the model and relating them to the number of proteins determined by live cell microscopy (Picco *et al.*, 2015) might further improve the temporal alignment of the snapshots along the whole endocytic timeline. Furthermore, it would be possible to also use quantitative information about the query protein to enhance the dynamic reconstruction. This proposal is contradictory to the idea of keeping the query protein totally independent from the reference structure. However, it would implicate nothing on the query protein at a structural level but include another valuable quantitative parameter.

Choice of fluorophore for the reference structure The choice of tagging the reference structure with mMaple and the query protein with SNAP-AF647 was based on two considerations. Firstly, the localization precision for AF647 is higher than for mMaple (Fig. 3.13). As we want to determine the structural rearrangement of the query protein with the highest resolution, we chose the synthetic dye for the query protein. Secondly, the labeling of SNAP with AF647 adds another step that complicates quantitative analysis of the localization data. Therefore, we labeled the reference structure with mMaple to be able to retrieve additional quantitative data from the reference channel as described in the previous paragraph.

4.2.3.4 Phenotype of multiply tagged yeast strains

Morphological differences in tagged strains When we went on to further validate the reference structure by reconstructing the rearrangements of a first query protein, we observed aberrant cell shapes and unexpected endocytic structures (Fig. 3.19A, B). The morphological phenotype was also detected in a strain where one of the two reference proteins and the query protein were exchanged (Fig. 3.19E to H). These initial observations were based on our experience in yeast imaging and were not quantified. It is known that epitope tagging can affect growth fitness and the localization of the target protein (Weill *et al.*, 2019). However, we know that the affected proteins, when tagged exclusively, localize to endocytic sites both in live cell and super-resolution experiments (Kaksonen *et al.*, 2003; Mund *et al.*, 2018). N- and C-terminal tagging of Las17 was reported to affect endocytic dynamics similarly to mutants lacking the CA domain, suggesting defects in Las17's actin nucleation promoting activity (Galletta *et al.*, 2008). This observation was supported by slowed

endocytosis determined by longer Abp1 lifetimes at endocytic sites in strains that had Las17 tagged C-terminally with GFP (Picco *et al.*, 2015). In light of these reports, it is plausible that tagging of multiple proteins in the same biological process could lead to functional defects, particularly since endocytic proteins constitute a large network mediated by extensive protein-protein interactions (Boettner *et al.*, 2012; Goode *et al.*, 2015). Since endocytosis is counterbalancing exocytosis, which is important to ensure the localization of enzymes mediating cell wall remodeling and synthesis at sites of polarized growth (Lesage and Bussey, 2006), defects in endocytosis could lead to the detected morphological phenotype.

Combinatorial reference structure The reference structures tested so far consisted of either Las17 or Myo5 as base protein and Sla2 as coat protein. We had chosen them based on their good contrast in super-resolution microscopy and their presence at endocytic sites throughout the mobile phase of endocytosis. In the plethora of endocytic proteins, there are multiple ones that could potentially serve as base or coat proteins in the reference structure. We reasoned that we could find a combination of a base and a coat protein in which the C-terminal tagging does not affect the cell morphology. Accordingly, we generated strains where each of the candidate proteins was tagged with mMaple and generated the strains with all possible combinations for the reference structure by manual SGA (Fig. 3.21). The combinations were generated in wild-type background as well as three backgrounds, in which different query proteins had been tagged. Additionally, we generated versions of the strains in which we had initially seen the aberrant morphology with longer linkers between the protein of interest and the tag (17 vs. 10 amino acids). The extension increases the flexibility and the distance between the C-terminus and the tag, potentially restoring interactions disturbed previously.

Quantitative analysis of multiply tagged strains In total, more than 300 strains were generated and their morphology needed to be analyzed. To make a more substantiated statement, we chose to evaluate their geometric features quantitatively. For this analysis, we chose to use confocal microscopy as diffraction-limited resolution was enough to quantify the cells' shapes and the strains could be imaged in 96-well format. We started by performing control experiments with wild-type strains, the strains where we had encountered the aberrant morphology, the corresponding strains with longer linkers, and those generated by SGA. Initially, the cells were automatically segmented using the channel in which the cell wall was stained and the one with stained imaging medium. The segmentation worked reliable, however, the quantitative analysis did not show any considerable differences between the strains (Fig. 3.23). To exclude that the morphological changes were too subtle to be detected by the segmentation pipeline, I manually annotated more than 20 000 cells without knowing which strain was being analyzed. The classification showed that there were no morphological differences between the different strains, even

for those where we had observed abnormalities in super-resolution experiments more than a year before. In very recent SMLM acquisitions, we also did not detect any aberrant morphology. To date, we have not found a satisfactory explanation for the inconsistencies with the earlier experiments (Fig. 3.19), but we will continue to vigorously control the quality of the imaging data.

Differences in growth fitness in multiply tagged strains The same strains from the morphological analysis were subjected to growth tests to assess their fitness (Fig. 3.25). Interestingly, there were differences between the two wild-type backgrounds. The multiply tagged strains based on the common lab strain BY4741 (Winston *et al.*, 1995) were growing as the wild-type. However, the strains in the MK100 background showed additive defects in growth fitness, with Las17/Sla2/Sac6 growing the slowest. We obtained consistent results from growth tests on solid and in liquid medium. The MK100 strain is from Marko Kaksonen's lab (University of Geneva) and is identical to the strain DDY130 from David Drubin's lab (University of California, Berkeley). It was originally derived from the diploid strain DDY426 (Moon *et al.*, 1993). The differences in growth raised the question which wild-type background we should use for the dynamic reconstruction by model fitting. On the one hand, the MK100 background helps us with finding detrimental combinations of tagged proteins. On the other hand, the BY4741 strains seem to not be affected by tagging of different endocytic proteins and grow generally faster. But even if endocytosis is decelerated in the MK100 strains, the important condition for our approach is that it progresses through the same stages.

Quality control of multiply tagged strains The observed differences in cell shape and growth fitness show the importance of quality control. Which further validation experiments can we perform? The state of the art to assess endocytic function in live cell imaging is timing of the mobile phase by measuring the lifetime of fluorescently labeled Abp1 (Picco *et al.*, 2015). However, since this means introducing an additional tag, it would obscure if a change in Abp1 lifetime is also present in the strain without tagged Abp1. The lipophilic dye FM4-64 (Vida and Emr, 1995) would allow a label-free approach that has previously been used to find endocytic mutants (Wiederkehr *et al.*, 2001), but it is not clear if the endocytic phenotype is strong enough to be detected by this method. For the initial proof of concept for our reference structure approach, we decided to use SMLM data acquired in the MK100 background. Before acquiring more data for a comprehensive dataset, we will perform an in-depth nanoscale analysis of SMLM data from both wild-type backgrounds to make a more profound decision.

4.2.3.5 Validation of dynamic reconstruction

Reconstruction of four query proteins The dynamic reconstructions of four proteins representative for the functional modules showed largely expected distributions but also some discrepancies (Fig. 3.26). For the coat protein End3, one part moved into the cytosol together with the upper part of the model, but some of the signal also stayed at the base of the invagination (Fig. 3.26A). This bipartite distribution was also evident at single sites, but as a control we will have to investigate if is also present in a single-color dataset of a strain where only End3 is tagged. Las17 stayed at the base of the plasma membrane, we did not observe a subset of the signal moving in with the coat as reported previously (Fig. 3.26B; Idrissi *et al.*, 2008; Idrissi *et al.*, 2012). Moreover, for the third and fourth bin, two maxima were discernible left and right of the invaginated membrane, as expected for the 2D projection of a ring. In the last two time points, Las17 showed a larger distribution along the axis of invagination. This could have the biological cause of Las17 being more broadly distributed in the lower part of the actin network, or it could be an artifact caused by inaccurate spatial alignment of the late stages of the reference structure. To discriminate these two hypotheses, more experiments are needed, for example, a comparison of the distribution of Las17 with other proteins of the WASP/Myo complex. The actin cross-linking protein Sac6 could be observed at endocytic sites immediately after coat movement started and the distribution gained in height over time, with the highest density between both parts of the reference structure (Fig. 3.26C). This observation suggests that the actin network is most dense in this region. Moreover, the structure formed by Sac6 has a slight offset in the axis of invagination, indicating that there is a zone at the plasma membrane, where actin filaments are nucleated that get subsequently cross-linked further away from that nucleation zone. This is an encouraging result to investigate the distribution of more proteins that are part of the actin network and fulfill different functions therein. Rvs167, which binds to the neck of the invagination, was present in the later time points in the region where one would expect the tubular part of the membrane, but also in the first bin (Fig. 3.26D).

Sorting of the first bin The presence of Rvs167 in the first bin is in parallel with the unexpected observation that the reference structure is very wide, which is most obvious for the datasets with Las17 and Rvs167 as query proteins (Fig. 3.26B, D). The reason for this is that we sorted the sites where mainly one of the two parts of the model ($> 95\,\%$) was fitted to the beginning of the list, therefore, they are averaged in the first bin. As one of the two parts dominated the fitting, the resulting geometric parameters are less reliable. The fact that we saw signal from Rvs167 in the first bin suggests that we also misclassified late sites, potentially by wrongly sorting sites with mainly signal from Myo5 to the top of the list. To get hold of this problem, we will try to improve the sorting in these early sites by taking into account the number of localizations and potentially the query channel. Another option to consider and

evaluate cautiously would be to exclude the sites with mainly one fitted model from further analysis. However, this misclassification did not influence the reconstruction of the mobile phase, during which the major rearrangements happen.

Combination of datasets Our ultimate goal is to merge the dynamic rearrangements of the different query proteins into one reconstruction. The individual reconstructions of the different datasets (Fig. 3.26A to D) revealed that the trajectories of the reference structure were not comparable, for example the fifth bin of the reference structure in the End3 dataset (Fig. 3.26A) had a similar shape as the third one in the Sac6 dataset (Fig. 3.26C). Therefore, we will need to develop computational tools to temporally align the different datasets. Furthermore, it is necessary to increase the size of the datasets to make sure that in all of them the mobile phase is sampled well enough.

Next steps After performing the necessary validations and improvements mentioned above, we will acquire super-resolution data for more query proteins to generate a comprehensive dataset for the dynamic reconstruction. An insightful addition to the dataset would be to analyze the positioning of the N-terminus in comparison to the C-terminus for key proteins.

5 Future outlook

Starting from the proof of concept with four query proteins, we are going to extend the dynamic reconstruction to more proteins. A dynamic reconstruction with more proteins will allow us to start answering functionally relevant biological questions. For example, imaging of proteins that bind either to the barbed or pointed ends of actin filaments can help to elucidate the filament orientation. Preferential localization of actin network remodeling proteins would aid in the refinement of the computational models of force generation.

Once established, we envision the approach to also be valuable for the characterization of mild endocytic mutants. For the analysis of these mutants, control experiments to validate that the reference structure is not affected by the mutation are indispensable. Further insights can be provided by new labeling approaches, which are compatible with super-resolution microscopy, to directly visualize actin, cargo molecules, and lipids like PI(4,5)P_2.

To date, we applied the model fitting approach to 2D images of yeast endocytosis, however, the approach was already successfully applied to 3D data. Localization microscopy with a 4Pi microscope would allow to get a 3D image of the endocytic process, which would improve both the spatial and temporal resolution of the dynamic reconstruction.

Super-resolution microscopy of endocytosis in living yeast would be the ultimate goal. The recent development of MINFLUX enables imaging at unprecedented resolution and with further methodological improvements it will be applicable to dynamic processes in living cells.

6 | Materials & Methods

6.1 Materials

6.1.1 Primers

The primers in this list that contain JR in their number, are from our lab, the ones containing MK have been provided by Marko Kaksonen's lab, and the ones containing PH have been designed by me. The remaining ones are sequencing primers from GATC or have no dedicated number.

Table 6.1 | List of primers used in this work

Oligo number	Oligo name	Sequence	Purpose
—	CYC1 Term Rev	AGCGTGACATAACTAATTACATG	Sequencing from the CYC1 terminator upstream
—	GATC: CMV-F	CGCAAATGGGCGGTAGGCGTG	Sequencing from CMV promoter
—	GATC: LPP1	ATACGACTCACTATAGGGAGAC	Sequencing from T7 promoter
—	GATC: SP6	ATTTAGGTGACACTATAGAA	Sequencing from SP6 promoter
—	GATC: T7	TAATACGACTCACTATAGGG	Sequencing from T7 promoter
—	GATC: pBR1	CGAAAAGTGCCACCTGAC	Sequencing
—	GATC: pET-RP	CTAGTTATTGCTCAGCGG	Sequencing from T7 terminator upstream
—	GATC: pGBT9-RP	CGTTTTAAAACCTAAGAGTCAC	Sequencing from ADH1 terminator upstream
—	NUP188 S2	CTTGCACTGTTCATTATTATATTATGTAGCTTTACATAACCTGCAAAATAAGTTAATCGATGAATTCGAGCTCG	C-terminal tagging of NUP188
—	NUP188 S3	CAAGGGTATCAGCAGAGACATTAAAGCATTACAAGATTCACTATTTAAGGACGTTCGTACGCTGCAGGTCGAAC	C-terminal tagging of NUP188
—	NUP188 check Rev	CAAAGCATGAGAGTCTTCGG	Control primer for C-terminal tagging of NUP188
—	NUP49 S2	CATTTGTACTTGTTATACGCACTATATAAACTTTCAGGGCGATTTACTCAATCGATGAATTCGAGCTCG	C-terminal tagging of NUP49

Continued on the next page

Table 6.1 Continued from the previous page

Oligo number	Oligo name	Sequence	Purpose
—	NUP49 S3	GAATCGCCGTGTTACATCAAAA AACGAAAACACTGGCATCATT GAGCATACGTACGCTGCAGGT CGAC	C-terminal tagging of NUP49
—	NUP49 check Rev	TGGCTTGCCTGTTCGATAAC	Control primer for C-terminal tagging of NUP49
oJR034	SAC6 S2	AACAAGAAAGCTGAGTAGAAA ACAGGTTACGAAAGTTGTTTGT TGGCTCAATCGATGAATTCGAG CTCG	C-terminal tagging of SAC6
oJR035	SAC6 S3	GTGCAAGATTAATTATTACTTTT ATCGCTTCGTTAATGACTTTGA ACAAACGTACGCTGCAGGTCG AC	C-terminal tagging of SAC6
oMK0005	ABP1 S3	AAAAGGTCTCTTCCCCAGCAAT TATGTGTCTTTGGGCAACCGTA CGCTGCAGGTCGAC	C-terminal tagging of ABP1
oMK0006	ABP1 S2	ACGTAAGAATAATATAATAGC ATGACGCTGACGTGTGATTATC GATGAATTCGAGCTCG	C-terminal tagging of ABP1
oMK0007	SLA1 S3	ACAATCAAGGCAAGCCAACAT ATTCAATGCTACTGCATCAAAT CCGTTTGGATTCCGTACGCTGC AGGTCGAC	C-terminal tagging of SLA1
oMK0008	SLA1 S2	GTTTTAGTTATTATCCTATAAAA TCTTAAAATACATTAATATCGA TGAATTCGAGCTCG	C-terminal tagging of SLA1
oMK0010	SLA1 check Rev	TGTACGAAACTATTTCATATAG C	Control primer for C-terminal tagging of SLA1
oMK0014	SAC6 check Rev	AATGGCTCAGTAATCACG	Control primer for C-terminal tagging of SAC6
oMK0098	YAP1801 S3	GTTTTAGGAAACCAATATGCTA ACAACCTCAATTTAATTGATAT GCGTACGCTGCAGGTCGAC	C-terminal tagging of YAP1801
oMK0099	YAP1801 S2	ATGCACTTGAGTACTCCCTTAC ATACCTGATTATACTAGATATT AATCGATGAATTCGAGCTCG	C-terminal tagging of YAP1801
oMK0118	YAP1801 check Rev	CGGGAGGAATTGAAGACAGT	Control primer for C-terminal tagging of YAP1801
oMK0213	PAN1 S2	AAATTAGTATACATACGTATCT ATAGAAAGCAAATTAAATCTTC AATCGATGAATTCGAGCTCG	C-terminal tagging of PAN1
oMK0214	PAN1 S3	CCATCAATTCCACCTGCAGGTA TTCCTCCACCCCCACCCCTTCC ACGTACGCTGCAGGTCGAC	C-terminal tagging of PAN1
oMK0220	MYO5 S3	AGTGATGACGAGGAGGCTAAC GAAGATGAAGAGGAAGATGAT TGGCGTACGCTGCAGGTCGAC	C-terminal tagging of MYO5
oMK0221	MYO5 S2	TATTTGCTCGTATAGAGTATAT ACTCGCTAAATACATTTTGATT AATCGATGAATTCGAGCTCG	C-terminal tagging of MYO5
oMK0222	MYO5 check Rev	GGGTTACGCCAATATTTTTCA	Control primer for C-terminal tagging of MYO5

Continued on the next page

Table 6.1 Continued from the previous page

Oligo number	Oligo name	Sequence	Purpose
oMK0224	SLA2 S3	TTGGGCGAGATAAGAAGGCAT GCCTACTATAACCAGGATGATG ATCGTACGCTGCAGGTCGAC	C-terminal tagging of SLA2
oMK0225	SLA2 S2	ATATTAACGTTTATCTTTATATA TAAAAAGTACAATTCATGATCA ATCGATGAATTCGAGCTCG	C-terminal tagging of SLA2
oMK0227	SLA2 check Rev	GAAGCAAAATGGTAGACTCCT ACA	Control primer for C-terminal tagging of SLA2
oMK0270	RVS167 S2	TAGAAGGTAATGAATACAGAG GGATGCAGGGGCCTCCTCTAAT CGATGAATTCGAGCTCG	C-terminal tagging of RVS167
oMK0271	RVS167 S3	CAAGGTGTGTTTCCTGGGAACT ACGTGCAACTCAACAAGAACC GTACGCTGCAGGTCGAC	C-terminal tagging of RVS167
oMK0287	END3 S3	AATAAGAGACACGAATTGCAA GCATTACAAGCAGAAATCAAT CGTACGCTGCAGGTCGAC	C-terminal tagging of END3
oMK0288	END3 S2	TAAATATTACACATTCATGTAC ATAAAATTAATTATCGGTGATC GATGAATTCGAGCTCG	C-terminal tagging of END3
oMK0289	LAS17 S3	AAAGTGGGAGCTCATGACGAT ATGGACAATGGTGATGATTGGC GTACGCTGCAGGTCGAC	C-terminal tagging of LAS17
oMK0290	LAS17 S2	TTTTCTATAACAGTAGTTTCATC TTTGTTTGCATTCCATTAATCGA TGAATTCGAGCTCG	C-terminal tagging of LAS17
oMK0291	ENT1 S3	AATAATGGCTCAAATAACCGG GGATATACTCTAATTGATTTAC GTACGCTGCAGGTCGAC	C-terminal tagging of ENT1
oMK0292	ENT1 S2	ATCTGATTAGAAATGCGGACTG GAATGACAGAATCACTTCAATC GATGAATTCGAGCTCG	C-terminal tagging of ENT1
oMK0308	END3 check Rev	ACAGAAACTAAGTCACTGTTTC	Control primer for C-terminal tagging of END3
oMK0310	LAS17 check Rev	TTTCTCAAACATTTGAAACGG	Control primer for C-terminal tagging of LAS17
oMK0312	ABP1 check reverse	TATGTTCGAGGTTTTGACAAC	Control primer for C-terminal tagging of ABP1
oMK0313	ENT1 check Rev	TCTTTCAGTCGTCCTGAACTAC G	Control primer for C-terminal tagging of ENT1
oMK0318	RVS167 check Rev	CCTTCCCTTTTGGGATATTGT	Control primer for C-terminal tagging of RVS167
oMK0463	VRP1	ATCCAAGTGGAAAGGGTAGTA GTGTGCCATTGGACTTAACATT ATTTACGCGTACGCTGCAGGTC GAC	C-terminal tagging of VRP1
oMK0464	VRP1	ATTATTTTCTTGTTCTTCAGTGA TTTATTGTAACCATGGAGAAAT GCTCAATCGATGAATTCGAGCT CG	C-terminal tagging of VRP1
oMK0466	VRP1 check Rev	GGCTATCTTTAGTTAAGATGAG GC	Control primer for C-terminal tagging of VRP1

Continued on the next page

Table 6.1 Continued from the previous page

Oligo number	Oligo name	Sequence	Purpose
oMK0479	BBC1 S3	GTGGGAAGTTAAAGGTTTTCAGAATTGTTGCGAGAGGATACGTAGGTTGGCGTACGCTGCAGGTCGAC	C-terminal tagging of BBC1
oMK0480	BBC1 S2	ATGAAATCGAAAGCATTCACAATTTCCCCTTGGAAGCATTGGGTAAATTAATCGATGAATTCGAGCTCG	C-terminal tagging of BBC1
oMK0482	BBC1 check Rev	TTGACGGCGGTAAGATAAGTG	Control primer for C-terminal tagging of BBC1
oMK0483	BZZ1 S3	ATGGTGAATGTGACGGATTGAAAGGTCTATTTCCTACAAGTTACTGTAAACGTACGCTGCAGGTCGAC	C-terminal tagging of BZZ1
oMK0484	BZZ1 S2	AGTGGCGGCCAGGGAAAATATTTAATAGTTTCAGTTCATTCCTTCGTTCAATCGATGAATTCGAGCTCG	C-terminal tagging of BZZ1
oMK0486	BZZ1 check Rev	GAATTCGAAAACGAGGACGAA	Control primer for C-terminal tagging of BZZ1
oMK0487	LSB3 S3	GAGTCAACGGTAGAGAAGGTATATTCCCAGCAAATTACGTTGAACTAGTTCGTACGCTGCAGGTCGAC	C-terminal tagging of LSB3
oMK0488	LSB3 S2	TGTAAATCAATAACGTTTCTCGTATTCTTTACTCTCCTTCAAATTTTTTAATCGATGAATTCGAGCTCG	C-terminal tagging of LSB3
oMK0490	LSB3 check Rev	GAATGTCTCTTTGTTAATTTAGCTAG	Control primer for C-terminal tagging of LSB3
oMK0586	kanMX4 check FW	CCAGATGCGAAGTTAAGTGCG	Control primer for C-terminal tagging with kanMX4 cassette
oMK0882	PAN1 check Rev	GCTGTAAAGGAAGAATTGGATCG	Control primer for C-terminal tagging of PAN1
oMK0988	hphNT1 check Rev	AGTTATGTTAGTATTAAGAACG	Control primer for C-terminal tagging with hphNT1 cassette
oMK1219	HIS3MX6 check Rev	CATCATCTGCCCAGATGCG	Control primer for C-terminal tagging with HIS3MX6 cassette
oMK1322	kanMX4 check FW	TGAGTTTTCTCCTTCATTACAG	Control primer for C-terminal tagging with kanMX4 cassette
oMM219	MYO3 S3	CGATGATGATAATGACGATGGCGATGATGATGATGACTGGCGTACGCTGCAGGTCGAC	C-terminal tagging of MYO3
oMM220	MYO3 S2	TTCTATAAGAGACTAAACATCTATATATTCATGTTAATTAATCGATGAATTCGAGCTCG	C-terminal tagging of MYO3
oPH008	SpyCatcher pETM-11 FW	GATTTAACTTTAAGAAGGAGATATACCATG	Amplification of synthesized SpyCatcher & flanking regions
oPH009	SpyCatcher pETM-11 Rev	GGATCCGGTACCACTAGTTAG	Amplification of synthesized SpyCatcher & flanking regions
oPH010	mMaple3-HIS3MX6 FW	TCGACGGAGCAGGTGCTGGTGCTGGTGCTGGAGCAATGGTTAGCAAGGGCG	Amplification of mMaple3 to generate pPH005, pPH009, and pPH010

Continued on the next page

Table 6.1 Continued from the previous page

Oligo number	Oligo name	Sequence	Purpose
oPH011	mMaple3-HIS3MX6 Rev	GCAGCGTAATCTGGAACGTCATATGGATAGGATCCTTATTTGTACAGCTCATCCATG	Amplification of mMaple3 to generate pPH005, pPH009, and pPH010
oPH012	pFA6a-HIS3MX6 backbone FW	TGCTCCAGCACCAG	Amplification of pFA6a-HIS3MX6 backbone
oPH013	pFA6a-HIS3MX6 backbone Rev	GGATCCTATCCATATGACGTTC	Amplification of pFA6a-HIS3MX6 backbone
oPH014	AmpR FW	CCCAGTGCTGCAATGA	Splitting of AmpR ORF for Gibson Cloning
oPH015	AmpR Rev	GAGCGTGGGTCTCG	Splitting of AmpR ORF for Gibson Cloning
oPH016	mEos3.2-A69T-HIS3MX6 FW	TCGACGGAGCAGGTGCTGGTGCTGGTGCTGGAGCAATGTCTGCCATTAAACCGG	Amplification of mEos3.2-A69T to generate pPH006
oPH017	mEos3.2-A69T-HIS3MX6 Rev	GCAGCGTAATCTGGAACGTCATATGGATAGGATCCTTAGCGACGCGCATTATC	Amplification of mEos3.2-A69T to generate pPH006
oPH019	pETM-11 backbone FW	CATGGTATATCTCCTTCTTAAAGTTAAATC	Amplification of pETM-11 backbone
oPH020	pETM-11 backbone Rev	CTAACTAGTGGTACCGGATCC	Amplification of pETM-11 backbone
oPH021	pFA6a-hphNT1 backbone Rev	GGATCCCCGGGTTAATTAAG	Cloning of mMaple3 into pFA6a-hphNT1
oPH022	mMaple3-hphNT1 Rev	ACAGATCTGGCGCGCCTTAATTAACCCGGGGATCCTTATTTGTACAGCTCATCCATG	Cloning of mMaple3 into pFA6a-hphNT1
oPH023	pPH002 backbone FW	CCCGGGTTAATTAAGCAGG	Amplification of pFA6a-LEU2 backbone
oPH024	mMaple3-Leu2 Rev	TACAGGTTCCGGTTAGCCTGCTTAATTAACCCGGGTTATTTGTACAGCTCATCCATG	Amplification of mMaple3 to generate pPH010
oPH030	pFA6a backbone Rev	AAGCTTCAGCTGGCG	Cloning of pPH021
oPH031	pFA6a S3 insert FW	GTGACACTATAGAACGCGGCCGCCAGCTGAAGCTTCGTACGCTGCAGGTC	Cloning of pPH021
oPH039	natNT2 check FW	TTCACCCAATTGTAGATATG	Control primer for C-terminal tagging with natNT2 cassette
oPH050	natNT2 check FW	ATCTCGAGGCGAATTTC	Control primer for C-terminal tagging with natNT2 cassette
oPH053	PAN1 check Rev short	AGGAAGAATTGGATCG	Control primer for C-terminal tagging of PAN1
oPH062	mMaple(3)-HA-kanMX4 Rev	TTAGAAGTGGCGCGCCTTAATTAACCCGGGGATCCCTAGCACTGAGCAGCG	Cloning of pPH021
oPH067	MAT downstream	AGTCACATCAAGATCGTTTATGG	Determination of mating type (Illuxley *et al.*, 1990)
oPH068	MAT upstream (α specific)	GCACGGAATATGGGACTACTTCG	Determination of mating type (Illuxley *et al.*, 1990)
oPH069	MAT upstream (a specific)	ACTCCACTTCAAGTAAGAGTTTG	Determination of mating type (Illuxley *et al.*, 1990)
oPH070	MYO3 check reverse	CTTTCTGCGAGAGTATGTTTAAAAG	Control primer for C-terminal tagging of MYO3

Continued on the next page

Table 6.1 Continued from the previous page

Oligo number	Oligo name	Sequence	Purpose
oPH082	ALFA-eGFP FW	CCCAGCAGACTGGAGGAGGAG CTGAGAAGAAGACTGACCGAG CCCGTGAGCAAGGGCGAG	Inserting N-terminal ALFA tag into peGFP-Nup107
oPH083	ALFA-eGFP Rev	GGGCTCGGTCAGTCTTCTTCTC AGCTCCTCCTCCAGTCTGCTGG GCATGGTGGCGACCG	Inserting N-terminal ALFA tag into peGFP-Nup107
oPH084	Spy-eGFP FW	GCCCACATCGTGATGGTGGACG CCTACAAGCCCACCAAGGTGA GCAAGGGCGAG	Inserting N-terminal Spy tag into peGFP-Nup107
oPH085	Spy-eGFP Rev	CTTGGTGGGCTTGTAGGCGTCC ACCATCACGATGTGGGCCATGG TGGCGACCG	Inserting N-terminal Spy tag into peGFP-Nup107
oPH086	SPOT-eGFP FW	CCCGACAGAGTGAGAGCCGTG AGCCACTGGAGCAGCGTGAGC AAGGGCGAG	Inserting N-terminal SPOT tag into peGFP-Nup107
oPH087	SPOT-eGFP Rev	GCTGCTCCAGTGGCTCACGGCT CTCACTCTGTCGGGCATGGTGG CGACCG	Inserting N-terminal SPOT tag into peGFP-Nup107
oPH088	KanR FW	CGGCTATGACTGGGC	Splitting of KanR ORF for Gibson Cloning
oPH089	KanR Rev	AGCAGCCGATTGTCTG	Splitting of KanR ORF for Gibson Cloning
oPH092	S3 Seq FW	CGTACGCTGCAGGTCGAC	Sequencing from S3 sequence
oPH126	17×Linker-pFA6a Rev	ACTAGCTCCGCCGCCACCAGA ACCACCACCTGAACCACCCCCT CCTCCGGAGTCGACCTGCAGCG	Replacing 5xGA with a 17×Linker in the pFA6a series
oPH127	17×Linker-$SNAP_f$ FW	GTTCAGGTGGTGGTTCTGGTGG CGGCGGAGCTAGTATGGACAA AGACTGCG	Replacing 5xGA with a 17×Linker in the pFA6a series
oPH128	17×Linker-mMaple3 FW	GTTCAGGTGGTGGTTCTGGTGG CGGCGGAGCTAGTATGGTTAGC AAGGGCG	Replacing 5xGA with a 17×Linker in the pFA6a series

6.1.2 Plasmids

Table 6.2 | List of plasmids used in this work

Plasmid number	Plasmid name	Purpose	Source
—	pEGFP-Nup107-s32727res	Template for pPH040, pPH041, pPH042	Ellenberg Lab (Szymborska *et al.*, 2013)
—	pETM-11	Backbone for protein expression in *E. coli*	EMBL PepCore (Dümmler *et al.*, 2005)
—	pFA6a-mMaple-LEU2	Tagging protein of interest with mMaple3 using the LEU2 cassette	Ries Lab (Markus Mund)
—	pRSET-mMaple3	Expression of mMaple3 in *E. coli*; template for mMaple3 cloning	Endesfelder Lab
—	pRSETa-mEos3.2-A69T	Expression of mEos3.2-A69T in *E. coli*; template for mEos3.2-A69T cloning	Endesfelder Lab

Continued on the next page

Table 6.2 Continued from the previous page

Plasmid number	Plasmid name	Purpose	Source
JRP035	pFA6a-SNAP$_f$-natNT2	Tagging protein of interest with SNAP$_f$ using the natNT2 cassette	Ries Lab
JRP039	pFA6a-SNAP$_f$-kanMX4	Tagging protein of interest with SNAP$_f$ using the kanMX4 cassette	Ries Lab
pPH005	pFA6a-mMaple3-HIS3MX6	Tagging protein of interest with mMaple3 using the HIS3MX6 cassette	This work
pPH006	pFA6a-mEos3.2-A69T-HIS3MX6	Tagging protein of interest with mEos3.2-A69T using the HIS3MX6 cassette	This work
pPH007	pETM-11-SpyCatcherS35C-His	Expression of SpyCatcherS35C-His in *E. coli*	This work
pPH008	pFA6a-mMaple3-natNT2	Tagging protein of interest with mMaple3 using the natNT2 cassette	This work
pPH009	pFA6a-mMaple3-hphNT1	Tagging protein of interest with mMaple3 using the hphNT1 cassette	This work
pPH010	pFA6a-mMaple3-LEU2	Tagging protein of interest with mMaple3 using the LEU2 cassette	This work
pPH021	pFA6a-mMaple-HA-kanMX4	Tagging protein of interest with mMaple-HA using the kanMX4 cassette	This work
pPH040	pALFA-EGFP-Nup107-s32727res	Testing the ALFA peptide tag in mammalian cells	This work
pPH041	pSpy-EGFP-Nup107-s32727res	Testing the SpyTag peptide tag in mammalian cells	This work
pPH042	pBC2-EGFP-Nup107-s32727res	Testing the SPOT peptide tag in mammalian cells	This work
pPH052	pFA6a-17×Linker-SNAP$_f$-kanMX4	Tagging protein of interest with 17×Linker-SNAP$_f$ using the kanMX4 cassette	This work
pPH053	pFA6a-17×Linker-mMaple3-hphNT1	Tagging protein of interest with 17×Linker-mMaple3 using the hphNT1 cassette	This work
pPH054	pFA6a-17×Linker-mMaple3-natNT2	Tagging protein of interest with 17×Linker-mMaple3 using the natNT2 cassette	This work

6.1.3 Yeast strains

See table 6.3 starting on the next page.

Table 6.3 | List of yeast strains used in this work

Strain number	Description	Genotype	Source
—	BY4741	*MATa, his3Δ1, leu2Δ0, met15Δ0, ura3Δ0*	Knop Lab
—	BY4742	*MATα, his3Δ1, leu2Δ0, met15Δ0, ura3Δ0*	Patil Lab
—	Y8205	*MATα, can1Δ::STE2pr-Sp_his5, lyp1Δ::STE3pr-LEU2, his3Δ1, leu2Δ0, ura3Δ0*	Boone Lab/ Knop Lab
MKY0100	wild-type MATa	*MATa, his3Δ200, leu2-3,112, ura3-52, lys2-801*	Kaksonen Lab
MKY0102	wild-type MATα	*MATα, his3Δ200, leu2-3,112, ura3-52, lys2-801*	Kaksonen Lab
	MKY0100 Myo5-mMaple-HA (Kan) MATα	*MATα, his3Δ200, leu2-3,112, ura3-52, lys2-801, MYO5-mMaple-HA::kanMX4*	This work
—	MKY0100 Nic96-SNAP$_f$ (HIS) MATa	*MATa, his3Δ200, leu2-3,112, ura3-52, lys2-801, NIC96-SNAP$_f$:HIS3MX6*	Ries Lab (Markus Mund)
—	MKY0100 Nup188-mMaple (Hph) Abp1-EGFP (HIS) MATa	*MATa, his3Δ200, leu2-3,112, ura3-52, lys2-801, NUP188-mMaple::hphNT1, ABP1-EGFP::HIS3MX6*	Ries Lab (Thevathasan *et al.*, 2019)
JRY0014	MKY0100 Las17-SNAP$_f$ (HIS) Abp1-mMaple (Hph) MATa	*MATa, his3Δ200, leu2-3,112, ura3-52, lys2-801, LAS17-SNAP$_f$:HIS3MX6, ABP1-mMaple::hphNT1*	Ries Lab (Mund *et al.*, 2018)
JRY0034	MKY0102 Ede1-mMaple (Hph) Sla2-EGFP (HIS) MATα	*MATα, his3Δ200, leu2-3,112, ura3-52, lys2-801, EDE1-mMaple::hphNT1, SLA2-EGFP::HIS3MX6*	Ries Lab (Mund *et al.*, 2018)
JRY0041	MKY0100 Abp1-EGFP (HIS) Las17-mMaple (Hph) MATa	*MATa, his3Δ200, leu2-3,112, ura3-52, lys2-801, ABP1-EGFP::HIS3MX6, LAS17-mMaple::hphNT1*	Ries Lab (Mund *et al.*, 2018)
JRY0081	MKY0100 Pan1-mMaple (Hph) Abp1-EGFP (HIS) MATa	*MATa, his3Δ200, leu2-3,112, ura3-52, lys2-801, ABP1-EGFP::HIS3MX6, PAN1-mMaple::hphNT1*	Ries Lab (Mund *et al.*, 2018)
JRY0083	MKY0100 Abp1-mMaple (Hph) Rvs-167-EGFP (HIS) MATa	*MATa, his3Δ200, leu2-3,112, ura3-52, lys2-801, RVS167-EGFP::HIS3MX6, ABP1-mMaple::hphNT1*	Ries Lab (Mund *et al.*, 2018)
MKY0122	MKY0102 Abp1-EGFP (HIS) MATa	*MATa, his3Δ200, leu2-3,112, ura3-52, lys2-801, ABP1-EGFP::HIS3MX6*	Kaksonen Lab
MKY2832	MKY0100 Rvs167-EGFP (HIS) MATa	*MATa, his3Δ200, leu2-3,112, ura3-52, lys2-801, RVS167-EGFP::HIS3MX6*	Kaksonen Lab
yPH014	MKY0100 Nup49-mMaple3 (HIS) MATa	*MATa, his3Δ200, leu2-3,112, ura3-52, lys2-801, NUP49-mMaple3::HIS3MX6*	This work
yPH015	MKY0100 Nup49-mEos3.2-A69T (HIS) MATa	*MATa, his3Δ200, leu2-3,112, ura3-52, lys2-801, NUP49-mEos3.2-A69T::HIS3MX6*	This work
yPH033	MKY0100 Nup188-mMaple3 (HIS) MATa	*MATa, his3Δ200, leu2-3,112, ura3-52, lys2-801, NUP188-mMaple3::HIS3MX6*	This work
yPH063	MKY0100 Abp1-EGFP (HIS) Las17-mMaple (Hph) Sla2-mMaple (LEU) MATa	*MATa, his3Δ200, leu2-3,112, ura3-52, lys2-801, ABP1-EGFP::HIS3MX6, LAS17-mMaple::hphNT1, SLA2-mMaple::LEU2*	This work

Continued on the next page

Table 6.3 Continued from the previous page

Strain number	Description	Genotype	Source
yPH069	MKY0100 Abp1-EGFP (HIS) Las17-mMaple (Hph) Sla2-SNAP$_f$ (Nat) MATa	*MATa, his3Δ200, leu2-3,112, ura3-52, lys2-801, ABP1-EGFP::HIS3MX6, LAS17-mMaple::hphNT1, SLA2-SNAP$_f$::natNT2*	This work
yPH073	MKY0100 Abp1-EGFP (HIS) Las17-mMaple (Hph) Sla2-mMaple (LEU) Sla1-SNAP$_f$ (Nat) MATa	*MATa, his3Δ200, leu2-3,112, ura3-52, lys2-801, ABP1-EGFP::HIS3MX6, LAS17-mMaple::hphNT1, SLA2-mMaple::LEU2, SLA1-SNAP$_f$::natNT2*	This work
yPH083	MKY0100 Las17-mMaple (Hph) Sla2-mMaple (LEU) Sla1-SNAP$_f$ (Nat) MATa	*MATa, his3Δ200, leu2-3,112, ura3-52, lys2-801, LAS17-mMaple::hphNT1, SLA2-mMaple::LEU2, SLA1-SNAP$_f$::natNT2*	This work
yPH132	MKY0100 Sla2-mMaple (LEU) Sla1-SNAP$_f$ (Nat) Myo5-mMaple-HA (Kan) MATa	*MATα, his3Δ200, leu2-3,112, ura3-52, lys2-801, SLA2-mMaple::LEU2, SLA1-SNAP$_f$::natNT2, MYO5-mMaple-HA::kanMX4*	This work
yPH230	MKY0100 Myo5-mMaple3 (Hph) MATa	*MATa, his3Δ200, leu2-3,112, ura3-52, lys2-801, MYO5-mMaple3::hphNT1*	This work
yPH243	MKY0100 Myo5-mMaple3 (Hph) Sla2-mMaple3 (LEU) MATa	*MATa, his3Δ200, leu2-3,112, ura3-52, lys2-801, MYO5-mMaple3::hphNT1, SLA2-mMaple3::LEU2*	This work
yPH245	MKY0100 Myo5-mMaple3 (Hph) Sla2-mMaple3 (LEU) End3-SNAP$_f$ (Nat) MATa	*MATa, his3Δ200, leu2-3,112, ura3-52, lys2-801, MYO5-mMaple3::hphNT1, SLA2-mMaple3::LEU2, END3-SNAP$_f$::natNT2*	This work (generated by Yu-Le Wu)
yPH246	MKY0100 Myo5-mMaple3 (Hph) Sla2-mMaple3 (LEU) Las17-SNAP$_f$ (Nat) MATa	*MATa, his3Δ200, leu2-3,112, ura3-52, lys2-801, MYO5-mMaple3::hphNT1, SLA2-mMaple3::LEU2, LAS17-SNAP$_f$::natNT2*	This work (generated by Yu-Le Wu)
yPH247	MKY0100 Myo5-mMaple3 (Hph) Sla2-mMaple3 (LEU) Rvs167-SNAP$_f$ (Nat) MATa	*MATa, his3Δ200, leu2-3,112, ura3-52, lys2-801, MYO5-mMaple3::hphNT1, SLA2-mMaple3::LEU2, RVS167-SNAP$_f$::natNT2*	This work (generated by Yu-Le Wu)
yPH249	MKY0100 Myo5-mMaple3 (Hph) Sla2-mMaple3 (LEU) Sac6-SNAP$_f$ (Nat) MATa	*MATa, his3Δ200, leu2-3,112, ura3-52, lys2-801, MYO5-mMaple3::hphNT1, SLA2-mMaple3::LEU2, SAC6-SNAP$_f$::natNT2*	This work (generated by Yu-Le Wu)
yPH288	BY4741 Sac6-SNAP$_f$ (Kan) MATa	*MATa, his3Δ1, leu2Δ0, met15Δ0, ura3Δ0, SAC6-SNAP$_f$::kanMX4*	This work
yPH289	BY4741 End3-SNAP$_f$ (Kan) MATa	*MATa, his3Δ1, leu2Δ0, met15Δ0, ura3Δ0, END3-SNAP$_f$::kanMX4*	This work
yPH290	BY4741 Las17-SNAP$_f$ (Kan) MATa	*MATa, his3Δ1, leu2Δ0, met15Δ0, ura3Δ0, LAS17-SNAP$_f$::kanMX4*	This work
yPH291	Y8205 Lsb3-mMaple3 (Hph) MATα	*MATα, can1Δ::STE2pr-Sp_his5, lyp1Δ::STE3pr-LEU2, his3Δ1, leu2Δ0, ura3Δ0, LSB3-mMaple3::hphNT1*	This work
yPH292	Y8205 Vrp1-mMaple3 (Hph) MATα	*MATα, can1Δ::STE2pr-Sp_his5, lyp1Δ::STE3pr-LEU2, his3Δ1, leu2Δ0, ura3Δ0, VRP1mMaple3::hphNT1*	This work

Continued on the next page

Table 6.3 Continued from the previous page

Strain number	Description	Genotype	Source
yPH293	Y8205 Las17-mMaple3 (Hph) MATα	*MATα, can1Δ::STE2pr-Sp_his5, lyp1Δ::STE3pr-LEU2, his3Δ1, leu2Δ0, ura3Δ0, LAS17-mMaple3::hphNT1*	This work
yPH294	Y8205 Bzz1-mMaple3 (Hph) MATα	*MATα, can1Δ::STE2pr-Sp_his5, lyp1Δ::STE3pr-LEU2, his3Δ1, leu2Δ0, ura3Δ0, BZZ1-mMaple3::hphNT1*	This work
yPH295	Y8205 Myo5-mMaple3 (Hph) MATα	*MATα, can1Δ::STE2pr-Sp_his5, lyp1Δ::STE3pr-LEU2, his3Δ1, leu2Δ0, ura3Δ0, MYO5-mMaple3::hphNT1*	This work
yPH296	Y8205 Bbc1-mMaple3 (Hph) MATα	*MATα, can1Δ::STE2pr-Sp_his5, lyp1Δ::STE3pr-LEU2, his3Δ1, leu2Δ0, ura3Δ0, BBC1-mMaple3::hphNT1*	This work
yPH297	Y8205 Myo3-mMaple3 (Hph) MATα	*MATα, can1Δ::STE2pr-Sp_his5, lyp1Δ::STE3pr-LEU2, his3Δ1, leu2Δ0, ura3Δ0, MYO3-mMaple3::hphNT1*	This work
yPH298	BY4741 Yap1801-mMaple3 (Nat) MATa	*MATa, his3Δ1, leu2Δ0, met15Δ0, ura3Δ0, YAP1801-mMaple3::natNT2*	This work
yPH299	BY4741 End3-mMaple3 (Nat) MATa	*MATa, his3Δ1, leu2Δ0, met15Δ0, ura3Δ0, END3-mMaple3::natNT2*	This work
yPH300	BY4741 Sla1-mMaple3 (Nat) MATa	*MATa, his3Δ1, leu2Δ0, met15Δ0, ura3Δ0, SLA1-mMaple3::natNT2*	This work
yPH301	BY4741 Ent1-mMaple3 (Nat) MATa	*MATa, his3Δ1, leu2Δ0, met15Δ0, ura3Δ0, ENT1-mMaple3::natNT2*	This work
yPH302	BY4741 Pan1-mMaple3 (Nat) MATa	*MATa, his3Δ1, leu2Δ0, met15Δ0, ura3Δ0, PAN1-mMaple3::natNT2*	This work
yPH303	BY4741 Sla2-mMaple3 (Nat) MATa	*MATa, his3Δ1, leu2Δ0, met15Δ0, ura3Δ0, SLA2-mMaple3::natNT2*	This work
yPH304	BY4741 Las17-SNAP$_f$ (Kan) End3-mMaple3 (Nat) MATa	*MATa, his3Δ1, leu2Δ0, met15Δ0, ura3Δ0, LAS17-SNAP$_f$:kanMX4, END3-mMaple3::natNT2*	This work
yPH305	BY4741 Las17-SNAP$_f$ (Kan) Ent1-mMaple3 (Nat) MATa	*MATa, his3Δ1, leu2Δ0, met15Δ0, ura3Δ0, LAS17-SNAP$_f$:kanMX4, ENT1-mMaple3::natNT2*	This work
yPH306	BY4741 Sac6-SNAP$_f$ (Kan) End3-mMaple3 (Nat) MATa	*MATa, his3Δ1, leu2Δ0, met15Δ0, ura3Δ0, SAC6-SNAP$_f$:kanMX4, END3-mMaple3::natNT2*	This work
yPH307	BY4741 End3-SNAP$_f$ (Kan) Ent1-mMaple3 (Nat) MATa	*MATa, his3Δ1, leu2Δ0, met15Δ0, ura3Δ0, END3-SNAP$_f$:kanMX4, ENT1-mMaple3::natNT2*	This work
yPH308	BY4741 Las17-SNAP$_f$ (Kan) Sla1-mMaple3 (Nat) MATa	*MATa, his3Δ1, leu2Δ0, met15Δ0, ura3Δ0, LAS17-SNAP$_f$:kanMX4, SLA1-mMaple3::natNT2*	This work
yPH309	BY4741 Las17-SNAP$_f$ (Kan) Sla2-mMaple3 (Nat) MATa	*MATa, his3Δ1, leu2Δ0, met15Δ0, ura3Δ0, LAS17-SNAP$_f$:kanMX4, SLA2-mMaple3::natNT2*	This work
yPH310	BY4741 Las17-SNAP$_f$ (Kan) Pan1-mMaple3 (Nat) MATa	*MATa, his3Δ1, leu2Δ0, met15Δ0, ura3Δ0, LAS17-SNAP$_f$:kanMX4, PAN1-mMaple3::natNT2*	This work

Continued on the next page

Table 6.3 Continued from the previous page

Strain number	Description	Genotype	Source
yPH311	BY4741 Las17-SNAP$_f$ (Kan) Yap1801-mMaple3 (Nat) MATa	*MATa, his3Δ1, leu2Δ0, met15Δ0, ura3Δ0, LAS17-SNAP$_f$::kanMX4, YAP1801-mMaple3::natNT2*	This work
yPH312	BY4741 Sac6-SNAP$_f$ (Kan) Sla1-mMaple3 (Nat) MATa	*MATa, his3Δ1, leu2Δ0, met15Δ0, ura3Δ0, SAC6-SNAP$_f$::kanMX4, SLA1-mMaple3::natNT2*	This work
yPH313	BY4741 Sac6-SNAP$_f$ (Kan) Sla2-mMaple3 (Nat) MATa	*MATa, his3Δ1, leu2Δ0, met15Δ0, ura3Δ0, SAC6-SNAP$_f$::kanMX4, SLA2-mMaple3::natNT2*	This work
yPH314	BY4741 Sac6-SNAP$_f$ (Kan) Pan1-mMaple3 (Nat) MATa	*MATa, his3Δ1, leu2Δ0, met15Δ0, ura3Δ0, SAC6-SNAP$_f$::kanMX4, PAN1-mMaple3::natNT2*	This work
yPH315	BY4741 Sac6-SNAP$_f$ (Kan) Ent1-mMaple3 (Nat) MATa	*MATa, his3Δ1, leu2Δ0, met15Δ0, ura3Δ0, SAC6-SNAP$_f$::kanMX4, ENT1-mMaple3::natNT2*	This work
yPH316	BY4741 Sac6-SNAP$_f$ (Kan) Yap1801-mMaple3 (Nat) MATa	*MATa, his3Δ1, leu2Δ0, met15Δ0, ura3Δ0, SAC6-SNAP$_f$::kanMX4, YAP1801-mMaple3::natNT2*	This work
yPH317	BY4741 End3-SNAP$_f$ (Kan) Sla1-mMaple3 (Nat) MATa	*MATa, his3Δ1, leu2Δ0, met15Δ0, ura3Δ0, END3-SNAP$_f$::kanMX4, SLA1-mMaple3::natNT2*	This work
yPH318	BY4741 End3-SNAP$_f$ (Kan) Sla2-mMaple3 (Nat) MATa	*MATa, his3Δ1, leu2Δ0, met15Δ0, ura3Δ0, END3-SNAP$_f$::kanMX4, SLA2-mMaple3::natNT2*	This work
yPH319	BY4741 End3-SNAP$_f$ (Kan) Pan1-mMaple3 (Nat) MATa	*MATa, his3Δ1, leu2Δ0, met15Δ0, ura3Δ0, END3-SNAP$_f$::kanMX4, PAN1-mMaple3::natNT2*	This work
yPH320	BY4741 End3-SNAP$_f$ (Kan) Yap1801-mMaple3 (Nat) MATa	*MATa, his3Δ1, leu2Δ0, met15Δ0, ura3Δ0, END3-SNAP$_f$::kanMX4, YAP1801-mMaple3::natNT2*	This work
yPH328	BY4741 Sla2-17×Linker-mMaple3 (Nat) MATa	*MATa, his3Δ1, leu2Δ0, met15Δ0, ura3Δ0, SLA2-17×Linker-mMaple3::natNT2*	This work
yPH331	BY4741 Myo5-17×Linker-mMaple3 (Hph) Sla2-17×Linker-mMaple3 (Nat) MATa	*MATa, his3Δ1, leu2Δ0, met15Δ0, ura3Δ0, MYO5-17×Linker-mMaple3::hphNT1, SLA2-17×Linker-mMaple3::natNT2*	This work
yPH332	BY4741 Myo5-17×Linker-mMaple3 (Hph) Sla2-17×Linker-mMaple3 (Nat) End3-17×Linker-SNAP$_f$ (Kan) MATa	*MATa, his3Δ1, leu2Δ0, met15Δ0, ura3Δ0, MYO5-17×Linker-mMaple3::hphNT1, SLA2-17×Linker-mMaple3::natNT2, END3-17×Linker-SNAP$_f$::kanMX4*	This work
yPH333	BY4741 Myo5-17×Linker-mMaple3 (Hph) Sla2-17×Linker-mMaple3 (Nat) Las17-17×Linker-SNAP$_f$ (Kan) MATa	*MATa, his3Δ1, leu2Δ0, met15Δ0, ura3Δ0, MYO5-17×Linker-mMaple3::hphNT1, SLA2-17×Linker-mMaple3::natNT2, LAS17-17×Linker-SNAP$_f$::kanMX4*	This work

Continued on the next page

Table 6.3 Continued from the previous page

Strain number	Description	Genotype	Source
yPH334	BY4741 Myo5-17×Linker-mMaple3 (Hph) Sla2-17×Linker-mMaple3 (Nat) Sac6-17×Linker-SNAP$_f$ (Kan) MATa	*MATa, his3Δ1, leu2Δ0, met15Δ0, ura3Δ0, MYO5-17×Linker-mMaple3::hphNT1, SLA2-17×Linker-mMaple3::natNT2, SAC6-17×Linker-SNAP$_f$::kanMX4*	This work
yPH335	BY4741 Myo5-17×Linker-mMaple3 (Hph) Sla2-17×Linker-mMaple3 (Nat) Rvs167-17×Linker-SNAP$_f$ (Kan) MATa	*MATa, his3Δ1, leu2Δ0, met15Δ0, ura3Δ0, MYO5-17×Linker-mMaple3::hphNT1, SLA2-17×Linker-mMaple3::natNT2, RVS167-17×Linker-SNAP$_f$::kanMX4*	This work
yPH341	SGA Myo5-mMaple3 (Hph) Sla2-mMaple3 (Nat) End3-SNAP$_f$ (Kan) MATa	*MATa, can1Δ::STE2pr-Sp_his5, lyp1Δ::STE3pr-LEU2, his3Δ1, leu2Δ0, ura3Δ0, MYO5-mMaple3::hphNT1, SLA2-mMaple3::natNT2, END3-SNAP$_f$::kanMX4*	This work
yPH342	SGA Myo5-mMaple3 (Hph) Sla2-mMaple3 (Nat) End3-SNAP$_f$ (Kan) MATα	*MATα, can1Δ::STE2pr-Sp_his5, lyp1Δ::STE3pr-LEU2, his3Δ1, leu2Δ0, ura3Δ0, MYO5-mMaple3::hphNT1, SLA2-mMaple3::natNT2, END3-SNAP$_f$::kanMX4*	This work
yPH343	SGA Myo5-mMaple3 (Hph) Sla2-mMaple3 (Nat) Las17-SNAP$_f$ (Kan) MATa	*MATa, can1Δ::STE2pr-Sp_his5, lyp1Δ::STE3pr-LEU2, his3Δ1, leu2Δ0, ura3Δ0, MYO5-mMaple3::hphNT1, SLA2-mMaple3::natNT2, LAS17-SNAP$_f$::kanMX4*	This work
yPH344	SGA Myo5-mMaple3 (Hph) Sla2-mMaple3 (Nat) Las17-SNAP$_f$(Kan) MATα	*MATα, can1Δ::STE2pr-Sp_his5, lyp1Δ::STE3pr-LEU2, his3Δ1, leu2Δ0, ura3Δ0, MYO5-mMaple3::hphNT1, SLA2-mMaple3::natNT2, LAS17-SNAP$_f$::kanMX4*	This work
yPH345	SGA Myo5-mMaple3 (Hph) Sla2-mMaple3 (Nat) Sac6-SNAP$_f$ (Kan) MATa	*MATa, can1Δ::STE2pr-Sp_his5, lyp1Δ::STE3pr-LEU2, his3Δ1, leu2Δ0, ura3Δ0, MYO5-mMaple3::hphNT1, SLA2-mMaple3::natNT2, SAC6-SNAP$_f$::kanMX4*	This work
yPH346	SGA Myo5-mMaple3 (Hph) Sla2-mMaple3 (Nat) Sac6-SNAP$_f$(Kan) MATα	*MATα, can1Δ::STE2pr-Sp_his5, lyp1Δ::STE3pr-LEU2, his3Δ1, leu2Δ0, ura3Δ0, MYO5-mMaple3::hphNT1, SLA2-mMaple3::natNT2, SAC6-SNAP$_f$::kanMX4*	This work

6.1.4 Chemicals

Table 6.4 | List of chemicals used in this work

Name	Supplier	Order number
1,3,5,7-Cyclooctatetraene (COT)	Alfa Aesar, Haverhill, MA, USA	B22636
2-Mercaptoethanol (2-ME)	Sigma-Aldrich, St. Louis, MO, USA	M3148
2x Phusion polymerase	EMBL Pepcore, Heidelberg, Germany	—
3,4-Dihydroxybenzoic acid (PCA)	Sigma-Aldrich, St. Louis, MO, USA	37580
4-Aminobenzoic acid	Merck, Darmstadt, Germany	822312
Adenine	Sigma-Aldrich, St. Louis, MO, USA	A8626
Adenine hemisulfate salt	Sigma-Aldrich, St. Louis, MO, USA	A3159
Agarose	Sigma-Aldrich, St. Louis, MO, USA	A9539
Ammonium acetate	Merck, Darmstadt, Germany	1116
Ammonium chloride	Merck, Darmstadt, Germany	101145
Ampicillin sodium salt	Carl Roth, Karlsruhe, Germany	K029.1
Bacto Agar	BD Biosciences, San Jose, CA, USA	214010
BivBC2 Nanobody conjugated to AF647	Rothbauer Lab, Universität Tübingen, Germany	Lot 81
Bovine Serum Albumin	Sigma-Aldrich, St. Louis, MO, USA	A7030
Calcium chloride dihydrate	Merck, Darmstadt, Germany	102382
Catalase from bovine liver	Sigma-Aldrich, St. Louis, MO, USA	C3155
cOmplete™, EDTA-free Protease Inhibitor Cocktail	Sigma-Aldrich, St. Louis, MO, USA	11873580001
Concanavalin A	Sigma-Aldrich, St. Louis, MO, USA	C2010
Concanavalin A-Alexa Fluor™ 488	Pepperkok Lab, EMBL Heidelberg, Germany	—
COT (1,3,5,7-Cyclooctatetraene)	Alfa Aesar, Haverhill, MA, USA	B22636
Cysteamine	Sigma-Aldrich, St. Louis, MO, USA	30070
D(+)-Glucose monohydrate	Merck, Darmstadt, Germany	104074
D-Sorbitol	Sigma-Aldrich, St. Louis, MO, USA	S3889
Deuterium oxide (99.8 %)	Eurisotop, Saint-Aubin, France	216L-MPT
Dextran, Alexa Fluor™ 647; 10,000 MW	Thermo Fisher, Waltham, MA, USA	D22914
Di-potassium hydrogen phosphate trihydrate	Merck, Darmstadt, Germany	105099
Di-sodium hydrogen phosphate	Merck, Darmstadt, Germany	106586
DMEM (high-glucose, w/o phenol red)	Thermo Fisher, Waltham, MA, USA	11880-028
DMSO, anhydrous	Sigma-Aldrich, St. Louis, MO, USA	276855
dNTP Mix (10 mM each)	Thermo Fisher, Waltham, MA, USA	R0191
DTT	Sigma-Aldrich, St. Louis, MO, USA	43819
EDTA	Merck, Darmstadt, Germany	108418
Ethidium bromide solution, 1 %	Carl Roth, Karlsruhe, Germany	2218.1
Fetal calf serum	Thermo Fisher, Waltham, MA, USA	10270-106
FluoTag®-X2 anti-ALFA Alexa Fluor™ 647	NanoTag, Göttingen, Germany	N1502-AF647-S
FluoTag®-X4 anti-GFP Alexa Fluor™ 647	NanoTag, Göttingen, Germany	N0304
Formaldehyde solution, about 37 %	Merck, Darmstadt, Germany	104003
Formaldehyde, 16 %	Electron Microscopy Science, Hatfield, PA, USA	RT 15710
Geneticin (G418 Sulfate)	Thermo Fisher, Waltham, MA, USA	11811023
Glucose oxidase from *Aspergillus niger*	Sigma-Aldrich, St. Louis, MO, USA	49180
GlutaMAX™	Thermo Fisher, Waltham, MA, USA	35050-038
Glutamine	Sigma-Aldrich, St. Louis, MO, USA	P0380
Glycerol	Merck, Darmstadt, Germany	1.04093
Glycine	Sigma-Aldrich, St. Louis, MO, USA	G7126
HEPES	Biomol, Hamburg, Germany	5288
Hydrochloric acid fuming, 37 %	Merck, Darmstadt, Germany	100317
Hygromycin B	Carl Roth, Karlsruhe, Germany	CP13

Continued on the next page

Table 6.4 Continued from the previous page

Name	Supplier	Order number
Image-iT™ FX Signal Enhancer	Thermo Fisher, Waltham, MA, USA	I36933
Immersol™ 518 F	Zeiss, Oberkochen, Germany	444964
Kanamycin A sulfate	Carl Roth, Karlsruhe, Germany	T832.1
L-Alanine	Sigma-Aldrich, St. Louis, MO, USA	A7627
L-Arginine	Sigma-Aldrich, St. Louis, MO, USA	A5006
L-Asparagine	Sigma-Aldrich, St. Louis, MO, USA	A0884
L-Aspartic acid	Sigma-Aldrich, St. Louis, MO, USA	A9256
L-Canavanine sulfate salt	Sigma-Aldrich, St. Louis, MO, USA	C9758
L-Cysteine hydrochloride monohydrate	Sigma-Aldrich, St. Louis, MO, USA	C7880
L-Glutamic acid	Sigma-Aldrich, St. Louis, MO, USA	G1251
L-Glutamic acid monosodium salt hydrate	Sigma-Aldrich, St. Louis, MO, USA	G1626
L-Histidine	Sigma-Aldrich, St. Louis, MO, USA	H8000
L-Isoleucine	Sigma-Aldrich, St. Louis, MO, USA	I2752
L-Leucine	Sigma-Aldrich, St. Louis, MO, USA	L8000
L-Lysine monohydrochloride	Sigma-Aldrich, St. Louis, MO, USA	L5626
L-Methionine	Sigma-Aldrich, St. Louis, MO, USA	M9625
L-Phenylalanine	Sigma-Aldrich, St. Louis, MO, USA	P2126
L-Proline	Sigma-Aldrich, St. Louis, MO, USA	P0380
L-Serine	Sigma-Aldrich, St. Louis, MO, USA	S4500
L-Threonine	Sigma-Aldrich, St. Louis, MO, USA	T8625
L-Tryptophan	Sigma-Aldrich, St. Louis, MO, USA	T0254
L-Tyrosine	Sigma-Aldrich, St. Louis, MO, USA	T3754
L-Valine	Sigma-Aldrich, St. Louis, MO, USA	V0500
Lactose monohydrate	Merck, Darmstadt, Germany	107657
Latrunculin A (LatA)	abcam, Cambridge, UK	ab144290
Lipofectamine™ 2000 transfection reagent	Thermo Fisher, Waltham, MA, USA	11668019
Lithium acetate dihydrate	Sigma-Aldrich, St. Louis, MO, USA	L6883
Lyticase from *Arthrobacter luteus*	Sigma-Aldrich, St. Louis, MO, USA	L4025
Mach1™ T1 *E. coli*	Thermo Fisher, Waltham, MA, USA	C862003
Magnesium chloride	Merck, Darmstadt, Germany	105833
Magnesium sulfate heptahydrate	Merck, Darmstadt, Germany	105886
Maleimide-Alexa Fluor™ 647	Thermo Fisher, Waltham, MA, USA	A20347
Manganese(II) chloride	Sigma-Aldrich, St. Louis, MO, USA	M3634
Methanol	Merck, Darmstadt, Germany	106009
Monarch™ DNA Gel Extraction Kit	New England Biolabs, Ipswich, MA, USA	T1020S
myo-Inositol	Sigma-Aldrich, St. Louis, MO, USA	I7508
NEBuilder HiFi DNA Assembly Master Mix	New England Biolabs, Ipswich, MA, USA	E2621S
Ni-NTA Agarose	QIAGEN, Hilden, Germany	30210
Non-essential amino acids (100x)	Thermo Fisher, Waltham, MA, USA	11140-035
Nourseothricin	Jena Bioscience, Jena, Germany	AB-102L
OneTaq Quick Load 2X Master Mix with Standard Buffer	New England Biolabs, Ipswich, MA, USA	M0486S
Opti-MEM™ Reduced Serum Medium with GlutaMAX™ Supplement	Thermo Fisher, Waltham, MA, USA	51985026
OxyFluor™	Oxyrase Inc., Mansfield, OH, USA	OF-0005
Peptone	BD Biosciences, San Jose, CA, USA	211677
Plasmid Midi Kit	QIAGEN, Hilden, Germany	12143
Poly(ethylene glycol) 3350	Sigma-Aldrich, St. Louis, MO, USA	P3640
Potassium acetate	Merck, Darmstadt, Germany	104820
Potassium chloride	Merck, Darmstadt, Germany	104936
Potassium dihydrogen phosphate	Merck, Darmstadt, Germany	104873
Protocatechuate 3,4-Dioxygenase (PCD) from *Pseudomonas sp.*	Sigma-Aldrich, St. Louis, MO, USA	P8279
Pyranose oxidase	Sigma-Aldrich, St. Louis, MO, USA	P4234

Continued on the next page

Table 6.4 Continued from the previous page

Name	Supplier	Order number
Q5 polymerase	New England Biolabs, Ipswich, MA, USA	M0491S
QIAprep Spin Miniprep Kit	QIAGEN, Hilden, Germany	27106
S-(2-Aminoethyl)-L-cysteine hydrochlorid	Sigma-Aldrich, St. Louis, MO, USA	A2636
Salmon Sperm DNA	Sigma-Aldrich, St. Louis, MO, USA	D1626
SNAP-Surface® Alexa Fluor™ 647	New England Biolabs, Ipswich, MA, USA	S9136S
Sodium azide	Sigma-Aldrich, St. Louis, MO, USA	S2002
Sodium chloride	Merck, Darmstadt, Germany	106404
Sodium DL-lactate	Sigma-Aldrich, St. Louis, MO, USA	L1375
Sodium dodecyl sulfate (SDS)	Serva, Heidelberg, Germany	20765
Sodium sulfite	Merck, Darmstadt, Germany	106652
Sucrose	Sigma-Aldrich, St. Louis, MO, USA	S0389
TetraSpeck™ beads (0.1 µm)	Thermo Fisher, Waltham, MA, USA	T7279
Tris(2-hydroxyethyl)phosphine hydrochloride (TCEP)	Sigma-Aldrich, St. Louis, MO, USA	646547
Triton™ X-100	Sigma-Aldrich, St. Louis, MO, USA	X100
Trizma base	Sigma-Aldrich, St. Louis, MO, USA	T1503
Trolox	Merck, Darmstadt, Germany	238813
Tryptone	BD Biosciences, San Jose, CA, USA	211705
Uracil	Sigma-Aldrich, St. Louis, MO, USA	U0750
Velocity DNA polymerase	Bioline, Taunton, MA, USA	BIO-21098
Yeast extract	BD Biosciences, San Jose, CA, USA	212750
Yeast Nitrogen Base w/o amino acids	BD Biosciences, San Jose, CA, USA	291940
Yeast Nitrogen Base w/o amino acids and ammonium sulfate	BD Biosciences, San Jose, CA, USA	233520
ZellShield®	Minerva Biolabs, Berlin, Germany	13-0050

6.1.5 Consumables

Table 6.5 | List of consumables used in this work

Name	Supplier	Order number
6-Well cell culture plates	Thermo Fisher, Waltham, MA, USA	140675
96-Well, Flat-Bottom Microplate	Thermo Fisher, Waltham, MA, USA	167008
Amicon Ultra-15, PLBC Ultracel-PL Membran, 3 kDa	Merck, Darmstadt, Germany	UFC900324
Cellvis 96 Well Glass Bottom Black Plates #1.5H	IBL, Vienna, Austria	P96-1.5H-N
Coverslips No. 1.5H	Marienfeld, Lauda-Königshofen, Germany	117640
Parafilm	Bemis Company, Neenah, WI, USA	PM996
pH-Indicator Strips pH 0 - 14	Merck, Darmstadt, Germany	109535
pH-Indicator Strips pH 6.5 - 10.0	Merck, Darmstadt, Germany	109543
Vivaspin(R) 500 Centrifugal Concentrators 5000 MWCO PES	Sartorius, Göttingen, Germany	VS0111

6.1.6 Equipment

6.1.6.1 Microscopes

Standard microscope for localization microscopy (M2) Most of the localization microscopy data in this thesis was acquired on a custom-built setup that was published previously (Deschamps *et al.*, 2016). The specific components of the microscope are described in table 6.6.

The free output of the laser box was collimated and focused on the polymer diffuser of the speckle reducer. The booster laser was coupled in via a polarization beam splitter and focused onto the speckle reducer as well. The diverging beam was collimated again and focused on the input of a multi-mode fiber. This input was mounted on an xyz translational stage to optimize the coupling efficiency. For additional mixing of the laser modes, the 2 m long fiber was coiled. The output of the multi-mode fiber was magnified by an achromatic lens and guided through a laser clean-up filter to eliminate fiber-generated fluorescence. The laser beam was reflected into the 160× TIRF objective by a dichroic mirror and focused into the sample to homogeneously illuminate an area of about 1000 µm^2. Emitted fluorescence was collected by the objective and subsequently filtered by the corresponding band-pass filter for the respective excitation wavelength in the filter wheel. Finally, the image was focused onto the chip of the EMCCD (Electron-multiplying charge-coupled device) camera by a tube lens to yield an effective pixel size of 127 nm. For dual-color imaging, a dichroic mirror (640LP) was placed in the emission beam path to separate the emission of mMaple (reflected channel) and AF647 (transmitted channel). In this case, no filter was inserted via the filter wheel, but the filters were placed in the two channels individually. Then, the two channels were focused onto the camera and imaged side by side. The transformation of the two channels onto each other was performed in a post-processing step (see section 6.2.7.2). The system was equipped with an automatic focus stabilization. For this, an infrared-laser (785 nm) was coupled in via a dichroic mirror and totally internally reflected on the glass coverslip. This reflection was then detected by a quadrant photodiode which was in closed-loop feedback with the objective positioner. With this system, focal shifts were detected and corrected during the acquisition. A flip-in lens enabled imaging of the back focal plane (BFP) to visually inspect it for bubbles in the oil. All microscope components were controlled via a custom-written plug-in (an earlier version of the EMU software published in Deschamps and Ries, 2020) for µManager (Edelstein *et al.*, 2014). Within this plug-in, the amount of blinking molecules per frame was estimated by a simple algorithm. This number was compared to the input parameter of desired molecules and the pulse length of the 405 nm laser was controlled in a way to maintain this number throughout the experiment. The sample stage could be covered by a box that fitted on top of the main body of the microscope to maintain a constant temperature of the sample. This prevented thermal drift and effects on the photophysics of fluorescent proteins and dyes. Furthermore, this lid was equipped

Table 6.6 | Components of the standard microscope for SMLM (M2)

Component	Specification	Manufacturer
Laserbox	LightHub equipped with Luxx 405, 488 and 638	Omicron-Laserage Laserprodukte, Rodgau, Germany
	and Cobolt 561 lasers	Cobolt, Solna, Sweden
Booster laser	640 nm, iBeam Smart	Toptica, Gräfelfing, Germany
Speckle reducer	LSR-3005-17S-VIS	Optotune, Dietikon, Switzerland
Multi-mode fiber	M105L02S-A	Thorlabs, Newton, NJ, USA
New square multi-mode fiber	M103L05	Thorlabs, Newton, NJ, USA
Laser clean-up filter	390/482/563/640 HC Quad	AHF, Tübingen, Germany
Dichroic mirror below objective	TIRF Quad Line Beamsplitter zt405/488/561/640rpc	Chroma, Bellows Falls, VT, USA
Objective	HCX PL APO 160×/1.43 NA	Leica, Wetzlar, Germany
Piezo objective positioner	P-726	Physik Instrumente, Karlsruhe, Germany
Sample stage	HCU-3D	SmarAct, Oldenburg, Germany
Band-pass filters in filter wheel	525/50 (FF03-525/50-25) 600/60 (NC458462) 700/100 (ET700/100m)	Semrock, Rochester, NY, USA Chroma, Bellows Falls, VT, USA Chroma, Bellows Falls, VT, USA
Dichroic mirror in dual-color path	640LP (ZT640rdc)	Chroma, Bellows Falls, VT, USA
Bandpass filters in dual-color path	transmitted: 676/37 (FF01-676/37-25) reflected: 600/60 (NC458462)	Semrock, Rochester, NY, USA Chroma, Bellows Falls, VT, USA
EMCCCD camera	Evolve512D	Photometrics, Tucson, AZ, USA
Perfect-focus laser	iBeam Smart 785	Toptica, Gräfelfing, Germany
Perfect focus dichroic mirror	SP beam splitter T750SPXRXT	Chroma, Bellows Falls, VT, USA
Quadrant photodiode	SD197-23-21-041	Laser Components, Olching, Germany
Field-programmable gate array	Mojo	Alchitry (former: Embedded Micro), Littleton, CO, USA

with light-emitting diodes (LED) to obtain a bright-field image of the sample. All data that was not acquired with one of the following microscopes was acquired on this microscope.

Recently, the illumination was updated to a new method for scrambling the laser's modes (Schroeder *et al.*, 2019). For this, the free output of the laser box was focused on the input of a square multi-mode fiber. The fiber was intertwined with elastic rubber strings that were suspended in an aluminum box. Additionally, an imbalanced motor was attached to the strings whose vibrations scramble the laser's modes. The output of the fiber was guided through a cleanup-filter and laterally constricted by slits. Furthermore, the control software was updated to the latest version of EMU (Deschamps and Ries, 2020). All dual-color super-resolution data in the results chapter after section 3.4.4.2 were acquired with this new configuration.

Alternative microscope for localization microscopy (M1) The dual-color data in figures 3.3, 3.16, and 4.1 has been acquired with this microscope. The specific components of the microscope are described in table 6.7. The output of the commercial laser box was collimated, focused on the BFP of the TIRF objective, and adjusted for epi illumination. The emitted fluorescence was laterally constricted by a slit, split by a dichroic mirror, filtered by the respective bandpass filters, and imaged on two parts of the camera. The focus was stabilized as described for the system above.

Table 6.7 | Components of the alternative microscope used for localization microscopy (M1)

Component	Specification	Manufacturer
Lasers	iChrome MLE laser box (405 nm, 488 nm, 561 nm, 640 nm) coupled via single-mode for epi illumination	Toptica, Gräfelfing, Germany
	640 nm booster	Toptica, Gräfelfing, Germany
Objective	60× NA 1.49 TIRF	Nikon, Shinagawa, Tokyo, Japan
4× bandpass emission filter	FF01-446/523/600/677	Semrock, Rochester, NY, USA
Dichroic mirror in dual-color path	640LP (ZT640rdc)	Chroma, Bellows Falls, VT, USA
Bandpass filters in dual-color path	transmitted: 676/37 (FF01-676/37-25)	Semrock, Rochester, NY, USA
	reflected: 600/60 (NC458462)	Chroma, Bellows Falls, VT, USA
EMCCCD camera	iXON Ultra	Andor Technology, Belfast, United Kingdom

Primed conversion localization microscopy The primed conversion SMLM data with a 730 nm laser for conversion in figure 3.4 was acquired in Ulrike Endesfelder's lab at the Max Planck Institute for Terrestrial Microbiology in Marburg, Germany. The components of the microscope can be found in table 6.8. They were controlled using µManager (Edelstein *et al.*, 2014) and the camera had a pixel size of 129 nm.

Table 6.8 | Components of the microscope used for primed conversion (730 nm)

Component	Specification	Manufacturer
Body	Ti Eclipse	Nikon, Shinagawa, Tokyo, Japan
Lasers	405 nm OBIS	Coherent, Inc., Santa Clara, CA, USA
	561 nm OBIS	
	640 nm OBIS	
	730 nm OBIS	
	488 nm Sapphire	
AOTF	Modulation of laser intensity (except 730 nm)	Ilminster, United Kingdom
Objective	CFI Apo TIRF 100× oil objective (NA 1.49)	Nikon, Shinagawa, Tokyo, Japan
	Perfect Focus System	Nikon, Shinagawa, Tokyo, Japan
EMCCCD camera	iXON Ultra 888	Andor Technology, Belfast, United Kingdom

Spinning disc confocal microscopy The confocal imaging of yeast was performed on the commercial system iXplore SPIN SR spinning disc confocal microscope (Olympus, Shinjuku, Tokyo, Japan) in EMBL's Advanced Light Microscopy Facility. The components of the microscope can be found in table 6.9. The data in figures 3.22, 3.23, and 3.24 have been acquired on this microscope.

Table 6.9 | Components of the iXplore SPIN SR spinning disc confocal microscope

Component	Specification	Manufacturer
Body	IX83 P2ZF	Olympus, Shinjuku, Tokyo, Japan
Objective	UPLSAPO 100× silicon oil (NA 1.35)	Olympus, Shinjuku, Tokyo, Japan
Stage	M-MS-IX3-2	Märzhäuser, Wetzlar, Germany
Laser	100 mW 488 nm DPSS	Coherent, Inc., Santa Clara, CA, USA
	100 mW 640 nm diode	
Transmitted illumination	IX3-LHLEDC white LED	Olympus, Shinjuku, Tokyo, Japan
Main dichroic	D405/488/561/640	Hamamatsu Photonics, Hamamatsu, Shizuoka, Japan
Filters	525/50	Hamamatsu Photonics, Hamamatsu, Shizuoka, Japan
	685/40	
Confocal scanner	CSUW1-TS 2D 50 µm	Yokogawa, Musashino, Tokyo, Japan
Cameras	2× ORCA-Flash4.0 V3 (6.5 µm pixel size)	Hamamatsu Photonics, Hamamatsu, Shizuoka, Japan

6.1.6.2 List of other equipment

Table 6.10 | List of equipment used in this work

Item	Supplier
Certomat BS-1 Incubation Shaking Cabinet	Sartorius, Göttingen, Germany
Dissection Microscope MSM 400	Singer Instruments, Watchet, UK
Midi 40 Cell Culture Incubator	Thermo Fisher, Waltham, MA, USA
Optima L-100 XP ultracentrifuge	Beckman Coulter, Brea, CA, USA
Plasma Prep 2 Plasma Cleaner	GaLa Instrumente, Bad Schwalbach, Germany
Poly-Prep® Chromatography Columns	Bio-Rad Laboratories, Hercules, CA, USA
Portable Photometer Ultrospec™ 10	Biochrom, Holliston, MA, USA
Synergy 4 Microplate Reader	Biotek, Winooski, VT, USA
Type 45 Ti Rotor	Beckman Coulter, Brea, CA, USA
Ultrospec 2100 pro Spectrophotometer	Amersham Biosciences, Little Chalfont, UK
70 mL Polycarbonate Tubes (Cat# 355622)	Beckman Coulter, Brea, CA, USA

6.1.7 Buffers, solutions and media

If not stated differently, all buffers, solutions and media were prepared with Milli-Q® ultrapure water.

6.1.7.1 Buffer, solutions and media for bacteria

Ampicillin 1000× stock solution	
10 % [w/v]	Ampicillin sodium salt in 70 % [v/v] EtOH

CCMB80 buffer	
10 mM	KOAc pH 7.0
80 mM	$CaCl_2 \cdot 2\ H_2O$
20 mM	$MnCl_2 \cdot 4\ H_2O$
10 mM	$MgCl_2 \cdot 6\ H_2O$
10 % [v/v]	Glycerol

Kanamycin 2000× stock solution	
8 % [w/v]	Kanamycin A

LB medium (Miller)	
0.5 % [w/v]	Yeast extract
1 % [w/v]	Tryptone
0.5 % [w/v]	NaCl

LB plates (Lennox)	
0.5 % [w/v]	Yeast extract
1 % [w/v]	Tryptone
1 % [w/v]	NaCl
1.5 % [w/v]	Bacto agar (for plates)

SOB medium	
0.5 % [w/v]	Yeast extract
2 % [w/v]	Tryptone
10 mM	NaCl
2.5 mM	KCl

SOC medium

0.5 % [w/v]	Yeast extract
2 % [w/v]	Tryptone
10 mM	NaCl
2.5 mM	KCl
1 mM	$MgCl_2$
10 mM	$MgSO_4$
0.4 % [w/v]	D-Glucose

6.1.7.2 Buffer, solutions and media for yeast strain maintenance and creation

Amino acid mix for synthetic complete media

0.5 g	Adenine
2 g	L-Alanine
2 g	4-Aminobenzoic acid
2 g	L-Arginine
2 g	L-Asparagine
2 g	L-Aspartic acid
2 g	L-Cysteine hydrochloride monohydrate
2 g	L-Glutamine
2 g	L-Glutamic acid
2 g	Glycine
2 g	L-Histidine
2 g	*myo*-Inositol
2 g	L-Isoleucine
10 g	L-Leucine
2 g	L-Lysine monohydrochloride
2 g	L-Methionine
2 g	L-Phenylalanine
2 g	L-Proline
2 g	L-Serine
2 g	L-Threonine
2 g	L-Tryptophan
2 g	L-Tyrosine
2 g	Uracil
2 g	L-Valine

Amino acid solution for synthetic complete media

2 % [w/v]	Amino acid mix for synthetic complete media w/o the respective amino acids

Amino acid solution for sporulation plates

0.2 % [w/v]	Uracil
0.3 % [w/v]	L-Leucine
0.3 % [w/v]	L-Lysine monohydrochloride
0.2 % [w/v]	L-Histidine
0.2 % [w/v]	L-Methionine

Canavanine 1000× stock solution

5 % [w/v]	L-Canavanine sulfate salt

G418 1000× stock solution

10 % [w/v]	Geneticin (G418 sulfate) in PBS

Hygromycin B 166× stock solution

5 % [w/v]	Hygromycin B

LiOAc-SDS solution

200 mM	Lithium acetate dihydrate
1 % [w/v]	Sodium dodecyl sulfate (SDS)

Lyticase solution

0.1 % [w/v]	Lyticase

Nourseothrycin 1000× stock solution

10 % [w/v]	Nourseothrycin

PEG solution

100 mM	Lithium acetate
10 mM	Tris-HCl pH 8
1 mM	EDTA pH 8
4 % [w/v]	PEG 3350

SC (Synthetic complete) -HIS selective plates

10 % [v/v]	Amino acid solution for SC media -HIS
2 % [w/v]	D-Glucose
0.67 % [w/v]	Yeast Nitrogen Base w/o amino acids
2 % [w/v]	Bacto agar

SC -LEU selective plates

10 % [v/v]	Amino acid solution for SC media -LEU
2 % [w/v]	D-Glucose
0.67 % [w/v]	Yeast Nitrogen Base w/o amino acids
2 % [w/v]	Bacto agar

SGA selective plates

10 % [v/v]	Amino acid solution for SC media -ARG -LYS -HIS/-LEU
2 % [w/v]	D-Glucose
0.17 % [w/v]	Yeast Nitrogen Base w/o amino acids and ammonium sulfate
0.1 % [w/v]	Monosodium glutamic acid
2 % [w/v]	Bacto agar
0.1 % [v/v]	Canavanine 1000× stock solution
0.1 % [v/v]	Thialysine 1000× stock solution
0.3 % [v/v]	Hygromycin B 166× stock solution
0.1 % [v/v]	G418 1000× stock solution
0.1 % [v/v]	Nourseothrycin 1000× stock solution

Solution A (for genomic DNA extraction)

50 mM	Tris-HCl pH 7.5
10 mM	EDTA pH 8
0.3 % [v/v]	2-Mercaptoethanol
0.05 % [w/v]	Lyticase

SORB solution

100 mM	Lithium acetate
10 mM	Tris-HCl pH 8
1 mM	EDTA pH 8
1 M	Sorbitol

Sporulation plates

0.25 % [v/v]	Amino acid solution for sporulation plates
1 % [w/v]	Potassium acetate
2 % [w/v]	Bacto agar

SC plates

10 % [v/v]	Amino acid solution for SC media
2 % [w/v]	D-Glucose
0.67 % [w/v]	Yeast Nitrogen Base w/o amino acids
2 % [w/v]	Bacto agar

Thialysine 1000× stock solution

5 % [w/v]	S-(2-Aminoethyl)-L-cysteine hydrochlorid

YPAD (Yeast extract Peptone Adenine Dextrose) medium (plates)

1 % [w/v]	Yeast extract
2 % [w/v]	Bacto peptone
0.004 % [w/v]	Adenine hemisulfate
2 % [w/v]	D-Glucose
2 % [w/v]	Bacto agar (for plates)

6.1.7.3 Buffer, solutions and media for protein production & purification

10× FB salts

0.17 M	KH_2PO_4
0.72 M	K_2HPO_4

Ni-Lysis buffer

50 mM	Tris-HCl pH 8 (4 °C)
300 mM	NaCl
20 mM	Imidazole

TB-FB medium

2.4 % [w/v]	Yeast extract
1.2 % [w/v]	Tryptone
0.4 % [v/v]	Glycerol
	pH adjusted to 7.2
10 % [v/v]	10× FB salts (added after separate autoclaving)

TB-FB auto-induction medium

1 L	TB-FB medium
75 mL	20 % [w/v] Lactose
2.5 mL	20 % [w/v] Glucose
2 mL	1 M $MgSO_4$

6.1.7.4 Buffer, solutions and media for yeast sample preparation

ConA solution

0.4 % [w/v]	Concanavalin A
	in PBS

Formaldehyde (FA) fixation solution

4 % [w/v]	Formaldehyde (from 37 %, MeOH stabilized)
2 % [w/v]	Sucrose
	in PBS

PBS

2.7 mM	KCl
1.5 mM	KH_2PO_4
8.1 mM	Na_2HPO_4
137 mM	NaCl

Quenching solution

100 mM	Ammonium chloride
	in PBS

Permeabilization and blocking solution

50 % [v/v]	Image-iT™ FX Signal Enhancer
0.25 % [v/v]	Triton™ X-100
	in PBS

SNAP-tag staining solution

1 µM	SNAP Surface® Alexa Fluor 647™
1 % [w/v]	BSA
0.25 % [v/v]	Triton™ X-100
1 mM	DTT
	in PBS

6.1.7.5 Buffer, solutions and media for mammalian sample preparation

Fixation solution

2.4 % [w/v]	Formaldehyde (from 16 % [w/v] stock solution)
	in PBS

Permeabilization solution

0.4 % [v/v]	Triton™ X-100
	in PBS

Quenching solution

100 mM	Ammonium chloride
	in PBS

Staining solution

1 µM	SNAP Surface® Alexa Fluor™ 647
1 mM	DTT
0.5 % [w/v]	BSA
	in PBS

6.1.7.6 Imaging buffers

GLOX buffer (Heilemann *et al.*, 2005)

50 mM	Tris-HCl pH 8
10 mM	NaCl
100 U mL^{-1}	Glucose oxidase
0.004 % [w/v]	Catalase
10 % [w/v]	D-Glucose
35 mM	Cysteamine

GLOX buffer with higher buffer capacity

150 mM	Tris-HCl pH 8
10 mM	NaCl
100 U mL^{-1}	Glucose oxidase
0.004 % [w/v]	Catalase
10 % [w/v]	D-Glucose
35 mM	Cysteamine

GLOX buffer with D_2O (Klehs *et al.*, 2014)

50 mM	Tris-HCl pH 8
10 mM	NaCl
100 U mL^{-1}	Glucose oxidase
0.004 % [w/v]	Catalase
10 % [w/v]	D-Glucose
20 mM	Cysteamine
	in 90 % [w/v] D_2O

OxEA buffer (Nahidiazar *et al.*, 2016)

50 mM	Cysteamine
3 % [v/v]	OxyFlour™
20 % [v/v]	Sodium DL-lactate
	in PBS, pH adjusted to 8 to 8.5 with NaOH

PCD buffer (Patil and Ballou, 2000; Aitken *et al.*, 2008; Shi *et al.*, 2010)

50 mM	Tris-HCl pH 8
10 mM	NaCl
50 nM	Protocatechuate 3,4-dioxygenase (PCD), dissolved in 100 mM Tris-HCl pH 8, 50 mM KCl, 1 mM EDTA, 50 % [w/v] glycerol
2.5 mM	3,4-Dihydroxybenzoic acid (PCA)
2 mM	1,3,5,7-Cyclooctatetraene (COT)
10 mM	Cysteamine

POX buffer (Swoboda *et al.*, 2012)

50 mM	Tris-HCl pH 8
10 mM	NaCl
3.125 U mL^{-1}	Pyranose oxidase
0.004 % [w/v]	Catalase
10 % [w/v]	D-Glucose
35 mM	Cysteamine

Sulfite buffer (Hartwich *et al.*, 2018)

10 to 50 mM	Sodium sulfite
10 to 35 mM	Cysteamine
	in PBS

Sulfite Tris buffer

50 mM	Sodium sulfite
50 mM	Tris-HCl pH 8
10 to 35 mM	Cysteamine

Sulfite Tris buffer with 2-Mercaptoethanol

50 mM	Sodium sulfite
50 mM	Tris-HCl pH 8
72 or 143 mM	2-Mercaptoethanol

Tris D_2O buffer (Ong *et al.*, 2015)

50 mM	Tris-HCl pH 8
95 % [v/v]	D_2O

Tris H_2O buffer

50 mM	Tris-HCl pH 8

6.2 Methods

6.2.1 Molecular biology

6.2.1.1 PCR

Preparative polymerase chain reactions (PCR) for molecular cloning and yeast transformation were performed with either the Velocity, Q5, or Phusion polymerase.

Velocity polymerase Amplification of DNA fragments with the Velocity polymerase was performed with the reaction mix described in table 6.11 and the PCR program specified in table 6.12.

Table 6.11 | Composition of the PCR reaction for the Velocity polymerase

Component	Volume [µL]
5× reaction buffer	10
50 mM $MgCl_2$	2
10 mM dNTP	1.25
10 µM forward primer	2.5
10 µM reverse primer	2.5
DNA (100 ng μL^{-1})	1
Velocity polymerase	0.25
dH_2O	30.5
DMSO (if needed)	1.5

Table 6.12 | PCR program used to amplify DNA fragments with the Velocity polymerase

Step		Temperature [°C]	Time [s]
Initial denaturation		98	120
35 cycles	Denaturation	98	30
	Annealing	56 (for S2/S3)	30
	Extension	72	30 s kb^{-1}
Final extension		72	180
Hold		4	∞

Q5 polymerase For amplification of DNA fragments with the Q5 polymerase, the reaction mix (table 6.13) was subjected to the program described in table 6.14.

Phusion polymerase Moreover, DNA fragments were amplified by the Phusion polymerase for which the Protein Expression and Purification Core Facility at EMBL provides a master mix. The reaction was assembled as in table 6.15 and run in a thermocycler according to the program in table 6.16.

Table 6.13 | Composition of the PCR reaction for the Q5 polymerase

Component	Volume [µL]
5× Q5 reaction buffer	10
10 mM dNTP	1
10 µM forward primer	2.5
10 µM reverse primer	2.5
DNA (100 ng μL^{-1})	1
Q5 polymerase	0.5
dH_2O	30.5
DMSO (if needed)	2

Table 6.14 | PCR program used to amplify DNA fragments with the Q5 polymerase

Step		Temperature [°C]	Time [s]
Initial denaturation		98	30
35 cycles	Denaturation	98	30
	Annealing	According to NEB Tm calculator	30
	Extension	72	20-30 s kb^{-1}
Final extension		72	180
Hold		23	∞

Table 6.15 | Composition of the PCR reaction for the Phusion polymerase

Component	Volume [µL]
2× Phusion master mix	25
10 µM forward primer	2.5
10 µM reverse primer	2.5
DNA (100 ng μL^{-1})	1
dH_2O	19

Table 6.16 | PCR program used to amplify DNA fragments with the Phusion polymerase

Step		Temperature [°C]	Time [s]
Initial denaturation		98	30
35 cycles	Denaturation	98	10
	Annealing	According to NEB Tm calculator	30
	Extension	72	15-30 s kb^{-1}
Final extension		72	300
Hold		23	∞

6.2.1.2 AQUA cloning & Gibson assembly

New plasmids were generated by dividing the plasmid into 2-4 segments that were individually amplified by PCR (see 6.2.1.1) with overhangs of 35 bp. The individual fragments were subjected to agarose gel electrophoresis and subsequently purified from excised gel pieces. The purified DNA segments were mixed in a volume of 5 µL in a molar ratio so that the smaller fragments were 2-3 times as abundant as the largest one. The resulting amount of DNA was in the range of 200 to 500 ng. The mixture of DNA was either mixed with water and incubated for 1 h at room temperature (RT) or mixed with 2× NEBuilder mix and incubated for 30 min at 50 °C. The former is also referred to as *AQUA cloning* (Beyer *et al.*, 2015) and was used for the assembly of up to 3 individual fragments, for more complicated assemblies the enzymatic reaction was preferred. To decrease the occurrence of false positive colonies in the subsequent bacterial transformation, the bacterial antibiotic marker was split into different fragments (using the primers oPH015 and oPH016, see 6.1.1).

6.2.1.3 Preparation of chemically competent *E. coli* cells

All glassware was filled to 3/4 with ultrapure water and autoclaved before use to eliminate residual detergent. A 1 mL seed stock of Mach1™ T1 (provided by the Neveu lab at EMBL) was thawed at RT and used to inoculate an overnight culture of 100 mL SOB medium which was grown at 30 °C. The main culture (1 L SOB) was inoculated the next morning with 10 mL of the overnight culture. The optical density at 600 nm (OD_{600}) was measured repeatedly until a value of 0.2 to 0.3 was reached. Then, the culture was spun down in a precooled centrifuge (2250 × g at 4 °C for 10 min). The resulting pellet was resuspended in 10 mL ice-cold CCMB80 buffer and filled up to reach an OD_{600} of 5.0 to 7.5. Finally, the competent cells were aliquoted (100 µL), flash frozen in liquid nitrogen, and stored at −80 °C.

6.2.1.4 Bacterial transformation

An aliquot of chemically competent *E. coli* cells (see 6.2.1.4) was thawed on ice. Next, 2 µL of the AQUA cloning or NEBuilder (see 6.2.1.2) was added to 50 µL of competent cells, mixed by flicking the tube and incubated for 15 min on ice. After a heat shock at 42 °C for 45 s, the cells were placed on ice again for 5 min. For recovery, 950 µL of SOC medium were added and the cells were incubated shaking at 1000 rpm and 37 °C for 1 h. The cells were spun down (800 × g at RT for 5 min), resuspended in about 200 µL of residual medium, plated with glass beads on plates supplemented with the appropriate antibiotic, and incubated overnight at 37 °C.

6.2.1.5 Colony PCR, plasmid isolation, and Sanger sequencing

Colony PCR For experiments where the newly cloned plasmid was distinguishable from the mother plasmid by PCR with available primers, a colony PCR was

performed. For this, the PCR reaction was prepared as described in table 6.17. Initially, only water and primers were mixed, a colony was dipped in and streaked on a new LB plate supplemented with the appropriate antibiotic. Then, the master mix was added and the PCR was carried out (program see table 6.18) before it was analyzed on an agarose gel.

Table 6.17 | Composition of the PCR reaction for colony PCR with the OneTaq Quick Load 2× Master Mix

Component	Volume [µL]
2× OneTaq master mix	10
10 µM forward primer	1
10 µM reverse primer	1
dH_2O	8

Table 6.18 | Colony PCR program used with the OneTaq Quick Load 2× Master Mix

Step		Temperature [°C]	Time [s]
Initial denaturation		94	300
30 cycles	Denaturation	94	30
	Annealing	According to NEB Tm calculator	30
	Extension	68	60
Final extension		68	300
Hold		23	∞

Plasmid isolation For positive colonies and plasmids where a colony PCR was not suitable, a 4 mL overnight culture in LB medium supplemented with the appropriate antibiotic was grown. The next morning, it was spun down (16 800 × g at RT for 1 min). Then, the plasmids were isolated according to the protocol of the commercial Miniprep kit. For transfection in mammalian cells, plasmids were purified from a 50 mL culture using a commercial Midiprep kit according to the included protocol.

Sanger sequencing Candidate plasmids were then sent for Sanger sequencing and checked for mutations in the coding regions and the overlaps of Gibson assembly.

6.2.1.6 Bacterial stock preparation

One positive clone for each new plasmid was grown overnight in LB medium at 37 °C. From this culture, 750 µL were mixed with 750 µL of 80 % [v/v] glycerol. The mixture was left at RT for about 30 min to allow uptake of glycerol by the cells and subsequently frozen and stored at −80 °C.

6.2.2 Yeast biology

6.2.2.1 Yeast strain creation

Most yeast strains were generated by consecutive rounds of transformation (see section 6.2.2.3). The strain yPH083 was generated by mating of yPH073 and the MK0102 wild-type strain, yPH132 was generated by mating of yPH073 and yPH081 (see section 6.2.2.4). Moreover, the strains yPH341 to yPH346 have been generated by manual SGA (see section 6.2.2.9). All tags had the linker sequence RTLQVD (S3 primer) and 5×GA, except for the 17×Linker strains, where instead of the 5×GA linker the sequence SGGGGGSGGGSGGGGAS was introduced (Haruki *et al.*, 2008). This linker is referred to as 17×Linker in this work.

6.2.2.2 Preparation of competent yeast cells

An overnight culture from a single colony of the respective strain (freshly thawed or from a very recent plate) was grown in 10 mL YPAD at 30 °C and 200 rpm shaking. The next morning, the culture was diluted to an OD_{600} of 0.2 and grown for about 3 h to reach a final OD_{600} of 0.5 to 0.7. Then, the culture was spun down (200 × g at RT for 5 min), washed with 10 mL of ultrapure water, and spun down again with the same settings. After another wash with 5 mL of SORB solution and centrifugation with the above settings, the pellet was resuspended in 360 µL of SORB solution. Next, 40 µL of previously boiled (95 °C for 10 min) salmon sperm DNA were added. The mixture was aliquoted (50 µL) and stored at −80 °C without shock freezing.

6.2.2.3 Yeast transformation

For C-terminal tagging of target proteins, the S2/S3 system was used (Janke *et al.*, 2004). In short, primers were designed that have 50 bp homology with the gene of interest and bind to the S2/S3 sites surrounding the protein tag and the selection cassette in the respective plasmid from the pFA6a series (see section 6.1.1 for the different primers and section 6.1.2 for the plasmids). The respective DNA fragment was amplified by PCR (see section 6.2.1.1 for PCR protocols) and checked for the correct size by analytical gel electrophoresis.

Per transformation reaction, one aliquot of competent yeast cells (see section 6.2.2.2) was thawed at RT and mixed with 10 µL of the unpurified PCR reaction. After addition of 360 µL of PEG (polyethylene glycol) solution and mixing by pipetting, the transformation reaction was incubated at RT for 30 min. Next, 47 µL of DMSO (dimethyl sulfoxide) were added followed by mixing by pipetting. The yeast cells were heat-shocked at 42 °C for 15 min. Then, the transformation reaction was centrifuged twice while turning the reaction tube between runs to get a nice pellet (200 to 350 × g). Subsequently, most of the supernatant was removed with a blue tip to not disturb the pellet. The gentle centrifugation was repeated as before and the remaining supernatant removed with a yellow tip. For auxotrophic markers

(HIS3MX6, LEU2), the pellet was resuspended in 150 to 200 µL of 1 M sterile sorbitol and distributed on the respective plate using glass beads. When an antibiotic marker (hphNT1, natNT2, kanMX4) was used, the pellet was resuspended in 500 µL of YPAD, mixed with 4.5 mL of YPAD and recovered for 3 to 4 h at 30 °C and 200 rpm shaking. Then, the yeast cells were pelleted (500 × g at RT for 5 min), resuspended in 150 to 200 µL of 1 M sterile sorbitol, and spread on plates supplemented with the appropriate antibiotic. After 2 to 3 d at 30 °C single colonies could be observed, which were validated by colony PCR (see section 6.2.2.5) and imaging.

6.2.2.4 Mating of yeast

For mating of yeast, each of the respective strains was freshly thawed from a glycerol stock or freshly restreaked if it had been generated recently. Then, one colony of each strain was mixed on a new YPAD plate in a thumbnail-sized spot. After about 4 h of mating, a small amount of yeast was recovered, resuspended in 50 µL of YPAD, spread out at the top of a fresh YPAD plate, and allowed to dry. Using a dissection microscope, zygotes were picked and separated on a grid at the lower part of the plate. After 1 to 2 d of recovery at 30 °C, the diploid colonies were spread on a thumbnail-sized spot on a sporulation plate. After 7 to 14 d of sporulation at 23 °C, a small amount of yeast was recovered, resuspended in 40 µL of YPAD mixed with 10 µL of lyticase solution to digest the ascus surrounding the tetrads. Incubation times varied between 5 to 10 min and were optimized each time for dissectable tetrads. Next, the mixture was spread out at the top of a fresh YPAD plate and subjected to dissection. Typically, 10 tetrads were dissected per diploid and there were 2 to 3 diploids dissected per mating. The dissected tetrads were grown to single colonies for 1 to 2 d at 30 °C. To determine the genotype of the individual haploid tetrads, the plate was replicated on selective plates for the respective cassettes of the maternal strains. The mating type was determined by replication on two synthetic complete plates where on each plate a complementary tester strain with either mating type MATa or MATα, respectively, was spread out. Alternatively, the mating type was identified by PCR (Illuxley *et al.*, 1990).

6.2.2.5 Yeast colony PCR

To test for integration of the tagging cassettes at the correct position in the yeast genome, a colony PCR was performed on six colonies per strain (see table 6.17 for composition and table 6.18 for the PCR program). A tiny amount of yeast from individual colonies was added to the mixture of water and primers (before addition of the master mix) and subsequently restreaked on a fresh selective plate. The forward primer used was binding at the 3′ end of the cassette, whereas the reverse primer was binding downstream of the gene of interest (in the 3′ untranslated region; see section 6.1.1 for primers). The size of the resulting amplicons (200 to 500 bp) was analyzed by agarose gel electrophoresis. Based on these results together with

visual inspection of the growth of transformants (to exclude small colony variants), a clone was selected and furthermore confirmed by fluorescence or super-resolution microscopy.

6.2.2.6 Yeast genomic DNA extraction

For amplification of longer DNA segments, genomic DNA was extracted using a lithium acetate & SDS-based protocol (Lõoke *et al.*, 2011). First, one yeast colony from a plate was resuspended in 100 µL of LiOAc-SDS solution. Alternatively, 100 to 200 µL of liquid yeast culture (OD_{600} = 0.4) was spun down (200 × g at RT for 5 min) and resuspended. The cells were incubated at 70 °C for 5 min. Subsequently, 300 µL of 100 % ethanol were added, the solution was vortexed and centrifuged (15 000 × g at RT for 3 min). The pellet was washed with 70 % [v/v] ethanol and afterwards resuspended in dH_2O. The undissolved debris was pelleted (15 000 × g at RT for 3 s) and 1 µL of the supernatant was used for amplification by PCR.

When higher quality genomic DNA was needed (e.g., if the PCR with the previous protocol failed or if the PCR was subsequently sequenced), the following method was used. It is based on a protocol from the labs of Nikolaus Pfanner (Albert-Ludwigs-Universität Freiburg, Germany) and Bernard Guiard (Centre de Génétique Moléculaire, CNRS, Gif-sur-Yvette, France). The volume equivalent to 3.5 OD_{600} of yeast was pelleted (16 800 × g at RT for 1 min), resuspended in 150 µL of Solution A, and incubated at 37 °C for 1 h with shaking. To the solution, 20 µL of 10 % [w/v] SDS was added and the mixture was vortexed. Proteins were precipitated by addition of 100 µL of 8 M ammonium acetate, vortexing and subsequent incubation at −20 °C for 15 min. The precipitate was pelleted by centrifugation (16 800 × g at 4 °C for 15 min). From the supernatant, 180 µL were transferred to a new reaction tube and mixed with 120 µL of isopropanol. The precipitated DNA was pelleted (16 800 × g at 4 °C for 15 min), washed with 70 % [v/v] ethanol, and spun again (16 800 × g at 4 °C for 15 min). The pellet was dried and resuspended in 20 to 30 µL of 10 mM Tris-HCl pH 8.5, of which 1 to 2 µL were used per PCR reaction.

6.2.2.7 Yeast growth assay on plates

The respective yeast strains were grown in a 10 mL YPAD culture at 30 °C and 200 rpm during the day. In the evening, the OD_{600} of the culture was measured and diluted to 0.001 in 10 mL YPAD. After overnight growth at 30 °C and 200 rpm, the OD_{600} was measured again. 1 OD_{600} of yeast cells was spun down (200 × g at RT for 5 min) and resuspended in 1 mL of dH_2O. Serial dilutions with OD_{600} of 0.1, 0.01, 0.002, 0.0004, and 0.0002 in dH_2O were prepared and 5 µL each were dropped onto YPAD agar plates. The plates were incubated at 23 °C, 30 °C, and 37 °C until adequate growth (typically 2 to 3 d) was observed and subsequently photographed with a mobile phone.

6.2.2.8 Yeast growth assay in liquid culture

For liquid growth assays, the respective strains were inoculated in 5 mL YPAD in the morning and grown during the day at 30 °C and 200 rpm. In the evening, the OD_{600} of the culture was measured and diluted to 0.2 with YPAD in a first step. Then the OD_{600} was measured again and diluted to 0.1 with YPAD. The dilution in two steps assured that measurement errors due to different optical densities in the day cultures were not present in the final dilutions. From these dilutions, 200 µL were pipetted in triplicate into a 96-well plate. The plate was incubated overnight in a microplate reader at 30 °C without shaking and the OD_{600} was measured every 15 min.

6.2.2.9 Manual synthetic genetic arraying

The SGA was performed in the background of BY4741 (Winston *et al.*, 1995) and its query strain Y8205 (Tong and Boone, 2006) according to Tong and Boone (2007). In a first step, either Sac6, End3, or Las17 were tagged with the $SNAP_f$ tag in BY4741 (yPH288, yPH289, and yPH290) by using the kanMX4 cassette as the selectable marker. Based on these strains and BY4741, all *coat strains* were generated by tagging Yap1801, End3, Sla1, Ent1, Pan1, or Sla2 with mMaple3 (yPH298 to yPH320; selectable marker: natNT2). In parallel, the different *base strains* were generated in the Y8205 background by tagging Lsb3, Vrp1, Las17, Bzz1, Myo5, Bbc1, or Myo3 with mMaple3 (yPH291 to yPH297; selectable marker: hphNT1). The respective *coat* and *base strains* were streaked in parallel stripes on individual large YPAD plates (Fig. 3.21) resulting in four plates with *coat strains* in the different backgrounds and one plate for the *base strains*. After 1 d of growth at 30 °C, the respective plates were replicated onto a new YPAD plate for mating. Each of the four plates with *coat strains* was combined with the plate with *base strains* turned by 90° (Fig. 3.21). After mating for 1 d at 30 °C, diploid cells were selected by replication on a YPAD plate supplemented with G418, nourseothricin, and hygromycin B for 1 d at 30 °C. The diploid selection was repeated once to eliminate all remaining haploid cells. Next, the diploid cells were replicated onto a mating plate and incubated for 4 to 8 d at 23 °C. The triple-tagged haploid cells were obtained by replication on the respective selective plates (see section 6.1.7.2). The correct triple-tagging and mating type was checked for a few selected strains by colony PCR.

6.2.2.10 Yeast stock preparation

For the preparation of yeast stocks for long-term storage, 500 µL of 50 % [v/v] glycerol was added in 2 mL cryovials and autoclaved. For the respective strain, a 5 mL overnight culture was grown at 30 °C and 200 rpm. After the culture was let sediment for about 1 h at RT, 1 mL of the culture was pipetted from the bottom and added to the glycerol in the cryovial (16.67 % [v/v] final concentration of glycerol). The yeast stocks were frozen and stored at −80 °C without shock freezing.

6.2.3 Protein biochemistry

6.2.3.1 Purification of SpyCatcher

Codon-optimized SpyCatcher with a serine to cysteine modification (S35C), an N-terminal hexahistidine tag followed by a linker and a TEV cleavage site and overhangs complementary to pETM-11 on both the 5'- and 3'-end was ordered as custom-synthesized double-stranded DNA (GeneArt Strings™, Life Technologies GmbH, Darmstadt, Germany). The DNA block was inserted into pETM-11 (Dümmler *et al.*, 2005) using AQUA cloning (see section 6.2.1.2) resulting in the plasmid pPH007. The plasmid pPH007 was transformed into BL21-Gold(DE3) competent *E. coli* cells by electroporation and the bacteria were plated on an agar plate supplemented with kanamycin.

The protein was expressed and purified by Nikolay Dobrev in EMBL's Protein Expression and Purification Core Facility. First, an overnight culture was started from a single colony in LB medium supplemented with 2 mM $MgSO_4$ and 30 µg mL^{-1} kanamycin, which was incubated overnight at 37 °C and shaken at 180 rpm. In the morning, the culture was used to inoculate a 1 L culture in a 5 L flask with TB-FB auto induction medium at a ratio of 1:100, and incubated at 37 °C and 200 rpm until the OD_{600} reached a value of 0.8. Next, the temperature was shifted to 18 °C and the protein production was performed overnight (18 h). The culture was harvested by centrifugation at 4000 × g and 4 °C for 30 min, and the bacterial pellet was directly used for protein purification. The pellet was resuspended in Ni-Lysis buffer supplemented with cOmplete™ EDTA-free protease inhibitor cocktail and disrupted by using a microfluidizer. The system was cooled down using a mixture of water and ice to prevent overheating of the sample during the lysis. In total, 5 cycles were performed to lyse the cells. Next, the lysate was cleared by centrifugation at 50 000 × g and 4 °C for 30 min using 70 mL polycarbonate tubes and a 45 Ti Rotor in an Optima L-100 XP ultracentrifuge.

The SpyCatcher protein was purified by standard immobilized metal affinity chromatography protein purification procedures using 20 mL Poly-Prep® chromatography columns containing 0.5 mL Ni-NTA agarose pre-equilibrated with wash buffer. The protein was loaded onto the column and washed with 20 column volumes of Ni-Lysis buffer. The bound protein was eluted by on-column TEV cleavage (incubation with 0.2 mg GST-TEV protease in 2.5 mL Ni-Lysis buffer for 2 h at 8 °C) and the GST-tagged TEV protease was subsequently removed by running the eluate over a GSH affinity column. Finally, the SpyCatcher protein was further purified by size exclusion chromatography using a S75 16/60 column. The fractions containing the monomeric protein were pooled together and concentrated up to 6.06 mg mL^{-1} in 1.8 mL using Amicon Ultra 15 mL centrifugal filters with 3 kDa cutoff. The final protein sample was in a buffer containing 20 mM HEPES pH 8.0 and 300 mM NaCl.

6.2.3.2 Labeling of SpyCatcher

The labeling of SpyCatcher with the fluorophore AF647 was performed by Eric Maurer, an intern I supervised. First, 6 µL of 1 M HEPES was added to 160 µL of the purified SpyCatcher (≈ 1 mg) to adjust the pH to about 6.5 to 7.0. Then, SpyCatcher was reduced for 2 h at RT by addition of 16 µL of 500 mM TCEP (≈ 100× molar excess) and kept under argon to prevent reoxidation. The coupling reaction was performed by addition of 80 µL of maleimide-AF647 (10 mM; dissolved in anhydrous DMSO) which corresponds to ≈ 10× molar excess. The reaction was incubated overnight at 4 °C under argon. The next morning, the coupling reaction was quenched by addition of 8 µL of 1 M DTT (Dithiothreitol; ≈ 10× molar excess compared to maleimide-AF647) and incubation for 2 h at RT. Labeled SpyCatcher was washed in its original buffer (20 mM HEPES pH 8.0 and 300 mM NaCl) in a concentrator to remove excess dye, DMSO, TCEP, and DTT. Finally, the protein was again purified by size exclusion chromatography to fully remove unbound maleimide-AF647. The degree of labeling was determined based on the theoretical extinction coefficient of SpyCatcher using two different nanodrop devices. The results were 17.6 % and 12.4 %, respectively.

6.2.4 Mammalian cell culture

The NPC cell lines (U2OS Nup107-SNAP$_f$ and U2OS Nup96-SNAP$_f$) have been generated in collaboration between our lab and the Ellenberg lab at EMBL (Li *et al.*, 2018; Thevathasan *et al.*, 2019). In short, using CRISPR-Cas9 technology (Koch *et al.*, 2018), the respective genes have been endogenously and homozygously tagged with the SNAP$_f$-tag (Sun *et al.*, 2011) in the U2OS cell line (Ponten and Saksela, 1967). The cell lines were cultured under adherent conditions in Dulbecco's Modified Eagle Medium (DMEM) supplemented with 10 % [v/v] fetal calf serum, non-essential amino acids, 2 mM L-glutamine (GlutaMAX™), and ZellShield® at 37 °C, 5 % CO_2, and 100 % humidity. Cells were split at a 1:1 ratio every 2 to 3 d. Samples were seeded on coverslips at a density so they would reach a confluency of 50 to 70 % at the time of fixation (2 d later).

6.2.5 Sample preparation for localization microscopy

The protocols for preparation of the different samples described below have been previously published:

- Mund *et al.* (2014) & Mund *et al.* (2018) for yeast protocols
- Li *et al.* (2018) & Thevathasan *et al.* (2019) for mammalian protocols

Cleaning of coverslips In a first step, the coverslips were cleaned overnight in a mixture of methanol and hydrochloric acid (50/50) while stirring. Next, they were washed in ultrapure water until the washing solution remained neutral. After drying

overnight in a laminar flow hood, the coverslips were sterilized by UV illumination for 30 min.

6.2.5.1 Preparation of ConA-coated coverslips

ConA solution was prepared and aliquoted to avoid freeze-thaw cycles. One aliquot was thawed and any precipitate was pelleted (16 800 × g at 4 °C for 15 to 20 min). Clean coverslips were first subjected to plasma cleaning for 10 min. Then, 20 µL of the ConA solution was pipetted to the center of the coverslip and distributed in a thumbnail-sized spot. The coverslips were incubated in a humidified atmosphere for 30 min before the residual solution was removed by pipetting or blotting on a paper tissue. After drying overnight at RT or for several hours at 37 °C, the coverslips were stored at RT.

6.2.5.2 Sample preparation for single-color SMLM in yeast

The respective yeast strain was grown overnight in 10 mL of YPAD in an Erlenmeyer flask at 30 °C and 200 rpm shaking. In the morning, the OD_{600} was measured and the culture was diluted to an OD_{600} of 0.25 in 10 mL. After growth for 3 h, 2 mL of the culture were harvested in log phase (500 × g at RT for 3.5 min). In the meantime, a ConA-coated coverslip was washed with ultrapure water to remove residual salts from the PBS and unbound ConA and placed on a parafilm-covered metal block. Most of the supernatant was discarded and the pellet was resuspended in 200 to 300 µL of the remaining medium. Next, this solution was pipetted onto the center of the coverslip. A wet Kimwipe was put next to the coverslip and everything was covered air-tight to keep a humidified atmosphere and prevent evaporation from the coverslip. Furthermore, the coverslip was covered lightproof to avoid photoconversion or bleaching of the fluorophores. Yeast cells were allowed to settle on the coverslip and bind to the ConA for 15 min. Subsequently, the medium was blotted and the coverslip was immersed in 4 mL of FA fixation solution in a 6-well plate. All following incubation steps were carried out protected from light on an orbital shaker at RT. After 15 min of fixation, the coverslip was transferred into a new well with 4 mL of quenching solution and incubated for 15 min. The quenching step was repeated once before the coverslip was washed 3 times for 5 min in 4 mL of PBS. Next, the coverslip was mounted in the custom sample holder and covered with the respective imaging buffer.

6.2.5.3 LatA treatment

For the imaging of LatA-treated cells, the overnight culture was grown in YPAD as described above but diluted the next morning in SC-Trp to reduce autofluorescence of the medium. When the culture reached the log phase, 200 µL were mixed with 2 µL of 20 mM LatA in DMSO (f.c. 200 µM) and added on a ConA-coated coverslip. After 15 min of incubation, the medium was replaced by 200 µL of fresh SC-Trp

supplemented with 200 µM LatA to further reduce autofluorescence. The sample was mounted and imaged until the endocytic sites started to cluster what typically happened after 45 min. The fixed sample of LatA-treated cells was prepared from the same diluted culture. In log phase, 1 mL of the culture was spun down (500 × g at RT for 3.5 min), the pellet was resuspended in 100 µL of SC-Trp, and mixed with 1 µL of 20 mM LatA. After 10 min of incubation, 100 µL of 8 % [w/v] FA in SC-Trp was added and the sample was incubated for 10 min. Following fixation, the sample was prepared as described above for single-color SMLM (see section 6.2.5.2).

6.2.5.4 Sample preparation for dual-color SMLM in yeast

The first steps of the sample preparation are the same as described above for single-color samples. All subsequent steps were carried out at RT and lightproof. After quenching and the first washing step in PBS, the coverslip was again put face-up on the parafilm-covered metal block. Then, 300 µL of permeabilization and blocking solution were carefully added onto the coverslip by pipetting the solution at the edge of it. The sample was incubated in a humidified atmosphere for 30 min. Next, the sample was washed twice in 4 mL of PBS for 5 min on an orbital shaker. A 100 µL drop of the respective staining solution was pipetted onto the parafilm. Subsequently, the coverslip was gently put face-down on the drop and incubated in a humidified atmosphere for 90 min. Afterwards, the coverslip was carefully recovered from the drop and submerged in 4 mL of PBS. It was washed three times for a couple of seconds each and then three times for 5 min on an orbital shaker before imaging.

6.2.5.5 Sample preparation for NPC-SNAP in mammalian cells

All incubation steps of this protocol were carried out at RT. The coverslip was transferred from the cell culture medium to 2 mL of fixation solution in a 6-well plate and prefixed for 30 s. Next, the coverslip was incubated in 2 mL of permeabilization solution for 3 min. Full fixation was carried out in the same solution as before for 30 min on an orbital shaker. Subsequently, the sample was transferred to 4 mL of quenching solution for 5 min and washed twice in 4 mL of PBS for 5 min, all while shaking. A drop of 100 µL Image-iT™ FX Signal Enhancer was pipetted onto a parafilm-covered metal block and the coverslip was put on the drop face-down and incubated for 30 min in a humidified atmosphere. Afterwards, the coverslip was transferred to a drop of 100 µL of staining solution and incubated again face-down for 90 min lightproof and in a humidified atmosphere. Finally, the coverslip was washed three times with PBS for a couple of seconds each and three times for 5 min on an orbital shaker protected from light.

6.2.5.6 Sample preparation for peptide tags in mammalian cells

U2OS cells were transfected with 1 µg of the respective plasmid with Lipofectamine 2000 according to the manufacturer's protocol. After 24 h, the medium was changed

back to DMEM and the cells were grown for another 24 h before they were fixed and permeabilized as described in the previous section. Next, the coverslips were blocked with 1 % [w/v] BSA in PBS for 1 h at RT. The concentrations of the different labeling reagents were as follows: 25 nM for the anti-GFP nanobody, 5 nM for the anti-ALFA nanobody, 0.25 µg mL^{-1} for the bivalent anti-BC2 nanobody, and 2.1 µg mL^{-1} for SpyCatcher-AF647. The stainings were performed overnight at 4 °C in 1 % [w/v] BSA in PBS. The final washing steps were performed as described above for SNAP labeling in mammalian cells.

6.2.5.7 Preparation of bead sample

In dual-color SMLM of AF647 and mMaple it is necessary to calculate a transformation from one channel onto the other. For this purpose, beads are imaged that fluoresce in both channels and therefore the same beads can be identified in both channels. In our lab, we use TetraSpeck™ beads that are 100 nm in size and fluoresce in all 4 standard channels (blue, green, red, and far red). First, the beads were mixed with a vortexer and subsequently diluted 1:450 in 360 µL ultrapure water. Then, 40 µL of 1 M $MgCl_2$ were added on an off-the-shelf (i.e., not cleaned as described above since the fluorescence of the beads is a lot stronger than any contaminant) coverslip in the sample holder. The diluted bead solution was vortexed again to prevent aggregates and then mixed with the $MgCl_2$ solution by pipetting onto the coverslip (the f.c. of $MgCl_2$ was 100 mM). Magnesium facilitates the binding of the beads to the glass coverslip. The beads were allowed to adhere to the coverslip for 3 to 5 min before the solution was replaced by 400 µL ultrapure water and the sample mounted on the microscope.

6.2.6 Localization microscopy

The prepared samples were mounted on a custom-made sample holder (Fig. 6.1A). It consisted of a metal base plate and a magnetic ring that held the coverslip in place and allowed to apply the sample buffer. For mounting, the magnetic ring was covered with parafilm to protect the sample from dirt (Fig. 6.1B). Then, the round coverslip was placed in the center of the metal plate and the magnetic ring was applied. Next, the respective imaging buffer was pipetted carefully into the hole of the magnetic ring to not disturb the cells on the coverslip. Typically, 500 µL of the respective buffer was used. For short-term measurements in GLOX buffer, the respective buffer was replaced after 1 to 2 h. For long-term imaging, the magnetic ring was covered with a piece of parafilm to prevent evaporation. For the method determined to be the best for long-term dual-color imaging, about 1100 µL of GLOX buffer (for yeast experiments the buffer was prepared in D_2O) were used and the magnetic ring was covered tight with a piece of parafilm (Fig. 6.1C). After the imaging session, the pH of the imaging buffer was checked using a pH-indicator strip.

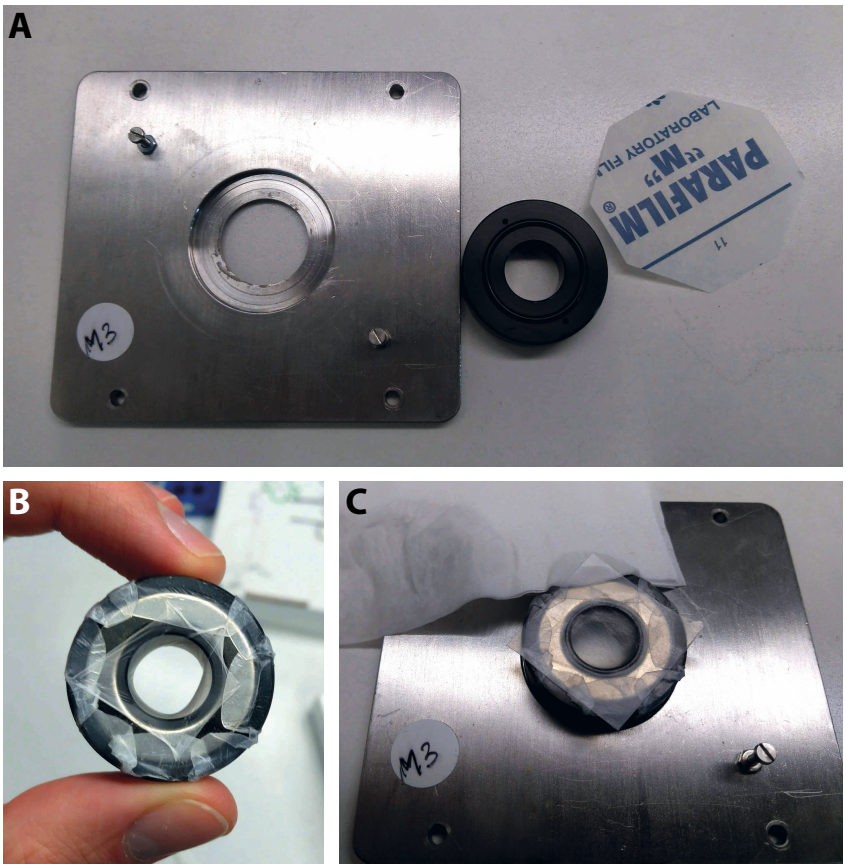

Figure 6.1 | Custom-made sample holder for localization microscopy and airtight sealing. (**A**) Individual parts of the sample holder: Metal base plate, magnetic ring and parafilm for covering. The side of the magnetic ring with the O-ring will be facing the coverslip. (**B**) The magnetic ring covered in parafilm. (**C**) The sample holder being ready for long-term imaging in GLOX buffer. After buffer was added, a second piece of parafilm was applied to the top and excess liquid was absorbed with a tissue.

Before mounting, the coverslip was dried from the bottom and subsequently cleaned with 70 % [v/v] ethanol. Immersion oil was applied to the objective and the sample holder was carefully mounted. The BFP was visually inspected for air bubbles in the oil by moving of the respective lens into the detection path. In case an air bubble was observed, the sample was unmounted, the objective and the coverslip were cleaned, new immersion oil was applied, and the sample was remounted.

6.2.6.1 Data acquisition

In the first step, the correct focal plane was determined. Depending on the organism and the fluorophore, this is done in three different ways: (1) For samples stained with AF647, focusing can be achieved by exciting AF647 with low laser intensity to visualize the structures of interest. (2) In yeast samples that only contain mMaple, the green state of the fluorescent protein can be excited by the 488 nm laser. However, in this case, the focal shift between the two detection channels (GFP vs. RFP) and the bleaching of mMaple in its green form had to be considered. (3) As an alternative, the bright-field image obtained by switching on the LEDs in the box to cover the

stage was used for focusing. Next, the photophysical behavior of the fluorophore was checked by moving to a new cell (for mammalian samples) or FOV (for yeast samples) and switching on the respective laser at full power. If single-molecule blinking was observed that could be controlled with the 405 nm laser, this test was deemed successful.

Then, the stage was moved to a new cell or FOV and the BFP was checked again for air bubbles. For AF647 imaging, a diffraction-limited single snapshot with low laser intensity was taken and saved. Then, the raw data was acquired by setting all necessary parameters in µManager and the custom plug-in. These parameters encompass laser intensities, exposure time, EM gain and readout rate of the camera, number of frames, and the target number of blinking events per frame. Table 6.19 shows typical values for laser intensities and exposure times. The parameters of the EMCCD camera were an EM gain of 200, a readout rate of 10 MHz, and a bit depth of 16 bit. The number of frames was chosen rather conservatively from experience since experiments could be stopped before the maximum of frames was reached. The number of desired number of blinking events per frame was set in a way that the density of blinks was rather low to avoid overlapping PSFs and errors in localization resulting from that. If it was required for an experiment, a snapshot or z-stack in the GFP channel was acquired after collection of the localization microscopy data. This order was chosen to prevent cross-talk with mMaple's green form.

Table 6.19 | Typical acquisition parameters for SMLM of different samples

Type of experiment	Laser intensities [kW cm^{-2}]	Exposure time [ms]
Single-color AF647	638 nm: 11.4	15 to 65, typically 35
mMaple/mMaple3	561 nm: 7.0 to 8.7	25
Dual-color: AF647 and mMaple/mMaple3	638 nm: 7.0 561 nm: 7.0 to 8.7	35

6.2.6.2 Automated high-throughput SMLM

The procedure of automated high-throughput SMLM has been developed by Joran Deschamps and Markus Mund in our lab (Deschamps, 2017; Mund *et al.*, 2018; Deschamps and Ries, 2020). To perform automated localization microscopy, a list of stage positions that would be imaged one after the other was needed. For mammalian samples, individual nuclei were searched for in live mode and the positions were saved in the *Stage Position List* of µManager. Since the whole coverslip was covered with a layer of yeast cells, an automatically generated grid could be used for yeast samples. The individual positions of the grid were 200 µm apart from each other to avoid pre-activation and pre-bleaching by scattered laser light. Next, the

experiment to be performed at every position was defined. Each experiment consisted of subtasks that were automatically performed by the microscope one after the other. The first of these subtasks was the acquisition of the raw localization data. The main parameters were the same as above (see section 6.2.6.1), the main difference were the two criteria that defined the end of this subtask: Either it was finished when the maximum number of frames was reached or when the pulse length of the activation laser (405 nm) reached a predefined maximal value. After this maximum was reached, data was acquired for 5 s more. In case GFP data was needed, a z-stack was acquired as the next subtask (typically from −2 to 2 µm in 50 nm steps). At the very end of the experiment at each position, an image of the BFP was taken. After the position was changed, the system was given 3 s to equilibrate and in between the individual subtasks a break of 3 s was defined to give the microscope time to change the hardware (e.g. moving filters & lenses).

6.2.6.3 Primed conversion

Primed conversion was performed by illuminating the sample continuously with light of 730 nm and 561 nm at intensities of 450 W cm^{-2} and 1 kW cm^{-2}, respectively. The 488 nm laser was pulsed in every 10$^{\text{th}}$ frame at an intensity increasing from 1 to 240 W cm^{-2}. The positive control was acquired with UV activation. For this, the sample was continuously illuminated with 561 nm at the intensity as before and the 405 nm laser was pulsed in every 10$^{\text{th}}$ frame at an intensity increasing from 1 to 9 W cm^{-2}.

6.2.7 Processing of SMLM data

All steps described below were performed in SMAP (Super-resolution Microscopy Analysis Platform; Ries, 2020), a MATLAB based software developed by Jonas Ries (available from `https://github.com/jries/SMAP`). The MATLAB versions used were 9.1 (R2016b) to 9.9 (R2020b). If not stated differently, all plug-ins mentioned below were written by Jonas Ries.

6.2.7.1 Localization of single molecules in raw data

Basic fitting All data has been fitted using the workflow *fit_fastsimple* within the *Localize* module of SMAP. The raw TIFF (Tagged Image File Format) files were loaded, the camera parameters were automatically detected and converted from analog-to-digital units to photons. After the image was normalized by an Anscombe transformation, a difference of Gaussians filter was applied to the image (parameter value: 1.2). Subsequently, the parts of the camera chip that had not been illuminated by the emitted fluorescence were excluded from further analysis by defining a ROI. In the next step, individual peaks were detected in the image by local maximum finding. Here, the cutoff was based on the distribution of pixel intensities which was dynamically calculated for every frame (dynamic factor: 1.5). For the detected peaks,

a square of 13×13 px was cut out and sent to the fitter. The individual maxima were fitted on the graphics processing unit using a maximum likelihood estimation (MLE) based algorithm (Li *et al.*, 2018). The fitted parameters returned from the fitter were saved in a localization table as a MATLAB file. These parameters include the x and y coordinates, the peak and background photons, the size of the PSF, the relative log-likelihood returned from the MLE, the frame the peak was detected in and the determined localization precision. The fitting procedure was started while the raw data was acquired and performed simultaneously. Intermediate super-resolved images were reconstructed based on the fitted data up to that point in time to evaluate the quality of the sample of the current acquisition. Finally, localizations that originated from the same fluorescent molecule were grouped together. This was done based on the criterion that localizations that were detected in sequential frames within 35 nm of one another with a maximum of one frame dark time in between to account for flickering molecules. The new x- and y-coordinates were calculated from their averages (weighted by the localization precision) and the numbers of peak and background photons were summed up.

Fitting of automatically acquired data For automated high-throughput imaging, online fitting was performed to have the localized data ready for subsequent analysis when the experiment was finished. For this, all fitting parameters were set for the initially acquired dataset and saved as a `_batch` file. This file was loaded into the *Batch Processor* of SMAP and the folder to watch for new SMLM datasets was defined. Every folder identified to contain raw data was then automatically subjected to fitting.

6.2.7.2 Transformation of dual-color data

For dual-color imaging of AF647 alongside with mMaple, the individual channels were detected side by side on the same camera. To merge the two channels into a single super-resolved image, the localizations in one channel have to be transformed to the other. This transformation was determined by imaging beads that fluoresce in both channels (see section 6.2.5.7 for preparation of the sample). Individual snapshots of multiple ROIs (≈ 225) of the beads were acquired and fitted like frames of single-molecule data. Then, the transformation was calculated with the following algorithm on ungrouped data. First, the cross-correlation between the two channels was calculated with a pixel size of 100 nm to determine their relative shift and approximately register them. The localizations from the same bead in both channels were linked and used as anchor points to calculate a projective transformation. These steps were repeated with a pixel size of 10 nm. If no clear maximum in the cross-correlation could be determined, the parameter for the maximal initial shift was relaxed. The residual error of the final transformation was typically on the order of 10 nm. After applying the transformation, the FOV was inspected for systematic errors in the registration of the two channels.

Due to focal and lateral shifts between different fluorescent channels, a transformation is also needed to merge super-resolved data based on mMaple and diffraction-limited imaging of GFP from the same FOV. In this case, the same beads as above were imaged, however, at each of the multiple positions an image in the GFP and the RFP channel was taken. Each channel was then localized separately and the two resulting files were registered to one another as described above to calculate the transformation between the two channels.

6.2.7.3 Quality control of high-throughput data

Before performing downstream analysis on high-throughput data, initial quality control screens were performed. First, the acquired images of the BFP at every position were visually inspected for the occurrence of an air bubble as this would deteriorate the PSF of the microscope. Besides that, it could lead to loss of the focus as the infrared laser is aberrated or blocked. Next, the objective position was plotted against the number of the position in the sample to check if the focus was retained correctly. Finally, various statistics across the SMLM data at all positions of the sample were calculated in SMAP to detect systematic trends that might be caused by thermal effects, evaporation of the imaging buffer, or other problematic changes. These statistics comprise the number of frames, the total number of localizations, the average number of photons, the maximum and the rising edge of the distribution of the localization precision, the fluorophore on-time (calculated as the number of frames from the grouped data), the number of background photons, and the size of the PSF.

6.2.7.4 Drift correction

The drift caused by temperature fluctuations was corrected by redundant cross-correlation (Wang *et al.*, 2014b). The SMLM data was subdivided into ten serial segments and a super-resolved image was reconstructed for each of them individually. Then, the cross-correlation of each segment with all others was calculated. The shifts between the individual segments were plotted and interpolated by a smoothed spline function. Based on this function, the x- and y-coordinates of the localizations were corrected. Typical values of drift in x and y after thermal equilibration of the sample on the microscope were 10 to 50 nm h^{-1}.

6.2.7.5 Data visualization

Rendering of localization microscopy data as an image was achieved by plotting a two-dimensional Gaussian distribution at the respective x, y coordinates of each localization. The standard deviation σ of the distribution was proportional to the localization precision with a proportionality factor of 0.4. However, the minimal standard deviation was set to 0.7 px or 3 nm (6 nm for mMaple and yeast dual-color data) to aid the visual impression by preventing too small points. The reconstructed

images were typically rendered with the *red hot* lookup table (LUT) for single-color data or in combination with the *cyan cold* LUT for dual-color data. The LUT was mapped to the distribution of pixel intensities in a way so that 0.03 to 0.1 % of the pixels were saturated. The images in figure 3.18D and E were reconstructed with the maximum of the LUT set to 0.4. For the reconstructions in 3.18, the color range was adjusted to 0.05 to 1.1 to reduce background localizations.

6.2.7.6 Filtering of localizations

Before rendering, the displayed localizations were filtered based on some of their properties determined during fitting. The localization precision was filtered to discard dim localizations (displayed localizations: 0 to 15 nm for AF647 data and 0 to 25 nm for mMaple). Furthermore, only localizations whose size was below 160 nm were displayed to exclude out-of-focus fluorophores. For AF647 data, the first couple of 100 frames were rejected as localizations in this range might be skewed due to the high density of blinking fluorophores in the initial off-switching phase. Moreover, molecules that fluoresce for more than 15 frames were discarded. To further filter out localizations that might result from fitting a PSF to more than one fluorescent molecule, the relative log-likelihood was limited to −1.5 to 0.

6.2.7.7 Segmentation of structures of interest

SMAP contains a plug-in, the *ROI Manager*, which allows to define ROIs in a single or across multiple files (e.g., from high-throughput data). These ROIs can be individual NPCs or endocytic sites, for example. Definition of the ROIs can be done by manual, automatic, or semi-automatic segmentation. Subsequently, different analysis plug-ins can be applied to the ROIs to extract the desired data. In the following, this workflow is described for different datasets.

The *ROI Manager* is organized hierarchically. Each super-resolved image (termed *file*) is subdivided into several FOVs (termed *cells)* which themselves are subdivided into smaller FOVs (termed *sites*). Each *site* contains one ROI which is the basis for subsequent analysis. The terminology just mentioned is due to the fact that the *ROI Manager* was initially developed for the segmentation of endocytic sites in yeast (Mund, 2016; Mund *et al.*, 2018).

Automatic segmentation of nuclear pores in mammalian cells The approach described in this paragraph has been published previously (Thevathasan *et al.*, 2019). Initially, the parameters for the *ROI Manager* were set to the values in table 6.20. Then, the whole nucleus was segmented into a grid of large FOVs (*cells*) followed by segmentation of the NPCs in a hand-drawn outline of the nucleus using the plug-in *segmentNPC*. In this plug-in, the super-resolved image is convoluted with a ring-shaped kernel (parameters $diameterNPC = 110\,\text{nm}$ and $rim = 20\,\text{nm}$) that itself is convoluted with a Gaussian kernel. In the resulting image, peaks above a

threshold (parameter *cutoff* $= 0.04$) were saved as *sites* in the *ROI Manager*. As this segmentation step detects many structures that are not NPCs, the *sites* are further cleaned up. This was either done manually or using the plug-in *NPCsegmentCleanup*. Here, the quality of the selected NPCs is checked in two steps. First, a circle is fitted to the candidate NPC with the radius as a fitting parameter. Only if the radius is between 40 and 70 nm, the structure is kept. Second, a ring is fitted with a fixed radius ($r = 55$ nm; $dR = 15$ nm) and the structure is discarded if more than 25 % of the localizations are within a radius of 40 nm or if more than 40 % of the localizations are further away than 70 nm. Based on this last criterion, almost all ROIs that contained more than one NPC were excluded.

Table 6.20 | Parameters in the *ROI Manager* for the segmentation of mammalian NPCs

	Pixel size [nm]	Field of view [nm]	ROI [nm]
Site	3	400	200
Cell	10	5000	

Semi-automatic segmentation of nuclear pores in yeast cells Before the segmentation, the parameters for the *ROI Manager* were set to the values in table 6.21. In a first step, yeast cells were segmented by the plug-in *segmentCellsCME* where the reconstructed super-resolution image was convoluted with a large Gaussian filter. In the filtered image, peaks above a user-defined threshold were detected as individual cells. Then, the NPCs were either manually picked or segmented by repurposing SMAP's segmentation plug-in *segmentSitesPolarCME* from its original application for segmentation of polar endocytic sites by adjusting the parameters (Mund *et al.*, 2018). Initially, the super-resolution image was reconstructed with a pixel size of 200 nm and masked with a user-defined threshold (15), which resulted in the approximate outline of the nucleus. Then, a convex hull was defined by the localizations within the mask. The convex hull was shrunk iteratively over three rounds by removing the outer localizations that defined the convex hull. Next, the convex hull was scaled down by 20 %, which was the basis for the actual segmentation of nuclear pores. The different size reduction steps of the initial mask helped to exclude tilted and out-of-focus structures at the rim of the nucleus. For the segmentation of NPCs, the super-resolution image was rendered with a pixel size of 40 nm. Subsequently, peaks above a user-defined threshold (8) were detected and kept if the standard deviation of the respective localizations in x and y were in the range of 10 to 50 nm.

Automatic segmentation of polar endocytic sites This procedure was performed as described in Mund *et al.* (2018). Cells were segmented as reported above with the plug-in *segmentCellsCME* followed by segmentation of endocytic sites using the plug-in *segmentSitesPolarCME*. Different from above, the user-defined threshold was once

Table 6.21 | Parameters in the *ROI Manager* for the segmentation of yeast NPCs

	Pixel size [nm]	Field of view [nm]	ROI [nm]
Site	3	500	160
Cell	10	5000	

adjusted to the abundance of each endocytic protein and the mask after shrinking of the convex hull was reduced by 30 % to restrict the mask to the central part of the cell to exclude endocytic sites that were tilted. Finally, the cell was reconstructed with a pixel size of 100 nm and the peaks above a user-defined threshold (adjusted for every endocytic protein) within the mask were segmented as endocytic sites. An upper size limit was set to exclude peaks that consisted of multiple endocytic sites. In the LatA-treated live cells, the endocytic sites were picked manually.

Automatic segmentation of yeast endocytic sites in equatorial view The segmentation pipeline described in the following was developed by Yu-Le Wu with input from both of us. First, cells were segmented by intensity-based masks. Based on the masks, cells that were incomplete due to their location at the rim of the FOV and small cells were discarded. Within each retained cell, localizations were transformed to the polar coordinate system, where a spline was fitted to the outline of the cell. Non-round cells were further discarded. Moreover, cells with missing labeling in the AF647 channel were removed. Then, the rim of the cell was scanned along the outline and peaks were detected as endocytic sites. The tangent line at the respective points of the spline was used for rotation of the sites. The rotation was performed in a way that the direction of endocytosis was pointing upwards, so the cell membrane was at the bottom with the cytosol above. At this step, very wide endocytic sites that most likely represented double sites were discarded. Besides, sites were ignored that were too close to neighboring cells. This was done to not have localizations that were not part of the actual endocytic structure influencing the downstream analysis.

6.2.7.8 Analysis of polar endocytic sites

Segmented polar endocytic sites were analyzed by fitting a geometric model as described in Mund *et al.* (2018). For this purpose, the sites were rendered with a pixel size of 3 nm and either fitted as a ring or a patch. The model was based on a ring with diameter r_{out} and thickness of the rim dr around the central hole. For values of $r_{\mathrm{out}} > dr$ this model describes a ring, whereas for $r_{\mathrm{out}} \leq dr$ it describes a patch. The model was formalized as follows:

$$f(X,Y) = A\left(\mathrm{erf}\left(\frac{r_{\mathrm{out}} - R(X,Y))}{\sqrt{2}\sigma}\right) - \mathrm{erf}\left(\frac{r_{\mathrm{out}} - dr - R(X,Y))}{\sqrt{2}\sigma}\right)\right)$$

$$R(X,Y) = \sqrt{(X - x_0)^2 + (Y - y_0)^2}$$

with the pixelated image $I(X,Y)$, the outer radius r_{out}, the rim thickness dr, a scaling factor A, and the central coordinates x_0 and y_0. Furthermore, the image was blurred with $\sigma = 15\,\mathrm{nm}$ to account for the localization precision of the data. The model was optimized by least-squares fitting of the following equation:

$$\{dr, r_{\mathrm{out}}, x_0, y_0\} = \underset{dr, r_{\mathrm{out}}, x_0, y_0}{\arg\min} \left(\sum_{X,Y} \left(I(X,Y) - f(X,Y) \right)^2 \right)$$

For subsequent analysis, structures with less than 30 localizations or a fitted outer radius of less than 30 nm were excluded (the last criterion was not applied during the analysis of the coat protein Pan1). The radial distributions of individual proteins were calculated by accumulating all localizations around the fitted center of the model.

Quantification of GFP intensity For staging the endocytic sites by diffraction limited imaging, the GFP intensity was extracted as described in Mund *et al.* (2018). The GFP had been acquired after the super-resolution experiment as z-stack with a step size of $\Delta z = 50\,\mathrm{nm}$ over a range from −2 to 2 µm. The illumination intensity was adjusted in a way so that the detected signal stayed within the linear range of the EMCCD camera. For analysis, the 7 central slices of the z-stack were merged by a maximum intensity projection, the background was calculated by a level 3 wavelet filter and subtracted. Chromatic aberrations were corrected for by calculating a transformation between the GFP and mMaple channel based on beads as described in section 6.2.7.2. Then, at each endocytic site, 3 Gaussians were fitted to the GFP signal. The first one was fixed at the central coordinates x_0 and y_0 determined by geometric fitting (see section 6.2.7.8), whereas the other two were at least 350 nm away from the first one and each other. To correct for overlapping GFP signals, endocytic sites where the GFP intensity was above 150 % of the 80$^{\mathrm{th}}$ percentile of the GFP intensity distribution were excluded. For binning, endocytic sites with a GFP intensity of less than 10 % of the 80$^{\mathrm{th}}$ percentile were classified as *no GFP*; for *low*, *medium*, and *high GFP*, the remaining sites were split into these groups in equal numbers.

6.2.7.9 Quantification of SMLM data

All quantitative analyses described below were visualized using custom written code in Python (version 3.6.10; van Rossum and Drake, 2009) using the libraries Matplotlib (version 3.3.1; Hunter, 2007), seaborn (version 0.11.0; Waskom *et al.*, 2020), pandas (version 1.1.2; McKinney *et al.*, 2010) and NumPy (version 1.19.1; Harris *et al.*, 2020).

Extracting quantitative parameters from the whole FOV For the analysis of photophysical statistics across the whole nucleus, SMAP's *Statistics* plug-in was used. The photon count was determined by fitting an exponential distribution in the range 800 to 1000 photons and reporting the expected value. Moreover, the localization precision was calculated as the rising edge of a fitted log-normal distribution. For the fluorophore on-time, the expected value of a fitted exponential function in the range 1 to 30 frames was reported. The number of background photons per pixel and localization was determined as the most frequently occurring value. All quantitative analyses were performed on grouped data.

Extracting quantitative parameters from mammalian NPCs To determine the ELE and the mean number of localizations per NPC, the following procedure was performed which has been published in Thevathasan *et al.* (2019). In the evaluation plug-in *NPCLabelingQuantify*, the localizations in the ROI were again fitted with a circle ($R = 50\,\text{nm}$ and $dR = 15\,\text{nm}$) and any localizations outside of this circle were discarded. Then, the localizations' coordinates were converted from the Cartesian to the polar system (ϕ_i, r_i). The fitted ring was split in 8 equal segments (the number of corners of the NPC) and it was rotated in a way that the corners of the NPC correlated with the centers of the segments by minimizing:

$$\phi_{\text{rot}} = \arg\min_{\phi_{\text{rot}}}(\phi_{\text{rot}} - \phi_i \bmod \frac{2\pi}{4})$$

Next, the number of segments were counted that contained at least one localization. In the next plug-in, *NPCLabelingEfficiency*, the number of segments with localizations from all NPCs in the dataset were plotted as a histogram. Subsequently, a probabilistic model with the ELE as a free parameter was fitted to the histogram. The model was based on the binomial distribution

$$B(k \mid n, p) = \binom{n}{k} p^k (1-p)^{n-k}$$

$$p_{\text{dark}} = B(0 \mid 4, p_{\text{label}})$$

where p_{label} is the ELE. The probability to observe at least one localization per corner of the NPC is thus:

$$p_{\text{bright}} = 1 - p_{\text{dark}} = 1 - B(0 \mid 4, p_{\text{label}})$$

Finally, the probability to observe N out of 8 labeled corners with the ELE p_{label} can be written as:

$$p(N \mid p_{\text{label}}) = B(N \mid 8, p_{\text{bright}}) = B(N \mid 8, 1 - B(0 \mid 4, p_{\text{label}}))$$

The indicated errors were derived by bootstrapping with typically 20 resampled data sets.

Extracting quantitative parameters from yeast NPCs Yeast nuclear pores are smaller and appear less structured in SMLM images. For this reason, it was not possible to discriminate individual corners to determine the ELE. Thus, similar to the analysis of whole mammalian nuclei, crucial parameters (number of localization, number of photons, localization precision ...) were extracted from individual NPCs with the evaluation plug-in *generalStatistics* (with a circular ROI) and analyzed over time or compared between different imaging conditions. The localization precision and number of photons were reported as the median of all localizations in the ROI, the fluorophore on-time as mean, and the number of background photons per pixel as the most frequently occurring value. All quantitative analyses were performed on grouped data.

6.2.7.10 Model fitting of endocytic sites in yeast

The super-resolution data was fitted with a geometric model $f(p)$ to extract quantitative measures. The set of K localizations was represented as $\vec{x} = \{x, y\}$, where x and y describe the coordinates of each localization k. Then, MLE was used to find the set of parameters $\hat{p}$ that fits the geometric model $f(p)$ best to the localization data $\vec{x}$. For this, the geometric model $f(p)$ was converted to the probability density function (PDF) $M(\vec{x}, \sigma|p)$. The likelihood can then be written as

$$L(p) = \prod_k M(\vec{x}, \sigma|p)$$

and maximized by

$$\hat{p} = \arg\max_p L(p)$$

Here, σ, which was set to 15 nm in this work, is the standard deviation of the symmetric 2D Gaussian function the geometric models are convoluted with to ensure smoothed PDFs.

The geometric models used were a thick ring, a hemi-sphere, and a hemi-ellipsoid. Their PDFs were constructed as smoothed side-view intensity maps derived from calculating the normalized cumulative volumes along the projection axis, followed by a convolution with the Gaussian function. The PDFs were then fitted to the endocytic sites with the settings depicted in tables 6.22, 6.23, and 6.24. The parameters of each of the second models were relative to the first one and the parameters which are not explicitly stated, were taken from the first model (e.g., x coordinate).

6.2.8 Confocal imaging of yeast

6.2.8.1 Sample preparation for confocal imaging of yeast

All steps of this sample preparation were carried out at RT. First, the glass bottom 96-well plate was plasma cleaned as described above (see section 6.2.5.2) and the ConA solution was diluted to 0.1 % [w/v] in dH_2O. After spinning down precipitates in

Table 6.22 | Parameters for the model fitting of Las17/Abp1 in dual-color

	Parameter		Value
Las17 (ring)	x coordinate	fitted	–30 to 30 nm
	y coordinate	fitted	med(y_k) ± 50 nm
	Rotational angle	fitted	–15 to 15°
	Inner radius	fixed	40 nm
	Outer radius	fixed	70 nm
	Ring thickness	fixed	60 nm
	Background weight	fitted	0.001 to 0.999
Abp1 (hemi-ellipsoid)	y coordinate	fitted	–300 to 50 nm
	Half short axis	fixed	76.5 nm
	Half long axis	fitted	0 to 250 nm
	Background weight	fitted	0.001 to 0.999

Table 6.23 | Parameters for the model fitting of Las17/Sla2 in single-color

	Parameter		Value
Las17 (ring)	x coordinate	fitted	–100 to 100 nm
	y coordinate	fitted	80 to 120 nm
	Rotational angle	fitted	–15 to 15°
	Inner radius	fixed	40 nm
	Outer radius	fixed	70 nm
	Ring thickness	fixed	60 nm
	Weight	fitted	0 to 1
Sla2 (hemi-sphere)	y coordinate	fitted	–200 to 0 nm
	Radius	fixed	40 nm
	Weight	fitted	0 to 1
Common background	Weight	fitted	0 to 0.99

Table 6.24 | Parameters for the model fitting of Moy5/Sla2 in single-color

	Parameter		Value
Myo5 (ring)	x coordinate	fitted	–30 to 30 nm
	y coordinate	fitted	0 to 120 nm
	Rotational angle	fitted	–25 to 25°
	Inner radius	fixed	20 nm
	Outer radius	fixed	90 nm
	Ring thickness	fixed	60 nm
	Weight	fitted	0.000 01 to 1
Sla2 (hemi-sphere)	y coordinate	fitted	–260 to 20 nm
	Radius	fixed	40 nm
	Weight	fitted	0.000 01 to 1
Common background	Weight	fitted	0.001 to 0.999

the diluted ConA solution (16 800 × g at 4 °C for 15 min), 10 µL of the solution was pipetted into each well. After 10 min, the remaining liquid was removed and the plate was dried.

Overnight cultures were grown as described in section 6.2.5.2. The wells of the coated 96-well plate were washed with 200 µL of dH_2O to remove residual salts. Then, 300 µL of each yeast culture was pipetted into a well and the cells were settled for 15 min. The medium was removed and the cells were fixed by addition of 100 µL of FA fixation solution per well and incubation for 15 min on an orbital shaker. After removal of the fixation solution, any remainder was quenched by two incubation steps with 100 µL of quenching solution for 15 min on an orbital shaker. Next, the fixed cells were washed with 100 µL of PBS for 5 min on an orbital shaker. The yeast cell wall was stained using concanavalin A coupled to Alexa Fluor™ 488 (ConA-AF488, provided by the Pepperkok lab at EMBL). ConA-AF488 was diluted 1:1000 in PBS and 100 µL were added per well and incubated for 30 min in the dark. After one washing step (5 min PBS on an orbital shaker), 100 µL dextran-AF647 was added at a concentration of 0.002 % [w/v], and sodium azide was added.

6.2.8.2 Data acquisition in confocal imaging of yeast

Confocal imaging of yeast was performed in EMBL's Advanced Light Microscopy Facility with the help of Marko Lampe on an iXplore SPIN SR spinning disc confocal microscope (Olympus), which was controlled by the cellSens Dimension software in version 3.1 (Build 21199). The images were acquired as a z-stack with a step size of 280 nm and a pinhole size of 50 µm. For the two fluorescent channels (ConA-AF488 and dextran-AF647), the exposure time was 500 ms, and for the transmitted channel 50 ms. The sample was illuminated with 25 % (488 nm channel) or 100 % (640 nm channel) laser intensity. For the transmission channel, the LED intensity was set to 130 (maximum: 255).

6.2.8.3 Post-processing and quantification of data from confocal yeast imaging

Image handling and manipulation The images were exported as TIFF stacks using the microscope control software. The stacks were opened in Fiji (Schindelin *et al.*, 2012; Rueden *et al.*, 2017) to find the z-plane where most of the yeast cells were imaged in the equatorial plane. The respective slices were exported for subsequent analysis. For figure 3.22, the contrast was automatically adjusted and the background of the ConA-AF647 channel was subtracted using the rolling ball algorithm with a size of 50 px.

Automated segmentation The exported TIFF slices were analyzed in Python (version 3.6.10; van Rossum and Drake, 2009). First, the dextran channel was loaded and inverted using the packages scikit-image (version 0.16.2; van der Walt *et al.*, 2014) and NumPy (version 1.19.1; Harris *et al.*, 2020), respectively.

Next, the image was rescaled to the 1st and 99th percentile (scikit-image's method `exposure.rescale_intensity`). After applying a Gaussian filter with $\sigma = 5$, the image was binarized by `filters.threshold_local` in scikit-image (with the parameters `block_size` = 151 and `offset` = –0.04). A distance map was calculated from the binarized image using Scipy's (version 1.5.2; Virtanen *et al.*, 2020) method `ndimage.distance_transform_edt` (Maurer *et al.*, 2003) and its local maxima were detected by scikit-image's method `filters.threshold_local` (minimal distance 10 px). The maxima were dilated by a disk with a diameter of 11 px (`morphology.binary_dilation` in scikit-image) and intersected by a logical and (Numpy's method `logical_and`). Any structure remaining that was smaller than the disk by which the maxima were enlarged by was removed using scikit-image's method `morphology.remove_small_objects`. The resulting binary image was used as the seed in a watershed algorithm (`segmentation.watershed` in scikit-image) applied to the rescaled ConA image of the same FOV (same parameters for rescaling as for the dextran image). The resulting segmentation was cleared by removing objects smaller than 500 px^2 and larger than 8000 px^2. Quantitative measures were extracted by the method `measure.regionprops_table` in scikit-image and handled by a DataFrame in pandas (version 1.1.2; McKinney *et al.*, 2010). The roundness R of each cell was calculated based on the area A and perimeter P using the following equation:

$$R = \frac{4\pi A}{P^2}$$

While testing the sequence and choice of algorithms, intermediate results were visualized using napari (version 0.3.6; Sofroniew *et al.*, 2020). The exported quantitative parameters were visualized using ggplot2 (version 3.3.2; Wickham, 2016) and RainCloudPlots (Allen *et al.*, 2019) in R (version 4.0.2; R Core Team, 2017).

Manual classification For the manual classification of yeast cells, the whole stacks of the two fluorescent channels were loaded in napari (version 0.3.6; Sofroniew *et al.*, 2020) and manually annotated on different point layers. The count statistics of the different strains were visualized using the libraries Matplotlib (version 3.3.1; Hunter, 2007) and seaborn (version 0.11.0; Waskom *et al.*, 2020).

A Quantitative data of cell morphology analysis

Strain	Replicate	# total cells	# normal cells	# buds	# interm. cells	# aberr. cells	# large cells	# autom. segm. cells
BY4741	1	437	271	160	6	0	0	382
	2	286	170	107	6	3	0	247
	3	255	148	102	5	0	0	237
Y8205	1	239	144	92	1	0	2	216
	2	283	176	105	2	0	0	254
	3	341	202	135	2	0	2	307
MK100	1	371	242	125	4	0	0	319
	2	356	210	139	5	1	1	317
	3	267	153	106	6	2	0	239
MK102	1	324	196	123	5	0	0	293
	2	314	185	125	2	0	2	287
	3	332	203	127	1	1	0	305
MKY100 Myo5-mM3 Sla2-mM3 End3-SNAP$_f$ MATa	1	365	242	118	5	0	0	318
	2	387	249	129	7	0	2	354
	3	412	267	139	5	1	0	376
MKY100 Myo5-mM3 Sla2-mM3 Las17-SNAP$_f$ MATa	1	437	279	148	8	2	0	406
	2	433	278	150	3	2	0	384
	3	451	278	164	9	0	0	416
MKY100 Myo5-mM3 Sla2-mM3 Rvs167-SNAP$_f$ MATa	1	357	217	137	0	0	3	309
	2	345	207	134	2	0	2	314
	3	390	256	131	3	0	0	355
MKY100 Myo5-mM3 Sla2-mM3 Sac6-SNAP$_f$ MATa	1	278	182	96	0	0	0	256
	2	251	154	95	2	0	0	218
	3	270	175	94	1	0	0	242
BY4741 Myo5-17×L-mM3 Sla2-17×L-mM3 End3-17×L-SNAP$_f$ MATa	1	363	219	139	4	1	0	310
	2	265	162	96	3	4	0	236
	3	462	281	176	3	1	1	412
BY4741 Myo5-17×L-mM3 Sla2-17×L-mM3 Las17-17×L-SNAP$_f$ MATa	1	322	205	113	3	1	0	293
	2	227	134	88	4	1	0	209
	3	274	165	103	5	1	0	259
BY4741 Myo5-17×L-mM3 Sla2-17×L-mM3 Sac6-17×L-SNAP$_f$ MATa	1	261	153	104	3	1	0	230
	2	221	133	85	2	1	0	198
	3	349	207	136	5	1	0	316
BY4741 Myo5-17×L-mM3 Sla2-17×L-mM3 Rvs167-17×L-SNAP$_f$ MATa	1	547	343	192	7	0	5	474
	2	410	251	154	5	0	0	347
	3	295	174	113	8	0	0	248
SGA Myo5-mM3 Sla2-mM3 End3-SNAP$_f$ MATa	1	375	230	138	6	1	0	333
	2	427	258	164	3	1	1	381
	3	346	200	133	8	3	2	303
SGA Myo5-mM3 Sla2-mM3 End3-SNAP$_f$ MATα	1	492	299	193	0	0	0	418
	2	466	292	172	2	0	0	412
	3	581	352	219	4	0	6	487
SGA Myo5-mM3 Sla2-mM3 Las17-SNAP$_f$ MATa	1	410	262	145	1	2	0	357
	2	258	155	100	3	0	0	230
	3	409	250	153	5	1	0	366
SGA Myo5-mM3 Sla2-mM3 Las17-SNAP$_f$ MATα	1	595	372	220	3	0	0	509
	2	367	222	137	3	1	4	344
	3	560	345	213	2	0	0	480
SGA Myo5-mM3 Sla2-mM3 Sac6-SNAP$_f$ MATa	1	537	306	216	12	3	0	464
	2	543	325	206	8	2	2	487
	3	577	370	198	5	0	4	475
SGA Myo5-mM3 Sla2-mM3 Sac6-SNAP$_f$ MATα	1	469	286	178	5	0	0	400
	2	403	242	156	5	0	0	355
	3	509	325	181	3	0	0	439

LaTeX

I composed this thesis with Overleaf, and used a custom document structure based on the 'Masters/Doctoral Thesis' LaTeXtemplate (www.latextemplates.com, authors Steve Gunn, Sunil Patel, vel@latextemplates), modified by Markus Mund & Jervis Vermal Thevathasan, which is available under CC BY-NC-SA 3.0.

Licenses used in this thesis

- CC BY-NC-SA 3.0: http://creativecommons.org/licenses/by-nc-sa/3.0/
- CC BY 4.0: https://creativecommons.org/licenses/by/4.0/

Bibliography

Abbe, E. 1873. Beiträge zur Theorie des Mikroskops und der mikroskopischen Wahrnehmung. *Archiv für Mikroskopische Anatomie* **9(1)**: 413–468. DOI: 10.1007/BF02956173.

Abella, M., L. Andruck, G. Malengo, and M. Skruzny. 2020. Force requirements of endocytic vesicle formation. *bioRxiv*: 2020.11.11.378273. DOI: 10.1101/2020.11.11.378273.

Adams, A. E. and J. R. Pringle. 1984. Relationship of actin and tubulin distribution to bud growth in wild-type and morphogenetic-mutant *Saccharomyces cerevisiae*. *Journal of Cell Biology* **98(3)**: 934–945. DOI: 10.1083/jcb.98.3.934.

Aghamohammadzadeh, S. and K. R. Ayscough. 2009. Differential requirements for actin during yeast and mammalian endocytosis. *Nature Cell Biology* **11(8)**: 1039–1042. DOI: 10.1038/ncb1918.

Aitken, C. E., R. A. Marshall, and J. D. Puglisi. 2008. An Oxygen Scavenging System for Improvement of Dye Stability in Single-Molecule Fluorescence Experiments. *Biophysical Journal* **94(5)**: 1826–1835. DOI: 10.1529/biophysj.107.117689.

Akamatsu, M., R. Vasan, D. Serwas, M. A. Ferrin, P. Rangamani, and D. G. Drubin. 2020. Principles of self-organization and load adaptation by the actin cytoskeleton during clathrin-mediated endocytosis. *eLife* **9** e49840. DOI: 10.7554/eLife.49840.

Alberts, B., A. Johnson, J. Lewis, K. Roberts, M. Raff, and P. Walter. 2008. Molecular Biology of the Cell. Garland Science. ISBN: 978-0-8153-4111-6.

Allen, M., D. Poggiali, K. Whitaker, T. R. Marshall, and R. A. Kievit. 2019. Raincloud plots: a multi-platform tool for robust data visualization. *Wellcome Open Research* **4(63)**. DOI: 10.12688/wellcomeopenres.15191.1.

Almada, P., P. M. Pereira, S. Culley, G. Caillol, F. Boroni-Rueda, C. L. Dix, G. Charras, B. Baum, R. F. Laine, C. Leterrier, and R. Henriques. 2019. Automating multimodal microscopy with NanoJ-Fluidics. *Nature Communications* **10(1)**: 1223. DOI: 10.1038/s41467-019-09231-9.

Amatruda, J. F. and J. A. Cooper. 1992. Purification, characterization, and immunofluorescence localization of *Saccharomyces cerevisiae* capping protein. *Journal of Cell Biology* **117(5)**: 1067–1076. DOI: 10.1083/jcb.117.5.1067.

Ando, R., H. Mizuno, and A. Miyawaki. 2004. Regulated Fast Nucleocytoplasmic Shuttling Observed by Reversible Protein Highlighting. *Science* **306(5700)**: 1370–1373. DOI: 10.1126/science.1102506.

Antonny, B., C. Burd, P. De Camilli, E. Chen, O. Daumke, K. Faelber, M. Ford, V. A. Frolov, A. Frost, J. E. Hinshaw, T. Kirchhausen, M. M. Kozlov, M. Lenz, H. H. Low, H. T. McMahon, C. Merrifield, T. D. Pollard, P. J. Robinson, A. Roux, and S. L. Schmid. 2016. Membrane fission by dynamin: what we know and what we need to know. *The EMBO Journal* **35(21)**: 2270–2284. DOI: 10.15252/embj.201694613.

Aquino, D., A. Schönle, C. Geisler, C. von Middendorff, C. A. Wurm, Y. Okamura, T. Lang, S. W. Hell, and A. Egner. 2011. Two-color nanoscopy of three-dimensional volumes by 4Pi detection of stochastically switched fluorophores. *Nature Methods* **8(4)**: 353–359. DOI: 10.1038/nmeth.1583.

Arasada, R. and T. D. Pollard. 2011. Distinct Roles for F-BAR Proteins Cdc15p and Bzz1p in Actin Polymerization at Sites of Endocytosis in Fission Yeast. *Current Biology* **21(17)**: 1450–1459. DOI: 10.1016/j.cub.2011.07.046.

Arasada, R., W. A. Sayyad, J. Berro, and T. D. Pollard. 2018. High-speed superresolution imaging of the proteins in fission yeast clathrin-mediated endocytic actin patches. *Molecular Biology of the Cell* **29(3)**: 295–303. DOI: 10.1091/mbc.E17-06-0415.

Archetti, A., E. Glushkov, C. Sieben, A. Stroganov, A. Radenovic, and S. Manley. 2019. Waveguide-PAINT offers an open platform for large field-of-view super-resolution imaging. *Nature Communications* **10(1)**: 1267. DOI: 10.1038/s41467-019-09247-1.

Arnold, A. M., M. C. Schneider, C. Hüsson, R. Sablatnig, M. Brameshuber, F. Baumgart, and G. J. Schütz. 2020. Verifying molecular clusters by 2-color localization microscopy and significance testing. *Scientific Reports* **10(1)**: 1–12. DOI: 10.1038/s41598-020-60976-6.

Balcer, H. I., A. L. Goodman, A. A. Rodal, E. Smith, J. Kugler, J. E. Heuser, and B. L. Goode. 2003. Coordinated Regulation of Actin Filament Turnover by a High-Molecular-Weight Srv2/CAP Complex, Cofilin, Profilin, and Aip1. *Current Biology* **13(24)**: 2159–2169. DOI: 10.1016/j.cub.2003.11.051.

Ball, G., J. Demmerle, R. Kaufmann, I. Davis, I. M. Dobbie, and L. Schermelleh. 2015. SIMcheck: a Toolbox for Successful Super-resolution Structured Illumination Microscopy. *Scientific Reports* **5(1)**: 15915. DOI: 10.1038/srep15915.

Balzarotti, F., Y. Eilers, K. C. Gwosch, A. H. Gynnå, V. Westphal, F. D. Stefani, J. Elf, and S. W. Hell. 2017. Nanometer resolution imaging and tracking of fluorescent molecules with minimal photon fluxes. *Science* **355(6325)**: 606–612. DOI: 10.1126/science.aak9913.

Balzer, C. J., A. R. Wagner, L. A. Helgeson, and B. J. Nolen. 2019. Single-Turnover Activation of Arp2/3 Complex by Dip1 May Balance Nucleation of Linear versus Branched Actin Filaments. *Current Biology* **29(19)**: 3331–3338.e7. DOI: 10.1016/j.cub.2019.08.023.

Baranov, M. V., R. A. Olea, and G. van den Bogaart. 2019. Chasing Uptake: Super-Resolution Microscopy in Endocytosis and Phagocytosis. *Trends in Cell Biology* **29(9)**: 727–739. DOI: 10.1016/j.tcb.2019.05.006.

Barentine, A. E. S., Y. Lin, M. Liu, P. Kidd, L. Balduf, M. R. Grace, S. Wang, J. Bewersdorf, and D. Baddeley. 2019. 3D Multicolor Nanoscopy at 10,000 Cells a Day. *bioRxiv*: 606954. DOI: 10.1101/606954.

Barker, S. L., L. Lee, B. D. Pierce, L. Maldonado-Báez, D. G. Drubin, and B. Wendland. 2007. Interaction of the Endocytic Scaffold Protein Pan1 with the Type I Myosins Contributes to the Late Stages of Endocytosis. *Molecular Biology of the Cell* **18(8)**: 2893–2903. DOI: 10.1091/mbc.e07-05-0436.

Bates, M., T. R. Blosser, and X. Zhuang. 2005. Short-Range Spectroscopic Ruler Based on a Single-Molecule Optical Switch. *Physical Review Letters* **94(10)**: 108101. DOI: 10.1103/PhysRevLett.94.108101.

Bates, M., B. Huang, G. T. Dempsey, and X. Zhuang. 2007. Multicolor Super-Resolution Imaging with Photo-Switchable Fluorescent Probes. *Science* **317(5845)**: 1749–1753. DOI: 10.1126/science.1146598.

Bayati, A., R. Kumar, V. Francis, and P. S. McPherson. 2020. SARS-CoV-2 infects cells following viral entry via clathrin-mediated endocytosis. *bioRxiv*: 2020.07.13.201509. DOI: 10.1101/2020.07.13.201509.

Beghin, A., A. Kechkar, C. Butler, F. Levet, M. Cabillic, O. Rossier, G. Giannone, R. Galland, D. Choquet, and J.-B. Sibarita. 2017. Localization-based super-resolution imaging meets high-content screening. *Nature Methods* **14(12)**: 1184–1190. DOI: 10.1038/nmeth.4486.

Beliveau, B. J., E. F. Joyce, N. Apostolopoulos, F. Yilmaz, C. Y. Fonseka, R. B. McCole, Y. Chang, J. B. Li, T. N. Senaratne, B. R. Williams, J.-M. Rouillard, and C.-t. Wu. 2012. Versatile design and synthesis platform for visualizing genomes with Oligopaint FISH probes. *Proceedings of the National Academy of Sciences* **109(52)**: 21301–21306. DOI: 10.1073/pnas.1213818110.

Bendall, S. C., K. L. Davis, E.-a. D. Amir, M. D. Tadmor, E. F. Simonds, T. J. Chen, D. K. Shenfeld, G. P. Nolan, and D. Pe'er. 2014. Single-Cell Trajectory Detection Uncovers Progression and Regulatory Coordination in Human B Cell Development. *Cell* **157(3)**: 714–725. DOI: 10.1016/j.cell.2014.04.005.

Bendall, S. C., E. F. Simonds, P. Qiu, E.-a. D. Amir, P. O. Krutzik, R. Finck, R. V. Bruggner, R. Melamed, A. Trejo, O. I. Ornatsky, R. S. Balderas, S. K. Plevritis, K. Sachs, D. Pe'er, S. D. Tanner, and G. P. Nolan. 2011. Single-Cell Mass Cytometry of Differential Immune and Drug Responses Across a Human Hematopoietic Continuum. *Science* **332(6030)**: 687–696. DOI: 10.1126/science.1198704.

Betzig, E., G. H. Patterson, R. Sougrat, O. W. Lindwasser, S. Olenych, J. S. Bonifacino, M. W. Davidson, J. Lippincott-Schwartz, and H. F. Hess. 2006. Imaging Intracellular Fluorescent Proteins at Nanometer Resolution. *Science* **313(5793)**: 1642–1645. DOI: 10.1126/science.1127344.

Beyer, H. M., P. Gonschorek, S. L. Samodelov, M. Meier, W. Weber, and M. D. Zurbriggen. 2015. AQUA Cloning: A Versatile and Simple Enzyme-Free Cloning Approach. *PLOS ONE* **10(9)**: e0137652. DOI: 10.1371/journal.pone.0137652.

Bock, H., C. Geisler, C. A. Wurm, C. von Middendorff, S. Jakobs, A. Schönle, A. Egner, S. W. Hell, and C. Eggeling. 2007. Two-color far-field fluorescence nanoscopy based on photoswitchable emitters. *Applied Physics B* **88(2)**: 161–165. DOI: 10.1007/s00340-007-2729-0.

Boczkowska, M., G. Rebowski, and R. Dominguez. 2013. Glia Maturation Factor (GMF) Interacts with Arp2/3 Complex in a Nucleotide State-dependent Manner. *Journal of Biological Chemistry* **288(36)**: 25683–25688. DOI: 10.1074/jbc.C113.493338.

Boeke, D., S. Trautmann, M. Meurer, M. Wachsmuth, C. Godlee, M. Knop, and M. Kaksonen. 2014. Quantification of cytosolic interactions identifies Ede1 oligomers as key organizers of endocytosis. *Molecular Systems Biology* **10(11)**: 756. DOI: 10.15252/msb.20145422.

Boettner, D. R., R. J. Chi, and S. K. Lemmon. 2012. Lessons from yeast for clathrin-mediated endocytosis. *Nature Cell Biology* **14(1)**: 2–10. DOI: 10.1038/ncb2403.

Boettner, D. R., J. L. D'Agostino, O. T. Torres, K. Daugherty-Clarke, A. Uygur, A. Reider, B. Wendland, S. K. Lemmon, and B. L. Goode. 2009. The F-BAR Protein Syp1 Negatively Regulates WASp-Arp2/3 Complex Activity during Endocytic Patch Formation. *Current Biology* **19(23)**: 1979–1987. DOI: 10.1016/j.cub.2009.10.062.

Bossi, M., J. Fölling, V. N. Belov, V. P. Boyarskiy, R. Medda, A. Egner, C. Eggeling, A. Schönle, and S. W. Hell. 2008. Multicolor Far-Field Fluorescence Nanoscopy through Isolated Detection of Distinct Molecular Species. *Nano Letters* **8(8)**: 2463–2468. DOI: 10.1021/nl801471d.

Boulant, S., C. Kural, J.-C. Zeeh, F. Ubelmann, and T. Kirchhausen. 2011. Actin dynamics counteract membrane tension during clathrin-mediated endocytosis. *Nature Cell Biology* **13(9)**: 1124–1131. DOI: 10.1038/ncb2307.

Bourg, N., C. Mayet, G. Dupuis, T. Barroca, P. Bon, S. Lécart, E. Fort, and S. Lévêque-Fort. 2015. Direct optical nanoscopy with axially localized detection. *Nature Photonics* **9(9)**: 587–593. DOI: 10.1038/nphoton.2015.132.

Bourgeois, D., A. Regis-Faro, and V. Adam. 2012. Photoactivated structural dynamics of fluorescent proteins. *Biochemical Society Transactions* **40(3)**: 531–538. DOI: 10.1042/BST20120002.

Brach, T., C. Godlee, I. Moeller-Hansen, D. Boeke, and M. Kaksonen. 2014. The Initiation of Clathrin-Mediated Endocytosis Is Mechanistically Highly Flexible. *Current Biology* **24(5)**: 548–554. DOI: 10.1016/j.cub.2014.01.048.

Cabriel, C., N. Bourg, P. Jouchet, G. Dupuis, C. Leterrier, A. Baron, M.-A. Badet-Denisot, B. Vauzeilles, E. Fort, and S. Lévêque-Fort. 2019. Combining 3D single molecule localization strategies for reproducible bioimaging. *Nature Communications* **10(1)**: 1980. DOI: 10.1038/s41467-019-09901-8.

Canton, J. 2018. Macropinocytosis: New Insights Into Its Underappreciated Role in Innate Immune Cell Surveillance. *Frontiers in Immunology* **9** 2286. DOI: 10.3389/fimmu.2018.02286.

Carroll, S. Y., H. E. M. Stimpson, J. Weinberg, C. P. Toret, Y. Sun, and D. G. Drubin. 2011. Analysis of yeast endocytic site formation and maturation through a regulatory transition point. *Molecular Biology of the Cell* **23(4)**: 657–668. DOI: 10.1091/mbc.e11-02-0108.

Cataldo, A., G. W. Rebeck, B. Ghetti, C. Hulette, C. Lippa, C. V. Broeckhoven, C. V. Duijn, P. Cras, N. Bogdanovic, T. Bird, C. Peterhoff, and R. Nixon. 2001. Endocytic disturbances distinguish among subtypes of alzheimer's disease and related disorders. *Annals of Neurology* **50(5)**: 661–665. DOI: 10.1002/ana.1254.

Chan, M. M., Z. D. Smith, S. Grosswendt, H. Kretzmer, T. M. Norman, B. Adamson, M. Jost, J. J. Quinn, D. Yang, M. G. Jones, A. Khodaverdian, N. Yosef, A. Meissner, and J. S. Weissman. 2019. Molecular recording of mammalian embryogenesis. *Nature* **570(7759)**: 77–82. DOI: 10.1038/s41586-019-1184-5.

Chang, J.-B., F. Chen, Y.-G. Yoon, E. E. Jung, H. P. Babcock, J. S. Kang, S. M. Asano, H.-J. Suk, N. Pak, P. W. Tillberg, A. T. Wassie, D. Cai, and E. S. Boyden. 2017. Iterative expansion microscopy. *Nature Methods* **14(6)**: 593–599. DOI: 10.1038/nmeth.4261.

Chen, F., P. W. Tillberg, and E. S. Boyden. 2015a. Expansion microscopy. *Science* **347(6221)**: 543–548. DOI: 10.1126/science.1260088.

Chen, F., A. T. Wassie, A. J. Cote, A. Sinha, S. Alon, S. M. Asano, E. R. Daugharthy, J.-B. Chang, A. Marblestone, G. M. Church, A. Raj, and E. S. Boyden. 2016. Nanoscale imaging of RNA with expansion microscopy. *Nature Methods* **13(8)**: 679–684. DOI: 10.1038/nmeth.3899.

Chen, K. H., A. N. Boettiger, J. R. Moffitt, S. Wang, and X. Zhuang. 2015b. Spatially resolved, highly multiplexed RNA profiling in single cells. *Science* **348(6233)**: aaa6090. DOI: 10.1126/science.aaa6090.

Chen, Q. and T. D. Pollard. 2013. Actin Filament Severing by Cofilin Dismantles Actin Patches and Produces Mother Filaments for New Patches. *Current Biology* **23(13)**: 1154–1162. DOI: 10.1016/j.cub.2013.05.005.

Chin, J. W. 2017. Expanding and reprogramming the genetic code. *Nature* **550(7674)**: 53–60. DOI: 10.1038/nature24031.

Chmyrov, A., J. Keller, T. Grotjohann, M. Ratz, E. d'Este, S. Jakobs, C. Eggeling, and S. W. Hell. 2013. Nanoscopy with more than 100,000 'doughnuts'. *Nature Methods* **10(8)**: 737–740. DOI: 10.1038/nmeth.2556.

Cloin, B. M. C., E. D. Zitter, D. Salas, V. Gielen, G. E. Folkers, M. Mikhaylova, M. Bergeler, B. Krajnik, J. Harvey, C. C. Hoogenraad, L. V. Meervelt, P. Dedecker, and L. C. Kapitein. 2017. Efficient switching of mCherry fluorescence using chemical caging. *Proceedings of the National Academy of Sciences* **114(27)**: 7013–7018. DOI: 10.1073/pnas.1617280114.

Cnossen, J., T. Hinsdale, R. Ø. Thorsen, M. Siemons, F. Schueder, R. Jungmann, C. S. Smith, B. Rieger, and S. Stallinga. 2019. Localization microscopy at doubled precision with patterned illumination. *Nature Methods* **17(1)**: 59–63. DOI: 10.1038/s41592-019-0657-7.

Coons, A. H., H. J. Creech, R. N. Jones, and E. Berliner. 1942. The Demonstration of Pneumococcal Antigen in Tissues by the Use of Fluorescent Antibody. *The Journal of Immunology* **45(3)**: 159–170.

Cordes, T., J. Vogelsang, and P. Tinnefeld. 2009. On the Mechanism of Trolox as Antiblinking and Antibleaching Reagent. *Journal of the American Chemical Society* **131(14)**: 5018–5019. DOI: 10.1021/ja809117z.

Cox, S., E. Rosten, J. Monypenny, T. Jovanovic-Talisman, D. T. Burnette, J. Lippincott-Schwartz, G. E. Jones, and R. Heintzmann. 2012. Bayesian localization microscopy reveals nanoscale podosome dynamics. *Nature Methods* **9(2)**: 195–200. DOI: 10.1038/nmeth.1812.

Daumke, O., A. Roux, and V. Haucke. 2014. BAR Domain Scaffolds in Dynamin-Mediated Membrane Fission. *Cell* **156(5)**: 882–892. DOI: 10.1016/j.cell.2014.02.017.

Dave, R., D. S. Terry, J. B. Munro, and S. C. Blanchard. 2009. Mitigating Unwanted Photophysical Processes for Improved Single-Molecule Fluorescence Imaging. *Biophysical Journal* **96(6)**: 2371–2381. DOI: 10.1016/j.bpj.2008.11.061.

Davis, L. I. and G. Blobel. 1987. Nuclear pore complex contains a family of glycoproteins that includes p62: glycosylation through a previously unidentified cellular pathway. *Proceedings of the National Academy of Sciences* **84(21)**: 7552–7556. DOI: 10.1073/pnas.84.21.7552.

Dempsey, G. T., M. Bates, W. E. Kowtoniuk, D. R. Liu, R. Y. Tsien, and X. Zhuang. 2009. Photoswitching Mechanism of Cyanine Dyes. *Journal of the American Chemical Society* **131(51)**: 18192–18193. DOI: 10.1021/ja904588g.

Dempsey, G. T., J. C. Vaughan, K. H. Chen, M. Bates, and X. Zhuang. 2011. Evaluation of fluorophores for optimal performance in localization-based super-resolution imaging. *Nature Methods* **8(12)**: 1027–1036. DOI: 10.1038/nmeth.1768.

Dempsey, W. P., L. Georgieva, P. M. Helbling, A. Y. Sonay, T. V. Truong, M. Haffner, and P. Pantazis. 2015. *In vivo* single-cell labeling by confined primed conversion. *Nature Methods* **12(7)**: 645–648. DOI: 10.1038/nmeth.3405.

Dertinger, T., R. Colyer, G. Iyer, S. Weiss, and J. Enderlein. 2009. Fast, background-free, 3D super-resolution optical fluctuation imaging (SOFI). *Proceedings of the National Academy of Sciences* **106(52)**: 22287–22292. DOI: 10.1073/pnas.0907866106.

Deschamps, J. 2017. Towards quantitative high-throughput 3D localization microscopy. PhD Thesis. Ruprecht-Karls-Universität Heidelberg.

Deschamps, J., M. Mund, and J. Ries. 2014. 3D superresolution microscopy by supercritical angle detection. *Optics Express* **22(23)**: 29081–29091. DOI: 10.1364/OE.22.029081.

Deschamps, J. and J. Ries. 2020. EMU: reconfigurable graphical user interfaces for Micro-Manager. *BMC Bioinformatics* **21(1)**: 456. DOI: 10.1186/s12859-020-03727-8.

Deschamps, J., A. Rowald, and J. Ries. 2016. Efficient homogeneous illumination and optical sectioning for quantitative single-molecule localization microscopy. *Optics Express* **24(24)**: 28080–28090. DOI: 10.1364/OE.24.028080.

Di Talia, S., J. M. Skotheim, J. M. Bean, E. D. Siggia, and F. R. Cross. 2007. The effects of molecular noise and size control on variability in the budding yeast cell cycle. *Nature* **448(7156)**: 947–951. DOI: 10.1038/nature06072.

Diekmann, R., Ø. I. Helle, C. I. Øie, P. McCourt, T. R. Huser, M. Schüttpelz, and B. S. Ahluwalia. 2017. Chip-based wide field-of-view nanoscopy. *Nature Photonics* **11(5)**: 322–328. DOI: 10.1038/nphoton.2017.55.

Diekmann, R., M. Kahnwald, A. Schoenit, J. Deschamps, U. Matti, and J. Ries. 2020. Optimizing imaging speed and excitation intensity for single-molecule localization microscopy. *Nature Methods* **17(9)**: 909–912. DOI: 10.1038/s41592-020-0918-5.

Dmitrieff, S. and F. Nédélec. 2015. Membrane Mechanics of Endocytosis in Cells with Turgor. *PLOS Computational Biology* **11(10)**: e1004538. DOI: 10.1371/journal.pcbi.1004538.

Doherty, G. J. and H. T. McMahon. 2009. Mechanisms of Endocytosis. *Annual Review of Biochemistry* **78(1)**: 857–902. DOI: 10.1146/annurev.biochem.78.081307.110540.

Dominguez, R. and K. C. Holmes. 2011. Actin Structure and Function. *Annual Review of Biophysics* **40(1)**: 169–186. DOI: 10.1146/annurev-biophys-042910-155359.

Douglass, K. M., C. Sieben, A. Archetti, A. Lambert, and S. Manley. 2016. Super-resolution imaging of multiple cells by optimized flat-field epi-illumination. *Nature Photonics* **10(11)**: 705–708. DOI: 10.1038/nphoton.2016.200.

Dümmler, A., A.-M. Lawrence, and A. de Marco. 2005. Simplified screening for the detection of soluble fusion constructs expressed in *E. coli* using a modular set of vectors. *Microbial Cell Factories* **4(1)**: 34. DOI: 10.1186/1475-2859-4-34.

Duncan, M. C., M. J. T. V. Cope, B. L. Goode, B. Wendland, and D. G. Drubin. 2001. Yeast Eps15-like endocytic protein, Pan1p, activates the Arp2/3 complex. *Nature Cell Biology* **3(7)**: 687–690. DOI: 10.1038/35083087.

Edelstein, A. D., M. A. Tsuchida, N. Amodaj, H. Pinkard, R. D. Vale, and N. Stuurman. 2014. Advanced methods of microscope control using μManager software. *Journal of Biological Methods* **1(2)**: e10. DOI: 10.14440/jbm.2014.36.

Eilers, Y., H. Ta, K. C. Gwosch, F. Balzarotti, and S. W. Hell. 2018. MINFLUX monitors rapid molecular jumps with superior spatiotemporal resolution. *Proceedings of the National Academy of Sciences* **115(24)**: 6117–6122. DOI: 10.1073/pnas.1801672115.

Endesfelder, U., K. Finan, S. J. Holden, P. R. Cook, A. N. Kapanidis, and M. Heilemann. 2013. Multiscale Spatial Organization of RNA Polymerase in *Escherichia coli*. *Biophysical Journal* **105(1)**: 172–181. DOI: 10.1016/j.bpj.2013.05.048.

Erickson, H. P. 2009. Size and Shape of Protein Molecules at the Nanometer Level Determined by Sedimentation, Gel Filtration, and Electron Microscopy. *Biological Procedures Online* **11(1)**: 32–51. DOI: 10.1007/s12575-009-9008-x.

Finan, K., A. Raulf, and M. Heilemann. 2015. A Set of Homo-Oligomeric Standards Allows Accurate Protein Counting. *Angewandte Chemie International Edition* **54(41)**: 12049–12052. DOI: 10.1002/anie.201505664.

Footer, M. J., J. W. J. Kerssemakers, J. A. Theriot, and M. Dogterom. 2007. Direct measurement of force generation by actin filament polymerization using an optical trap. *Proceedings of the National Academy of Sciences* **104(7)**: 2181–2186. DOI: 10.1073/pnas.0607052104.

Förster, R., K. Wicker, W. Müller, A. Jost, and R. Heintzmann. 2016. Motion artefact detection in structured illumination microscopy for live cell imaging. *Optics Express* **24(19)**: 22121–22134. DOI: 10.1364/OE.24.022121.

Fotin, A., Y. Cheng, P. Sliz, N. Grigorieff, S. C. Harrison, T. Kirchhausen, and T. Walz. 2004. Molecular model for a complete clathrin lattice from electron cryomicroscopy. *Nature* **432(7017)**: 573–579. DOI: 10.1038/nature03079.

Frei, M. S., P. Hoess, M. Lampe, B. Nijmeijer, M. Kueblbeck, J. Ellenberg, H. Wadepohl, J. Ries, S. Pitsch, L. Reymond, and K. Johnsson. 2019. Photoactivation of silicon rhodamines via a light-induced protonation. *Nature Communications* **10(1)**: 4580. DOI: 10.1038/s41467-019-12480-3.

Friesen, H., C. Humphries, Y. Ho, O. Schub, K. Colwill, and B. J. Andrews. 2006. Characterization of the Yeast Amphiphysins Rvs161p and Rvs167p Reveals Roles for the Rvs Heterodimer *In Vivo*. *Molecular Biology of the Cell* **17(3)**: 1306–1321. DOI: 10.1091/mbc.e05-06-0476.

Fu, Z., D. Peng, M. Zhang, F. Xue, R. Zhang, W. He, T. Xu, and P. Xu. 2019. mEosEM withstands osmium staining and Epon embedding for super-resolution CLEM. *Nature Methods* **17(1)**: 55–58. DOI: 10.1038/s41592-019-0613-6.

Fu, Z., S. Kaledhonkar, A. Borg, M. Sun, B. Chen, R. A. Grassucci, M. Ehrenberg, and J. Frank. 2016. Key Intermediates in Ribosome Recycling Visualized by Time-Resolved Cryoelectron Microscopy. *Structure* **24(12)**: 2092–2101. DOI: 10.1016/j.str.2016.09.014.

Gagny, B., A. Wiederkehr, P. Dumoulin, B. Winsor, H. Riezman, and R. Haguenauer-Tsapis. 2000. A novel EH domain protein of *Saccharomyces cerevisiae*, Ede1p, involved in endocytosis. *Journal of Cell Science* **113(18)**: 3309–3319.

Galletta, B. J., D. Y. Chuang, and J. A. Cooper. 2008. Distinct Roles for Arp2/3 Regulators in Actin Assembly and Endocytosis. *PLOS Biology* **6(1)**: e1. DOI: 10.1371/journal.pbio.0060001.

Gambarotto, D., F. U. Zwettler, M. L. Guennec, M. Schmidt-Cernohorska, D. Fortun, S. Borgers, J. Heine, J.-G. Schloetel, M. Reuss, M. Unser, E. S. Boyden, M. Sauer, V. Hamel, and P. Guichard. 2018. Imaging cellular ultrastructures using expansion microscopy (U-ExM). *Nature Methods* **16(1)**: 71–74. DOI: 10.1038/s41592-018-0238-1.

Gandhi, M., B. A. Smith, M. Bovellan, V. Paavilainen, K. Daugherty-Clarke, J. Gelles, P. Lappalainen, and B. L. Goode. 2010. GMF Is a Cofilin Homolog that Binds Arp2/3 Complex to Stimulate Filament Debranching and Inhibit Actin Nucleation. *Current Biology* **20(9)**: 861–867. DOI: 10.1016/j.cub.2010.03.026.

Gao, R., S. M. Asano, S. Upadhyayula, I. Pisarev, D. E. Milkie, T.-L. Liu, V. Singh, A. Graves, G. H. Huynh, Y. Zhao, J. Bogovic, J. Colonell, C. M. Ott, C. Zugates, S. Tappan, A. Rodriguez, K. R. Mosaliganti, S.-H. Sheu, H. A. Pasolli, S. Pang, C. S. Xu, S. G. Megason, H. F. Hess, J. Lippincott-Schwartz, A. Hantman, G. M. Rubin, T. Kirchhausen, S. Saalfeld, Y. Aso, E. S. Boyden, and E. Betzig. 2019. Cortical column and whole-brain imaging with molecular contrast and nanoscale resolution. *Science* **363(6424)**: eaau8302. DOI: 10.1126/science.aau8302.

Gautier, A., A. Juillerat, C. Heinis, I. R. Corrêa, M. Kindermann, F. Beaufils, and K. Johnsson. 2008. An Engineered Protein Tag for Multiprotein Labeling in Living Cells. *Chemistry & Biology* **15(2)**: 128–136. DOI: 10.1016/j.chembiol.2008.01.007.

Gebhardt, C., M. Lehmann, M. Reif, M. Zacharias, and T. Cordes. 2020. Molecular and spectroscopic characterization of green and red cyanine fluorophores from the Alexa Fluor and AF series. *bioRxiv*: 2020.11.13.381152. DOI: 10.1101/2020.11.13.381152.

Geli, M. I. and H. Riezman. 1996. Role of Type I Myosins in Receptor-Mediated Endocytosis in Yeast. *Science* **272(5261)**: 533–535. DOI: 10.1126/science.272.5261.533.

Gheorghe, D. M., S. Aghamohammadzadeh, I. I. S.-d. Rooij, E. G. Allwood, S. J. Winder, and K. R. Ayscough. 2008. Interactions between the Yeast SM22 Homologue Scp1 and Actin Demonstrate the Importance of Actin Bundling in Endocytosis. *Journal of Biological Chemistry* **283(22)**: 15037–15046. DOI: 10.1074/jbc.M710332200.

Goley, E. D. and M. D. Welch. 2006. The ARP2/3 complex: an actin nucleator comes of age. *Nature Reviews Molecular Cell Biology* **7(10)**: 713–726. DOI: 10.1038/nrm2026.

Goode, B. L., J. A. Eskin, and B. Wendland. 2015. Actin and Endocytosis in Budding Yeast. *Genetics* **199(2)**: 315–358. DOI: 10.1534/genetics.112.145540.

Goode, B. L., A. A. Rodal, G. Barnes, and D. G. Drubin. 2001. Activation of the Arp2/3 Complex by the Actin Filament Binding Protein Abp1p. *Journal of Cell Biology* **153(3)**: 627–634. DOI: 10.1083/jcb.153.3.627.

Götzke, H., M. Kilisch, M. Martínez-Carranza, S. Sograte-Idrissi, A. Rajavel, T. Schlichthaerle, N. Engels, R. Jungmann, P. Stenmark, F. Opazo, and S. Frey. 2019. The ALFA-tag is a highly versatile tool for nanobody-based bioscience applications. *Nature Communications* **10(1)**: 4403. DOI: 10.1038/s41467-019-12301-7.

Grimm, J. B., B. P. English, J. Chen, J. P. Slaughter, Z. Zhang, A. Revyakin, R. Patel, J. J. Macklin, D. Normanno, R. H. Singer, T. Lionnet, and L. D. Lavis. 2015. A general method to improve fluorophores for live-cell and single-molecule microscopy. *Nature Methods* **12(3)**: 244–250. DOI: 10.1038/nmeth.3256.

Grimm, J. B., B. P. English, H. Choi, A. K. Muthusamy, B. P. Mehl, P. Dong, T. A. Brown, J. Lippincott-Schwartz, Z. Liu, T. Lionnet, and L. D. Lavis. 2016. Bright photoactivatable fluorophores for single-molecule imaging. *Nature Methods* **13(12)**: 985–988. DOI: 10.1038/nmeth.4034.

Gu, L., Y. Li, S. Zhang, Y. Xue, W. Li, D. Li, T. Xu, and W. Ji. 2019. Molecular resolution imaging by repetitive optical selective exposure. *Nature Methods* **16(11)**: 1114–1118. DOI: 10.1038/s41592-019-0544-2.

Gunewardene, M. S., F. V. Subach, T. J. Gould, G. P. Penoncello, M. V. Gudheti, V. V. Verkhusha, and S. T. Hess. 2011. Superresolution Imaging of Multiple Fluorescent Proteins with Highly Overlapping Emission Spectra in Living Cells. *Biophysical Journal* **101(6)**: 1522–1528. DOI: 10.1016/j.bpj.2011.07.049.

Guo, F., M. Holla, M. M. Díaz, and M. Rosbash. 2018a. A Circadian Output Circuit Controls Sleep-Wake Arousal in *Drosophila*. *Neuron* **100(3)**: 624–635.e4. DOI: 10.1016/j.neuron.2018.09.002.

Guo, S., O. S. Sokolova, J. Chung, S. Padrick, J. Gelles, and B. L. Goode. 2018b. Abp1 promotes Arp2/3 complex-dependent actin nucleation and stabilizes branch junctions by antagonizing GMF. *Nature Communications* **9(1)**: 2895. DOI: 10.1038/s41467-018-05260-y.

Gurskaya, N. G., V. V. Verkhusha, A. S. Shcheglov, D. B. Staroverov, T. V. Chepurnykh, A. F. Fradkov, S. Lukyanov, and K. A. Lukyanov. 2006. Engineering of a monomeric green-to-red photoactivatable fluorescent protein induced by blue light. *Nature Biotechnology* **24(4)**: 461–465. DOI: 10.1038/nbt1191.

Gustafsson, M. G. L. 2000. Surpassing the lateral resolution limit by a factor of two using structured illumination microscopy. *Journal of Microscopy* **198(2)**: 82–87. DOI: 10.1046/j.1365-2818.2000.00710.x.

Gustafsson, M. G. L., L. Shao, P. M. Carlton, C. J. R. Wang, I. N. Golubovskaya, W. Z. Cande, D. A. Agard, and J. W. Sedat. 2008. Three-Dimensional Resolution Doubling in Wide-Field Fluorescence Microscopy by Structured Illumination. *Biophysical Journal* **94(12)**: 4957–4970. DOI: 10.1529/biophysj.107.120345.

Gustafsson, N., S. Culley, G. Ashdown, D. M. Owen, P. M. Pereira, and R. Henriques. 2016. Fast live-cell conventional fluorophore nanoscopy with ImageJ through super-resolution radial fluctuations. *Nature Communications* **7(1)**: 12471. DOI: 10.1038/ncomms12471.

Gwosch, K. C., J. K. Pape, F. Balzarotti, P. Hoess, J. Ellenberg, J. Ries, and S. W. Hell. 2020. MINFLUX nanoscopy delivers 3D multicolor nanometer resolution in cells. *Nature Methods* **17(2)**: 217–224. DOI: 10.1038/s41592-019-0688-0.

Ha, T. and P. Tinnefeld. 2012. Photophysics of Fluorescent Probes for Single-Molecule Biophysics and Super-Resolution Imaging. *Annual Review of Physical Chemistry* **63(1)**: 595–617. DOI: 10.1146/annurev-physchem-032210-103340.

Halpern, A. R., G. C. M. Alas, T. J. Chozinski, A. R. Paredez, and J. C. Vaughan. 2017. Hybrid Structured Illumination Expansion Microscopy Reveals Microbial Cytoskeleton Organization. *ACS Nano* **11(12)**: 12677–12686. DOI: 10.1021/acsnano.7b07200.

Harke, B., C. K. Ullal, J. Keller, and S. W. Hell. 2008. Three-Dimensional Nanoscopy of Colloidal Crystals. *Nano Letters* **8(5)**: 1309–1313. DOI: 10.1021/nl073164n.

Harris, C. R., K. J. Millman, S. J. van der Walt, R. Gommers, P. Virtanen, D. Cournapeau, E. Wieser, J. Taylor, S. Berg, N. J. Smith, R. Kern, M. Picus, S. Hoyer, M. H. van Kerkwijk, M. Brett, A. Haldane, J. F. del Río, M. Wiebe, P. Peterson, P. Gérard-Marchant, K. Sheppard, T. Reddy, W. Weckesser, H. Abbasi, C. Gohlke, and T. E. Oliphant. 2020. Array programming with NumPy. *Nature* **585(7825)**: 357–362. DOI: 10.1038/s41586-020-2649-2.

Hartwich, T. M. P., K. K. H. Chung, L. K. Schroeder, J. Bewersdorf, C. Soeller, and D. Baddeley. 2018. A stable, high refractive index, switching buffer for super-resolution imaging. *bioRxiv*: 465492. DOI: 10.1101/465492.

Haruki, H., J. Nishikawa, and U. K. Laemmli. 2008. The Anchor-Away Technique: Rapid, Conditional Establishment of Yeast Mutant Phenotypes. *Molecular Cell* **31(6)**: 925–932. DOI: 10.1016/j.molcel.2008.07.020.

Heilemann, M., E. Margeat, R. Kasper, M. Sauer, and P. Tinnefeld. 2005. Carbocyanine Dyes as Efficient Reversible Single-Molecule Optical Switch. *Journal of the American Chemical Society* **127(11)**: 3801–3806. DOI: 10.1021/ja044686x.

Heilemann, M., S. van de Linde, M. Schüttpelz, R. Kasper, B. Seefeldt, A. Mukherjee, P. Tinnefeld, and M. Sauer. 2008. Subdiffraction-Resolution Fluorescence Imaging with Conventional Fluorescent Probes. *Angewandte Chemie International Edition* **47(33)**: 6172–6176. DOI: 10.1002/anie.200802376.

Heimstädt, O. 1911. Das Fluoreszenzmikroskop. *Zeitschrift für wissenschaftliche Mikroskopie und mikroskopische Technik* **28** 330–337.

Hell, S. W. and E. H. K. Stelzer. 1992. Properties of a 4Pi confocal fluorescence microscope. *JOSA A* **9(12)**: 2159–2166. DOI: 10.1364/JOSAA.9.002159.

Hell, S. W. and J. Wichmann. 1994. Breaking the diffraction resolution limit by stimulated emission: stimulated-emission-depletion fluorescence microscopy. *Optics Letters* **19(11)**: 780–782. DOI: 10.1364/OL.19.000780.

Hess, S. T., T. P. K. Girirajan, and M. D. Mason. 2006. Ultra-High Resolution Imaging by Fluorescence Photoactivation Localization Microscopy. *Biophysical Journal* **91(11)**: 4258–4272. DOI: 10.1529/biophysj.106.091116.

Heydarian, H., A. Przybylski, F. Schueder, R. Jungmann, B. van Werkhoven, J. Keller-Findeisen, J. Ries, S. Stallinga, M. Bates, and B. Rieger. 2019. Three dimensional particle averaging for structural imaging of macromolecular complexes by localization microscopy. *bioRxiv*: 837575. DOI: 10.1101/837575.

Heydarian, H., F. Schueder, M. T. Strauss, B. van Werkhoven, M. Fazel, K. A. Lidke, R. Jungmann, S. Stallinga, and B. Rieger. 2018. Template-free 2D particle fusion in localization microscopy. *Nature Methods* **15(10)**: 781–784. DOI: 10.1038/s41592-018-0136-6.

Hinrichsen, L., A. Meyerholz, S. Groos, and E. J. Ungewickell. 2006. Bending a membrane: How clathrin affects budding. *Proceedings of the National Academy of Sciences* **103(23)**: 8715–8720. DOI: 10.1073/pnas.0600312103.

Ho, K.-C., J. K. Leach, K. Eley, R. B. Mikkelsen, and P.-S. Lin. 2003. A Simple Method of Producing Low Oxygen Conditions With Oxyrase for Cultured Cells Exposed to Radiation and Tirapazamine. *American Journal of Clinical Oncology* **26(4)**: e86. DOI: 10.1097/01.COC.0000077937.91824.44.

Hoess, P., M. Mund, M. Reitberger, and J. Ries. 2018. Dual-Color and 3D Super-Resolution Microscopy of Multi-protein Assemblies. *Protein Complex Assembly*. **1764** Springer: 237–251. ISBN: 978-1-4939-7758-1. DOI: 10.1007/978-1-4939-7759-8_14.

Hofmann, M., C. Eggeling, S. Jakobs, and S. W. Hell. 2005. Breaking the diffraction barrier in fluorescence microscopy at low light intensities by using reversibly photoswitchable proteins. *Proceedings of the National Academy of Sciences* **102(49)**: 17565–17569. DOI: 10.1073/pnas.0506010102.

Holden, S. J., T. Pengo, K. L. Meibom, C. F. Fernandez, J. Collier, and S. Manley. 2014. High throughput 3D super-resolution microscopy reveals *Caulobacter crescentus in vivo* Z-ring organization. *Proceedings of the National Academy of Sciences* **111(12)**: 4566–4571. DOI: 10.1073/pnas.1313368111.

Holden, S. J., S. Uphoff, and A. N. Kapanidis. 2011. DAOSTORM: an algorithm for high-density super-resolution microscopy. *Nature Methods* **8(4)**: 279–280. DOI: 10.1038/nmeth0411-279.

Huang, B., W. Wang, M. Bates, and X. Zhuang. 2008. Three-Dimensional Super-Resolution Imaging by Stochastic Optical Reconstruction Microscopy. *Science* **319(5864)**: 810–813. DOI: 10.1126/science.1153529.

Huang, F., T. M. P. Hartwich, F. E. Rivera-Molina, Y. Lin, W. C. Duim, J. J. Long, P. D. Uchil, J. R. Myers, M. A. Baird, W. Mothes, M. W. Davidson, D. Toomre, and J. Bewersdorf. 2013. Video-rate nanoscopy using sCMOS camera–specific single-molecule localization algorithms. *Nature Methods* **10(7)**: 653–658. DOI: 10.1038/nmeth.2488.

Huang, F., S. L. Schwartz, J. M. Byars, and K. A. Lidke. 2011. Simultaneous multiple-emitter fitting for single molecule super-resolution imaging. *Biomedical Optics Express* **2(5)**: 1377–1393. DOI: 10.1364/BOE.2.001377.

Huang, X., J. Fan, L. Li, H. Liu, R. Wu, Y. Wu, L. Wei, H. Mao, A. Lal, P. Xi, L. Tang, Y. Zhang, Y. Liu, S. Tan, and L. Chen. 2018. Fast, long-term, super-resolution imaging with Hessian structured illumination microscopy. *Nature Biotechnology* **36(5)**: 451–459. DOI: 10.1038/nbt.4115.

Hunter, J. D. 2007. Matplotlib: A 2D graphics environment. *Computing in Science Engineering* **9(3)**: 90–95. DOI: 10.1109/MCSE.2007.55.

Hurlock, M. E., I. Čavka, L. E. Kursel, J. Haversat, M. Wooten, Z. Nizami, R. Turniansky, P. Hoess, J. Ries, J. G. Gall, O. Rog, S. Köhler, and Y. Kim. 2020. Identification of novel synaptonemal complex components in *C. elegans*. *Journal of Cell Biology* **219(5)**. DOI: 10.1083/jcb.201910043.

Idrissi, F.-Z., A. Blasco, A. Espinal, and M. I. Geli. 2012. Ultrastructural dynamics of proteins involved in endocytic budding. *Proceedings of the National Academy of Sciences* **109(39)**: E2587–E2594. DOI: 10.1073/pnas.1202789109.

Idrissi, F.-Z., H. Grötsch, I. M. Fernández-Golbano, C. Presciatto-Baschong, H. Riezman, and M. I. Geli. 2008. Distinct acto/myosin-I structures associate with endocytic profiles at the plasma membrane. *Journal of Cell Biology* **180(6)**: 1219–1232. DOI: 10.1083/jcb.200708060.

Illuxley, C., E. D. Green, and I. Dunbam. 1990. Rapid assessment of *S. cerevisiae* mating type by PCR. *Trends in Genetics* **6** 236. DOI: 10.1016/0168-9525(90)90190-H.

Ingerman, E., J. Y. Hsiao, and R. D. Mullins. 2013. Arp2/3 complex ATP hydrolysis promotes lamellipodial actin network disassembly but is dispensable for assembly. *Journal of Cell Biology* **200(5)**: 619–633. DOI: 10.1083/jcb.201211069.

Janke, C., M. M. Magiera, N. Rathfelder, C. Taxis, S. Reber, H. Maekawa, A. Moreno-Borchart, G. Doenges, E. Schwob, E. Schiebel, and M. Knop. 2004. A versatile toolbox for PCR-based tagging of yeast genes: new fluorescent proteins, more markers and promoter substitution cassettes. *Yeast* **21(11)**: 947–962. DOI: 10.1002/yea.1142.

Jeger, S., K. Zimmermann, A. Blanc, J. Grünberg, M. Honer, P. Hunziker, H. Struthers, and R. Schibli. 2010. Site-Specific and Stoichiometric Modification of Antibodies by Bacterial Transglutaminase. *Angewandte Chemie International Edition* **49(51)**: 9995–9997. DOI: 10.1002/anie.201004243.

Jensen, N. A., I. Jansen, M. Kamper, and S. Jakobs. 2020. Reversibly Switchable Fluorescent Proteins for RESOLFT Nanoscopy. *Nanoscale Photonic Imaging*. Springer International Publishing: 241–261. ISBN: 978-3-030-34413-9. DOI: 10.1007/978-3-030-34413-9_9.

Jia, S., J. C. Vaughan, and X. Zhuang. 2014. Isotropic three-dimensional super-resolution imaging with a self-bending point spread function. *Nature Photonics* **8(4)**: 302–306. DOI: 10.1038/nphoton.2014.13.

Jimenez Sabinina, V., M. J. Hossain, J.-K. Heriche, P. Hoess, B. Nijmeijer, S. Mosalaganti, M. Kueblbeck, A. Callegari, A. Szymborska, M. Beck, J. Ries, and J. Ellenberg. 2020. 3D super-resolution fluorescence microscopy maps the variable molecular architecture of the Nuclear Pore Complex. *bioRxiv*: 2020.11.27.386599. DOI: 10.1101/2020.11.27.386599.

Jinek, M., A. East, A. T. Cheng, S. Lin, E. Ma, and J. Doudna. 2013. RNA-programmed genome editing in human cells. *eLife* **2** e00471. DOI: 10.7554/eLife.00471.

Johnston, A. B., A. Collins, and B. L. Goode. 2015. High-speed depolymerization at actin filament ends jointly catalysed by Twinfilin and Srv2/CAP. *Nature Cell Biology* **17(11)**: 1504–1511. DOI: 10.1038/ncb3252.

Jouchet, P., C. Cabriel, N. Bourg, M. Bardou, C. Pous, E. Fort, and S. Lévêque-Fort. 2019. Nanometric axial localization of single fluorescent molecules with modulated excitation. *bioRxiv*: 865865. DOI: 10.1101/865865.

Juette, M. F., T. J. Gould, M. D. Lessard, M. J. Mlodzianoski, B. S. Nagpure, B. T. Bennett, S. T. Hess, and J. Bewersdorf. 2008. Three-dimensional sub–100 nm resolution fluorescence microscopy of thick samples. *Nature Methods* **5(6)**: 527–529. DOI: 10.1038/nmeth.1211.

Jung, N. and V. Haucke. 2007. Clathrin-Mediated Endocytosis at Synapses. *Traffic* **8(9)**: 1129–1136. DOI: 10.1111/j.1600-0854.2007.00595.x.

Jungmann, R., M. S. Avendaño, M. Dai, J. B. Woehrstein, S. S. Agasti, Z. Feiger, A. Rodal, and P. Yin. 2016. Quantitative super-resolution imaging with qPAINT. *Nature Methods* **13(5)**: 439–442. DOI: 10.1038/nmeth.3804.

Jungmann, R., M. S. Avendaño, J. B. Woehrstein, M. Dai, W. M. Shih, and P. Yin. 2014. Multiplexed 3D cellular super-resolution imaging with DNA-PAINT and Exchange-PAINT. *Nature Methods* **11(3)**: 313–318. DOI: 10.1038/nmeth.2835.

Jungmann, R., C. Steinhauer, M. Scheible, A. Kuzyk, P. Tinnefeld, and F. C. Simmel. 2010. Single-Molecule Kinetics and Super-Resolution Microscopy by Fluorescence Imaging of Transient Binding on DNA Origami. *Nano Letters* **10(11)**: 4756–4761. DOI: 10.1021/nl103427w.

Kaksonen, M. and A. Roux. 2018. Mechanisms of clathrin-mediated endocytosis. *Nature Reviews Molecular Cell Biology* **19(5)**: 313–326. DOI: 10.1038/nrm.2017.132.

Kaksonen, M., Y. Sun, and D. G. Drubin. 2003. A Pathway for Association of Receptors, Adaptors, and Actin during Endocytic Internalization. *Cell* **115(4)**: 475–487. DOI: 10.1016/S0092-8674(03)00883-3.

Kaksonen, M., C. P. Toret, and D. G. Drubin. 2005. A Modular Design for the Clathrin- and Actin-Mediated Endocytosis Machinery. *Cell* **123(2)**: 305–320. DOI: 10.1016/j.cell.2005.09.024.

Kaksonen, M., C. P. Toret, and D. G. Drubin. 2006. Harnessing actin dynamics for clathrin-mediated endocytosis. *Nature Reviews Molecular Cell Biology* **7(6)**: 404–414. DOI: 10.1038/nrm1940.

Kaledhonkar, S., Z. Fu, H. White, and J. Frank. 2018. Time-Resolved Cryo-electron Microscopy Using a Microfluidic Chip. *Protein Complex Assembly*. **1764** Springer: 59–71. ISBN: 978-1-4939-7758-1. DOI: 10.1007/978-1-4939-7759-8_4.

Kanchanawong, P., G. Shtengel, A. M. Pasapera, E. B. Ramko, M. W. Davidson, H. F. Hess, and C. M. Waterman. 2010. Nanoscale architecture of integrin-based cell adhesions. *Nature* **468(7323)**: 580–584. DOI: 10.1038/nature09621.

Kaplan, C., S. J. Kenny, S. Chen, J. Schoeneberg, E. Sitarska, A. Diz-Muñoz, K. Xu, and D. G. Drubin. 2020. Adaptive actin organization counteracts elevated membrane tension to ensure robust endocytosis. *bioRxiv*: 2020.04.05.026559. DOI: 10.1101/2020.04.05.026559.

Kawaoka, K., A. U. Khan, and D. R. Kearns. 1967. Role of Singlet Excited States of Molecular Oxygen in the Quenching of Organic Triplet States. *The Journal of Chemical Physics* **46(5)**: 1842–1853. DOI: 10.1063/1.1840943.

Kechkar, A., D. Nair, M. Heilemann, D. Choquet, and J.-B. Sibarita. 2013. Real-Time Analysis and Visualization for Single-Molecule Based Super-Resolution Microscopy. *PLOS ONE* **8(4)**: e62918. DOI: 10.1371/journal.pone.0062918.

Keppler, A., S. Gendreizig, T. Gronemeyer, H. Pick, H. Vogel, and K. Johnsson. 2003. A general method for the covalent labeling of fusion proteins with small molecules *in vivo*. *Nature Biotechnology* **21(1)**: 86–89. DOI: 10.1038/nbt765.

Kilian, N., A. Goryaynov, M. D. Lessard, G. Hooker, D. Toomre, J. E. Rothman, and J. Bewersdorf. 2018. Assessing photodamage in live-cell STED microscopy. *Nature Methods* **15(10)**: 755–756. DOI: 10.1038/s41592-018-0145-5.

Klar, T. A. and S. W. Hell. 1999. Subdiffraction resolution in far-field fluorescence microscopy. *Optics Letters* **24(14)**: 954–956. DOI: 10.1364/OL.24.000954.

Klar, T. A., S. Jakobs, M. Dyba, A. Egner, and S. W. Hell. 2000. Fluorescence microscopy with diffraction resolution barrier broken by stimulated emission. *Proceedings of the National Academy of Sciences* **97(15)**: 8206–8210. DOI: 10.1073/pnas.97.15.8206.

Klehs, K., C. Spahn, U. Endesfelder, S. F. Lee, A. Fürstenberg, and M. Heilemann. 2014. Increasing the Brightness of Cyanine Fluorophores for Single-Molecule and Superresolution Imaging. *ChemPhysChem* **15(4)**: 637–641. DOI: 10.1002/cphc.201300874.

Klein, M. G., W. Shi, U. Ramagopal, Y. Tseng, D. Wirtz, D. R. Kovar, C. J. Staiger, and S. C. Almo. 2004. Structure of the Actin Crosslinking Core of Fimbrin. *Structure* **12(6)**: 999–1013. DOI: 10.1016/j.str.2004.04.010.

Klein, T., A. Löschberger, S. Proppert, S. Wolter, S. van de Linde, and M. Sauer. 2011. Live-cell dSTORM with SNAP-tag fusion proteins. *Nature Methods* **8(1)**: 7–9. DOI: 10.1038/nmeth0111-7b.

Klepeis, J. L., K. Lindorff-Larsen, R. O. Dror, and D. E. Shaw. 2009. Long-timescale molecular dynamics simulations of protein structure and function. *Current Opinion in Structural Biology* **19(2)**: 120–127. DOI: 10.1016/j.sbi.2009.03.004.

Koch, B., B. Nijmeijer, M. Kueblbeck, Y. Cai, N. Walther, and J. Ellenberg. 2018. Generation and validation of homozygous fluorescent knock-in cells using CRISPR–Cas9 genome editing. *Nature Protocols* **13(6)**: 1465–1487. DOI: 10.1038/nprot.2018.042.

Köhler, S., M. Wojcik, K. Xu, and A. F. Dernburg. 2017. Superresolution microscopy reveals the three-dimensional organization of meiotic chromosome axes in intact *Caenorhabditis elegans* tissue. *Proceedings of the National Academy of Sciences* **114(24)**: E4734–E4743. DOI: 10.1073/pnas.1702312114.

Kozak, M. and M. Kaksonen. 2019. Phase separation of Ede1 promotes the initiation of endocytic events. *bioRxiv*: 861203. DOI: 10.1101/861203.

Ku, T., J. Swaney, J.-Y. Park, A. Albanese, E. Murray, J. H. Cho, Y.-G. Park, V. Mangena, J. Chen, and K. Chung. 2016. Multiplexed and scalable super-resolution imaging of three-dimensional protein localization in size-adjustable tissues. *Nature Biotechnology* **34(9)**: 973–981. DOI: 10.1038/nbt.3641.

Kühlbrandt, W. 2014. The Resolution Revolution. *Science* **343(6178)**: 1443–1444. DOI: 10.1126/science.1251652.

Kukulski, W., A. Picco, T. Specht, J. A. G. Briggs, and M. Kaksonen. 2016. Clathrin modulates vesicle scission, but not invagination shape, in yeast endocytosis. *eLife* **5** e16036. DOI: 10.7554/eLife.16036.

Kukulski, W., M. Schorb, M. Kaksonen, and J. A. G. Briggs. 2012. Plasma Membrane Reshaping during Endocytosis Is Revealed by Time-Resolved Electron Tomography. *Cell* **150(3)**: 508–520. DOI: 10.1016/j.cell.2012.05.046.

Lacy, M. M., D. Baddeley, and J. Berro. 2019. Single-molecule turnover dynamics of actin and membrane coat proteins in clathrin-mediated endocytosis. *eLife* **8** e52355. DOI: 10.7554/eLife.52355.

Lee, S.-H., J. Y. Shin, A. Lee, and C. Bustamante. 2012. Counting single photoactivatable fluorescent molecules by photoactivated localization microscopy (PALM). *Proceedings of the National Academy of Sciences* **109(43)**: 17436–17441. DOI: 10.1073/pnas.1215175109.

Legant, W. R., L. Shao, J. B. Grimm, T. A. Brown, D. E. Milkie, B. B. Avants, L. D. Lavis, and E. Betzig. 2016. High-density three-dimensional localization microscopy across large volumes. *Nature Methods* **13(4)**: 359–365. DOI: 10.1038/nmeth.3797.

Lehmann, M., G. Lichtner, H. Klenz, and J. Schmoranzer. 2015. Novel organic dyes for multicolor localization-based super-resolution microscopy. *Journal of Biophotonics* **9(1-2)**: 161–170. DOI: 10.1002/jbio.201500119.

Lesage, G. and H. Bussey. 2006. Cell Wall Assembly in *Saccharomyces cerevisiae*. *Microbiology and Molecular Biology Reviews* **70(2)**: 317–343. DOI: 10.1128/MMBR.00038-05.

Levet, F., G. Julien, R. Galland, C. Butler, A. Beghin, A. Chazeau, P. Hoess, J. Ries, G. Giannone, and J.-B. Sibarita. 2019. A tessellation-based colocalization analysis approach for single-molecule localization microscopy. *Nature Communications* **10(1)**: 2379. DOI: 10.1038/s41467-019-10007-4.

Lewellyn, E. B., R. T. A. Pedersen, J. Hong, R. Lu, H. M. Morrison, and D. G. Drubin. 2015. An Engineered Minimal WASP-Myosin Fusion Protein Reveals Essential Functions for Endocytosis. *Developmental Cell* **35(3)**: 281–294. DOI: 10.1016/j.devcel.2015.10.007.

Li, Y., M. Mund, P. Hoess, J. Deschamps, U. Matti, B. Nijmeijer, V. J. Sabinina, J. Ellenberg, I. Schoen, and J. Ries. 2018. Real-time 3D single-molecule localization using experimental point spread functions. *Nature Methods* **15(5)**: 367–369. DOI: 10.1038/nmeth.4661.

Lichtman, J. W. and J.-A. Conchello. 2005. Fluorescence microscopy. *Nature Methods* **2(12)**: 910–919. DOI: 10.1038/nmeth817.

Lin, C. H., J. A. MacGurn, T. Chu, C. J. Stefan, and S. D. Emr. 2008. Arrestin-Related Ubiquitin-Ligase Adaptors Regulate Endocytosis and Protein Turnover at the Cell Surface. *Cell* **135(4)**: 714–725. DOI: 10.1016/j.cell.2008.09.025.

Lin, Y., J. J. Long, F. Huang, W. C. Duim, S. Kirschbaum, Y. Zhang, L. K. Schroeder, A. A. Rebane, M. G. M. Velasco, A. Virrueta, D. W. Moonan, J. Jiao, S. Y. Hernandez, Y. Zhang, and J. Bewersdorf. 2015. Quantifying and Optimizing Single-Molecule Switching Nanoscopy at High Speeds. *PLOS ONE* **10(5)**: e0128135. DOI: 10.1371/journal.pone.0128135.

Longtine, M. S., A. M. Iii, D. J. Demarini, N. G. Shah, A. Wach, A. Brachat, P. Philippsen, and J. R. Pringle. 1998. Additional modules for versatile and economical PCR-based gene deletion and modification in *Saccharomyces cerevisiae*. *Yeast* **14(10)**: 953–961. DOI: 10.1002/(SICI)1097-0061(199807)14:10<953::AID-YEA293>3.0.CO;2-U.

Lõoke, M., K. Kristjuhan, and A. Kristjuhan. 2011. Extraction of genomic DNA from yeasts for PCR-based applications. *BioTechniques* **50(5)**: 325–328. DOI: 10.2144/000113672.

Los, G. V., L. P. Encell, M. G. McDougall, D. D. Hartzell, N. Karassina, C. Zimprich, M. G. Wood, R. Learish, R. F. Ohana, M. Urh, D. Simpson, J. Mendez, K. Zimmerman, P. Otto, G. Vidugiris, J. Zhu, A. Darzins, D. H. Klaubert, R. F. Bulleit, and K. V. Wood. 2008. HaloTag: A Novel Protein Labeling Technology for Cell Imaging and Protein Analysis. *ACS Chemical Biology* **3(6)**: 373–382. DOI: 10.1021/cb800025k.

Löschberger, A., C. Franke, G. Krohne, S. van de Linde, and M. Sauer. 2014. Correlative super-resolution fluorescence and electron microscopy of the nuclear pore complex with molecular resolution. *Journal of Cell Science* **127(20)**: 4351–4355. DOI: 10.1242/jcs.156620.

M'Saad, O. and J. Bewersdorf. 2020. Light microscopy of proteins in their ultrastructural context. *Nature Communications* **11(1)**: 3850. DOI: 10.1038/s41467-020-17523-8.

Ma, R. and J. Berro. 2018. Structural organization and energy storage in crosslinked actin assemblies. *PLOS Computational Biology* **14(5)**: e1006150. DOI: 10.1371/journal.pcbi.1006150.

Ma, R. and J. Berro. 2019. Crosslinking actin networks produces compressive force. *Cytoskeleton* **76(5)**: 346–354. DOI: 10.1002/cm.21552.

Ma, R. and J. Berro. 2020. Endocytosis against high turgor pressure is made easier by partial protein coating and a freely rotating base. *bioRxiv*: 558890. DOI: 10.1101/558890.

Mahecic, D., I. Testa, J. Griffié, and S. Manley. 2019. Strategies for increasing the throughput of super-resolution microscopies. *Current Opinion in Chemical Biology* **51** 84–91. DOI: 10.1016/j.cbpa.2019.05.012.

Mali, P., L. Yang, K. M. Esvelt, J. Aach, M. Guell, J. E. DiCarlo, J. E. Norville, and G. M. Church. 2013. RNA-Guided Human Genome Engineering via Cas9. *Science* **339(6121)**: 823–826. DOI: 10.1126/science.1232033.

Malkusch, S., U. Endesfelder, J. Mondry, M. Gelléri, P. J. Verveer, and M. Heilemann. 2012. Coordinate-based colocalization analysis of single-molecule localization microscopy data. *Histochemistry and Cell Biology* **137(1)**: 1–10. DOI: 10.1007/s00418-011-0880-5.

Manenschijn, H. E., A. Picco, M. Mund, A.-S. Rivier-Cordey, J. Ries, and M. Kaksonen. 2019. Type-I myosins promote actin polymerization to drive membrane bending in endocytosis. *eLife* **8** e44215. DOI: 10.7554/eLife.44215.

Marsh, R. J., K. Pfisterer, P. Bennett, L. M. Hirvonen, M. Gautel, G. E. Jones, and S. Cox. 2018. Artifact-free high-density localization microscopy analysis. *Nature Methods* **15(9)**: 689–692. DOI: 10.1038/s41592-018-0072-5.

Matsunaga, Y. and Y. Sugita. 2018. Linking time-series of single-molecule experiments with molecular dynamics simulations by machine learning. *eLife* **7** e32668. DOI: 10.7554/eLife.32668.

Mau, A., K. Friedl, C. Leterrier, N. Bourg, and S. Lévêque-Fort. 2020. Fast scanned widefield scheme provides tunable and uniform illumination for optimized SMLM on large fields of view. *bioRxiv*: 2020.05.08.083774. DOI: 10.1101/2020.05.08.083774.

Maurer, C. R., R. Qi, and V. Raghavan. 2003. A linear time algorithm for computing exact Euclidean distance transforms of binary images in arbitrary dimensions. *IEEE Transactions on Pattern Analysis and Machine Intelligence* **25(2)**: 265–270. DOI: 10.1109/TPAMI.2003.1177156.

Mayor, S. and R. E. Pagano. 2007. Pathways of clathrin-independent endocytosis. *Nature Reviews Molecular Cell Biology* **8(8)**: 603–612. DOI: 10.1038/nrm2216.

McEvoy, A. L., H. Hoi, M. Bates, E. Platonova, P. J. Cranfill, M. A. Baird, M. W. Davidson, H. Ewers, J. Liphardt, and R. E. Campbell. 2012. mMaple: A Photoconvertible Fluorescent Protein for Use in Multiple Imaging Modalities. *PLOS ONE* **7(12)**: e51314. DOI: 10.1371/journal.pone.0051314.

McKinney, W. *et al.* 2010. Data structures for statistical computing in python. *Proceedings of the 9th python in science conference*. **445** 51–56.

McMahon, H. T. and E. Boucrot. 2011. Molecular mechanism and physiological functions of clathrin-mediated endocytosis. *Nature Reviews Molecular Cell Biology* **12(8)**: 517–533. DOI: 10.1038/nrm3151.

Mercer, J., M. Schelhaas, and A. Helenius. 2010. Virus Entry by Endocytosis. *Annual Review of Biochemistry* **79(1)**: 803–833. DOI: 10.1146/annurev-biochem-060208-104626.

Michelot, A., M. Costanzo, A. Sarkeshik, C. Boone, J. R. Yates, and D. G. Drubin. 2010. Reconstitution and Protein Composition Analysis of Endocytic Actin Patches. *Current Biology* **20(21)**: 1890–1899. DOI: 10.1016/j.cub.2010.10.016.

Michelot, A., A. Grassart, V. Okreglak, M. Costanzo, C. Boone, and D. G. Drubin. 2013. Actin Filament Elongation in Arp2/3-Derived Networks Is Controlled by Three Distinct Mechanisms. *Developmental Cell* **24(2)**: 182–195. DOI: 10.1016/j.devcel.2012.12.008.

Mikati, M. A., D. Breitsprecher, S. Jansen, E. Reisler, and B. L. Goode. 2015. Coronin Enhances Actin Filament Severing by Recruiting Cofilin to Filament Sides and Altering F-Actin Conformation. *Journal of Molecular Biology* **427(19)**: 3137–3147. DOI: 10.1016/j.jmb.2015.08.011.

Mikhaylova, M., B. M. C. Cloin, K. Finan, R. van den Berg, J. Teeuw, M. M. Kijanka, M. Sokolowski, E. A. Katrukha, M. Maidorn, F. Opazo, S. Moutel, M. Vantard, F. Perez, P. M. P. van Bergen en Henegouwen, C. C. Hoogenraad, H. Ewers, and L. C. Kapitein. 2015. Resolving bundled microtubules using anti-tubulin nanobodies. *Nature Communications* **6(1)**: 7933. DOI: 10.1038/ncomms8933.

Miller, J. C., S. Tan, G. Qiao, K. A. Barlow, J. Wang, D. F. Xia, X. Meng, D. E. Paschon, E. Leung, S. J. Hinkley, G. P. Dulay, K. L. Hua, I. Ankoudinova, G. J. Cost, F. D. Urnov, H. S. Zhang, M. C. Holmes, L. Zhang, P. D. Gregory, and E. J. Rebar. 2011. A TALE nuclease architecture for efficient genome editing. *Nature Biotechnology* **29(2)**: 143–148. DOI: 10.1038/nbt.1755.

Milles, S., S. Tyagi, N. Banterle, C. Koehler, V. VanDelinder, T. Plass, A. P. Neal, and E. A. Lemke. 2012. Click Strategies for Single-Molecule Protein Fluorescence. *Journal of the American Chemical Society* **134(11)**: 5187–5195. DOI: 10.1021/ja210587q.

Minc, N., A. Boudaoud, and F. Chang. 2009. Mechanical Forces of Fission Yeast Growth. *Current Biology* **19(13)**: 1096–1101. DOI: 10.1016/j.cub.2009.05.031.

Möckl, L. and W. E. Moerner. 2020. Super-resolution Microscopy with Single Molecules in Biology and Beyond–Essentials, Current Trends, and Future Challenges. *Journal of the American Chemical Society* **142(42)**: 17828–17844. DOI: 10.1021/jacs.0c08178.

Mogilner, A. and G. Oster. 1996. Cell motility driven by actin polymerization. *Biophysical Journal* **71(6)**: 3030–3045. DOI: 10.1016/S0006-3495(96)79496-1.

Moon, A. L., P. A. Janmey, K. A. Louie, and D. G. Drubin. 1993. Cofilin is an essential component of the yeast cortical cytoskeleton. *Journal of Cell Biology* **120(2)**: 421–435. DOI: 10.1083/jcb.120.2.421.

Mulholland, J., D. Preuss, A. Moon, A. Wong, D. G. Drubin, and D. Botstein. 1994. Ultrastructure of the yeast actin cytoskeleton and its association with the plasma membrane. *Journal of Cell Biology* **125(2)**: 381–391. DOI: 10.1083/jcb.125.2.381.

Mund, M. 2016. Superresolution imaging of clathrin-mediated endocytosis in yeast. PhD Thesis. Ruprecht-Karls-Universität Heidelberg.

Mund, M., C. Kaplan, and J. Ries. 2014. Localization microscopy in yeast. *Methods in Cell Biology*. **123** Elsevier: 253–271. ISBN: 978-0-12-420138-5. DOI: 10.1016/B978-0-12-420138-5.00014-8.

Mund, M., J. A. van der Beek, J. Deschamps, S. Dmitrieff, P. Hoess, J. L. Monster, A. Picco, F. Nédélec, M. Kaksonen, and J. Ries. 2018. Systematic Nanoscale Analysis of Endocytosis Links Efficient Vesicle Formation to Patterned Actin Nucleation. *Cell* **174(4)**: 884–896.e17. DOI: 10.1016/j.cell.2018.06.032.

Musy, M., K. Flaherty, J. Raspopovic, A. Robert-Moreno, J. T. Richtsmeier, and J. Sharpe. 2018. A quantitative method for staging mouse embryos based on limb morphometry. *Development* **145(7)**: dev154856. DOI: 10.1242/dev.154856.

Muyldermans, S. 2001. Single domain camel antibodies: current status. *Reviews in Molecular Biotechnology* **74(4)**: 277–302. DOI: 10.1016/S1389-0352(01)00021-6.

Nahidiazar, L., A. V. Agronskaia, J. Broertjes, B. van den Broek, and K. Jalink. 2016. Optimizing Imaging Conditions for Demanding Multi-Color Super Resolution Localization Microscopy. *PLOS ONE* **11(7)**: e0158884. DOI: 10.1371/journal.pone.0158884.

Nannapaneni, S., D. Wang, S. Jain, B. Schroeder, C. Highfill, L. Reustle, D. Pittsley, A. Maysent, S. Moulder, R. McDowell, and K. Kim. 2010. The yeast dynamin-like protein Vps1:*vps1* mutations perturb the internalization and the motility of endocytic vesicles and endosomes via disorganization of the actin cytoskeleton. *European Journal of Cell Biology* **89(7)**: 499–508. DOI: 10.1016/j.ejcb.2010.02.002.

Nickaeen, M., J. Berro, T. D. Pollard, and B. M. Slepchenko. 2019. Actin assembly produces sufficient forces for endocytosis in yeast. *Molecular Biology of the Cell* **30(16)**: 2014–2024. DOI: 10.1091/mbc.E19-01-0059.

Nienhaus, K., G. U. Nienhaus, J. Wiedenmann, and H. Nar. 2005. Structural basis for photo-induced protein cleavage and green-to-red conversion of fluorescent protein EosFP. *Proceedings of the National Academy of Sciences* **102(26)**: 9156–9159. DOI: 10.1073/pnas.0501874102.

Nieuwenhuizen, R. P. J., M. Bates, A. Szymborska, K. A. Lidke, B. Rieger, and S. Stallinga. 2015. Quantitative Localization Microscopy: Effects of Photophysics and Labeling Stoichiometry. *PLOS ONE* **10(5)**: e0127989. DOI: 10.1371/journal.pone.0127989.

Nyquist, H. 1928. Certain Topics in Telegraph Transmission Theory. *Transactions of the American Institute of Electrical Engineers* **47(2)**: 617–644. DOI: 10.1109/T-AIEE.1928.5055024.

Olivier, N., D. Keller, P. Gönczy, and S. Manley. 2013. Resolution Doubling in 3D-STORM Imaging through Improved Buffers. *PLOS ONE* **8(7)**: e69004. DOI: 10.1371/journal.pone.0069004.

Ong, W. Q., Y. R. Citron, J. Schnitzbauer, D. Kamiyama, and B. Huang. 2015. Heavy water: a simple solution to increasing the brightness of fluorescent proteins in super-resolution imaging. *Chemical Communications* **51(70)**: 13451–13453. DOI: 10.1039/C5CC04575D.

Owen, D. M., C. Rentero, J. Rossy, A. Magenau, D. Williamson, M. Rodriguez, and K. Gaus. 2010. PALM imaging and cluster analysis of protein heterogeneity at the cell surface. *Journal of Biophotonics* **3(7)**: 446–454. DOI: 10.1002/jbio.200900089.

Paez-Segala, M. G., M. G. Sun, G. Shtengel, S. Viswanathan, M. A. Baird, J. J. Macklin, R. Patel, J. R. Allen, E. S. Howe, G. Piszczek, H. F. Hess, M. W. Davidson, Y. Wang, and L. L. Looger. 2015. Fixation-resistant photoactivatable fluorescent proteins for CLEM. *Nature Methods* **12(3)**: 215–218. DOI: 10.1038/nmeth.3225.

Palade, G. 1975. Intracellular aspects of the process of protein synthesis. *Science* **189(4200)**: 347–358. DOI: 10.1126/science.1096303.

Pape, J. K., T. Stephan, F. Balzarotti, R. Büchner, F. Lange, D. Riedel, S. Jakobs, and S. W. Hell. 2020. Multicolor 3D MINFLUX nanoscopy of mitochondrial MICOS proteins. *Proceedings of the National Academy of Sciences* **117(34)**: 20607–20614. DOI: 10.1073/pnas.2009364117.

Park, J. J. and Y. P. Loh. 2008. Minireview: How Peptide Hormone Vesicles Are Transported to the Secretion Site for Exocytosis. *Molecular Endocrinology* **22(12)**: 2583–2595. DOI: 10.1210/me.2008-0209.

Patel, A. B., R. K. Louder, B. J. Greber, S. Grünberg, J. Luo, J. Fang, Y. Liu, J. Ranish, S. Hahn, and E. Nogales. 2018. Structure of human TFIID and mechanism of TBP loading onto promoter DNA. *Science* **362(6421)**: eaau8872. DOI: 10.1126/science.aau8872.

Patil, P. V. and D. P. Ballou. 2000. The Use of Protocatechuate Dioxygenase for Maintaining Anaerobic Conditions in Biochemical Experiments. *Analytical Biochemistry* **286(2)**: 187–192. DOI: 10.1006/abio.2000.4802.

Patterson, G. H. and J. Lippincott-Schwartz. 2002. A Photoactivatable GFP for Selective Photolabeling of Proteins and Cells. *Science* **297(5588)**: 1873–1877. DOI: 10.1126/science.1074952.

Pavani, S. R. P., M. A. Thompson, J. S. Biteen, S. J. Lord, N. Liu, R. J. Twieg, R. Piestun, and W. E. Moerner. 2009. Three-dimensional, single-molecule fluorescence imaging beyond the diffraction limit by using a double-helix point spread function. *Proceedings of the National Academy of Sciences* **106(9)**: 2995–2999. DOI: 10.1073/pnas.0900245106.

Pedersen, R. T. A. and D. G. Drubin. 2019. Type I myosins anchor actin assembly to the plasma membrane during clathrin-mediated endocytosis. *Journal of Cell Biology* **218(4)**: 1138–1147. DOI: 10.1083/jcb.201810005.

Pedersen, R. T. A., J. E. Hassinger, P. Marchando, and D. G. Drubin. 2020. Spatial regulation of clathrin-mediated endocytosis through position-dependent site maturation. *Journal of Cell Biology* **219(11)**. DOI: 10.1083/jcb.202002160.

Pereira, P. M., D. Albrecht, S. Culley, C. Jacobs, M. Marsh, J. Mercer, and R. Henriques. 2019. Fix Your Membrane Receptor Imaging: Actin Cytoskeleton and CD4 Membrane Organization Disruption by Chemical Fixation. *Frontiers in Immunology* **10** 675. DOI: 10.3389/fimmu.2019.00675.

Pesce, L., M. Cozzolino, L. Lanzanò, A. Diaspro, and P. Bianchini. 2019. Measuring expansion from macro- to nanoscale using NPC as intrinsic reporter. *Journal of Biophotonics* **12(8)**: e201900018. DOI: 10.1002/jbio.201900018.

Pessino, V., Y. R. Citron, S. Feng, and B. Huang. 2017. Covalent Protein Labeling by SpyTag-SpyCatcher in Fixed Cells for Super-Resolution Microscopy. *ChemBioChem* **18(15)**: 1492–1495. DOI: 10.1002/cbic.201700177.

Picco, A., M. Mund, J. Ries, F. Nédélec, and M. Kaksonen. 2015. Visualizing the functional architecture of the endocytic machinery. *eLife* **4** e04535. DOI: 10.7554/eLife.04535.

Pickering, R. J. 1979. Quality of Water Branch Technical Memorandum 79.10.

Pike, J. A., A. O. Khan, C. Pallini, S. G. Thomas, M. Mund, J. Ries, N. S. Poulter, and I. B. Styles. 2019. Topological data analysis quantifies biological nano-structure from single molecule localization microscopy. *Bioinformatics* **36(5)**: 1614–1621. DOI: 10.1093/bioinformatics/btz788.

Pleiner, T., M. Bates, and D. Görlich. 2018. A toolbox of anti–mouse and anti–rabbit IgG secondary nanobodies. *Journal of Cell Biology* **217(3)**: 1143–1154. DOI: 10.1083/jcb.201709115.

Pollard, T. D. and G. G. Borisy. 2003. Cellular Motility Driven by Assembly and Disassembly of Actin Filaments. *Cell* **112(4)**: 453–465. DOI: 10.1016/S0092-8674(03)00120-X.

Ponten, J. and E. Saksela. 1967. Two established *in vitro* cell lines from human mesenchymal tumours. *International Journal of Cancer* **2(5)**: 434–447. DOI: 10.1002/ijc.2910020505.

Quintero-Monzon, O., A. A. Rodal, B. Strokopytov, S. C. Almo, and B. L. Goode. 2005. Structural and Functional Dissection of the Abp1 ADFH Actin-binding Domain Reveals Versatile *In Vivo* Adapter Functions. *Molecular Biology of the Cell* **16(7)**: 3128–3139. DOI: 10.1091/mbc.e05-01-0059.

R Core Team. 2017. R: A language and environment for statistical computing.

Raths, S., J. Rohrer, F. Crausaz, and H. Riezman. 1993. *end3* and *end4*: two mutants defective in receptor-mediated and fluid-phase endocytosis in *Saccharomyces cerevisiae*. *Journal of Cell Biology* **120(1)**: 55–65. DOI: 10.1083/jcb.120.1.55.

Ratz, M., I. Testa, S. W. Hell, and S. Jakobs. 2015. CRISPR/Cas9-mediated endogenous protein tagging for RESOLFT super-resolution microscopy of living human cells. *Scientific Reports* **5(1)**: 9592. DOI: 10.1038/srep09592.

Reider, A., S. L. Barker, S. K. Mishra, Y. J. Im, L. Maldonado-Báez, J. H. Hurley, L. M. Traub, and B. Wendland. 2009. Syp1 is a conserved endocytic adaptor that contains domains involved in cargo selection and membrane tubulation. *The EMBO Journal* **28(20)**: 3103–3116. DOI: 10.1038/emboj.2009.248.

Reymond, L., T. Huser, V. Ruprecht, and S. Wieser. 2020. Modulation-enhanced localization microscopy. *Journal of Physics: Photonics* **2(4)**: 041001. DOI: 10.1088/2515-7647/ab9eac.

Reymond, L., J. Ziegler, C. Knapp, F.-C. Wang, T. R. Huser, V. Ruprecht, and S. Wieser. 2019. SIMPLE: Structured illumination based point localization estimator with enhanced precision. *Optics Express* **27(17)**: 24578–24590. DOI: 10.1364/OE.27.024578.

Riedl, J., A. H. Crevenna, K. Kessenbrock, J. H. Yu, D. Neukirchen, M. Bista, F. Bradke, D. Jenne, T. A. Holak, Z. Werb, M. Sixt, and R. Wedlich-Soldner. 2008. Lifeact: a versatile marker to visualize F-actin. *Nature Methods* **5(7)**: 605–607. DOI: 10.1038/nmeth.1220.

Ries, J. 2020. SMAP: a modular super-resolution microscopy analysis platform for SMLM data. *Nature Methods* **17(9)**: 870–872. DOI: 10.1038/s41592-020-0938-1.

Ries, J., C. Kaplan, E. Platonova, H. Eghlidi, and H. Ewers. 2012. A simple, versatile method for GFP-based super-resolution microscopy via nanobodies. *Nature Methods* **9(6)**: 582–584. DOI: 10.1038/nmeth.1991.

Rizzo, M. A., M. W. Davidson, and D. W. Piston. 2009. Fluorescent Protein Tracking and Detection: Applications Using Fluorescent Proteins in Living Cells. *Cold Spring Harbor Protocols* **2009(12)**: pdb.top64. DOI: 10.1101/pdb.top64.

Robertson, A. S., E. G. Allwood, A. P. Smith, F. C. Gardiner, R. Costa, S. J. Winder, and K. R. Ayscough. 2009. The WASP Homologue Las17 Activates the Novel Actin-regulatory Activity of Ysc84 to Promote Endocytosis in Yeast. *Molecular Biology of the Cell* **20(6)**: 1618–1628. DOI: 10.1091/mbc.e08-09-0982.

Rodal, A. A., L. Kozubowski, B. L. Goode, D. G. Drubin, and J. H. Hartwig. 2004. Actin and Septin Ultrastructures at the Budding Yeast Cell Cortex. *Molecular Biology of the Cell* **16(1)**: 372–384. DOI: 10.1091/mbc.e04-08-0734.

Rodal, A. A., A. L. Manning, B. L. Goode, and D. G. Drubin. 2003. Negative Regulation of Yeast WASp by Two SH3 Domain-Containing Proteins. *Current Biology* **13(12)**: 1000–1008. DOI: 10.1016/S0960-9822(03)00383-X.

Rossy, J., E. Cohen, K. Gaus, and D. M. Owen. 2014. Method for co-cluster analysis in multichannel single-molecule localisation data. *Histochemistry and Cell Biology* **141(6)**: 605–612. DOI: 10.1007/s00418-014-1208-z.

Rothbauer, U., K. Zolghadr, S. Tillib, D. Nowak, L. Schermelleh, A. Gahl, N. Backmann, K. Conrath, S. Muyldermans, M. C. Cardoso, and H. Leonhardt. 2006. Targeting and tracing antigens in live cells with fluorescent nanobodies. *Nature Methods* **3(11)**: 887–889. DOI: 10.1038/nmeth953.

Rueden, C. T., J. Schindelin, M. C. Hiner, B. E. DeZonia, A. E. Walter, E. T. Arena, and K. W. Eliceiri. 2017. ImageJ2: ImageJ for the next generation of scientific image data. *BMC Bioinformatics* **18(1)**: 529. DOI: 10.1186/s12859-017-1934-z.

Rust, M. J., M. Bates, and X. Zhuang. 2006. Sub-diffraction-limit imaging by stochastic optical reconstruction microscopy (STORM). *Nature Methods* **3(10)**: 793–796. DOI: 10.1038/nmeth929.

Rust, M. J., M. Lakadamyali, F. Zhang, and X. Zhuang. 2004. Assembly of endocytic machinery around individual influenza viruses during viral entry. *Nature Structural & Molecular Biology* **11(6)**: 567–573. DOI: 10.1038/nsmb769.

Saelens, W., R. Cannoodt, H. Todorov, and Y. Saeys. 2019. A comparison of single-cell trajectory inference methods. *Nature Biotechnology* **37(5)**: 547–554. DOI: 10.1038/s41587-019-0071-9.

Salvador-Gallego, R., M. Mund, K. Cosentino, J. Schneider, J. Unsay, U. Schraermeyer, J. Engelhardt, J. Ries, and A. J. García-Sáez. 2016. Bax assembly into rings and arcs in apoptotic mitochondria is linked to membrane pores. *The EMBO Journal* **35(4)**: 389–401. DOI: 10.15252/embj.201593384.

Schaber, J., M. À. Adrover, E. Eriksson, S. Pelet, E. Petelenz-Kurdziel, D. Klein, F. Posas, M. Goksör, M. Peter, S. Hohmann, and E. Klipp. 2010. Biophysical properties of *Saccharomyces cerevisiae* and their relationship with HOG pathway activation. *European Biophysics Journal* **39(11)**: 1547–1556. DOI: 10.1007/s00249-010-0612-0.

Schaefer, L. H., D. Schuster, and J. Schaffer. 2004. Structured illumination microscopy: artefact analysis and reduction utilizing a parameter optimization approach. *Journal of Microscopy* **216(2)**: 165–174. DOI: 10.1111/j.0022-2720.2004.01411.x.

Schafer, D. A., P. B. Jennings, and J. A. Cooper. 1996. Dynamics of capping protein and actin assembly *in vitro*: uncapping barbed ends by polyphosphoinositides. *Journal of Cell Biology* **135(1)**: 169–179. DOI: 10.1083/jcb.135.1.169.

Schermelleh, L., P. M. Carlton, S. Haase, L. Shao, L. Winoto, P. Kner, B. Burke, M. C. Cardoso, D. A. Agard, M. G. L. Gustafsson, H. Leonhardt, and J. W. Sedat. 2008. Subdiffraction Multicolor Imaging of the Nuclear Periphery with 3D Structured Illumination Microscopy. *Science* **320(5881)**: 1332–1336. DOI: 10.1126/science.1156947.

Schindelin, J., I. Arganda-Carreras, E. Frise, V. Kaynig, M. Longair, T. Pietzsch, S. Preibisch, C. T. Rueden, S. Saalfeld, B. Schmid, J.-Y. Tinevez, D. J. White, V. Hartenstein, K. W.

Eliceiri, P. Tomancak, and A. Cardona. 2012. Fiji: an open-source platform for biological-image analysis. *Nature Methods* **9(7)**: 676–682. DOI: 10.1038/nmeth.2019.

Schlichthaerle, T., A. S. Eklund, F. Schueder, M. T. Strauss, C. Tiede, A. Curd, J. Ries, M. Peckham, D. C. Tomlinson, and R. Jungmann. 2018. Site-Specific Labeling of Affimers for DNA-PAINT Microscopy. *Angewandte Chemie International Edition* **57(34)**: 11060–11063. DOI: 10.1002/anie.201804020.

Schmid, S. L. 2017. Reciprocal regulation of signaling and endocytosis: Implications for the evolving cancer cell. *Journal of Cell Biology* **216(9)**: 2623–2632. DOI: 10.1083/jcb.201705017.

Schmidt, R., C. A. Wurm, S. Jakobs, J. Engelhardt, A. Egner, and S. W. Hell. 2008. Spherical nanosized focal spot unravels the interior of cells. *Nature Methods* **5(6)**: 539–544. DOI: 10.1038/nmeth.1214.

Schöneberg, J., D. Dambournet, T.-L. Liu, R. Forster, D. Hockemeyer, E. Betzig, D. G. Drubin, and D. Barber. 2018. 4D cell biology: big data image analytics and lattice light-sheet imaging reveal dynamics of clathrin-mediated endocytosis in stem cell–derived intestinal organoids. *Molecular Biology of the Cell* **29(24)**: 2959–2968. DOI: 10.1091/mbc.E18-06-0375.

Schroeder, D., J. Deschamps, A. Dasgupta, U. Matti, and J. Ries. 2019. A cost-efficient open source laser engine for microscopy. *Biomedical Optics Express* **11(2)**: 609–623. DOI: 10.1364/BOE.380815.

Schroeder, L. K., A. E. S. Barentine, H. Merta, S. Schweighofer, Y. Zhang, D. Baddeley, J. Bewersdorf, and S. Bahmanyar. 2018. Dynamic nanoscale morphology of the ER surveyed by STED microscopy. *Journal of Cell Biology* **218(1)**: 83–96. DOI: 10.1083/jcb.201809107.

Schueder, F., J. Stein, F. Stehr, A. Auer, B. Sperl, M. T. Strauss, P. Schwille, and R. Jungmann. 2019. An order of magnitude faster DNA-PAINT imaging by optimized sequence design and buffer conditions. *Nature Methods* **16(11)**: 1101–1104. DOI: 10.1038/s41592-019-0584-7.

Sengupta, P., T. Jovanovic-Talisman, D. Skoko, M. Renz, S. L. Veatch, and J. Lippincott-Schwartz. 2011. Probing protein heterogeneity in the plasma membrane using PALM and pair correlation analysis. *Nature Methods* **8(11)**: 969–975. DOI: 10.1038/nmeth.1704.

Shaner, N. C., G. H. Patterson, and M. W. Davidson. 2007. Advances in fluorescent protein technology. *Journal of Cell Science* **120(24)**: 4247–4260. DOI: 10.1242/jcs.005801.

Shannon, C. E. 1949. Communication in the Presence of Noise. *Proceedings of the IRE* **37(1)**: 10–21. DOI: 10.1109/JRPROC.1949.232969.

Shao, L., P. Kner, E. H. Rego, and M. G. L. Gustafsson. 2011. Super-resolution 3D microscopy of live whole cells using structured illumination. *Nature Methods* **8(12)**: 1044–1046. DOI: 10.1038/nmeth.1734.

Sharonov, A. and R. M. Hochstrasser. 2006. Wide-field subdiffraction imaging by accumulated binding of diffusing probes. *Proceedings of the National Academy of Sciences* **103(50)**: 18911–18916. DOI: 10.1073/pnas.0609643104.

Shi, X., J. Lim, and T. Ha. 2010. Acidification of the Oxygen Scavenging System in Single-Molecule Fluorescence Studies: *In Situ* Sensing with a Ratiometric Dual-Emission Probe. *Analytical Chemistry* **82(14)**: 6132–6138. DOI: 10.1021/ac1008749.

Shroff, H., C. G. Galbraith, J. A. Galbraith, and E. Betzig. 2008. Live-cell photoactivated localization microscopy of nanoscale adhesion dynamics. *Nature Methods* **5(5)**: 417–423. DOI: 10.1038/nmeth.1202.

Shroff, H., C. G. Galbraith, J. A. Galbraith, H. White, J. M. Gillette, S. Olenych, M. W. Davidson, and E. Betzig. 2007. Dual-color superresolution imaging of genetically expressed probes within individual adhesion complexes. *Proceedings of the National Academy of Sciences* **104(51)**: 20308–20313. DOI: 10.1073/pnas.0710517105.

Shtengel, G., J. A. Galbraith, C. G. Galbraith, J. Lippincott-Schwartz, J. M. Gillette, S. Manley, R. Sougrat, C. M. Waterman, P. Kanchanawong, M. W. Davidson, R. D. Fetter, and H. F. Hess. 2009. Interferometric fluorescent super-resolution microscopy resolves 3D cellular ultrastructure. *Proceedings of the National Academy of Sciences* **106(9)**: 3125–3130. DOI: 10.1073/pnas.0813131106.

Sieben, C., N. Banterle, K. M. Douglass, P. Gönczy, and S. Manley. 2018. Multicolor single-particle reconstruction of protein complexes. *Nature Methods* **15(10)**: 777–780. DOI: 10.1038/s41592-018-0140-x.

Sirotkin, V., J. Berro, K. Macmillan, L. Zhao, and T. D. Pollard. 2010. Quantitative Analysis of the Mechanism of Endocytic Actin Patch Assembly and Disassembly in Fission Yeast. *Molecular Biology of the Cell* **21(16)**: 2894–2904. DOI: 10.1091/mbc.e10-02-0157.

Skruzny, M., T. Brach, R. Ciuffa, S. Rybina, M. Wachsmuth, and M. Kaksonen. 2012. Molecular basis for coupling the plasma membrane to the actin cytoskeleton during clathrin-mediated endocytosis. *Proceedings of the National Academy of Sciences* **109(38)**: E2533–E2542. DOI: 10.1073/pnas.1207011109.

Skruzny, M., E. Pohl, S. Gnoth, G. Malengo, and V. Sourjik. 2020. The protein architecture of the endocytic coat analyzed by FRET microscopy. *Molecular Systems Biology* **16(5)**: e9009. DOI: 10.15252/msb.20199009.

Sochacki, K. A., A. M. Dickey, M.-P. Strub, and J. W. Taraska. 2017. Endocytic proteins are partitioned at the edge of the clathrin lattice in mammalian cells. *Nature Cell Biology* **19(4)**: 352–361. DOI: 10.1038/ncb3498.

Sochacki, K. A., B. L. Heine, G. J. Haber, J. R. Jimah, B. Prasai, M. A. Alfonzo-Mendez, A. D. Roberts, A. Somasundaram, J. E. Hinshaw, and J. W. Taraska. 2020. The structure and spontaneous curvature of clathrin lattices at the plasma membrane. *bioRxiv*: 2020.07.18.207258. DOI: 10.1101/2020.07.18.207258.

Sofroniew, N., T. J. Lambert, K. Evans, J. Nunez-Iglesias, K. Yamauchi, A. C. Solak, G. Bokota, G. Buckley, ziyangczi, T. Tung, J. Freeman, M. Bussonnier, P. Boone, P. Winston, Hector, L. Royer, H. Har-Gil, DragaDoncila, S. Axelrod, A. Rokem, Bryant, J. Kiggins, M. Huang, P. Vemuri, R. Dunham, T. Manz, jakirkham, C. Wood, A. de Siqueira, and B. Chopra. 2020. napari/napari: 0.3.6rc2. DOI: 10.5281/zenodo.3951241.

Sograte-Idrissi, S., T. Schlichthaerle, C. J. Duque-Afonso, M. Alevra, S. Strauss, T. Moser, R. Jungmann, S. O. Rizzoli, and F. Opazo. 2020. Circumvention of common labelling artefacts using secondary nanobodies. *Nanoscale* **12(18)**: 10226–10239. DOI: 10.1039/D0NR00227E.

Sorkin, A. 2004. Cargo recognition during clathrin-mediated endocytosis: a team effort. *Current Opinion in Cell Biology* **16(4)**: 392–399. DOI: 10.1016/j.ceb.2004.06.001.

Soulard, A., S. Friant, C. Fitterer, C. Orange, G. Kaneva, G. Mirey, and B. Winsor. 2005. The WASP/Las17p-interacting protein Bzz1p functions with Myo5p in an early stage of endocytosis. *Protoplasma* **226(1)**: 89–101. DOI: 10.1007/s00709-005-0108-4.

Spahn, C., U. Endesfelder, and M. Heilemann. 2014. Super-resolution imaging of *Escherichia coli* nucleoids reveals highly structured and asymmetric segregation during fast growth. *Journal of Structural Biology* **185(3)**: 243–249. DOI: 10.1016/j.jsb.2014.01.007.

Speiser, A., L.-R. Müller, U. Matti, C. J. Obara, W. R. Legant, A. Kreshuk, J. H. Macke, J. Ries, and S. C. Turaga. 2020. Deep learning enables fast and dense single-molecule localization with high accuracy. *bioRxiv*: 2020.10.26.355164. DOI: 10.1101/2020.10.26.355164.

Stehr, F., J. Stein, F. Schueder, P. Schwille, and R. Jungmann. 2019. Flat-top TIRF illumination boosts DNA-PAINT imaging and quantification. *Nature Communications* **10(1)**: 1268. DOI: 10.1038/s41467-019-09064-6.

Stephan, T., A. Roesch, D. Riedel, and S. Jakobs. 2019. Live-cell STED nanoscopy of mitochondrial cristae. *Scientific Reports* **9(1)**: 12419. DOI: 10.1038/s41598-019-48838-2.

Stimpson, H. E. M., C. P. Toret, A. T. Cheng, B. S. Pauly, and D. G. Drubin. 2009. Early-Arriving Syp1p and Ede1p Function in Endocytic Site Placement and Formation in Budding Yeast. *Molecular Biology of the Cell* **20(22)**: 4640–4651. DOI: 10.1091/mbc.e09-05-0429.

Strauss, S. and R. Jungmann. 2020. Up to 100-fold speed-up and multiplexing in optimized DNA-PAINT. *Nature Methods* **17(8)**: 789–791. DOI: 10.1038/s41592-020-0869-x.

Subach, F. V., G. H. Patterson, S. Manley, J. M. Gillette, J. Lippincott-Schwartz, and V. V. Verkhusha. 2009. Photoactivatable mCherry for high-resolution two-color fluorescence microscopy. *Nature Methods* **6(2)**: 153–159. DOI: 10.1038/nmeth.1298.

Sun, D.-e., X. Fan, Y. Shi, H. Zhang, Z. Huang, B. Cheng, Q. Tang, W. Li, Y. Zhu, J. Bai, W. Liu, Y. Li, X. Wang, X. Lei, and X. Chen. 2020. Click-ExM enables expansion microscopy for all biomolecules. *Nature Methods*. DOI: 10.1038/s41592-020-01005-2.

Sun, X., A. Zhang, B. Baker, L. Sun, A. Howard, J. Buswell, D. Maurel, A. Masharina, K. Johnsson, C. J. Noren, M.-Q. Xu, and I. R. Corrêa. 2011. Development of SNAP-Tag Fluorogenic Probes for Wash-Free Fluorescence Imaging. *ChemBioChem* **12(14)**: 2217–2226. DOI: 10.1002/cbic.201100173.

Sun, Y., N. T. Leong, T. Wong, and D. G. Drubin. 2015. A Pan1/End3/Sla1 complex links Arp2/3-mediated actin assembly to sites of clathrin-mediated endocytosis. *Molecular Biology of the Cell* **26(21)**: 3841–3856. DOI: 10.1091/mbc.E15-04-0252.

Sun, Y., A. C. Martin, and D. G. Drubin. 2006. Endocytic Internalization in Budding Yeast Requires Coordinated Actin Nucleation and Myosin Motor Activity. *Developmental Cell* **11(1)**: 33–46. DOI: 10.1016/j.devcel.2006.05.008.

Sun, Y., J. Schöneberg, X. Chen, T. Jiang, C. Kaplan, K. Xu, T. D. Pollard, and D. G. Drubin. 2019. Direct comparison of clathrin-mediated endocytosis in budding and fission yeast reveals conserved and evolvable features. *eLife* **8** e50749. DOI: 10.7554/eLife.50749.

Sunbul, M., J. Lackner, A. Martin, D. Englert, B. Hacene, K. Nienhaus, G. U. Nienhaus, and A. Jäschke. 2020. RhoBAST - A Rhodamine-Binding Aptamer for Super-Resolution RNA Imaging. *bioRxiv*: 2020.03.12.988782. DOI: 10.1101/2020.03.12.988782.

Swoboda, M., J. Henig, H.-M. Cheng, D. Brugger, D. Haltrich, N. Plumeré, and M. Schlierf. 2012. Enzymatic Oxygen Scavenging for Photostability without pH Drop in Single-Molecule Experiments. *ACS Nano* **6(7)**: 6364–6369. DOI: 10.1021/nn301895c.

Szymborska, A., A. de Marco, N. Daigle, V. C. Cordes, J. A. G. Briggs, and J. Ellenberg. 2013. Nuclear Pore Scaffold Structure Analyzed by Super-Resolution Microscopy and Particle Averaging. *Science* **341(6146)**: 655–658. DOI: 10.1126/science.1240672.

Tam, J., G. A. Cordier, J. S. Borbely, Á. S. Álvarez, and M. Lakadamyali. 2014. Cross-Talk-Free Multi-Color STORM Imaging Using a Single Fluorophore. *PLOS ONE* **9(7)**: e101772. DOI: 10.1371/journal.pone.0101772.

Tandon, N., K. N. Thakkar, E. L. LaGory, Y. Liu, and A. J. Giaccia. 2018. Generation of Stable Expression Mammalian Cell Lines Using Lentivirus. *Bio-Protocol* **8(21)**: e3073–e3073. DOI: 10.21769/BioProtoc.3073.

Tang, H.-Y., J. Xu, and M. Cai. 2000. Pan1p, End3p, and Sla1p, Three Yeast Proteins Required for Normal Cortical Actin Cytoskeleton Organization, Associate with Each Other and Play Essential Roles in Cell Wall Morphogenesis. *Molecular and Cellular Biology* **20(1)**: 12–25. DOI: 10.1128/MCB.20.1.12-25.2000.

Testa, I., N. T. Urban, S. Jakobs, C. Eggeling, K. I. Willig, and S. W. Hell. 2012. Nanoscopy of Living Brain Slices with Low Light Levels. *Neuron* **75(6)**: 992–1000. DOI: 10.1016/j.neuron.2012.07.028.

Testa, I., C. A. Wurm, R. Medda, E. Rothermel, C. von Middendorff, J. Fölling, S. Jakobs, A. Schönle, S. W. Hell, and C. Eggeling. 2010. Multicolor Fluorescence Nanoscopy in Fixed and Living Cells by Exciting Conventional Fluorophores with a Single Wavelength. *Biophysical Journal* **99(8)**: 2686–2694. DOI: 10.1016/j.bpj.2010.08.012.

Thevathasan, J. V., M. Kahnwald, K. Cieśliński, P. Hoess, S. K. Peneti, M. Reitberger, D. Heid, K. C. Kasuba, S. J. Hoerner, Y. Li, Y.-L. Wu, M. Mund, U. Matti, P. M. Pereira, R. Henriques, B. Nijmeijer, M. Kueblbeck, V. J. Sabinina, J. Ellenberg, and J. Ries. 2019. Nuclear pores as versatile reference standards for quantitative superresolution microscopy. *Nature Methods* **16(10)**: 1045–1053. DOI: 10.1038/s41592-019-0574-9.

Thompson, R. E., D. R. Larson, and W. W. Webb. 2002. Precise Nanometer Localization Analysis for Individual Fluorescent Probes. *Biophysical Journal* **82(5)**: 2775–2783. DOI: 10.1016/S0006-3495(02)75618-X.

Tiede, C., R. Bedford, S. J. Heseltine, G. Smith, I. Wijetunga, R. Ross, D. AlQallaf, A. P. Roberts, A. Balls, A. Curd, R. E. Hughes, H. Martin, S. R. Needham, L. C. Zanetti-Domingues, Y. Sadigh, T. P. Peacock, A. A. Tang, N. Gibson, H. Kyle, G. W. Platt, N. Ingram, T. Taylor, L. P. Coletta, I. Manfield, M. Knowles, S. Bell, F. Esteves, A. Maqbool, R. K. Prasad, M. Drinkhill, R. S. Bon, V. Patel, S. A. Goodchild, M. Martin-Fernandez, R. J. Owens, J. E. Nettleship, M. E. Webb, M. Harrison, J. D. Lippiat, S. Ponnambalam, M. Peckham, A. Smith, P. K. Ferrigno, M. Johnson, M. J. McPherson, and D. C. Tomlinson. 2017. Affimer proteins are versatile and renewable affinity reagents. *eLife* **6** e24903. DOI: 10.7554/eLife.24903.

Tillberg, P. W. and F. Chen. 2019. Expansion Microscopy: Scalable and Convenient Super-Resolution Microscopy. *Annual Review of Cell and Developmental Biology* **35(1)**: 683–701. DOI: 10.1146/annurev-cellbio-100818-125320.

Tillberg, P. W., F. Chen, K. D. Piatkevich, Y. Zhao, C.-C. Yu, B. P. English, L. Gao, A. Martorell, H.-J. Suk, F. Yoshida, E. M. DeGennaro, D. H. Roossien, G. Gong, U. Seneviratne, S. R. Tannenbaum, R. Desimone, D. Cai, and E. S. Boyden. 2016. Protein-retention expansion microscopy of cells and tissues labeled using standard fluorescent proteins and antibodies. *Nature Biotechnology* **34(9)**: 987–992. DOI: 10.1038/nbt.3625.

Tolsma, T. O., H. P. Febvre, D. M. Olson, and S. M. D. Pietro. 2020. Cargo-mediated recruitment of the endocytic adaptor protein Sla1 in *S. cerevisiae*. *Journal of Cell Science* **133(19)**: jcs247684. DOI: 10.1242/jcs.247684.

Tong, A. H. Y. and C. Boone. 2006. Synthetic Genetic Array Analysis in *Saccharomyces cerevisiae*. *Yeast Protocol*. Humana Press: 171–191. ISBN: 978-1-59259-958-5. DOI: 10.1385/1-59259-958-3:171.

Tong, A. H. Y. and C. Boone. 2007. High-Throughput Strain Construction and Systematic Synthetic Lethal Screening in *Saccharomyces cerevisiae*. *Methods in Microbiology*. **36** Academic Press: 369–707. DOI: 10.1016/S0580-9517(06)36016-3.

Tong, A. H. Y., M. Evangelista, A. B. Parsons, H. Xu, G. D. Bader, N. Pagé, M. Robinson, S. Raghibizadeh, C. W. V. Hogue, H. Bussey, B. J. Andrews, M. Tyers, and C. Boone. 2001. Systematic Genetic Analysis with Ordered Arrays of Yeast Deletion Mutants. *Science* **294(5550)**: 2364–2368. DOI: 10.1126/science.1065810.

Traenkle, B., F. Emele, R. Anton, O. Poetz, R. S. Haeussler, J. Maier, P. D. Kaiser, A. M. Scholz, S. Nueske, A. Buchfellner, T. Romer, and U. Rothbauer. 2015. Monitoring Interactions and Dynamics of Endogenous Beta-catenin With Intracellular Nanobodies in Living Cells. *Molecular & Cellular Proteomics* **14(3)**: 707–723. DOI: 10.1074/mcp.M114.044016.

Traub, L. M. and J. S. Bonifacino. 2013. Cargo Recognition in Clathrin-Mediated Endocytosis. *Cold Spring Harbor Perspectives in Biology* **5(11)**: a016790. DOI: 10.1101/cshperspect.a016790.

Truckenbrodt, S., M. Maidorn, D. Crzan, H. Wildhagen, S. Kabatas, and S. O. Rizzoli. 2018. X10 expansion microscopy enables 25-nm resolution on conventional microscopes. *EMBO reports* **19(9)**: e45836. DOI: 10.15252/embr.201845836.

Tsutsui, H., S. Karasawa, H. Shimizu, N. Nukina, and A. Miyawaki. 2005. Semi-rational engineering of a coral fluorescent protein into an efficient highlighter. *EMBO reports* **6(3)**: 233–238. DOI: 10.1038/sj.embor.7400361.

Turkowyd, B., A. Balinovic, D. Virant, H. G. G. Carnero, F. Caldana, M. Endesfelder, D. Bourgeois, and U. Endesfelder. 2017. A General Mechanism of Photoconversion of Green-to-Red Fluorescent Proteins Based on Blue and Infrared Light Reduces Phototoxicity in Live-Cell Single-Molecule Imaging. *Angewandte Chemie International Edition* **56(38)**: 11634–11639. DOI: 10.1002/anie.201702870.

Ungewickell, E. J. and D. Branton. 1981. Assembly units of clathrin coats. *Nature* **289(5796)**: 420–422. DOI: 10.1038/289420a0.

Unlu, G., D. S. Levic, D. B. Melville, and E. W. Knapik. 2014. Trafficking mechanisms of extracellular matrix macromolecules: Insights from vertebrate development and human diseases. *The International Journal of Biochemistry & Cell Biology* **47** 57–67. DOI: 10.1016/j.biocel.2013.11.005.

Uribe-Querol, E. and C. Rosales. 2020. Phagocytosis: Our Current Understanding of a Universal Biological Process. *Frontiers in Immunology* **11** 1066. DOI: 10.3389/fimmu.2020.01066.

Urnov, F. D., E. J. Rebar, M. C. Holmes, H. S. Zhang, and P. D. Gregory. 2010. Genome editing with engineered zinc finger nucleases. *Nature Reviews Genetics* **11(9)**: 636–646. DOI: 10.1038/nrg2842.

Valley, C. C., S. Liu, D. S. Lidke, and K. A. Lidke. 2015. Sequential Superresolution Imaging of Multiple Targets Using a Single Fluorophore. *PLOS ONE* **10(4)**: e0123941. DOI: 10.1371/journal.pone.0123941.

van der Walt, S. J., J. L. Schönberger, J. Nunez-Iglesias, F. Boulogne, J. D. Warner, N. Yager, E. Gouillart, and T. Yu. 2014. scikit-image: image processing in Python. *PeerJ* **2** e453. DOI: 10.7717/peerj.453.

van Rossum, G. and F. L. Drake. 2009. Python 3 Reference Manual. CreateSpace. ISBN: 978-1-4414-1269-0.

Vasicova, P., M. Rinnerthaler, D. Haskova, L. Novakova, I. Malcova, M. Breitenbach, and J. Hasek. 2016. Formaldehyde fixation is detrimental to actin cables in glucose-depleted *S. cerevisiae* cells. *Microbial Cell* **3(5)**: 206–214. DOI: 10.15698/mic2016.05.499.

Vaughan, J. C., G. T. Dempsey, E. Sun, and X. Zhuang. 2013. Phosphine Quenching of Cyanine Dyes as a Versatile Tool for Fluorescence Microscopy. *Journal of the American Chemical Society* **135(4)**: 1197–1200. DOI: 10.1021/ja3105279.

Vida, T. A. and S. D. Emr. 1995. A new vital stain for visualizing vacuolar membrane dynamics and endocytosis in yeast. *Journal of Cell Biology* **128(5)**: 779–792. DOI: 10.1083/jcb.128.5.779.

Virant, D., B. Traenkle, J. Maier, P. D. Kaiser, M. Bodenhöfer, C. Schmees, I. Vojnovic, B. Pisak-Lukáts, U. Endesfelder, and U. Rothbauer. 2018. A peptide tag-specific nanobody enables high-quality labeling for dSTORM imaging. *Nature Communications* **9(1)**: 930. DOI: 10.1038/s41467-018-03191-2.

Virant, D., B. Turkowyd, A. Balinovic, and U. Endesfelder. 2017. Combining Primed Photoconversion and UV-Photoactivation for Aberration-Free, Live-Cell Compliant Multi-Color Single-Molecule Localization Microscopy Imaging. *International Journal of Molecular Sciences* **18(7)**: 1524. DOI: 10.3390/ijms18071524.

Virtanen, P., R. Gommers, T. E. Oliphant, M. Haberland, T. Reddy, D. Cournapeau, E. Burovski, P. Peterson, W. Weckesser, J. Bright, S. J. van der Walt, M. Brett, J. Wilson, K. J. Millman, N. Mayorov, A. R. J. Nelson, E. Jones, R. Kern, E. Larson, C. J. Carey, İ. Polat, Y. Feng, E. W. Moore, J. VanderPlas, D. Laxalde, J. Perktold, R. Cimrman, I. Henriksen, E. A. Quintero, C. R. Harris, A. M. Archibald, A. H. Ribeiro, F. Pedregosa, and P. van Mulbregt. 2020. SciPy 1.0: fundamental algorithms for scientific computing in Python. *Nature Methods* **17(3)**: 261–272. DOI: 10.1038/s41592-019-0686-2.

von Appen, A., J. Kosinski, L. Sparks, A. Ori, A. L. DiGuilio, B. Vollmer, M.-T. Mackmull, N. Banterle, L. Parca, P. Kastritis, K. Buczak, S. Mosalaganti, W. Hagen, A. Andres-Pons, E. A. Lemke, P. Bork, W. Antonin, J. S. Glavy, K. H. Bui, and M. Beck. 2015. *In situ* structural analysis of the human nuclear pore complex. *Nature* **526(7571)**: 140–143. DOI: 10.1038/nature15381.

Vreja, I. C., I. Nikić, F. Göttfert, M. Bates, K. Kröhnert, T. F. Outeiro, S. W. Hell, E. A. Lemke, and S. O. Rizzoli. 2015. Super-resolution Microscopy of Clickable Amino Acids Reveals the Effects of Fluorescent Protein Tagging on Protein Assemblies. *ACS Nano* **9(11)**: 11034–11041. DOI: 10.1021/acsnano.5b04434.

Wagner, A. R., Q. Luan, S.-L. Liu, and B. J. Nolen. 2013. Dip1 Defines a Class of Arp2/3 Complex Activators that Function without Preformed Actin Filaments. *Current Biology* **23(20)**: 1990–1998. DOI: 10.1016/j.cub.2013.08.029.

Wagner, H. J., S. Wehrle, E. Weiss, M. Cavallari, and W. Weber. 2018. A Two-Step Approach for the Design and Generation of Nanobodies. *International Journal of Molecular Sciences* **19(11)**: 3444. DOI: 10.3390/ijms19113444.

Wäldchen, S., J. Lehmann, T. Klein, S. van de Linde, and M. Sauer. 2015. Light-induced cell damage in live-cell super-resolution microscopy. *Scientific Reports* **5(1)**: 15348. DOI: 10.1038/srep15348.

Wang, G., J. R. Moffitt, and X. Zhuang. 2018. Multiplexed imaging of high-density libraries of RNAs with MERFISH and expansion microscopy. *Scientific Reports* **8(1)**: 4847. DOI: 10.1038/s41598-018-22297-7.

Wang, S., J. R. Moffitt, G. T. Dempsey, X. S. Xie, and X. Zhuang. 2014a. Characterization and development of photoactivatable fluorescent proteins for single-molecule-based superresolution imaging. *Proceedings of the National Academy of Sciences* **111(23)**: 8452–8457. DOI: 10.1073/pnas.1406593111.

Wang, Y., J. M. Lamim Ribeiro, and P. Tiwary. 2020. Machine learning approaches for analyzing and enhancing molecular dynamics simulations. *Current Opinion in Structural Biology* **61** 139–145. DOI: 10.1016/j.sbi.2019.12.016.

Wang, Y., J. Schnitzbauer, Z. Hu, X. Li, Y. Cheng, Z.-L. Huang, and B. Huang. 2014b. Localization events-based sample drift correction for localization microscopy with redundant cross-correlation algorithm. *Optics Express* **22(13)**: 15982–15991. DOI: 10.1364/OE.22.015982.

Warren, D. T., P. D. Andrews, C. W. Gourlay, and K. R. Ayscough. 2002. Sla1p couples the yeast endocytic machinery to proteins regulating actin dynamics. *Journal of Cell Science* **115(8)**: 1703–1715.

Waskom, M., O. Botvinnik, M. Gelbart, J. Ostblom, P. Hobson, S. Lukauskas, D. C. Gemperline, T. Augspurger, Y. Halchenko, J. Warmenhoven, J. B. Cole, J. de Ruiter, J. VanderPlas, S. Hoyer, C. Pye, A. Miles, C. Swain, K. Meyer, M. Martin, P. Bachant, E. A. Quintero, G. Kunter, S. Villalba, Brian, C. Fitzgerald, C. G. Evans, M. L. Williams, D. O'Kane, T. Yarkoni, and T. Brunner. 2020. mwaskom/seaborn: v0.11.0 (September 2020). DOI: 10.5281/zenodo.4019146.

Weber, M., M. Leutenegger, S. Stoldt, S. Jakobs, T. S. Mihaila, A. N. Butkevich, and S. W. Hell. 2020. MINSTED fluorescence localization and nanoscopy. *bioRxiv*: 2020.10.31.363424. DOI: 10.1101/2020.10.31.363424.

Weiland, Y., P. Lemmer, and C. Cremer. 2011. Combining FISH with localisation microscopy: Super-resolution imaging of nuclear genome nanostructures. *Chromosome Research* **19(1)**: 5–23. DOI: 10.1007/s10577-010-9171-6.

Weill, U., G. Krieger, Z. Avihou, R. Milo, M. Schuldiner, and D. Davidi. 2019. Assessment of GFP Tag Position on Protein Localization and Growth Fitness in Yeast. *Journal of Molecular Biology* **431(3)**: 636–641. DOI: 10.1016/j.jmb.2018.12.004.

Weiss, D. R. and M. Levitt. 2009. Can Morphing Methods Predict Intermediate Structures? *Journal of Molecular Biology* **385(2)**: 665–674. DOI: 10.1016/j.jmb.2008.10.064.

Wendland, B., J. M. McCaffery, Q. Xiao, and S. D. Emr. 1996. A novel fluorescence-activated cell sorter-based screen for yeast endocytosis mutants identifies a yeast homologue of mammalian eps15. *Journal of Cell Biology* **135(6)**: 1485–1500. DOI: 10.1083/jcb.135.6.1485.

Wendland, B. and S. D. Emr. 1998. Pan1p, Yeast eps15, Functions as a Multivalent Adaptor That Coordinates Protein–Protein Interactions Essential for Endocytosis. *Journal of Cell Biology* **141(1)**: 71–84. DOI: 10.1083/jcb.141.1.71.

Wendland, B., K. E. Steece, and S. D. Emr. 1999. Yeast epsins contain an essential N-terminal ENTH domain, bind clathrin and are required for endocytosis. *The EMBO Journal* **18(16)**: 4383–4393. DOI: 10.1093/emboj/18.16.4383.

Wesp, A., L. Hicke, J. Palecek, R. Lombardi, T. Aust, A. Munn, and H. Riezman. 1997. End4p/Sla2p Interacts with Actin-associated Proteins for Endocytosis in *Saccharomyces cerevisiae*. *Molecular Biology of the Cell* **8(11)**: 2291–2306. DOI: 10.1091/mbc.8.11.2291.

Wickham, H. 2016. ggplot2: Elegant Graphics for Data Analysis. Springer. ISBN: 978-0-387-98140-6.

Wiederkehr, A., K. D. Meier, and H. Riezman. 2001. Identification and characterization of *Saccharomyces cerevisiae* mutants defective in fluid-phase endocytosis. *Yeast* **18(8)**: 759–773. DOI: 10.1002/yea.726.

Wilfling, F., C.-W. Lee, P. S. Erdmann, Y. Zheng, D. Sherpa, S. Jentsch, B. Pfander, B. A. Schulman, and W. Baumeister. 2020. A Selective Autophagy Pathway for Phase-Separated Endocytic Protein Deposits. *Molecular Cell* **80(5)**: 764–778.e7. DOI: 10.1016/j.molcel.2020.10.030.

Winston, F., C. Dollard, and S. L. Ricupero-Hovasse. 1995. Construction of a set of convenient *Saccharomyces cerevisiae* strains that are isogenic to S288C. *Yeast* **11(1)**: 53–55. DOI: 10.1002/yea.320110107.

Winter, D., T. Lechler, and R. Li. 1999. Activation of the yeast Arp2/3 complex by Bee1p, a WASP-family protein. *Current Biology* **9(9)**: 501–505. DOI: 10.1016/S0960-9822(99)80218-8.

Wu, F. and P. J. Yao. 2009. Clathrin-mediated endocytosis and Alzheimer's disease: An update. *Ageing Research Reviews* **8(3)**: 147–149. DOI: 10.1016/j.arr.2009.03.002.

Wu, Y.-L., A. Tschanz, L. Krupnik, and J. Ries. 2020. Quantitative Data Analysis in Single-Molecule Localization Microscopy. *Trends in Cell Biology* **30(11)**: 837–851. DOI: 10.1016/j.tcb.2020.07.005.

Wu, Y. and H. Shroff. 2018. Faster, sharper, and deeper: structured illumination microscopy for biological imaging. *Nature Methods* **15(12)**: 1011–1019. DOI: 10.1038/s41592-018-0211-z.

Wulf, E., A. Deboben, F. A. Bautz, H. Faulstich, and T. Wieland. 1979. Fluorescent phallotoxin, a tool for the visualization of cellular actin. *Proceedings of the National Academy of Sciences* **76(9)**: 4498–4502. DOI: 10.1073/pnas.76.9.4498.

Xu, K., H. P. Babcock, and X. Zhuang. 2012. Dual-objective STORM reveals three-dimensional filament organization in the actin cytoskeleton. *Nature Methods* **9(2)**: 185–188. DOI: 10.1038/nmeth.1841.

Xu, K., G. Zhong, and X. Zhuang. 2013. Actin, Spectrin, and Associated Proteins Form a Periodic Cytoskeletal Structure in Axons. *Science* **339(6118)**: 452–456. DOI: 10.1126/science.1232251.

Yarar, D., C. M. Waterman-Storer, and S. L. Schmid. 2005. A Dynamic Actin Cytoskeleton Functions at Multiple Stages of Clathrin-mediated Endocytosis. *Molecular Biology of the Cell* **16(2)**: 964–975. DOI: 10.1091/mbc.e04-09-0774.

Yeung, B. G., H. L. Phan, and G. S. Payne. 1999. Adaptor Complex-independent Clathrin Function in Yeast. *Molecular Biology of the Cell* **10(11)**: 3643–3659. DOI: 10.1091/mbc.10.11.3643.

York, A. G., S. H. Parekh, D. D. Nogare, R. S. Fischer, K. Temprine, M. Mione, A. B. Chitnis, C. A. Combs, and H. Shroff. 2012. Resolution doubling in live, multicellular organisms via multifocal structured illumination microscopy. *Nature Methods* **9(7)**: 749–754. DOI: 10.1038/nmeth.2025.

Zakeri, B., J. O. Fierer, E. Celik, E. C. Chittock, U. Schwarz-Linek, V. T. Moy, and M. Howarth. 2012. Peptide tag forming a rapid covalent bond to a protein, through engineering a bacterial adhesin. *Proceedings of the National Academy of Sciences* **109(12)**: E690–E697. DOI: 10.1073/pnas.1115485109.

Zhang, Y., L. K. Schroeder, M. D. Lessard, P. Kidd, J. Chung, Y. Song, L. Benedetti, Y. Li, J. Ries, J. B. Grimm, L. D. Lavis, P. D. Camilli, J. E. Rothman, D. Baddeley, and J. Bewersdorf. 2020. Nanoscale subcellular architecture revealed by multicolor three-dimensional salvaged fluorescence imaging. *Nature Methods* **17(2)**: 225–231. DOI: 10.1038/s41592-019-0676-4.

Zhang, Z., S. J. Kenny, M. Hauser, W. Li, and K. Xu. 2015. Ultrahigh-throughput single-molecule spectroscopy and spectrally resolved super-resolution microscopy. *Nature Methods* **12(10)**: 935–938. DOI: 10.1038/nmeth.3528.

Zhao, T., Y. Wang, Y. Zhai, X. Qu, A. Cheng, S. Du, and M. M. T. Loy. 2015. A user-friendly two-color super-resolution localization microscope. *Optics Express* **23(2)**: 1879–1887. DOI: 10.1364/OE.23.001879.

Zhao, Y., O. Bucur, H. Irshad, F. Chen, A. Weins, A. L. Stancu, E.-Y. Oh, M. DiStasio, V. Torous, B. Glass, I. E. Stillman, S. J. Schnitt, A. H. Beck, and E. S. Boyden. 2017a. Nanoscale imaging of clinical specimens using pathology-optimized expansion microscopy. *Nature Biotechnology* **35(8)**: 757–764. DOI: 10.1038/nbt.3892.

Zhao, Z., B. Xin, L. Li, and Z.-L. Huang. 2017b. High-power homogeneous illumination for super-resolution localization microscopy with large field-of-view. *Optics Express* **25(12)**: 13382–13395. DOI: 10.1364/OE.25.013382.

Zheng, Q., S. Jockusch, Z. Zhou, R. B. Altman, J. D. Warren, N. J. Turro, and S. C. Blanchard. 2012. On the Mechanisms of Cyanine Fluorophore Photostabilization. *The Journal of Physical Chemistry Letters* **3(16)**: 2200–2203. DOI: 10.1021/jz300670p.

Zimmerli, C. E., M. Allegretti, V. Rantos, S. K. Goetz, A. Obarska-Kosinska, I. Zagoriy, A. Halavatyi, J. Mahamid, J. Kosinski, and M. Beck. 2020. Nuclear pores constrict upon energy depletion. *bioRxiv*: 2020.07.30.228585. DOI: 10.1101/2020.07.30.228585.

Zwettler, F. U., S. Reinhard, D. Gambarotto, T. D. M. Bell, V. Hamel, P. Guichard, and M. Sauer. 2020. Molecular resolution imaging by post-labeling expansion single-molecule localization microscopy (Ex-SMLM). *Nature Communications* **11(1)**: 3388. DOI: 10.1038/s41467-020-17086-8.